OPTICAL STUDIES OF SOOT FORMATION

AND THE ADDITION OF ORGANIC PEROXIDES TO FLAMES

by

Klaus Müller-Dethlefs, Dipl.-Chem.

April 1979

A thesis submitted for the degree of
Doctor of Philosophy of the
University of London and for the
Diploma of Imperial College

Department of Chemical Engineering
and Chemical Technology,
Imperial College,
London, S.W.7

ERRATA

Page	Line		Error	To be replaced by
1	2		Wavelegth	Wavelength
1	3		i = 1 to 4	n = 1 to 4
8	7		in nitric oxides	of nitric oxides
16	6		H_2O	N_2O
19	26		or	and
31	9		1.48 E12	1.48 E-2
68	32		over the	over to
145	29		applied for	applied to
146	11		V_V	V_S
147	33		increase	decrease
169	26		nucleation	nuclei
138	2		periodic	peroxidic
		for	vapourization read vapourized etc.	vaporization vaporized etc.

For Ulrike

ABSTRACT

The formation of soot in premixed and diffusion flames is studied by optical techniques and the effect of tertiary-butyl-hydroperoxide (TBHP) and di-tertiary-butylperoxide (DTBP) on soot formation is assessed. Laser light scattering and absorption measurements are used to evaluate the soot particle size and number density, assuming that the particles are spherical and monodisperse.

In all flames, a strong (unpolarised) fluorescence is excited by the laser wavelength of λ = 488 nm. This fluorescence shows no band structure, even with very high resolution spectroscopy. It is put forward that the fluorescence originates from polycyclic aromatic hydrocarbon(s) (radicals) containing more than 10 benzene rings. This is supported by the fluorescence efficiency of 11% and the Rayleigh depolarisation ratio of 0.1 found for the fluorescing molecules.

A new method for size and number density determination is described, which is based on the use of a fluorescence intensity measurement to obtain the correct absorption coefficient for the soot particles only. The soot particle absorption coefficients are found to be inversely proportional to the absorption wavelength - as expected for Rayleigh particles.

The depolarisation of the scattered light on the incident wavelength by the small soot particles in the premixed flames is attributed to anisotropy of refractive index rather than shape. In the diffusion flames, the depolarisation of the scattered light by the larger soot particles is interpreted by shape anisotropy, indicating an agglomeration process.

TBHP addition to premixed flames, in small concentrations, results in an increase in soot particle number density and a decrease in particle size, but the total soot volume fraction is slightly increased. DTBP in higher concentrations reduces number density and particle size in the later flame regions and also delays the onset of soot particle nucleation.

The results for particle size and number density are used to test the prediction of free molecule coagulation theory. The G factor and soot particle surface growth rates are determined.

In diffusion flames, both peroxides cause an increase in soot particle size and number density, when added to the fuel side. When added to the oxidant side, particle size and number density are reduced, but the effects are not very large.

Pyrolysis experiments of ethylene are used to monitor the effects of DTBP on small amounts of oxygen at temperatures below 1600 K. A new, very sensitive technique to measure burning velocities, based on laser Rayleigh scattering, is described. The method combines the porous plug method with optical temperature monitoring at a point above the flame. It is shown that organic peroxides do not increase burning velocity, whereas reductions in burning velocity by small traces of inhibitor could easily be detected.

ACKNOWLEDGEMENTS

I am greatly indebted to Professor F.J. Weinberg for his continuous encouragement and guidance throughout this work and to Dr A.R. Jones for his most helpful advice on light scattering.

It is a pleasure to thank Prof. A. D'Alessio and his colleagues, and Dr G. Prado (Mulhouse, France) for extremely useful discussions during the author's visit to the University of Naples.

I also wish to thank Dr B.R. Haynes (now M.I.T.) for the stimulating co-operation with him at the University of Göttingen, and Prof. H.Gg. Wagner for his continual interest in this work.

I gratefully appreciate the discussions with Prof. A.G. Gaydon, F.R.S., about the spectroscopy part of the work.

My thanks are also due to the Department technical staff, without whose skill and co-operation this project would not have been possible. In particular, I want to thank, for their qualified assistance, the mechanical workshop technicians: Mr R. Harris, Mr T. Stephenson and Mr R. King - for his efforts in building the burner system, the glassblowers: Mr C. Smith and Mr K. Grose, the laboratory technician: Mr A. Harrup and the electronic workshop technicians: Mr L. Tyley, Mr M. Dix, Mr D. Wood and Mr E. Jarrett.

I also want to express my gratitude to Herrn H. Schober for the photograph of the laboratory and, in particular, Mr L. Moulder, for his reproduction of the spectra.

My dedicated thanks are also due to Fr. U. Gaus for her love over these years and to my parents for their encouragement.

I also thank Miss E.R. Anderson for carefully typing the manuscript and correcting my English where necessary, and Mr B. Stallard, for tracing the diagrams.

Last but not least, I wish to express my gratitude to Interox Chemicals Ltd., for sponsorship of this project.

CONTENTS PAGE

PAGE

NOMENCLATURE

λ	Wavelegth of light
σ	Differential scattering cross-section
i_n	Intensity function (i = 1 to 4)
ϵ	Extinction (absorption) coefficient
ϕ	Soot particle volume fraction: $N\cdot(4\pi/3)\cdot a^3$
α	Particle size parameter: $2\pi a/\lambda$
a	Particle radius
N	Particle number density
k_1	Coagulation constant
m	Refractive index: n - ik
$Im\{(m^2-1)/(m^2+2)\}$	Imaginary part of { }
$\lvert(m^2-1)^2/(m^2+2)^2\rvert$	Absolute value of $(m^2-1)^2/(m^2+2)^2$
T_o	Room temperature
T_F	Flame temperature
n_o	Mole number of fresh gas mixture for one mole of ethylene
v_o	Fresh gas flow velocity
n_F	Mole number of burned gas corresponding to one mole of ethylene
v_F	Flow velocity in burned gas

LIST OF FIGURES PAGE

LIST OF PLATES

I INTRODUCTION

During the last decade, protection of the environment from combustion pollutants has been regarded as increasingly important and some remarkable successes have been achieved. Examples include virtually eliminating the London smog which had been due to incomplete and widespread combustion of coal and a reduction of the "Photochemical Smog" in California, caused by sunlight-induced reactions in nitric oxides with unburnt hydrocarbons emitted from internal combustion engines and stationary power plants. The production of some pollutants in flames is strongly related to the efficiency with which a fuel is burnt, so the efforts to decrease pollutant emission and increase combustion efficiency often go hand in hand. Most technical combustion processes are diffusion-controlled flames which maximise pollutants due to incomplete burning (soot, CO, hydrocarbons) and high temperature pollutants (e.g. NO_x) which mainly originate from the near-stoichiometric reaction zone at close to the highest possible (adiabatic) flame temperature[1]. Improvements can be made by burning the reactants premixed (insofar as the properties of the fuel allow this); e.g. a stoichiometric premixed flame does not produce soot or much CO but, because of the high temperatures and long residence times, generates NO_x.

The pollutant with which this work is concerned, is soot. In day to day life soot is a familiar phenomenon. It ranges from the illumination by candles and oil-lamps & radiation of soot from bonfires, to commercial carbon black production, e.g. in the manufacture of rubber. The radiative heat transfer from soot, e.g. in furnace flames, is regarded as highly desirable, whereas its emission from flues is not. Soot and some polynuclear aromatic hydrocarbons simultaneously formed with it are considered pollutants hazardous to human health. The amount of soot emitted into urban air is increasing steadily because of the more widespread use of the diesel engine for automotive transport. In order to control soot emission, the fundamental understanding of the mechanisms involved in its formation, is an essential condition.

Soot formation depends on a variety of parameters which are listed here for premixed and diffusion flames:-

I Premixed Flames

1) Type of fuel
2) C/O ratio (total and local)
3) Temperature (1400 K - 3000 K)
4) Reaction time (flow rate)
5) Heat recirculation (e.g. by radiation)
6) Additives
7) Electrical effects

II Diffusion Flames

(as I)

8) Flow structure (very important)

The appearance of the soot emitted can vary from amorphous carbon to a more graphite-like structure. Also, the amount of chloroform, benzene or toluene extractable material adsorbed on the solid surface can vary considerably.

For a typical flame, a very simplified scheme for the different steps involved in soot formation with an approximate timescale is given below:-

t/msec	
0 - 2	Formation of precursors
1 - 3	Nucleation
2 - 15	Surface growth on nuclei and coalescence of primary particles
5 -	Agglomeration into non-spherical particles
25 -	Soot volume fraction remains nearly constant, provided no oxidation by secondary air occurs.

Because of the availability of high power, stable and reliable CW lasers, a new field of research of combustion processes by optical means, has been opened. It is the main object of this study to use laser light scattering and absorption measurements to gain in situ information about soot particle and gaseous intermediate formation in premixed and diffusion flames. These techniques are then taken up to quantify the influence of a particular class of additives - organic peroxides - on soot formation and to assess their usefulness as combustion promoters. For this part of the project, a new, very sensitive technique of burning velocity measurement is put into practice.

II STATE OF THE ART

II-1 ADDITIVES

A number of workers have investigated the effect of chemicals added to fuels (e.g. diesel oil or gasoline) on their ignition temperatures, burning rates and combustion intensities, the onset of oxidation reactions and sooting. Aliphatic and aromatic nitro compounds and nitric acid esters were mainly studied as active promoters[2-4]. They have the great disadvantage of increased emission of nitric oxides because nearly all of the nitrogen in the fuel additive is transformed to NO and mostly even to NO_2[5].

Using peroxides instead would not give rise to this disadvantage. A number of patents[6-10] claim an increase in cetane number of diesel fuels by 10 - 15 units, when 0.01 - 0.05% of a polymeric organic peroxide or 1 - 5% of a monomeric peroxide (e.g. di-t-butylperoxide) is added to the fuel. Indications have been found of a more complete combustion process, better engine performance and less CO and soot emission in the exhaust.

The difference in action between the polymeric and monomeric peroxides is explained by the much faster vaporisation and thermal decomposition of the monomeric peroxide compared to the polymer in the supply line. Thus the actual amount of monomeric peroxide reaching the engine cylinder may be considerably smaller than the amount added to the fuel. A recent investigation[11] of di-t-butylperoxide, t-butyl-hydroperoxide, t-butyl perbenzoate and bicumyl as additives in a standardised diesel fuel powering a 4-cylinder diesel engine came to different conclusions. An amount of 1% of either of these compounds in the fuel showed no considerable effect on engine power, outlet exhaust smoke or fuel consumption, whereas the high concentration of 10% of di-t-butylperoxide or t-butyl hydroperoxide resulted in only a small reduction in emitted particulates and of the CO/CO_2 ratio in the exhaust gas.

The reactions of peroxides are a well researched subject of organic chemistry. However, most of the work has been carried out on reactions in the liquid phase as these are important in preparative organic chemistry.

For revision of the thermolytic and photolytic decomposition of peroxides see references 12 - 16.

The gas phase decomposition of pure di-t-butyl peroxide is essentially first order and yields as main products acetone and ethane[17-19].

$$(CH_3)_3\ COOC\ (CH_3)_3 \xrightarrow{k_1} 2(CH_3)_2\ CO + C_2H_6 \qquad \text{I-1}$$

The slowest, and thus rate determining step is the scission of the O-O bond which leads to two t-butoxy radicals

$$t - BuO - OBu - t \xrightarrow{k_1} 2t - BuO\cdot \qquad \text{I-2}$$

The t-butoxy radical then decomposes to acetone and a methyl radical

$$(CH_3)_3\ CO\cdot \longrightarrow (CH_3)_2\ CO + CH_3\cdot \qquad \text{I-3}$$

which, in the absence of other reaction partners, recombine to form ethane

$$2CH_3 + M \xrightarrow{(Wall)} C_2H_6 + M(Wall) \qquad \text{I-4}$$

Similarly, the thermal decomposition of t-butyl-hydroperoxide leads to a t-butoxy and an HO radical

$$(CH_3)_3\ COOH \xrightarrow{k_5} (CH_3)_3\ CO\cdot + HO\cdot \qquad \text{I-5}$$

Hydroperoxides are important in cool flames[19] and have also been associated with engine knock[20,21].

For the reactions of both peroxides in flames, which are only to be considered here, it is obvious that only reactions I-2 and I-5 are of importance as the t-butoxy and the HO radical will then take part in the complex chemistry of the flame itself. A good value for the rate coefficient for I-1 is given by

$$389K < T < 623K;\ k_1 = 7 \times 10^{15} \exp(-19100/T) \qquad \text{Ref 17-19}$$

and for I-5 it is estimated to

$$T > 573\ K;\ k_5 = 10^{15} \exp(-21000/T) \qquad \text{Ref. 19, 20}$$

In Table 1, the half-life times $\tau = \ell n2/k$ of decomposition are given for both peroxides as function of temperature.

T/K	τ(DTBP)/sec	τ(TBHP)/sec
500	3.8	1.2×10^{3}
550	0.12	2.6
600	6×10^{-3}	1.1
650	6×10^{-4}	7×10^{-2}
700	7×10^{-5}	7×10^{-3}
750		10^{-3}
800		2×10^{-4}
850		4×10^{-5}

Consecutive reaction of the t-butoxy and other alkoxy radicals are described in ref. 19-22.

The effect of additives on soot formation was investigated in 1955 by Street and Thomas[23]. They observed a shift in the critical C/O ratio for sooting to higher values for nitrogen-peroxide, amylnitrate, methanol and tetra-ethyl-lead. These substances had to be present in fairly large amounts to achieve a considerable soot reduction and they are all highly toxic or lead to other pollutants, which severely restricts their use. On the other hand, very small concentrations of halogens and especially sulphur trioxide showed a strong enhancement in soot formation. Müller-Dethlefs and Schlader[24] established a linear relationship between the increase in critical C/O ratio and the molar ratio of water and fuel for the addition of water vapour to a Bunsen flame. Also the amount of soot in a heavily sooting ethylene or propane flame was effectively reduced by water. These effects were attributed to an increase in HO concentration which acts as a rapid oxidant of soot in all stages of formation[42] and the inhibiting effect of hydrogen formed[21,39] by the shift in the water gas equilibrium.

The role of metal additives will be discussed later on.

II-2 SOOT FORMATION

Scientific studies of soot formation date back as early as 1892. Then, Smithels and Ingle[25] found a significant correlation between acetylene production in rich hydrogen flames and soot formation. A systematic classification of sooting flames for a variety of fuels was done by Behrens[26] and Street and Thomas[23]. The latter authors introduced a very useful parameter - the visual soot limit - and determined it for many hydrocarbon fuels. Jost et al[27], Jost and Krischer[28] and Krischer[29] demonstrated the significance of higher local C/O ratios than those in the fresh gas. This would partly explain the spatial soot distribution in distorted flames.

Wright[30] studied the critical C/O ratio for carbon formation of seventeen fuels in a well stirred reactor. Though, under these conditions, the values for $(C/O)_{critical}$ were higher than those evaluated from Bunsen or flat flames, they were still far away from the thermodynamically expected soot limit at C/O $\underset{\sim}{\sim}$ 1 (1.07 for C_2H_2).

Millikan[31] measured the temperature dependence of the critical C/O ratio and explained his results by invoking a difference in activation energy of 142 ± 42 KJ/mole between the soot oxidation and formation reactions.

In a well-known series of research works in Göttingen Homann, Wagner et al[32-37] probed the reaction zone of rich hydrocarbon flames at low pressures ($\underset{\sim}{<}$ 2.7 x 10^3 Pa) by mass-spectrometry and optical extinction measurements. This work is reviewed by Homann[38,39]. In C_2H_2 flames at C/O = 0.95 (near the visual soot limit) polyacetylenes up to C_8H_2 were found to have a maximum in the oxidation zone. These disappeared almost completely before the oxygen was consumed[32]. In sufficiently rich C_2H_2-O_2 flames the polyacetylenes were not completely consumed in the burnt gas[36]. Polycyclic aromatic hydrocarbons of higher molecular mass than 125 were identified by the same technique behind the oxidation zone[37]. The latter were thought to be mainly by-products whereas the polyacetylene concentration profiles strongly supported the soot precursor character of polyacetylenes.

Cullis and Franklin[40] studied the pyrolysis of acetylene in a static system between 673 and 1273K*. Under these conditions the product in the early stages of the reaction was found to be vinylacetylene. Carbonaceous material, together with ethylene, methane and hydrogen was eventually formed at longer reaction times. Consequently the thermal products of vinylacetylene and ^{14}C labelled acetylene were investigated[41]. This lead to the conclusion that vinylacetylene, compared to diacetylene, cannot be regarded as an important intermediate in soot formation.

The formation of polycyclic aromatic hydrocarbons (PCAH) was investigated by several authors. Zaghini et al.[42] analysed the distribution of PCAH and other hydrocarbons in a vertical flow reactor by gaschromatography mass-spectrometry. A similar reactor was employed by Franceschi et al.[43,44] who determined the concentration profile of the perinaphthenyl radical using electron paramagnetic resonance and correlated their results with the amount of soluble material extracted from simultaneously collected soot†.

Chakraborty and Long[46] analysed the chloroform soluble material from soot, obtained from ethylene and ethane diffusion flames at atmospheric pressure, for PCAH. They found a rapid decline to virtually zero of PCAH in the sampled soot, when the oxygen content of the synthetic air was increased or when some oxygen was added to the fuel.

Fenimore and Jones[47-50] came to the conclusion that the main oxidising agent of soot is the HO radical, removing one carbon atom from a soot particle surface per ten collisions. The rate of soot oxidation in an

---

*Though soot formation is not likely to always involve acetylene as an intermediate, the thermal products of acetylene are of considerable interest.

†PCAH emission into the urban air, traced back to combustion sources, has recently become of great concern. With modern selective analytical techniques it has now become possible to investigate the abundance of especially the most carcinogenic PCAH[45].

outer diffusion flame surrounding a sooting premixed flame at atmospheric pressure was found to be governed by the competitive HO removing reaction CO + HO $\longrightarrow$ CO_2 + H. If the soot particle radius was below 50 nm, all soot was oxidised in the outer diffusion flame, no matter how many particles were present and the upper flame region became smokeless. Burning ethylene or acetylene with H_2O instead of O_2 they discovered about an eight times higher soot yield. The concentrations of polyacetylenes were unchanged in these low pressure flames. These results were attributed to the higher oxidation rates of primary soot particles in the oxygen containing flame (higher HO concentration). Page et al.[51,52] also supported the suggestion of the HO radical as the main oxidiser of soot.

The oxidation of commercial carbon blacks under shock tube conditions at various oxygen concentrations was investigated by Park and Appleton[53,54]. The oxidation rates were first order in oxygen for a partial pressure below 10^5Pa) and showed an exponential temperature dependence up to 1800K with a maximum at 2000K.

Induction times, from shock wave experiments, characterised by the first measurable absorption or emission due to soot, were obtained by Fussey et al.[55,56]. They established a good linear correlation between the inverse temperature and the products of molar fuel density and measured induction times. This was the case for the low and high pressure ranges and compared well with very high pressure results communicated by Wagner[57].

II-2-1 PHYSICAL PROPERTIES OF SOOT PARTICLES

There has been substantial previous work concerned with the determination of size, number density, optical characteristics (refractive index) and shape of soot particles. The solution of the radiative transfer problem in flames[58-60], for example, requires this knowledge. The influence of particle shape on radiation processes has been discussed as a possible explanation for some discrepancies between theory and experiment[61-63]. Moreover, from the view of a better understanding of the chemical and physical mechanisms involved it is essential to obtain information about these properties during all stages of soot formation.

Medalia and Heckman[64] carried out electromicrographic analysis of some commercially produced carbon blacks. They found it to be comprised of primary particles fused together into irregular aggregates.*

In a series of researches in Howard's group[65-69], molecular beam sampling from flames was employed together with electromicrographic measurements of size, number density and size distribution. They observed the primary soot particles to be spherical, showing a very narrow size distribution in the early flame region. This result agrees well with Homann and Wagner's work[33]. The sampling system has recently been improved by Bittner[70].

Prado and Lahaye[71,72] also used electronmicrographic size analysis to follow the coagulation of primary particles into larger, non spherical, agglomerates in thermal flow systems (pyrolysing benzene at 1373K). Their most remarkable experimental finding was the constancy of the total number of primary particles contained in all agglomerates, independent of residence times. This was explained, assuming nucleus formation by spontaneous condensation from the supersaturated gas phase consisting of high molecular mass hydrocarbons. The nucleation process would then remove the supersaturation and no more nuclei could be formed.

As regards optical methods, e.g. for particle sizing, extinction or light-scattering techniques, or both, have been used. Measurements of the absorption coefficient, which should be proportional to the volume fraction of soot, showed deviation from the expected $1/\lambda$ dependence[34,73-75] (see chapter III). This has been explained by dispersion of the refractive index of the soot particles or by absorption from molecular species. The experimental values for the (complex) refractive index of soot, determined by Dalzell and Sarofim[76] show only a weak dependence on wavelength in the visible, whereas both real and imaginary part increase in the infrared. Because of its different properties (e.g. high hydrogen content), this might not apply

---

* One has to bear in mind, that conclusions in the shape of soot particles in the gas phase cannot be drawn from this work, as aggregation is more likely to occur during the collection of the carbon black.

to younger soot. Absorption in the visible, without soot particles being present, was found by Laud and Gaydon[143] in the fuel region of counterflow diffusion flames. This was attributed to molecular species preceding carbon formation.

Early light scattering measurements in flames by Hottel et al.[77,78] and Kunugi and Jinno[79] allowed only the investigation of relatively large soot particles because of the low intensity of the light sources employed. These difficulties were overcome by D'Alessio et al. and Graham et al., who combined laser light scattering and absorption measurements.

D'Alessio et al.[80-84] in a series of researches, investigated soot particle growth and particle concentration. This was done in rich, flat methane-oxygen flames at atmospheric pressure stabilised on a cooled sinter burner. The optical apparatus consisted of an argon ion laser as the light source* and a high pressure Xenon lamp for the absorption measurements. The angular pattern of the scattered intensity could then be fitted to the intensity functions obtained from Mie theory, thus obtaining a mean (spherical) particle volume. The number density was then evaluated from an absolute intensity calibration. In the early flame regions, where the angular intensity was constant, simpler Rayleigh theory could be applied. This group was the first to investigate the depolarised components of the scattered intensity[83,84] in order to obtain information about the anisotropy of the particles. The particle shape was then estimated either by Rayleigh's or by Stephenson's[85] approximation, for scattering by a small ellipsoid, which was suitably modified to include the complex refractive index[86,87]. Only a part of the depolarised scattering, however, could be attributed to anisotropy of the soot particles. Especially in the early region of the flame a significant amount originated from fluorescence of molecular species[88]. In combination with the optical measurements they also used gas chromatography for the analysis of gaseous products and thermogravimetry of soot samples with analysis of the volatiles.

Employing the same technique to follow the soot particle growth rate Graham et al.[89-94] pyrolysed aromatic hydrocarbons in incident shock

---

*A Xe lamp in the earlier work.

waves between 1600 and 2300K. By using a He-Ne laser at 3.39 μm for the absorption measurements, they could distinguish between attenuation from particles and molecular species[93]. The latter would only absorb very weakly in the infrared.

Haynes et al.[95] have also recently carried out L.L.S. and absorption measurements in ethylene-oxygen-nitrogen flat flames.

An interesting comparison between data from absorption and electron-microscopic sampling was made by Chippett and Gray[96]. They found the extinction coefficient to be too high, if the usual value for the refractive index for soot[76] were used. Instead, they found close agreement between particle size and number density measured from electron-microscopy and those calculated from the extinction coefficient, if a refractive index of $m = 1.9 - 0.35i$ were assumed.

II-2-2 GROWTH OF SOOT PARTICLES

Tesner et al.[97-100] measured the rates of particle formation in atmospheric diffusion flames. They quote a maximum of 10^{15} particles cm^{-3} sec^{-1} with the very high activation energy of radical nucleus formation of 700 kJ/mole. Their assumption of the C_2 radical as nucleus seems quite doubtful as their work does not account for coagulation and surface growth succeeding nucleation. Also, Homann[38] has pointed out that surface growth requires a higher activation energy than the fast radical reactions leading to nucleation.

The coagulation of particles and droplets by Brownian motion in aerosols has been of great interest in atmospheric physics[101-106]. Essentially it is very useful to distinguish between coagulation in the 'diffusion' or 'free molecule' regime, of which only the latter is of interest here. This is appropriate, if the mean free path λ_g of a molecule in the gas surrounding a particle of radius a is much larger than a, i.e., when the Knudsen number $\lambda_g/a > 10$. The particle collision rate can then be calculated from gas kinetic theory.

For metal oxide and silica particles in flames, Ulrich[107-109] observed

only poor agreement between measured and calculated coagulation rates.

Faster coagulation rates of soot particles then predicted were observed by researchers already mentioned[65-69,89-93,95]. These were partly explained due to van der Waals forces between particles, dispersion and electrostatic forces due to particle charging, all enhancing collision rates.

II-2-3 ELECTRICAL EFFECTS AND INFLUENCES OF METAL ADDITIVES

Weinberg et al.[110-113] showed that soot particles in flames, being all charged, could be manipulated by electric fields to control their residence times. The particle size and the total amount of soot formed could accordingly be controlled in counterflow diffusion flames. Plausible mechanisms for charge acquisition were proposed as diffusion, bombardment and thermionic emission charging[114]. Chemionisation during pyrolysis, which was also observed with the absence of oxygen[115], was discussed as a possible mechanism for the formation of charged soot nuclei.

Prado and Howard[117] concluded from their concentration measurements of large hydrocarbon ions in flames, that ionic nucleation could play an important role in soot formation. Howard et al.[65-67] demonstrated that soot particles in flames are charged without the presence of electric fields and studied the effect of charging on particle coagulation rates.

The ability of metal additives, especially Ba, to either suppress or enhance soot formation has been associated with an increase in free electron concentration produced by the metal. It was shown in a diffusion flame, that with a BaO coated wire, applying a small potential (<400V), the same effects on sooting could be produced as with Ba additive itself[116].

From their optical measurements of particle size and number density Haynes et al.[95] found an inhibition of coagulation in premixed flames with alkali and alkaline earth metal salt addition. This was attributed to an increase in ion concentration and, possibly, a chemical mechanism.

Jenkins et al.[118,119] and Feugier[120] supported an indirect catalytic mechanism of the metal additive, producing HO radicals from water. These would then act as rapid soot oxidisers.

II-2-4 CONCLUSIONS

The main steps in the mechanism of soot formation involve formation of precursors, nucleation, coalescence* of, and surface growth on the primary particles and agglomeration* into non spherical units. Except for simultaneous oxidation processes in premixed and diffusion flames, there seems to be similarity between thermal and flame systems. In flames, a distinction has to be made between the very rapid reactions in the oxidation zone and the slower pyrolysis of hydrocarbons in the flame gases. There is a difference in behaviour (e.g. the temperature dependence of soot formation) between aromatic (and cyclic) fuels and aliphatics. This can be explained directly, with the large aromatic structure acting as building bricks, or via fragmentation into smaller species. These are then supposed to lead to soot in the same way as aliphatics.

As precursors, polyacetylenes and also reactive polycyclic aromatics have to be considered. The nucleation step may involve a purely chemical mechanism, ionic initiation or condensation of liquid droplets from a supersaturated vapour. The latter has been discarded by Homann and Graham who favour chemical 'nucleation', although the distinction between large radicals and particle nuclei is an arbitrary one. Compared to 'older' soot, 'young' soot samples show very strong EPR signals, as evidence of their radical character[38].

---

*We must distinguish here between two types of coagulation. Coalescence is assumed to result in the virtually instantaneous fusion of two particles (droplets) into one of the same shape. Agglomeration denotes the formation of irregular assemblies with the individual particles sticking together.

Polycyclic aromatic hydrocarbons may be of importance as surface growth species causing particle growth.

The dependence of particle volume increase and number density decrease after nucleation can be explained, at least qualitatively, by free molecule coagulation theory.

For more extensive reviews on soot formation see ref. 121 - 124 and 147.

III LIGHT SCATTERING AND ABSORPTION BY PARTICLES AND MOLECULES

For this project laser-light scattering (L.L.S.) and absorption techniques were chosen as the method of investigation. The use of L.L.S. for in situ flame studies is one of the promising new applications of lasers. The main advantage of an optical system is that it does not perturb the flame. Also, by focusing the laser beam, a very good spatial resolution becomes possible. Only for very high power pulsed lasers, problems, for example of particle incandescence or light pressure effects have been encountered. Compared to that, any sampling technique will always cause some interference with the flame itself, though in recent years considerable improvements, e.g. in direct mass-spectrometry of atmospheric flames, have been made[70]. Before going into the details of the apparatus that was built for this research, a concise description of scattering and absorption is given in the next two paragraphs. For a full treatment, see ref.[125-128]

III-1 LIGHT SCATTERING THEORY

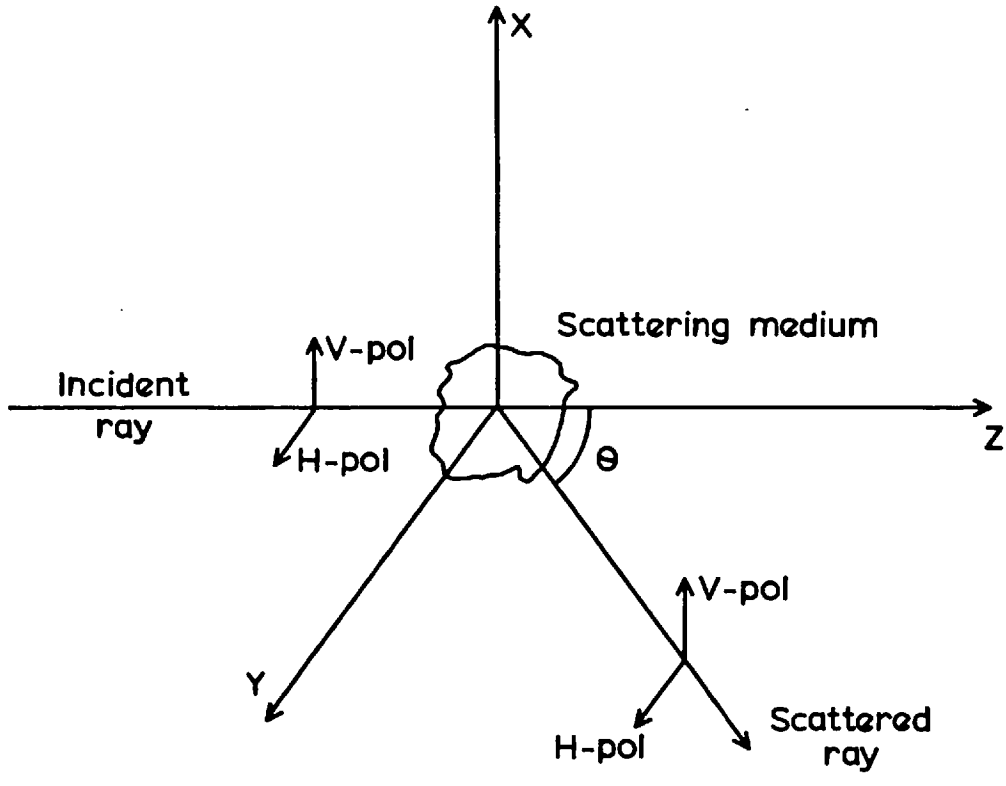

y-z plane is plane of observation and horizontal.

Consider a beam of light of vertical* or horizontal polarisation, of wavelength λ and intensity I_o, incident upon a particle cloud or a gas of number density N constituents per unit volume. Provided N is large, the particles are randomly orientated and are sufficiently separated to exclude multiple scattering, all phase effects will cancel. All scattering parameters (per unit volume scattering medium) will then add up incoherently[129]. The scattered intensity per unit volume, at distance r, which will usually consist of compounds polarised vertically and horizontally, is then given by

$$I_{VV} = \frac{I_o}{r^2} V_V = N \frac{I_o}{r^2} \frac{\lambda^2}{4\pi^2} i_1$$

$$I_{HH} = \frac{I_o}{r^2} H_H = N \frac{I_o}{r^2} \frac{\lambda^2}{4\pi^2} i_2 \qquad \text{III-1}$$

$$I_{HV} = \frac{I_o}{r^2} H_V = N \frac{I_o}{r^2} \frac{\lambda^2}{4\pi^2} i_3$$

$$I_{VH} = \frac{I_o}{r^2} V_H = N \frac{I_o}{r^2} \frac{\lambda^2}{4\pi^2} i_4$$

The "Rayleigh ratios"[126] V_V and H_V are the components of the scattered light for unit incidence intensity and unit distance r polarised vertically and horizontally for vertical incidence polarisation. H_H and V_H are the corresponding quantities for horizontally polarised incident light. The symbols i_n are called the intensity functions which depend on particle size, complex refractive index m = n-ik, scattering angle θ and particle shape. Only special solutions for the intensity function shall be considered here. The simplest case is Rayleigh scattering for spherical particles of equal radius a and size parameter $\alpha = 2\pi a/\lambda$.

*Polarisation with the electric vector perpendicular to the plane of observation is denoted vertical, and the orthogonal case horizontal.

The Rayleigh approximation is based on the assumption of a uniform electric field inside and outside the particle. This leads to the conditions $\alpha << 1$ and $\alpha\,|m-1| << 1$. Then $i_2\,(90^0) = i_3 = i_4 = 0$ and i_1 is independent of the scattering angle.

$$i_1 = \alpha^6 \left|\frac{m^2 - 1}{m^2 + 2}\right|^2 \qquad \text{III-2}$$

$$i_2 = i_1 \cos^2 \theta$$

$$V_V = N\sigma_o = N \frac{\lambda^2}{4\pi^2} \left|\frac{m^2 - 1}{m^2 + 2}\right|^2 \alpha^6 \qquad \text{and}$$

$$= N \left|\frac{2\pi}{\lambda}\right|^4 \left|\frac{m^2 - 1}{m^2 + 2}\right|^2 a^6 \qquad \text{III-3}$$

$$H_H = V_V \cos^2 \theta$$

The quantity $\sigma_0 = (\lambda^2/4\pi^2)i_1$ is usually called the differential cross-section of one particle (molecule). For a transparent gas, i.e. when λ is far away from resonances, σ_0 can be determined from the refractive index μ_o at S.T.P. of the gas. As the polarisability of a molecule is in most cases anisotropic, i.e. differs for the three axes, the i_2 of (90^0), i_3 and i_4 will no longer be zero, which means that the scattered light will partly be depolarised. Also the i_1 component will be enhanced by the 'Cabannes Factor'. Even for noble gases and molecules of spherical symmetry (e.g. CH_4) very small, non zero, depolarised components arise from non ideal gas behaviour (pressure dependent) and from quantum effects[130,131]. The depolarisation ratios ρ_V and ρ_H are defined as

$$\rho_V = \frac{H_V}{V_V} = \frac{i_3}{i_1} = \frac{I_{HV}}{I_{VV}} = \frac{\sigma_{HV}}{\sigma_{VV}} \qquad \text{III-4}$$

$$\rho_H = \frac{V_H}{H_H} = \frac{i_4}{i_2} = \frac{I_{VH}}{I_{HH}} = \frac{\sigma_{VH}}{\sigma_{HH}}$$

TABLE 2

The refractive indices[134], depolarisation ratios[132], absolute and relative cross-sections for some gases (λ = 488 nm)

Gas	$(\mu^0_{760} - 1)\ 10^6$	$100\ \rho_V^c$	$\sigma_0 . 10^{28}/cm^2$	σ_r
N_2	301.2	0.28	8.78	1
O_2	273.9	0.75	7.31	0.833
CO	336.9	0.15	10.97	1.25
CO_2	453.6	0.99	20.11	2.29
H_2O	254.6	0.4*	6.28	0.716
C_2H_4	737.1	0.1	52.47	5.97
CH_4	446.6	0.0	19.23	2.19
H_2	140.5	0.24	1.91	0.22

*assumed value

The differential cross-section for scattering is given by[130-132]

$$\sigma_o^c = \frac{4\pi^2(\mu_0-1)^2}{N_o^2\,\lambda^4} \quad \frac{3}{3 - 4\rho_V^c} \qquad \text{III-5}$$

where the superscript c means that only the central Rayleigh line at wavelength λ is considered and all the rotational Raman lines at $\lambda \pm (\Delta\lambda)_i$ are excluded.

For the case of a diatomic molecule the cross-section σ_o^t for the Rayleigh band (including rotational Raman) can be obtained by replacing ρ_V^c with the total depolarisation ratio ρ_V^t for the Rayleigh band . ρ_V^c and ρ_V^t can be calculated from molecular polarisabilities[133](or vice versa) and are related (for diatomics) by[132]

$$\rho_V^c = \frac{\rho_V^t}{4\,(1 - \rho_V^t)} \approx \rho_V^t / 4 \qquad \text{III-6}$$

The scattering for the central line is then described by;

$$\begin{aligned} \sigma_{VV} &= \sigma_o \\ \sigma_{HV} &= \sigma_{VH} = \sigma_{HH}(90^0) = \sigma_o\,\rho_V^c \\ \sigma_{HH} &= \sigma_o\left[(1 - \rho_V^c)\cos^2\theta + \rho_V^c\right] \end{aligned} \qquad \text{III-7}$$

Table 2 contains values for the absolute and relative differential cross-sections of some gases.

Two more parameters are needed to describe light scattering. The total scattering cross-section C_{sca} for one particle is defined with

$$P_{sca} = N\,C_{sca}.I_o$$

where P_{sca} is the power per unit volume scattered in all directions. The efficiency factor Q_{sca} of a particle of cross-sectional area A_{cp}

is given by

$$Q_{sca}/A_{cp}$$

Rayleigh theory for a spherical particle gives

$$C_{sca} = \frac{128\pi^5}{3\lambda^4}\left|\frac{m^2-1}{m^2+2}\right|^2 a^6 = \frac{2}{3\pi}\lambda^2\left|\frac{m^2-1}{m^2+.2}\right|\alpha^6 \qquad \text{III-8}$$

$$\text{and } Q_{sca} = \frac{128\pi^4}{3\lambda^4}\left|\frac{m^2-1}{m^2+2}\right|^2 a^4 = \frac{8}{3}\left|\frac{m^2-1}{m^2+2}\right|^2\alpha^4 \qquad \text{III-9}$$

Similarly, for gases (see III-5)

$$C_{sca} = \frac{8\pi}{3}\sigma_0\,(1+2\rho_V) \qquad \text{III-10}$$

The theory of dipolar scattering can be extended to ellipsoidal particles, provided these are still small compared to the wavelength[126,135]. Here only spheroids are to be considered. With axes a and b (a > b) and eccentricity $e_s = ((a^2-b^2)/a^2)^{\frac{1}{2}}$ the form factors[136] are then given by:

Oblate spheroid (a = c > b)

$$Pe' = \frac{4\pi}{e_s^2}\left[1-\left|\frac{1-e_s^2}{e_s^2}\right|^{\frac{1}{2}}\ \text{arc sin } e_s\right]$$

Prolate spheroid ($a > b = c$)

$$Pe' = 4\pi \frac{1 - e_s^2}{e_s^2} \left[\frac{1}{2e_s} \ln \frac{1 + e_s}{1 - e_s} - 1 \right] \qquad \text{III-11}$$

and $Pe'' = (4\pi - Pe')/2$

For a sphere $Pe' = Pe'' = 4\pi/3$

The polarisabilities are then given by

$$\alpha' = \frac{3V}{4\pi} L' \exp(-i\psi') = \frac{V(m^2 - 1)}{4\pi + (m^2 - 1)Pe'}$$

$$\alpha'' = \frac{3V}{4\pi} L'' \exp(-i\psi'') = \frac{V(m^2 - 1)}{4\pi + (m^2 - 1)Pe''} \qquad \text{III-12}$$

Correspondingly, after integrating over all directions assuming random particle orientation one obtains the Rayleigh ratio for particles of volume V:

$$V_V = N \frac{3\pi^2 V^2}{5\lambda^4} \left[3 (L')^2 + 4L'L'' \cos(\psi' - \psi'') + 8(L'')^2 \right]$$

$$V_H = H_V = N \frac{3\pi^2 V^2}{5\lambda^4} \left[(L')^2 - 2 L'L'' \cos(\psi' - \psi'') + (L'')^2 \right] \qquad \text{III-13}$$

$$H_H = V_V \cos^2\theta + H_V \sin^2\theta$$

So, if the refractive index is known, the depolarisation ratio ρ_V can be calculated for different axial ratios or vice versa from measured ρ_V's the eccentricity can be evaluated. This has been done in Table 3.

For the total scattering cross-section one obtains

$$C_{sca} = (8\pi^3/\lambda^4) V^2 \left[(L')^2 + 2(L'')^2 \right] \qquad \text{III-14}$$

TABLE 3a

Depolarisation ratios ρ_V for prolate spheroids of refractive index m = 1.54 - 0.56i for different axial ratios a/b, and Cabannes factors C, by which the V_V scattering component is enhanced compared to a sphere of equal volume. All values are calculated from III-3, III-4, III-12 and III-13.

a/b	ρ_V	C
1.1	2.04 E-4	1.0010
1.2	7.49 E-4	1.0036
1.3	1.55 E-3	1.0073
1.4	2.53 E-3	1.0118
1.5	3.65 E-3	1.0169
1.6	4.86 E-3	1.0222
1.7	6.13 E-3	1.0279
1.8	7.43 E-3	1.0337
1.9	8.75 E-3	1.0395
2.0	1.01 E-2	1.0453
2.5	1.64 E-2	1.0728
3.0	2.19 E-2	1.0967
4.0	3.04 E-2	1.1336

It should be noted here, that $C = 3/(3 - 4\rho_V)$ in III-5, is only a good approximation if m is real and near to 1.

TABLE 3b

Depolarisation ratios ρ_V for oblate spheroids as function of axial ratio a/b, and corresponding Cabannes factors C.

	m = 1.54 - 0.56i		m = 2.0 - 1.0i	
a/b	ρ_V	C	ρ_V	C
1.2	7.23 E-4	1.004		
1.5	3.43 E-3	1.019	6.13 E-3	2.30
2.0	9.20 E-3	1.055	1.58 E-2	2.48
2.5	1.48 E12	1.094	2.47 E-2	2.69
3.0	1.96 E-2	1.132	3.20 E-2	2.89
4.0	2.73 E-2	1.200	4.36 E-2	3.28
6.0	3.70 E-2	1.303	5.78 E-2	3.93
10.0	4.66 E-2	1.427	7.13 E-2	4.82

If the particle size is no longer small compared to the wavelength, Rayleigh theory is no longer applicable. No rigorous methods of solution are available for a particle of arbitrary size and shape.

Solutions have been given for spheroids of arbitrary size[137] and particle chains[129,138] as special cases. Jones[129] has shown that, for a chain of Rayleigh scatterers the angular dependence of i_1 can always be matched by the i_1 obtained for an equivalent sphere. However, the volume of the sphere is bigger than the sum of the individual particles in the chain.

The rigorous solution for scattering from a sphere of arbitrary size and homogeneous refractive index was found by Mie[139]. In this case the i_1 depends on the scattering angle and the $i_2(90^0)$ is no longer zero but still $i_3 = i_4 = 0$ (no depolarisation). The solution is expressed in terms of the size parameter $\alpha = 2\pi a/\lambda$, the refractive index $m = n - ik$ and the scattering angle θ. The intensity functions are

$$i_1 = |S_1|^2 \quad \text{and} \quad i_2 = |S_2|^2 \qquad \text{III-15}$$

$$\text{with} \quad S_1 = \sum_{n=1}^{\infty} \frac{2n+1}{n(n+1)} \left\{ a_n \pi_n (\cos\theta) + b_n \tau_n (\cos\theta) \right\} (-1)^{n+1}$$

$$S_2 = \sum_{n=1}^{\infty} \frac{2n+1}{n(n+1)} \left\{ a_n \tau_n (\cos\theta) + b_n \pi_n (\cos\theta) \right\} (-1)^{n+1}$$

$$\text{where} \quad \pi_n (\cos\theta) = \frac{P_n^{(1)}(\cos\theta)}{\sin\theta}$$

$$\text{and} \quad \tau_n (\cos\theta) = \frac{d}{d\theta} P_n^{(1)} (\cos\theta)$$

and $P_n^{(1)} (\cos\theta)$ are the associated Legendre polynomials of order n and degree one. The Mie coefficients a_n, b_n are obtained by use of the Ricatti-Bessel functions $\psi_n(z)$, $\zeta_n(z)$ and their derivatives.

$$a_n = \frac{\psi_n(\alpha)\ \psi_n'(m\alpha) - m\psi_n(m\alpha)\ \psi_n'(\alpha)}{\zeta_n(\alpha)\ \psi_n'(m\alpha) - m\psi_n(m\alpha)\ \zeta_n'(\alpha)}$$

$$b_n = \frac{m\psi_n(\alpha)\ \psi_n'(m\alpha) - \psi_n(m\alpha)\ \psi_n'(\alpha)}{m\zeta_n(\alpha)\ \psi_n'(m\alpha) - \psi_n(m\alpha)\ \zeta_n'(\alpha)}$$

The total scattering cross-section is given by

$$C_{sca} = (\lambda^2/2\pi) \sum_{n=1}^{\infty} (2n + 1) \left\{ |a_n|^2 + |b_n|^2 \right\}$$

and the efficiency factor

$$Q_{sca} = (2/\alpha^2) \sum_{n=1}^{\infty} (2n + 1) \left\{ |a_n|^2 + |b_n|^2 \right\}$$

For $\alpha < 1$, good agreement of the angular dependence of $i_1/i_1(90^0)$ from Mie theory with $i_1/i_1(90^0)$ from the Rayleigh-Gans-Debye approximation can be obtained, if $m - 1$ is replaced by

$$\frac{3}{2} \left| \frac{m^2 - 1}{m^2 + 2} \right|^2$$

The intensity functions are

$$i_1 = \left| \frac{m^2 - 1}{m^2 + 2} \right|^2 \alpha^6 \cdot P(\theta) \qquad \text{III-16}$$

$$i_2 = i_1 \cos^2 \theta$$

and $P(\theta)$ is given by

$$P(\theta) = \left[(3/u)^3 (\sin u - u \cos u) \right]^2 = (9\pi/2u^3)\ J_{\frac{3}{2}}^2(u)$$

where $u = 2\alpha \sin(\theta/2)$ and $J_{\frac{3}{2}}$ is the three halves order Bessel function.

Table 4 shows some values for intensity functions and total scattering and extinction cross-sections (see Chapter III-2).

TABLE 4

Intensity functions i_1, i_2 at $\theta = 90^0$ and total scattering and extinction cross-sections for some particles of size parameter α and refractive index $m = 1.54 - 0.56i$ as calculated from Mie theory. In comparison, note that $i_1 (N_2) = 4\pi^2 \sigma_0/\lambda^2 = 1.456 \times 10^{-17}$

α	i_1	i_2	C_{sca}/cm^2	C_{ext}/cm^2
0.1	0.2109 E-6	0.1194 E-12	1.066 E-16	2.032 E-13
0.2	0.1354 E-4	0.1231 E-9	6.844 E-15	1.661 E-12
0.3	0.1545 E-3	0.7188 E-8	7.808 E-14	5.809 E-12
0.4	0.8642 E-3	0.1299 E-6	4.372 E-13	1.444 E-11
0.5	0.3248 E-2	0.1238 E-5	1.645 E-12	2.981 E-11
0.7	0.2245 E-1	0.3804 E-4	1.146 E-11	9.174 E-11
1.0	0.1341	0.1462 E-2	7.146 E-11	2.970 E-10
1.2	0.2651	0.8848 E-2	1.530 E-10	5.139 E-10
1.5	0.4288	0.6042 E-1	3.299 E-10	9.402 E-10

III-2 ABSORPTION BY PARTICLES

Consider a beam of light of intensity I_o falling through a particle cloud of number density N. For an optical pathlength of ℓ the transmitted intensity I then obeys Lambert-Beer's law.

$$\ell n \frac{I}{I_o} = -\ell N C_{ext} = -\ell\varepsilon \qquad \text{III-17}$$

where C_{ext} is the extinction cross-section and ε is the extinction coeffiecient. In the Rayleigh limit, for a spherical particle, C_{ext} is given by (see III-8)

$$C_{ext} = C_{abs} + C_{sca}$$

$$C_{ext} = -\frac{8\pi^2}{\lambda} a^3 \, Im\left\{\frac{m^2 - 1}{m^2 + 2}\right\} + C_{sca} \qquad \text{III-18}$$

$$= -\frac{\lambda^2}{\pi} \alpha^3 \, Im\left\{\frac{m^2 - 1}{m^2 + 2}\right\} + C_{sca}$$

Usually, C_{sca} in III-18 can be neglected, even if k in m = n - ik is small, so that

$$C_{ext} = C_{abs}$$

The absorption efficiency $Q_{abs} = C_{abs}/A_{cp}$ is correspondingly

$$Q_{abs} = -\frac{8\pi}{\lambda} a \, Im\left\{\frac{m^2 - 1}{m^2 + 2}\right\} \qquad \text{III-19}$$

$$= -4 \alpha \, Im\left\{\frac{m^2 - 1}{m^2 + 2}\right\}$$

For the spheroid considered earlier, using III-12, C_{abs} is obtained as

$$C_{abs} = (2\pi V/\lambda) (L' \sin \psi' + 2L'' \sin \psi'')$$

Mie theory gives C_{ext} and Q_{ext} as

$$C_{ext} = (\lambda^2/2\pi) \sum_{n=1}^{\infty} (2n + 1) \left\{ Re(a_n + b_n) \right\}$$

$$Q_{ext} = (2/\alpha^2) \sum_{n=1}^{\infty} (2n + 1) \left\{ Re(a_n + b_n) \right\} \qquad \text{III-20}$$

and $C_{abs} = C_{ext} - C_{sca}$. Usually, the contribution of scattering compared to the total extinction can no longer be neglected.

Table 5 shows some values for $|(m^2 - 1)/(m^2 + 2)|^2$ and for $Im\left[(m^2 - 1)/(m^2 + 2)\right]$.

When the particles are too large to apply Rayleigh theory, the total particle volume fraction ϕ has to be calculated according to $\phi = N \cdot V$, after having obtained V from fitting a measured angular scattering pattern to the Mie intensity functions and having obtained N from an absolute intensity calibration (see below).

For the case of Rayleigh particles, ϕ is directly given from the absorption coefficient by

$$\phi = N \cdot V = -\varepsilon\lambda/\left[6\pi \; Im\{(m^2-1)/(m^2+2)\}\right] \qquad \text{III-21}$$

which, for $-Im\{\} = 0.27$ and ε in cm^{-1} becomes

$$\phi = 9.59 \cdot 10^{-6} \; \varepsilon \quad \text{for } \lambda = 488 \text{ nm}$$

$$\phi = 1.76 \cdot 10^{-5} \; \varepsilon \quad \text{for } \lambda = 894.3 \text{ nm}$$

TABLE 5

Values for a) $|(m^2 - 1)/(m^2 + 2)|$ and b) $-\mathrm{Im}\{(m^2 - 1)/(m^2 + 2)\}$ for several n, k's; $m = n - ik$.

	(a)	(b)	(a)	(b)	(a)	(b)
n \ k	0.3		0.4		0.5	
1.3	0.071	0.172	0.101	0.230	0.139	0.288
1.4	0.093	0.161	0.121	0.214	0.157	0.267
1.5	0.119	0.149	0.145	0.198	0.178	0.247
1.6	0.147	0.138	0.171	0.183	0.202	0.227
1.7	0.178	0.127	0.200	0.168	0.228	0.209
1.8	0.209	0.117	0.230	0.155	0.256	0.192
1.9	0.241	0.108	0.260	0.142	0.284	0.176
2.0	0.272	0.099	0.290	0.131	0.312	0.162

	(a)	(b)	(a)	(b)	(a)	(b)
n \ k	0.6		0.7		0.8	
1.3	0.188	0.346	0.247	0.403	0.318	0.458
1.4	0.202	0.319	0.256	0.370	0.319	0.419
1.5	0.219	0.294	0.269	0.340	0.326	0.383
1.6	0.240	0.270	0.286	0.311	0.338	0.350
1.7	0.263	0.248	0.305	0.285	0.352	0.320
1.8	0.288	0.228	0.326	0.261	0.369	0.293
1.9	0.313	0.209	0.348	0.240	0.387	0.269
2.0	0.339	0.192	0.370	0.220	0.406	0.246

IV APPARATUS

IV-1 OPTICAL SYSTEM AND SIGNAL DETECTION

The theoretical considerations described so far lead to the following experimental requirements:

i) a powerful continuous light source with changeable vertical and horizontal polarisation for light scattering measurements;

ii) measurement of the angular dependence of the scattered light including the depolarised components;

iii) analysis of the spectral composition of the scattered light

iv) extinction measurements over a wide wavelength range;

v) discrimination against flame radiation.

The experimental system designed and built to meet these requirements is shown in figs. 1 and 2. A Spectra-Physics CW argon ion laser (type 164) operating at 488 nm and producing about 1.4 W optical power was used as light source for the scattering measurements. The laser was mounted on an adjustable, heavy steel bench, which also allowed the stable maintenance of optical components in front of it. The normally vertical polarisation of the laser beam (quality 1:1000) could be rotated by two silica, optically contacted Fresnel rhombs (Rofin Ltd.). These were fitted into a specially made rotator incorporating a protractor. The whole device could then be turned easily by 45^0 between two fixed points, thus rotating the plane of polarisation by 90^0. The purity of polarisation of the beam was tested with a polariser (Polaroid HN22) for low, and with a Glan Thomson prism for high laser powers. It was found that the quality of the vertically polarised beam was reasonable, whereas the horizontally polarised beam still showed too much vertical polarisation. The elimination of this was essential and therefore a Glan Thomson prism polariser (Rofin Ltd.) was mounted into the beam. Thus, the polarisation purity was excellent for both vertical and horizontal polarisation. The beam was then focused into the test volume by an anti-reflection coated achromatic lens of f = 45 cm (Ealing

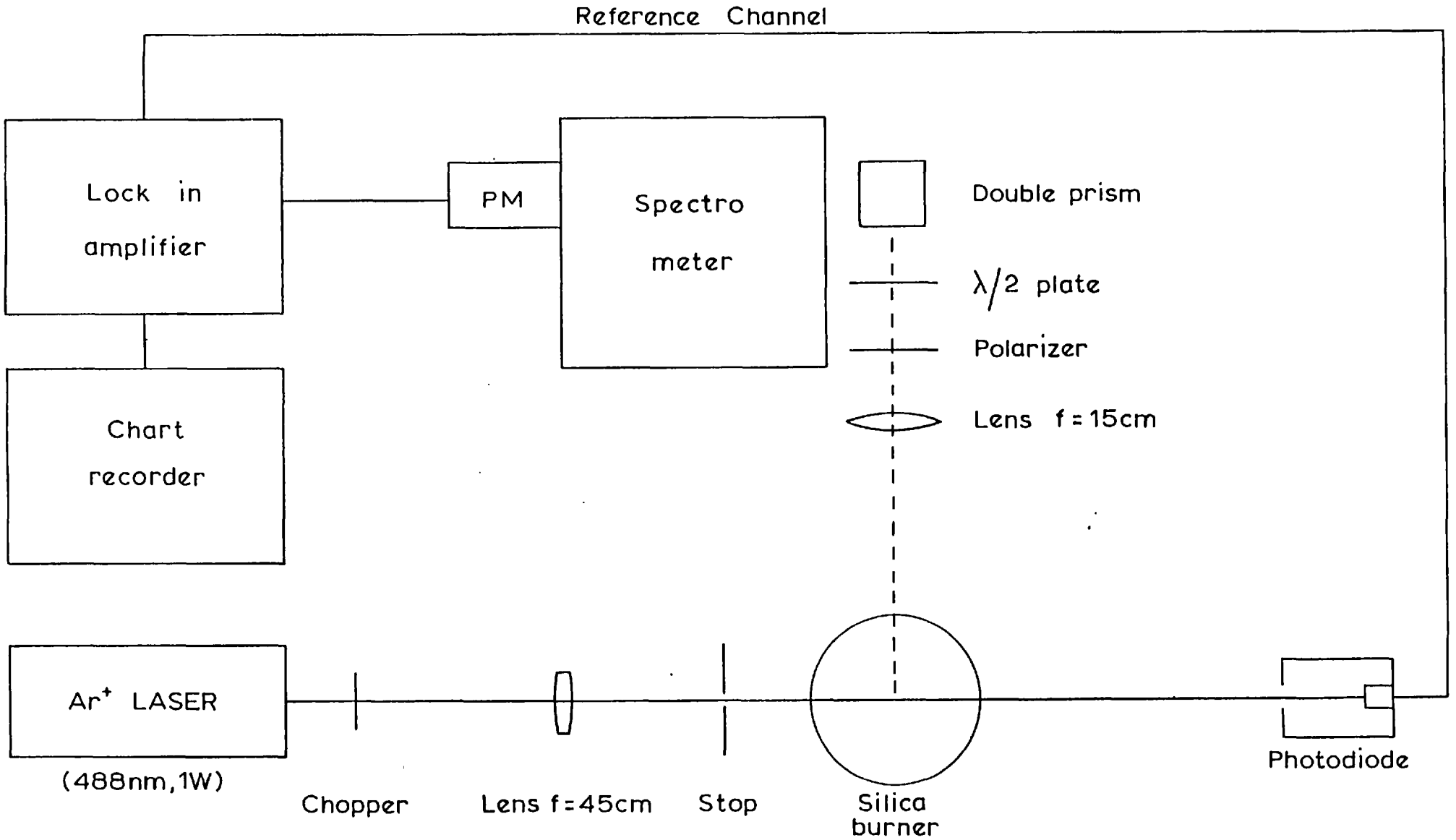

Fig. 1: Experimental system for fluorescence spectroscopy and light scattering at -90^0.

Beck Limited). The beam was focused to increase spatial resolution and to allow for the collection of a maximum of scattered light from a small scattering volume. The focal length of the lens was chosen so that over a range of 1 cm at the focus the beam could be regarded as being parallel. The $1/e^2$ diameter of the beam at the focus, for λ = 488 nm was calculated as[140]

(unfocused diameter d_o = 1.5 mm)

$$d_f = \left\{(4f\lambda/\pi d_o^2)/\left|1 + (4f\lambda/\pi d_o^2)^2\right|^{\frac{1}{2}}\right\} \cdot d_o = 0.19 \text{ mm}$$

A part of the scattered radiation at $\theta = -90^0$ was focused by a lens (f = 15 cm, 1:1 imaging) onto the entrance slit of a 0.5 m Hilger and Watts fast spectrometer. To maximise the collection of light into the monochromator without losing resolving power by increasing the slit width, the image of the test volume was rotated by 90^0. This is usually done by a Dove prism, but in this case was achieved by two contacted prisms (45^0-90^0-45^0). The prism assembly could be adjusted for optimum focusing and slit matching of the gaussian laser beam. The length of the test volume could then be selected by blocking off some length of the spectrometer slit. An HN22 polariser in a precision mount (angular accuracy ± 20') was employed as analyser. As the transmission of the monochromator depends strongly on polarisation and is highest for vertical polarisation, a half wave plate (λ = 488 nm) was put in. This could be turned by 45^0 so that the light entering the spectrometer was always vertically polarised. Compared to a polarisation scrambler, which is usually used, a twofold gain in light throughput was achieved. From the exit slit the light was focused onto a small area of the photocathode of an EMI 9558B(9658A) photomultiplier. This area was determined by a magnet, fitted onto the front window of the tube, which effectively inhibits dark current electrons from the large remaining part of the cathode to reach the first dynode. Employing this arrangement, the dark current was reduced about twenty times. In addition, the tube was cooled thermoelectrically to -20^0C, which resulted in a dark current reduction of 3 orders of magnitude. The photomultiplier housing (Products for Research Inc.) incorporated Mu-metal shielding against magnetic fields.

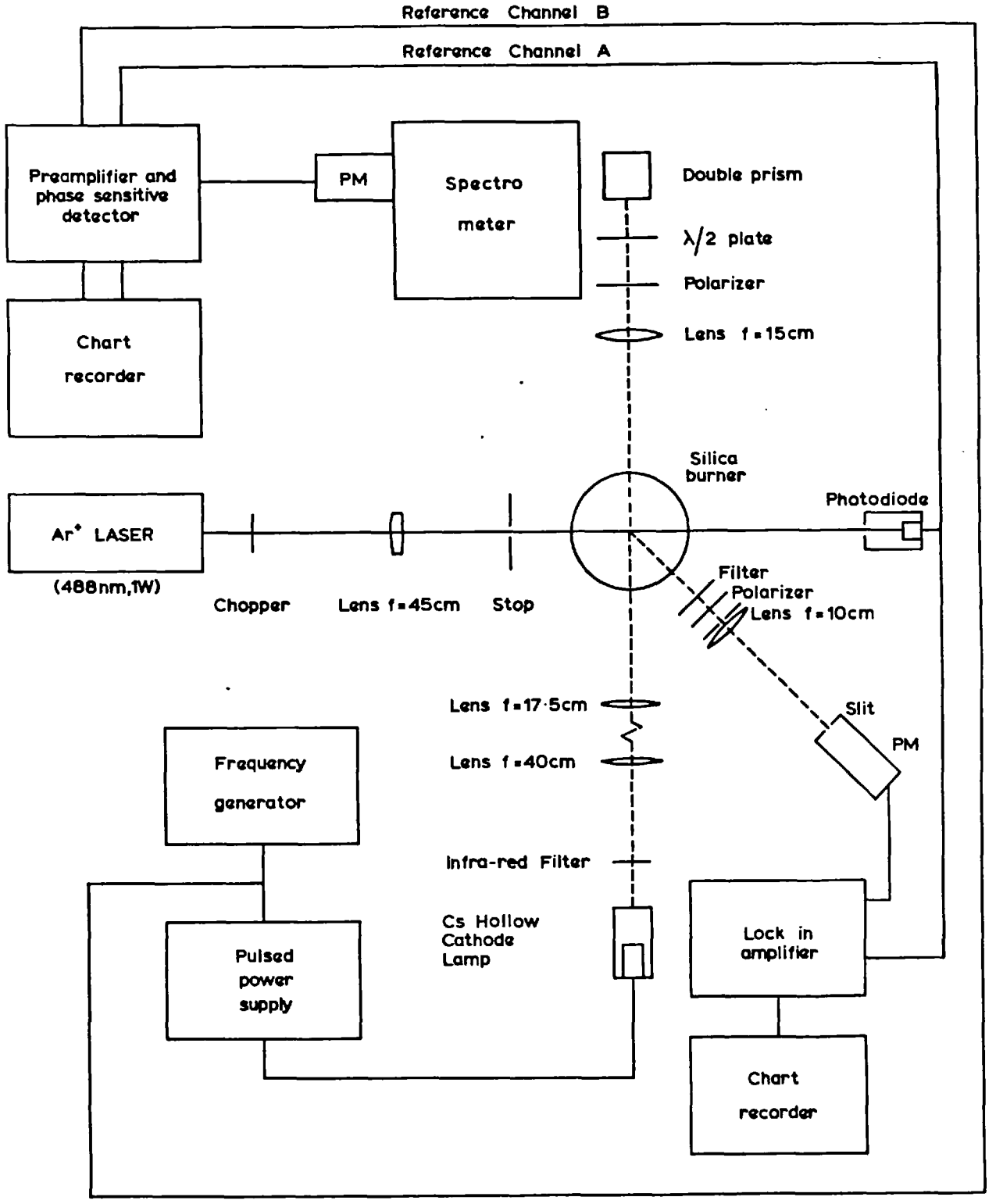

Fig. 2: Complete detection system for spectroscopy, light scattering and absorption measurements.

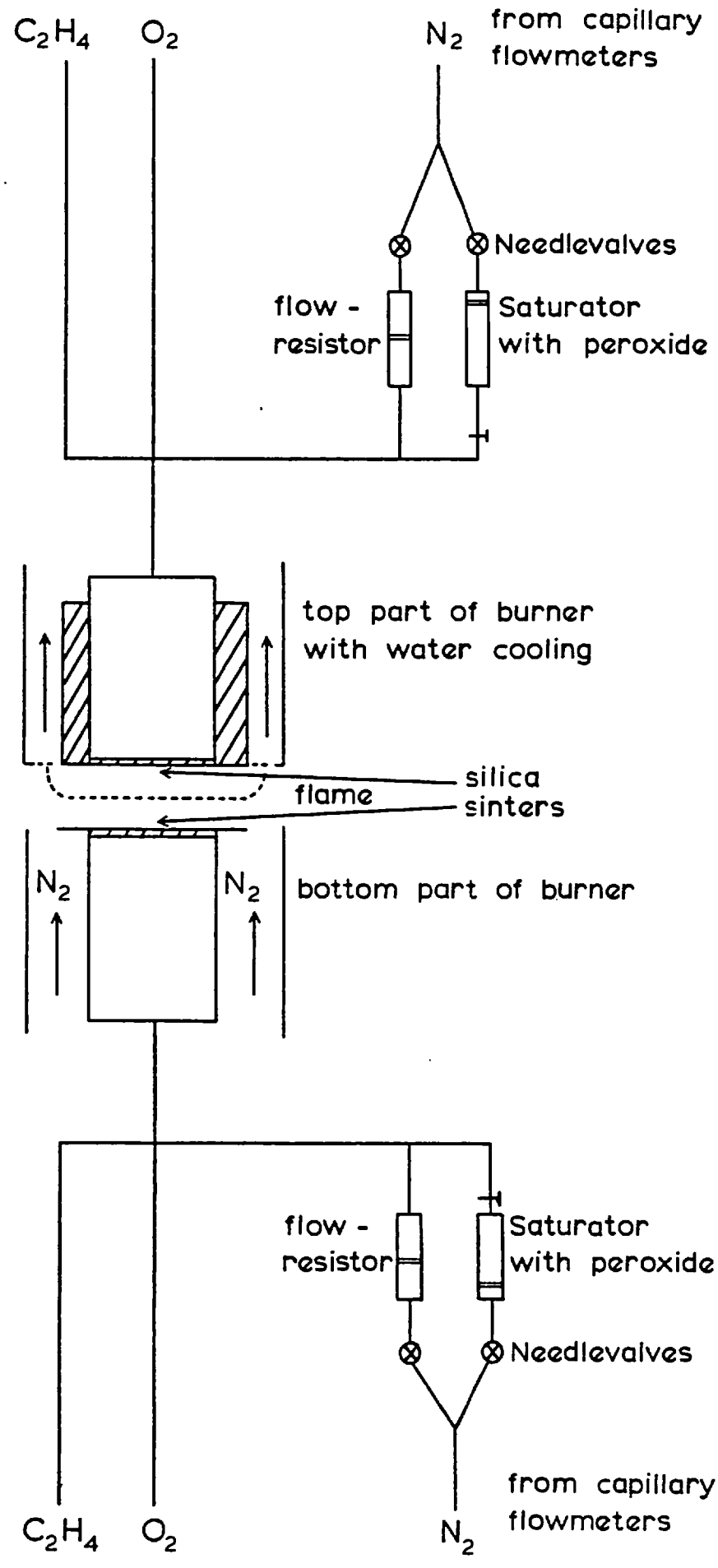

Fig. 3: Burner system

All these measures were taken in order to obtain good signal to noise ratios for very low light levels. Additionally, it was found to be very important to eliminate 'parasitic' light effects, e.g., background reflections and light scattered from the lens focusing the laser beam. This was achieved by two apertures, or stops, in front of the lens, as near as possible to the test volume, and by completely enclosing the laser beam. The diameter of the stops was chosen so as to cause minimal diffraction.

The angular dependence of all four components of the scattered light was measured with the following apparatus, called the L.L.S. detector, comprising an interference filter (λ = 488 nm, $\pm$ 5 nm band width, Grubb-Parsons Ltd.), a precision polariser ($\pm$ 20'), a lens (f = 10 cm) with changeable apertures (2, 1 and $\frac{1}{2}$"), a vertical and horizontal adjustable slit and a photomultiplier (EMI 9592B). The components were mounted on an optical bench supported on three points. This assembly, which was fixed onto a float glass plate could then be turned around a steel centrepiece from -60^0 to $+158^0$ without slipping. It was supported horizontally on another float glass plate and by a heavy table.

The alignment of the apparatus was done in the following way. First, a straight steel piece with a conical sharp tip was fitted into the centre hole. The laser focus was then adjusted to illuminate the tip. The L.L.S. detector, with the photomultiplier removed was then provisionally lined up to image the tip onto the slit (1:1). Replacing the tip with a hair on an adjustable mount the top glass plate was then turned through all angles and the position of the hair readjusted until the hair was properly positioned in the centre axis. The laser was then adjusted to illuminate the hair uniformly. After that, the hair was focused onto the slit and the optical bench was successively repositioned so that the position of the hair's image on the slit was the same for every scattering angle. The optical bench was then glued onto the glass plate. The scattering angle of 0^0 was found by moving the whole assembly into the laser beam and then fixing a 30 cm diameter protractor onto the top glass plate. The horizontal slit was closed as far as possible to limit the amount of flame radiation collected by the

photomultiplier. The vertical slit width was set to ½ mm to obtain good spatial resolution at small scattering angles. The dependence of the test volume on scattering angle as seen by the detector, had to be taken into account. This is given by $V_{test} = V_{test}(90^0)/\sin\theta$.

In a similar fashion, the monochromator assembly was aligned so that the image of the hair was positioned centrally on the entrance slit.

For the flame extinction measurements a caesium hollow cathode lamp, together with a pulsed power supply and frequency generator, was employed as a light source. Hollow cathode lamps, in general, are of superior stability compared to tungsten filament or Xenon lamps, because they are operated at low currents which are easily stabilised electronically. The Cs lamp was chosen for its strong infrared resonance lines at 852.1 and 894.3 nm. The lamp, containing some impurities, also showed suitably strong lines in the visible. These were at 764.3, 641.6, 501.8 and 460.5 nm. The photomultiplier tube (EMI 9658A) incorporates a corrugated S-20 cathode with increased quantum efficiency in the infrared. When measuring absorption in the infrared second grating orders were excluded by an infrared filter (Kodak Wratten 74) placed in front of the lamp. Schlieren effects were minimised by focusing the lamp into the test volume with a lens (f = 17.5 cm), before imaging it onto the spectrometer slit.

Flames always emit a considerable amount of light, especially under sooting conditions. In order to discriminate the scattered (and absorbed) light against flame emission, phase-sensitive detection had to be employed. In this, the signal, which is to be detected, has to be modulated. For this reason, a variable speed control chopper was incorporated, interrupting the laser beam with a frequency of $\sim$ 800 Hz. The necessary reference signal was produced by a photodiode, illuminated by the laser beam. This eliminated phase shifts between the photomultiplier and reference signals, which can cause instabilities during phase-sensitive detection. For the detection of the photomultiplier signals a Lock-in amplifier (Brookdeal 401A) and a combination of a.c. preamplifier (Brookdeal 452) and phase-sensitive detector (Brookdeal 411) were used. The outputs from these were recorded on two x-t chart recorders. After amplification the photomultiplier signals were monitored simultaneously on a dual channel oscilloscope, before phase-sensitive detection.

This experimental arrangement made it possible to carry out concurrently, the measurement of the scattered light at -90^0 using the monochromator and that at any angle with the L.L.S. detector. By setting the laser chopping frequency and the modulation frequency of the Cs lamp far enough apart, it was also possible to measure the scattered light at any angle with the L.L.S. detector and, at the same time, to use the spectrometer for the extinction measurements.

After passing through the flame, the laser power was measured with a pyroelectric laser power meter (Coherent Radiation Inc.), which gave the flame extinction coefficient at 488 nm, thus utilising the high spatial resolution available from the focused laser.

IV-2 CALIBRATION PROCEDURES AND SENSITIVITY TESTS

In order to measure light intensities over a wide range it was necessary to calibrate the L.L.S. detector and the spectrometer photomultiplier against the applied cathode voltage. These calibrations for the tubes used are shown in figs. 4 and 5. Calibrations were carried out using Rayleigh scattering from pure nitrogen and spectrum calibration lamps (Hg and Ne) for higher intensities and different wavelengths.

Sensitivity tests were carried out to determine the depolarisation ratios of some pure gases and the vibrational Raman cross-section of nitrogen at room temperature. These results are given in Table 6 and compared with values from other works.

Before this could be done, an additional alignment of the apparatus had to be carried out. This involved the correct setting of the plane of polarisation of the laser and the analysers, either parallel or perpendicular to the plane of observation. First, a polariser with approximately vertical polarisation was positioned in the laser beam (at lowest laser powers). The polarisation of the beam was then adjusted (approximately) horizontally with the Fresnel rhombs and the Glan Thomson prism. With the analysers set as near vertical as possible, the V_H scattering component from nitrogen was measured with the spectrometer and the L.L.S. detector at several angles. The V_H was then minimised by slightly adjusting the Glan-Thomson prism, thus correctly determining

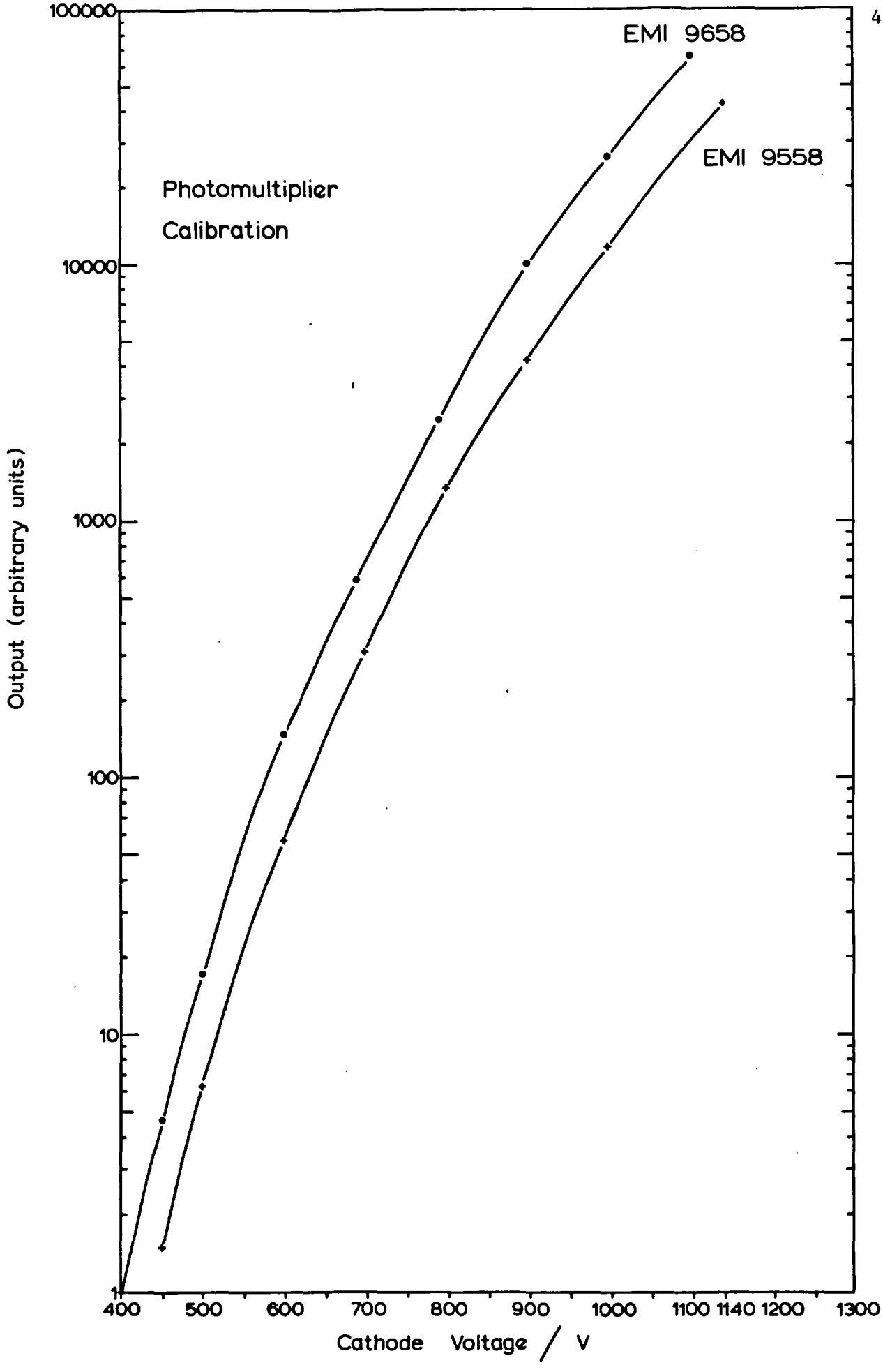

Fig. 4: Calibration for photomultipliers 9558B and 9658A used with the spectrometer (arbitrary independent units for both curves).

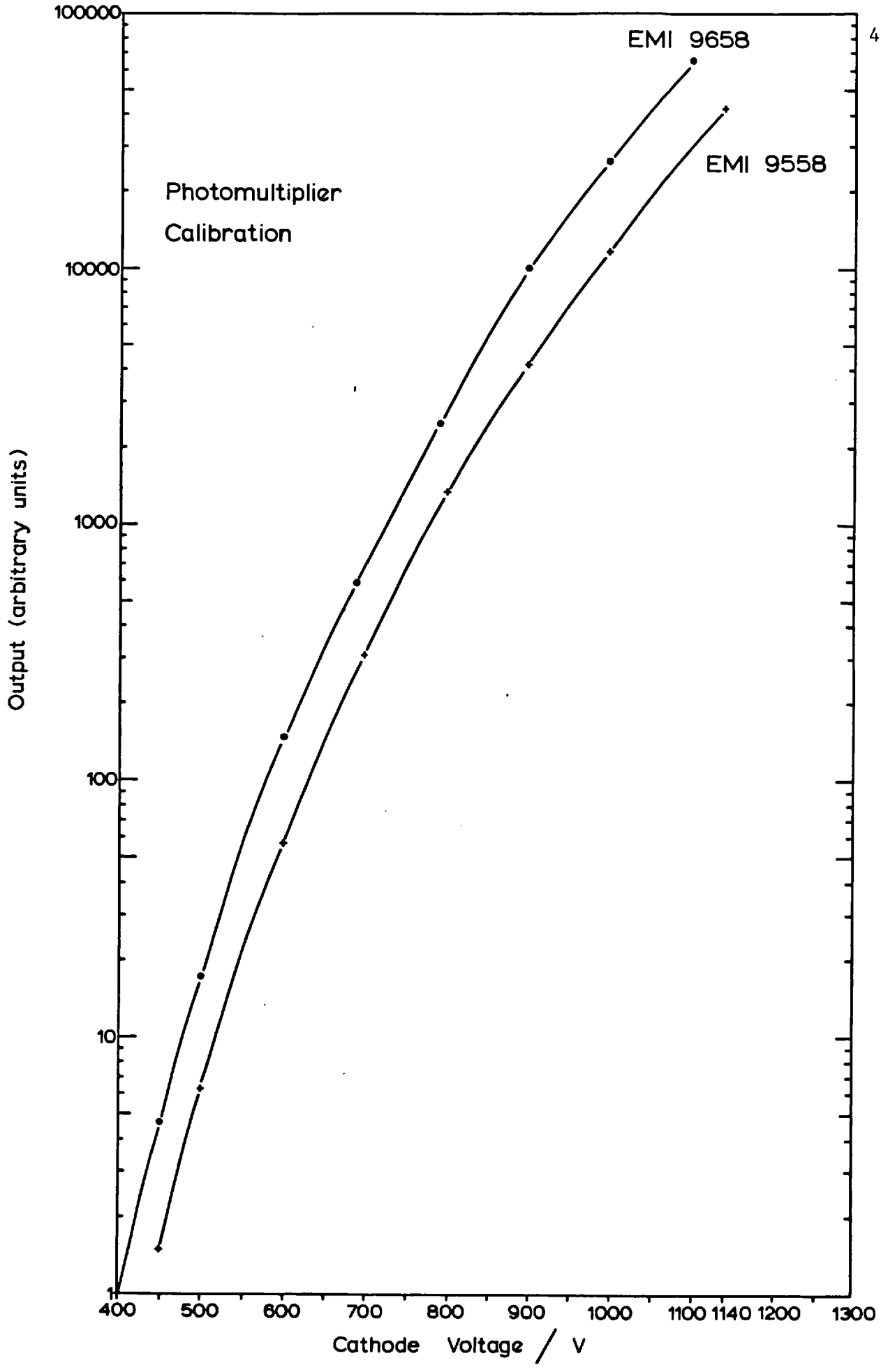

Fig. 5: Calibration for L.L.S. detector photomultiplier.

TABLE 6

a) Measured depolarisation ratios for the Rayleigh band (including rotational Raman), ρ_V^t, and the Rayleigh line, ρ_V^c.

	Ref. 131		This work		
			α)	β)	γ)
Gas	$100\ \rho_V^t$	$100\ \rho_V^c$	$100\ \rho_V^t$	$100\ \rho_V^c$	$100\ \rho_V^c$
N_2	1.08	0.31	1.08	0.28	0.275
O_2	2.882	0.78	2.88	0.76	0.74
C_2H_4	-	-	-	0.1	-

α) L.L.S. detector without interference filter

β) Low resolution

γ) High resolution

b) Vibrational (V = 1 ← V = 0) Raman cross-section of nitrogen.

	Ref. 145	This work
$\sigma_{RAMAN}\ (N_2)/cm^2$	5×10^{-31}	4.5×10^{-31}

the horizontal laser polarisation. A small deviation of the analyser position from vertical has no influence at all, in determining the minimum, wheras even the smallest fraction of vertical polarisation in the beam, due to misalignment, greatly increases the measured signal. The laser power was maximised by adjusting the Fresnel rhombs. With clamps, screwed onto both rotators, the position of the Fresnel rhombs and the G-T prism could always be reproduced. The vertical polarisation of the laser, which is less critical, was obtained by rotating the Fresnel rhombs by 45^0 and the G-T prism by 90^0. Again, clamps were used to reproduce these positions. Within the accuracy of the power meter, the laser power was found to be the same for both polarisations (about 1 W). With the laser polarisation being vertical, the analysers were then brought into approximately horizontal position and the H_V component was measured. This was then minimised by turning the analysers, until they were in the correct horizontal position.

After carrying out the procedure several times, the H_V equalled V_H, but the H_H component was measured as slightly greater. This was attributed to the apertures of the lenses being too large, thus collecting light from angles other than 90^0. After successively measuring H_V, V_H and H_H (90^0) with 2". 1" amd ½" apertures and extrapolating to zero aperture, perfect agreement was obtained between them. For a ½" aperture the H_H (90^0) was found to be only $\sim$ 5% bigger than the H_V and V_H. The ½" aperture was used throughout for all light scattering measurements with the L.L.S. detector and for most measurements with the monochromator.

IV-3 BURNER SYSTEM

Preliminary experiments and considerations in the early stage of this work showed that the apparatus to be constructed for this investigation should be based on a most versatile burner and flow system capable of producing a variety of flames. In addition, a safe method for the addition of the peroxides to the flames was required.

The problems regarding the burner and flow system were:

(i) to provide a system suitable for both diffusion controlled and premixed burning as well as for experiments pyrolysing fuel in counter-flow against a variously diluted flame (the 'hot plate' experiment),

(ii) to add peroxides on either the fuel or oxidant side, or both and to measure their flow;

(iii) to measure all gas flows with high accuracy and maintain flow and flame stability for long times (of the order of 8 hours);

(iv) to take into account all safety considerations, related to the risks of decomposition, high flammability in the presence of fuel or oxygen, as well as to the toxicity of the peroxides.

The burner system chosen is similar to the counter-flow diffusion flame burner, where the flow pattern has been studied[141]. Fuel (ethylene), oxygen, nitrogen and peroxide could be supplied separately to both top and bottom parts of the burner. Each part consisted of silica tubes with silica sinters (diameter 3 cm) in the mouths. No metal was used to avoid catalytic decomposition of the peroxides. Both burner tubes were surrounded by stainless steel flanges with an outer diameter of 6 cm. It was found necessary to water cool the top part of the burner and fill the silica tubes with quartz wool as protection against flash-back and to randomise flow and prevent the build up of a radial temperature distribution in the gas resulting from peripheral cooling.

The whole burner assembly could be moved horizontally with ± 0.5 mm and vertically with ± 0.1 mm accuracy. The spacing between the bottom and the top parts could be changed between 5 and 30 mm. An outer nitrogen shield allowed for the exclusion of air entrainment.

To be able to change the gas flows independently, the three gases, supplied by six gas cylinders, were separately regulated by needle-valves and their flowrate measured with calibrated capillary flow-meters. The total flowrate of the mixture entering the burner, could be changed by blowing off some of the mixture through a soap film flow meter.

For safety reasons the peroxides were added to the nitrogen stream only and the connections containing potentially hazardous mixtures were kept short. PTFE tubing was used throughout where peroxides were present. The peroxides were vapourised in saturators. The amount of peroxide added could be varied continuously by changing the ratio of nitrogen flow through the saturators and flow resistors, while the total flow

of nitrogen was kept constant. The flowrate of peroxide added was metered in terms of the time it took to vapourise a given amount (usually 1 - 2 cc) from the saturator.

A schematic diagram of the burner is shown in fig. 3. The complete apparatus can be seen in Plate 1.

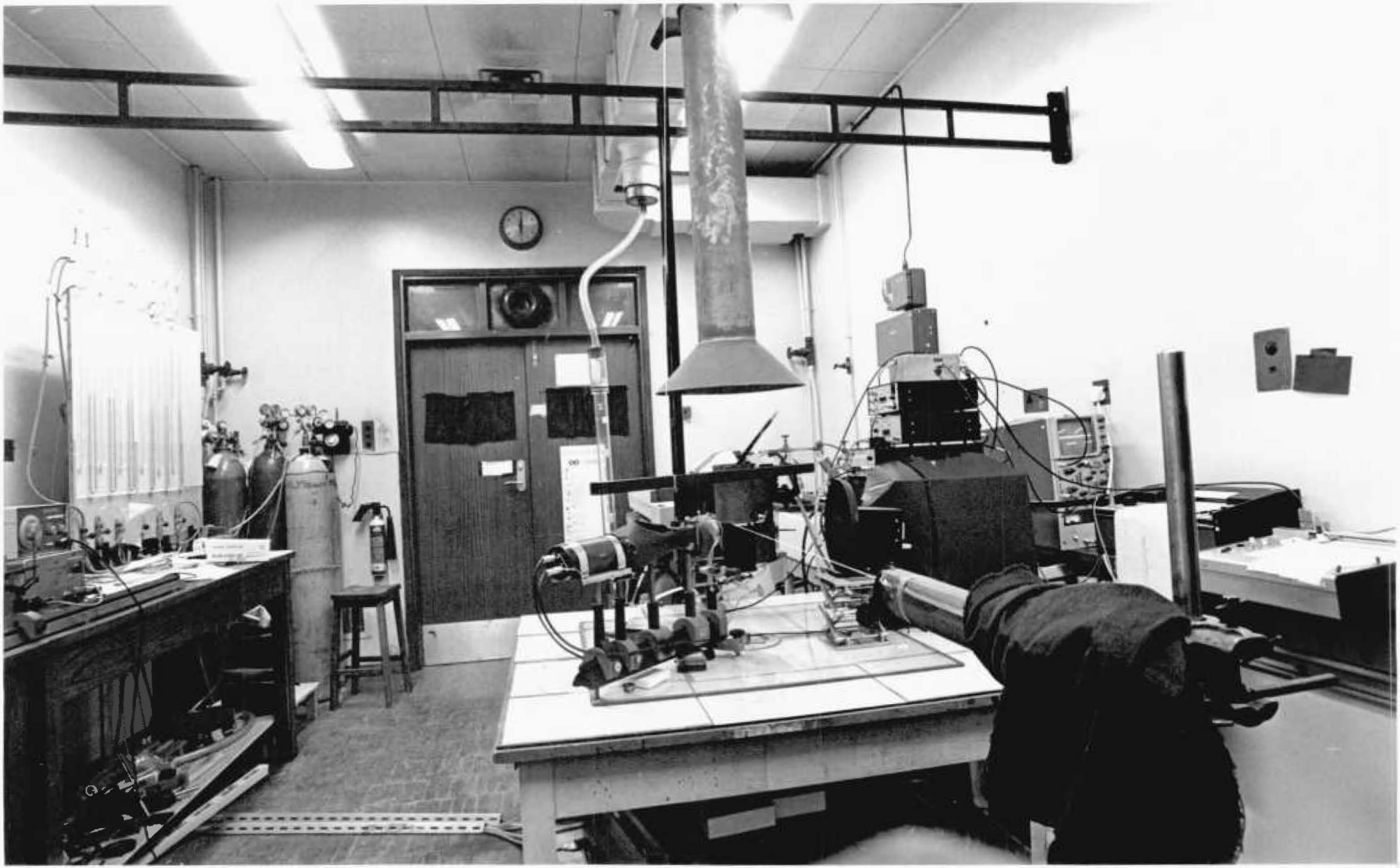

V RESULTS

V-1 SPECTRAL COMPOSITION OF SCATTERED LIGHT FROM SOOTING FLAMES

During early experiments of this work it was established that the light scattered from the early region of a sooting flame was almost completely depolarised. From formulae III-4 and III-13, it follows that the maximum (Rayleigh) depolarisation ratio of an infinite cylinder can only be 1/3. This suggested that a non-instantaneous scattering process, namely fluorescence was present. Usually one can expect the radiative lifetime of fluorescence to be much larger than the rotational frequency of the molecules. Thus the emitted radiation should be completely depolarised. This is not necessarily true for the liquid or solid phase but certainly applies to most gas phase conditions.

The spectral analysis of the scattered light was carried out with the monochromator apparatus shown in Fig.1. The spectral resolution, applying Rayleigh's criterion[142] and found from tests of the apparatus, was 0.17 nm for 100 μm and 0.34 nm for 200 μm slit widths.

The wavelength scale of the monochromator was calibrated with Hg and Ne spectral calibration lamps (incorporating a chopper with reference light source); the scale reading +2.5 nm gave the correct wavelength. The lamps were also used to test the transmission through the system for vertically and horizontally polarised light. It was found that, over a wide wavelength range, employing the half-wave plate as polarisation rotator, the transmission was virtually the same for both planes of polarisation.

To account for the spectrometer transmission and photomultiplier quantum efficiency, both strongly dependent on wavelength, the correction curves shown in Fig.6 were measured. This was done with the help of the tabulated relative line strengths of the sprectrum calibration lamps.

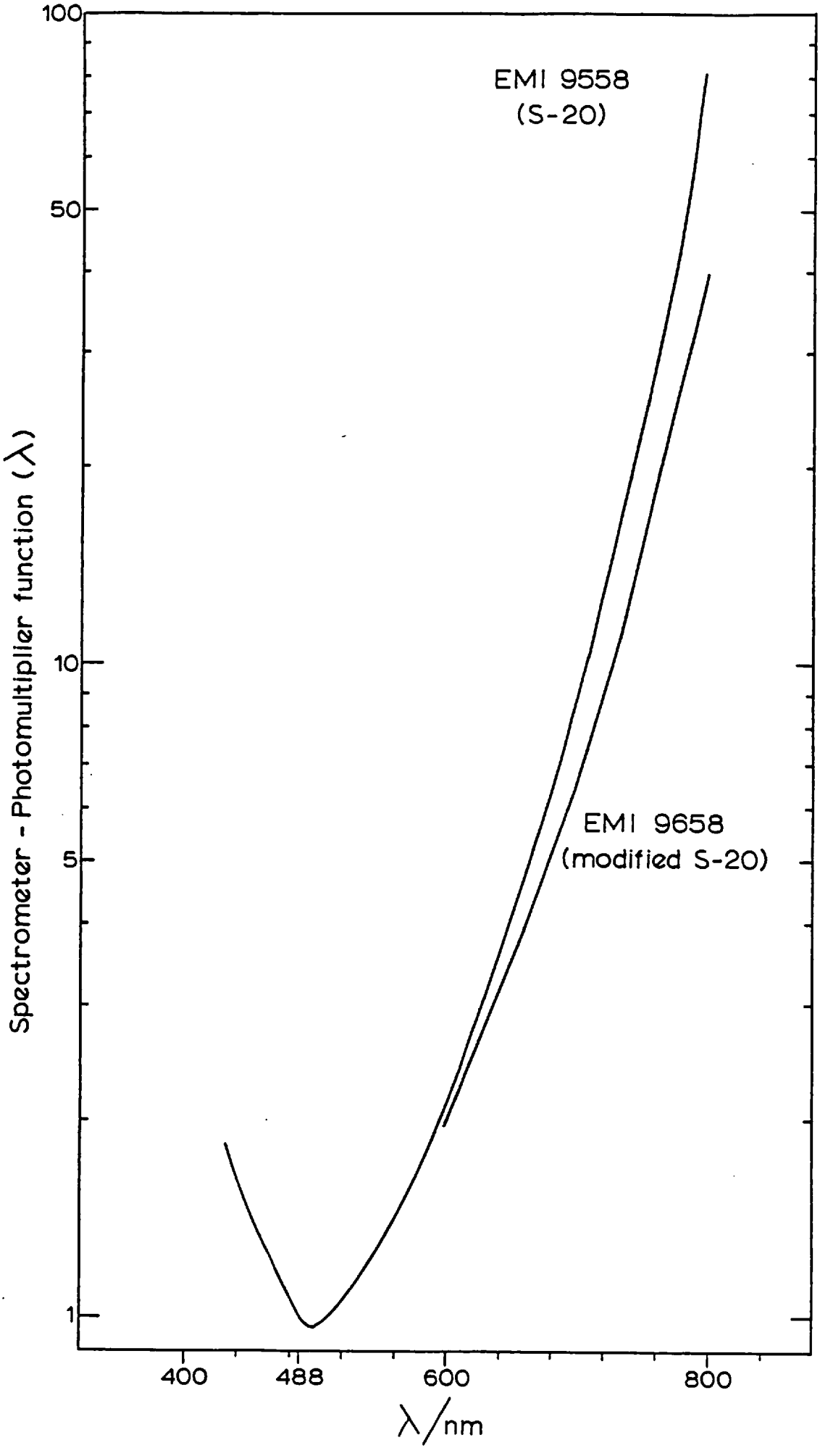

Fig. 6: Calibration of spectrometer-photomultiplier against wavelength, relative to 488 nm.

To obtain the absolute scattered power (intensity) at any wavelength, it was necessary to relate all measurements to a standard, which avoids the tedious procedure of obtaining the absolute scattered power (intensity) by evaluating all view factors, reflection losses etc. For this purpose, the V_V Rayleigh scattering from nitrogen was chosen, because its differential cross-section can be easily calculated (see Table 2) and is in agreement with the experiment[130]. To exclude small dust particles, which would lead to error, calibration measurements of $I_{VV}(N_2)$ were carried out with the nitrogen flowing through a grade 5 sinter. This sinter was then replaced by the burner and no difference in the signal could be detected, i.e. the gas was dust free. Similar measurements were done for oxygen and ethylene, giving good agreement with the relative cross-sections σ_r in Table 2. Similarly, all scattering and fluorescence measurements were carried out relative to I_{VV} (N_2), which was determined before and after each experiment, to account for drifts in photomultiplier gain and day to day changes in laser power.

The laser excited fluorescence was detected with the spectrometer-photomultiplier and lock-in amplifier from premixed or counterflow diffusion flames whenever soot was formed. Under conditions of heavy soot formation in the flame, the unpolarised fluorescence could only be seen by the naked eye when looking through a crossed polariser, because of the strong V_V particle scattering on the incident wavelength and the soot grey body emission. In the thin layer of highest soot volume fraction in counterflow diffusion flames, the depolarised H_V component of the light scattered from the soot particles (see Chapter V-4) was usually stronger in intensity than the fluorescence itself, thus making visual detection of the fluorescence impossible. However, there were special flame conditions, when the green fluorescence, clearly different in colour from the exciting laser line at λ = 488 nm, could easily be seen by eye even without the help of a crossed polariser. This was the case for the pyrolysis (fuel) region of counterflow diffusion flames (especially when these were made non-sooting by excessive nitrogen addition) and for premixed flames, either burning with a C/O ratio just below the visual soot limit (0.6 for ethylene) or extremely rich in fuel (C/O > 1.2).

For the investigation of the fluorescence it was highly desirable to look for conditions where the fluorescence intensity was highest and virtually no soot particles were present. The presence of soot particles was judged by the grey body emission from the flame (which is also a strong function of the temperature) and, more important, by the V_V scattering component and the absorption in the infrared (at 894.3 and 966 nm). It was found that, by increasing the C/O ratio above 1.4 and burning with excess oxygen compared to air (N_2/O_2 between 1.0 and 1.8)* the infrared absorption through the flame was near zero (compared to very high absorption in the visible) and also the V_V scattering component was small (see Fig. 22). The intensity of the flame emission was extremely low under these conditions, whereas the fluorescence intensity was considerably higher than, for example, at C/O = 1.

Before discussing this further in connection with particle size and number density determination (see V-2), the fluorescence spectra themselves should be described.

Fluorescence spectra were taken from premixed and counterflow diffusion flames. Figs. 7 and 10 show typical spectra from a flame with C/O = 1.43 and N_2/O_2 = 1.53 for two positions. As can be clearly seen by comparing figs. 7 and 8 or 9 and 10, the fluorescence is completely depolarised and the V_V (Rayleigh) scattering component is small. Also, figs. 8 and 10 show, that with the spectral resolution available, any H_V (depolarised Rayleigh) component at 488 nm is undetectable, as it is completely altered by the fluorescence. The spectra from the counterflow diffusion flame (taken 2.5 mm below the layer of highest soot concentration) look

---

*The stabilisation of a very rich unidimensional flame on a flat flame sinter burner, without an outer diffusion flame, is impossible above a certain C/O ratio (depending on the fuel), even if burning with excess or pure oxygen. However, with the burner system employed in this work (fig. 3), flame stabilisation was enforced by the divergence of the flow lines occurring at about 3/4 of the separation distance of the bottom and top sinters. Stability of the flame was achieved by setting the separation distance between 15 and 20 mm and also flowing a small amount of nitrogen through the top sinter, in counterflow to the flame. Though the flow pattern in the flame could therefore no longer be regarded as being perfectly one-dimensional, the assumption of unidimensional flow near the central flowline was well justified up to about 0.7 d.

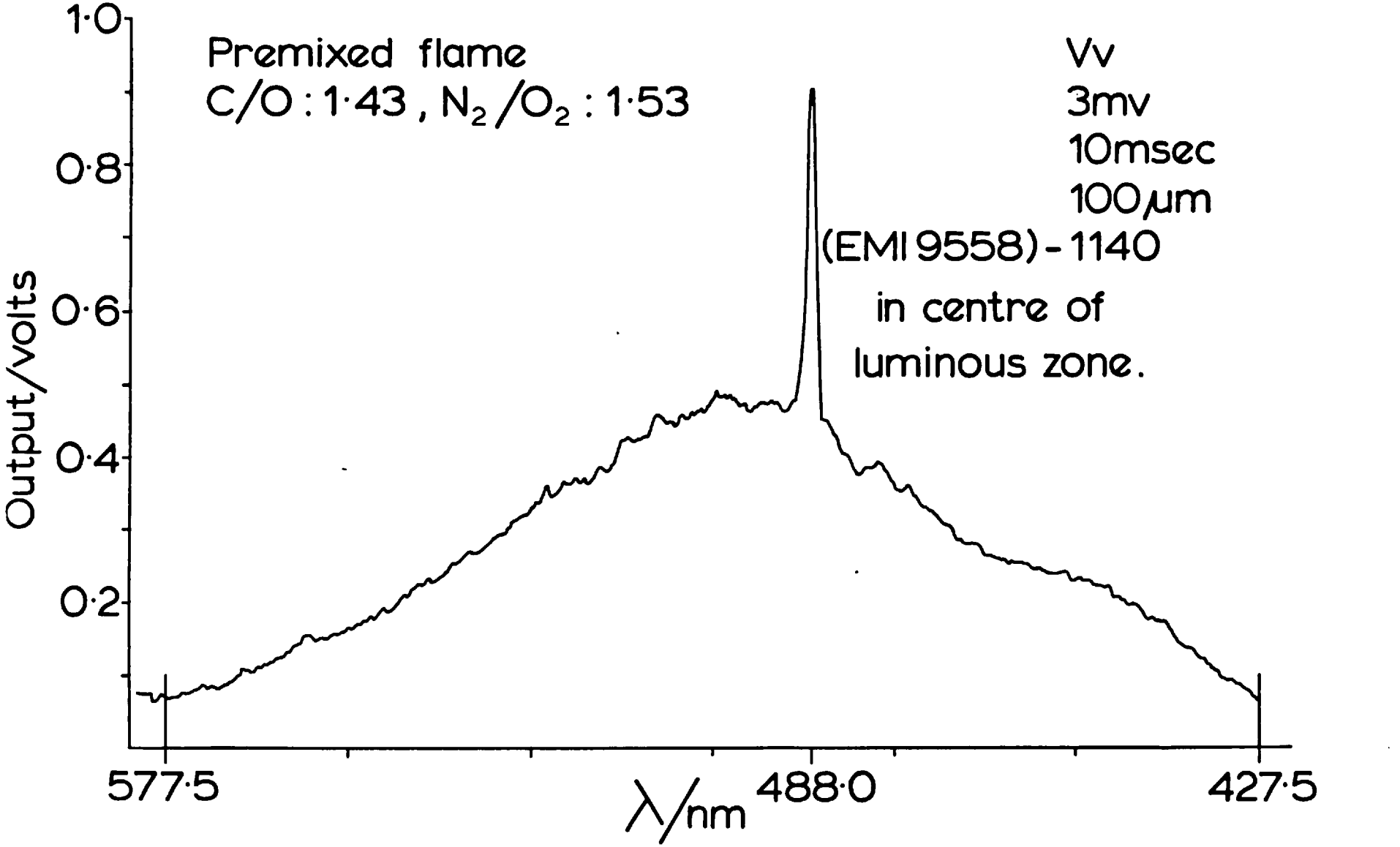

Fig. 7: Fluorescence spectrum from premixed flame. Height above burner h = 3.5 mm. Vertical incidence polarisation, vertical analyser. The $I_{VV}(N_2)$ corresponds to 0.75 mV.

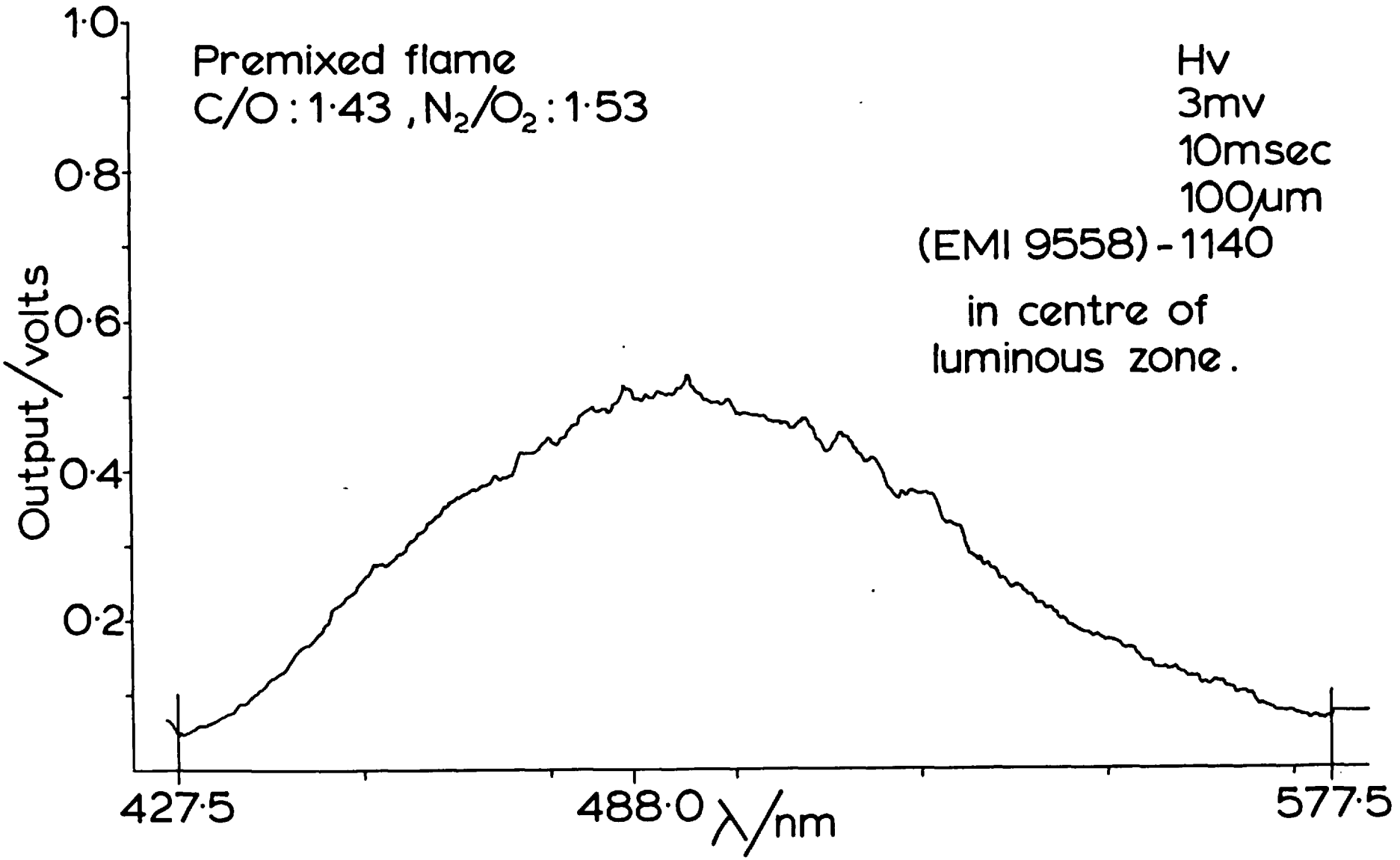

Fig. 8: As Fig. 7, but for horizontal analyser. Scanned from shorter to longer wavelengths.

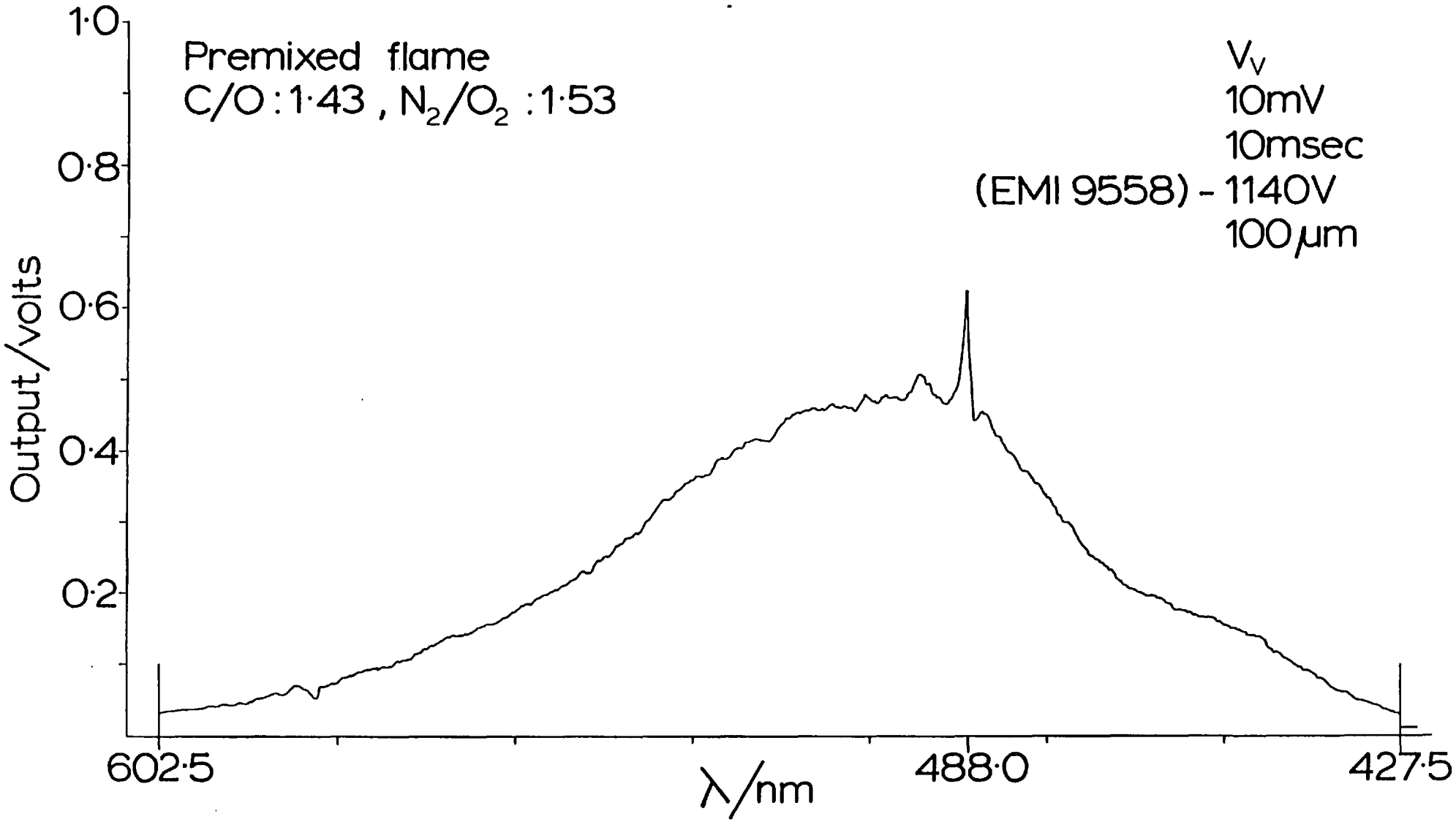

Fig. 9: As Figs. 7 and 8, but h = 10.5 mm. This corresponds to ∿1 mm above flame luminosity. Vertical incidence polarisation, vertical analyser.

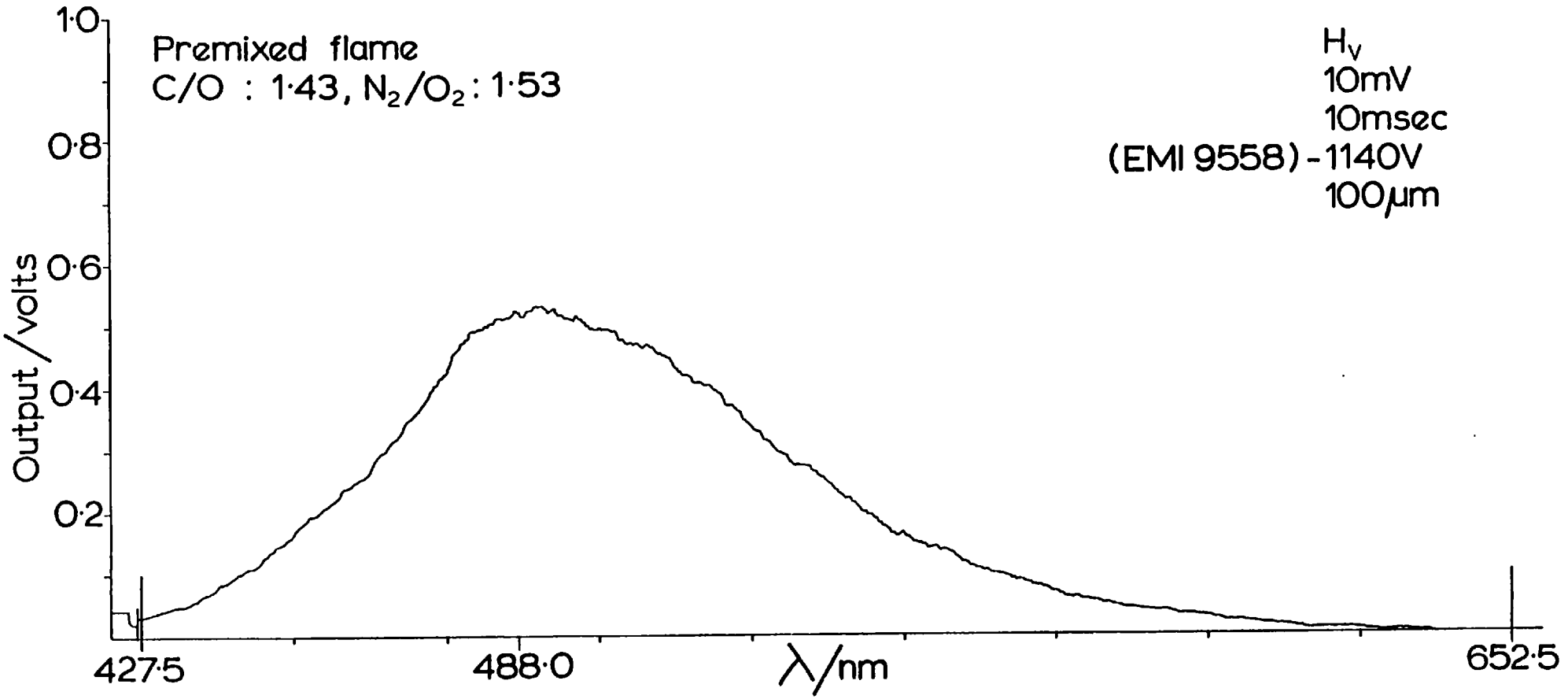

Fig. 10: As Fig. 9, but for horizontal analyser.

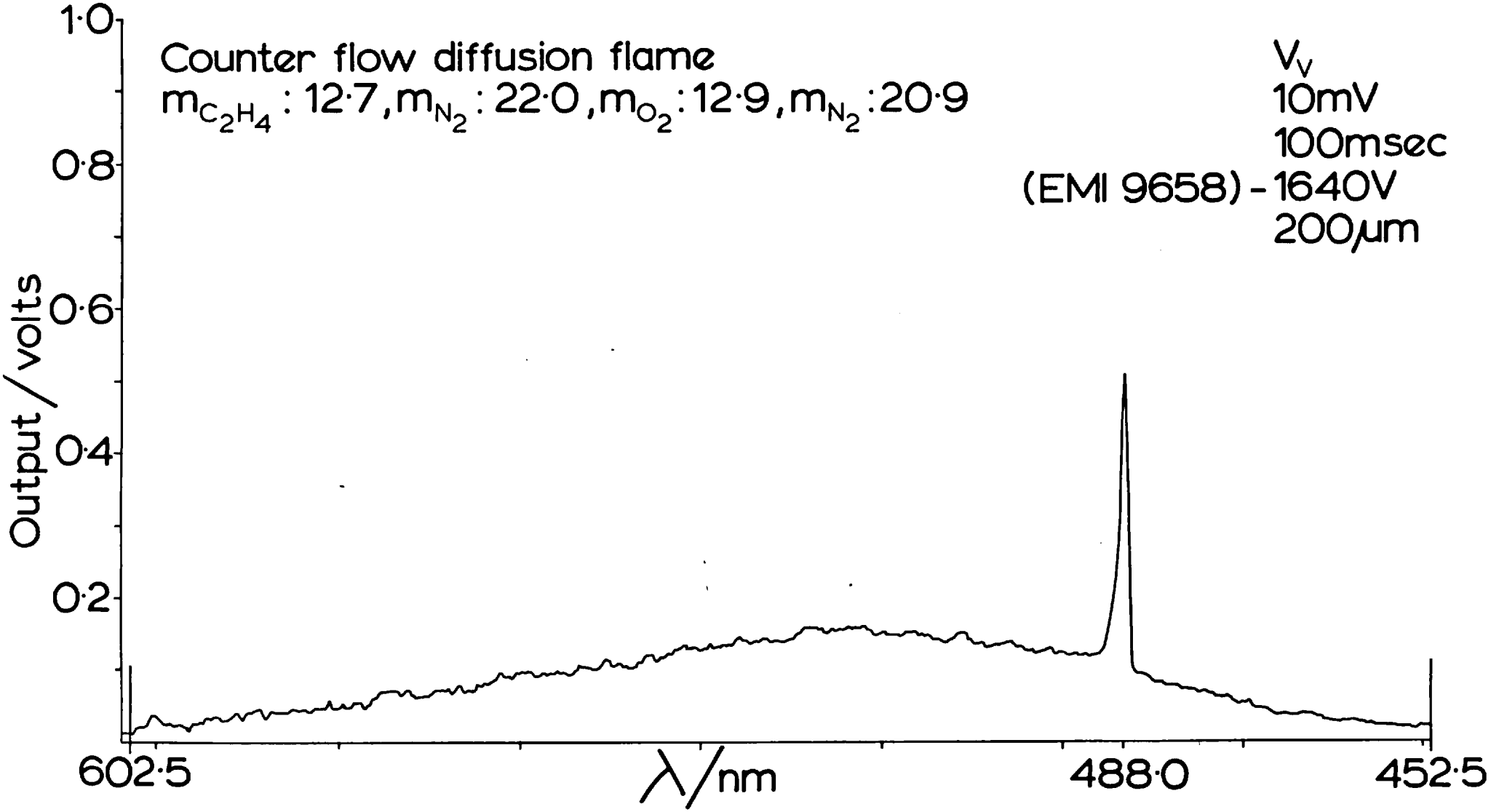

Fig. 11: Fluorescence spectrum of pyrolysis zone of counterflow diffusion flame. All massflows in mg/sec. Vertical incidence polarisation, vertical analyser. The $I_{VV}(N_2)$ corresponds to 3.2 mV.

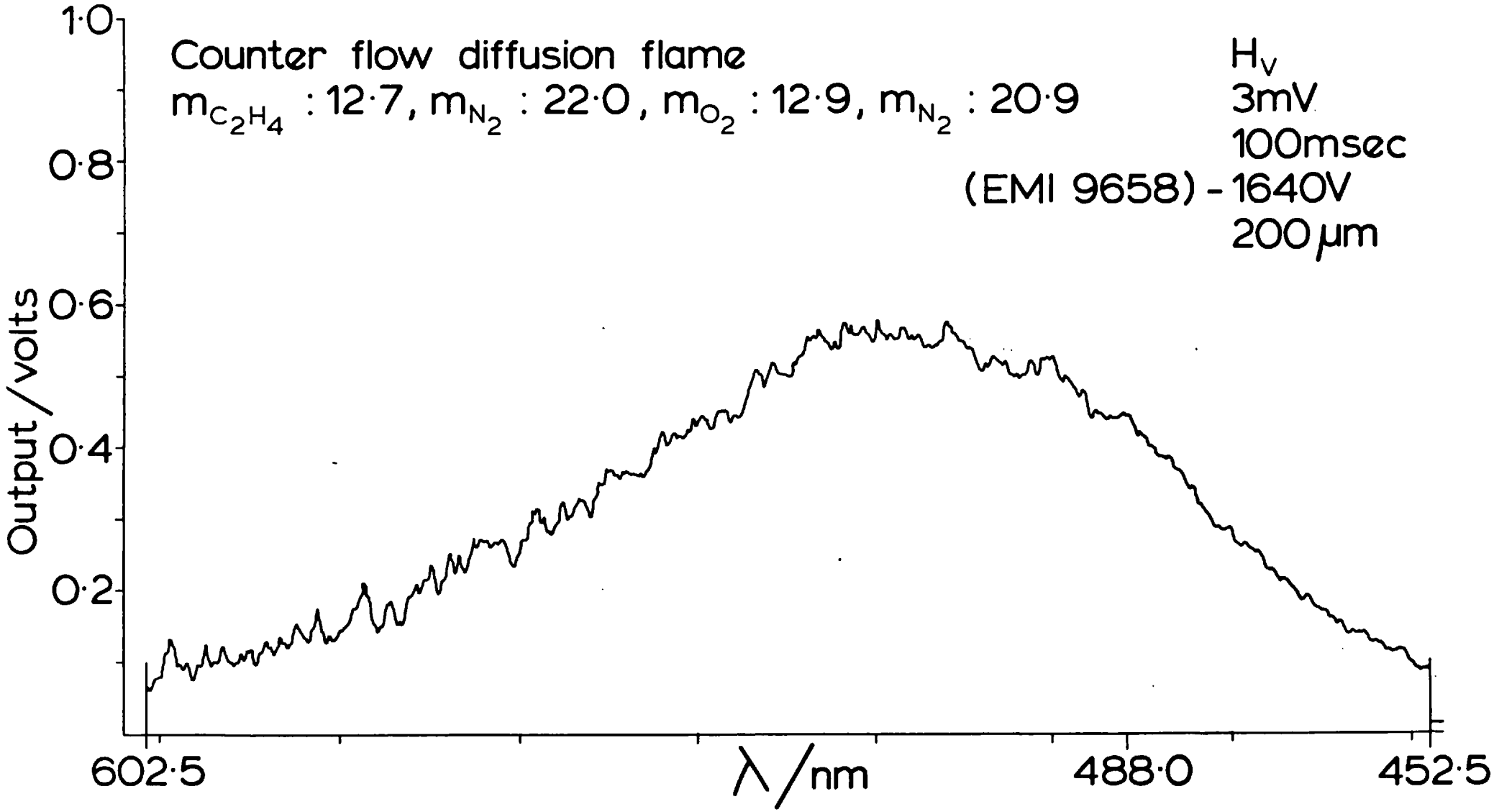

Fig. 12: As Fig. 11, but with horizontal analyser and 3.16 times higher sensitivity.

similar (figs. 11 and 12), but the fluorescence intensity is lower by a factor of $\sim$ 20) and the V_V (Rayleigh) scattering is relatively stronger.

The most important feature of all spectra is the lack of a band structure. The small deviations originate from slight flame movements. Continuous fluorescence spectra were also found by using a 0.5 m prism spectrograph and photographic recording. The spectra are shown in plate 2 (top part), compared with calibration spectra of Hg and Ne lamps and the continuous emission from flame soot. The flame was burning at a C/O ratio of 0.71 and N_2/O_2 = 3.16. The fluorescence spectra were taken from a flame region, where no soot emission was present, i.e. $\sim$ 1 mm above the soot luminosity, whereas the soot emission was recorded at 6 mm above the burner.

Another interesting feature of the spectra is the considerable amount of anti-Stokes fluorescence, on shorter wavelengths than the incident line. This can be explained by the elevated temperature, populating higher vibrational-rotational states of the molecule (radical) or by intersystem crossing.

The continuous character of the spectra leads to the interpretation that the molecules or radicals responsible for the fluorescence consist of a fairly large number of atoms, so that the energy differences of the vibrational-rotational levels are too small to be resolved. Also, the Doppler broadening of each individual transition, due to the elevated flame temperatures would merge any fine structure, which might be present at low temperatures.

The calibration of the spectrometer photomultiplier Lock-in amplifer system in terms of absolute scattered power (intensity) made it possible to determine the total light power contained in the fluorescence relative to the incidence laser power. In particular this could be compared to the fraction of the laser power absorbed while passing through the flame, thus allowing for the determination of the fluorescence and fluorescence quenching coefficients, $\varepsilon_{flu} = N \cdot C_{flu}$ and $\varepsilon_{quench} = N \cdot C_{quench}$ (with N denoting the number density of the fluorescing molecules or radicals).

We then have

$$\varepsilon_{total} = \varepsilon_{flu} + \varepsilon_{quench} \; (+\varepsilon_{abs.\ part.})$$

and as $\varepsilon_{abs.\ part.}$ is negligible under the conditions corresponding to figs. 7 - 10, we find

$$\varepsilon_{total} = \varepsilon_{flu} + \varepsilon_{quench}$$

The total fluorescence coefficients were calculated (for the spectra shown in figs. 7, 8 and 9, 10) in the following way. First, the wavelength correction according to fig. 6 was applied and the area (in mV·nm) underneath the spectrum was determined graphically, taking the sensitivity of the Lock-in amplifier into account. This area now had to be divided by the small but finite area corresponding to the V_V scattering component from nitrogen, whose accurate determination was crucial. For this purpose the laser wavelength, though not single mode, could be regarded as perfectly monochromatic, thus the problem was reduced to obtaining the slit function for a finite slit of an infinitely slowly scanning spectrometer. Approximating this slit function by a triangle and calculating the dispersion of the Hilger and Watts spectrometer[142], the baseline of the triangle was found to be 0.34 nm for a slitwidth of 100 μm. This was verified experimentally by scanning the V_V scattering component of nitrogen (488 nm) at a rate of 0.1 nm/min., using the fastest time constant of 10 msec on the Lock-in amplifier and a chart speed of 6 cm/min. Similarly, the same result for the area corresponding to the V_V scattering component of nitrogen can be obtained by multiplying the $\Delta\lambda$ determined by the slitwidth (0.17 nm for 100 μm and 0.34 nm for 200 μm) with the height of the signal. The area ratios obtained in this way were $A_r = 1780$ (figs. 7, 8) and $A_r = 6970$ (figs. 9, 10). The fluorescence coefficients could now be obtained by

$$\varepsilon_{flu} = 2 \cdot \exp(\ell\, \varepsilon_{total}) \cdot 4\pi \cdot N_{room}(N_2) \cdot \sigma_{VV}(N_2) \cdot A_r$$

Here, the factor of two accounts for the unpolarised fluorescence, $\ell = 3$ cm is the optical pathlength through the flame and $\exp(\ell\, \varepsilon_{total})$ accounts for both the decrease in laser power for a pathlength of $\ell/2$, and the attenuation of the fluorescence through the flame* (another $\ell/2$ pathlength),

*The attenuation coefficient of the fluorescence through the flame is of course smaller than ε_{total} for the higher wavelength. The correction factor

4π takes into account that the fluorescence is emitted uniformly over 4π steradians, $N_{room}(N_2) = 2.5 \cdot 10^{19}$ cm^{-3} is the ideal gas number density at 295 K and 1 bar and $\sigma_{VV}(N_2)$ is the differential cross-section for nitrogen. Thus we obtain

Spectrum	Position	ε_{total}	ε_{flu}	$\varepsilon_{flu}/\varepsilon_{total}$
Figs. 7, 8	h = 3.5 mm	0.009	$9.8 \cdot 10^{-4}$	0.11
Figs. 9, 10	h = 10.5 mm	0.041	$4.3 \cdot 10^{-3}$	0.105

with the interesting result of a fairly high fluorescence efficiency of $\sim$ 11%. In a similar way for the spectra from the counterflow diffusion flame (Figs. 11, 12) one obtains $\varepsilon_{flu}/\varepsilon_{total} = 0.05$. This value is much more inaccurate than those quoted above as ε_{total} in this case was approx. $4 \cdot 10^{-3}$, which corresponds to only 1% absorbed laser power, just the limit of accuracy of the laser power-meter. The value for ε_{total} could thus be easily smaller by a factor of two.

As the dispersion of the Hilger-Watts spectrometer was only 1.7 nm/mm it was decided not to leave the question of a possible fluorescence fine structure in the open and therefore some experiments were conducted with high spectral resolution.

A 2 m (Littrow-mounted grating) spectrograph with a dispersion of 0.1 nm/mm was employed for these experiments. With a slit width of 100 µm, the spectral resolution of 0.01 nm was near the Doppler width of 0.005 nm to be expected for flame temperatures[143].

The optical system (Fig. 13) incorporated an f = 15 cm lens (1:1.5 enlarging the test volume), an HN 22 polariser, a prism (45^0-90^0-45^0) to reflect the collected light upwards, and a special prism to turn the image of the test volume by 90^0 in order to use the whole length of the slit. This was done to obtain the spatial distribution of the fluorescence over a length of $\sim$ 1 cm in the flame.

---

exp (0.5 ℓ ε_{total}) is therefore only approximate.

The optical components and the spectrograph were aligned in the following way. A hair was positioned into the laser beam and imaged onto the centre of the slit. The tilting and incidence angle of the grating was then adjusted until the bright image of the hair could be seen in the focal plane of the spectrograph. The image of the hair was then focused in the plane of the spectrograph plate, by adjusting the grating distance. This was done for three laser wavelengths (488, 496.5 and 501.7 nm).

The spectra shown on plate 2 a) and b) were taken from a flame with C/O = 1.51 and N_2/O_2 = 1.53 in a region of no flame luminosity and 10 mm of the centre line*. The plane of polarisation of the laser was set vertically. In plate 2a), (α) was recorded with vertical and (β) with horizontal analyser. The transmission through the spectrograph depends on the polarisation of the light (the transmission ratio of vertically to horizontally polarised light was measured to be 3.0, see below). As the vertically polarised light, having passed the polariser, becomes horizontally polarised (and vice versa), caused by the reflections in the prisms (a)α) shows lower plate density than (a)β) though the exposure time was the same. No half wave plate was used in the optical arrangement.

There are two main features in plate 2a). First, the fluorescence is completely continuous (as already mentioned, great care was taken to properly focus the spectrograph) and secondly, the depolarised (Rayleigh) H_V component is clearly resolved.

The continuous character of the spectra, with a spectral resolution near the Doppler line broadening, prove quite clearly, that the fluorescence originates from polyatomic molecules or radicals. The most likely candidates are polycyclic aromatic hydrocarbons, of more than 10 benzene rings,

---

*The photographic plates used were Kodak spectrum analysis plates No. 3 and the exposure time was always 20 min. The supply of the plates from Dr U. Breitmeier is gratefully acknowledged.

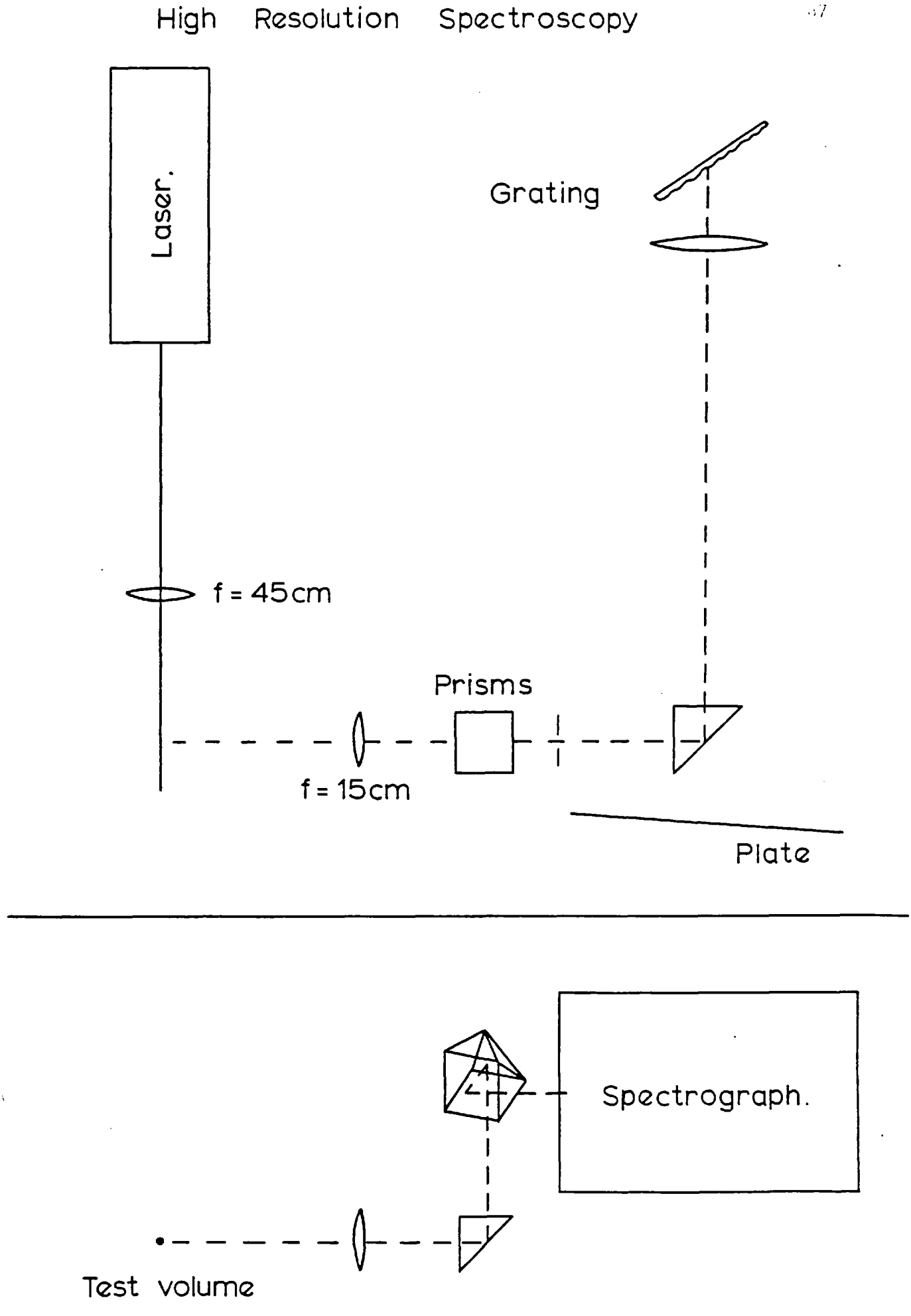

Fig. 13: Schematic diagram of the high resolution spectroscopy apparatus.

Spectra obtained with L.R. Prism Spectrograph

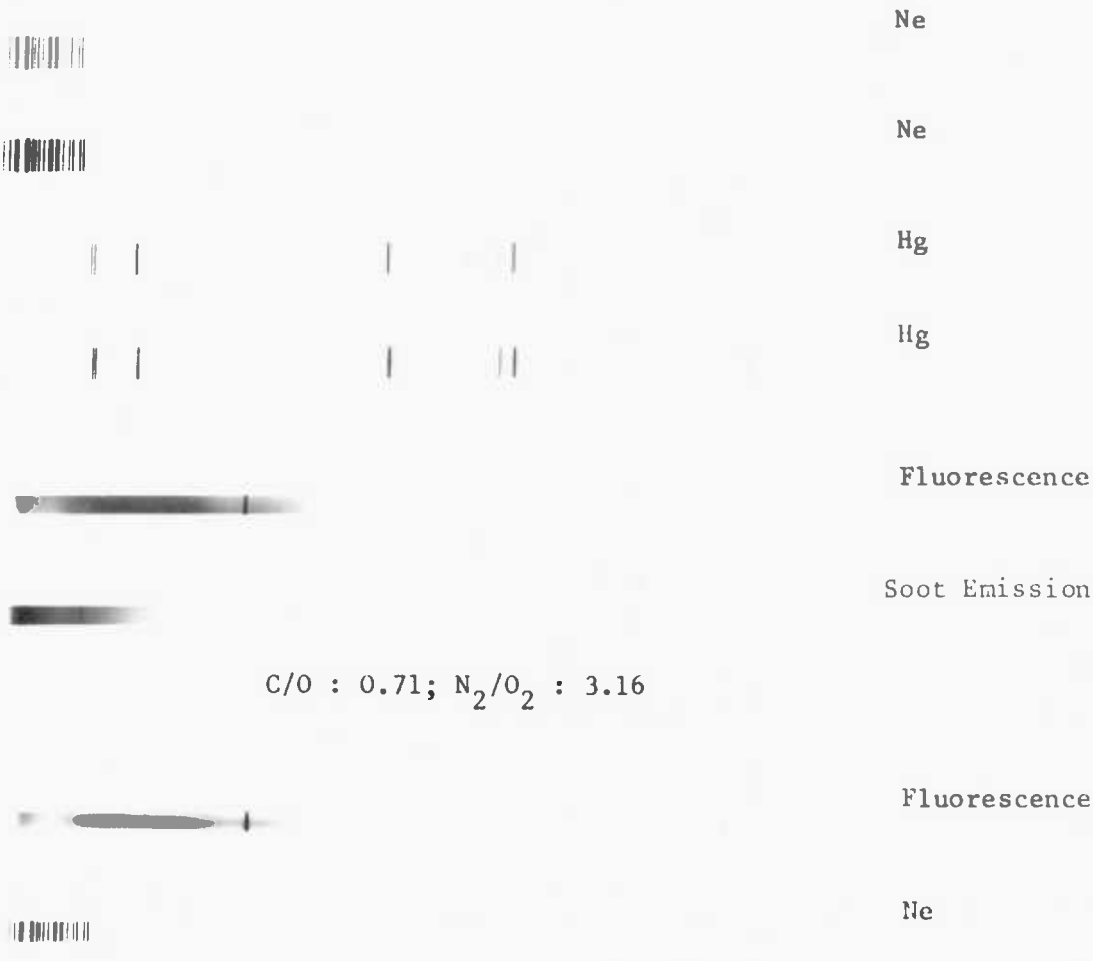

Spectra obtained with H.R. Grating Spectrograph

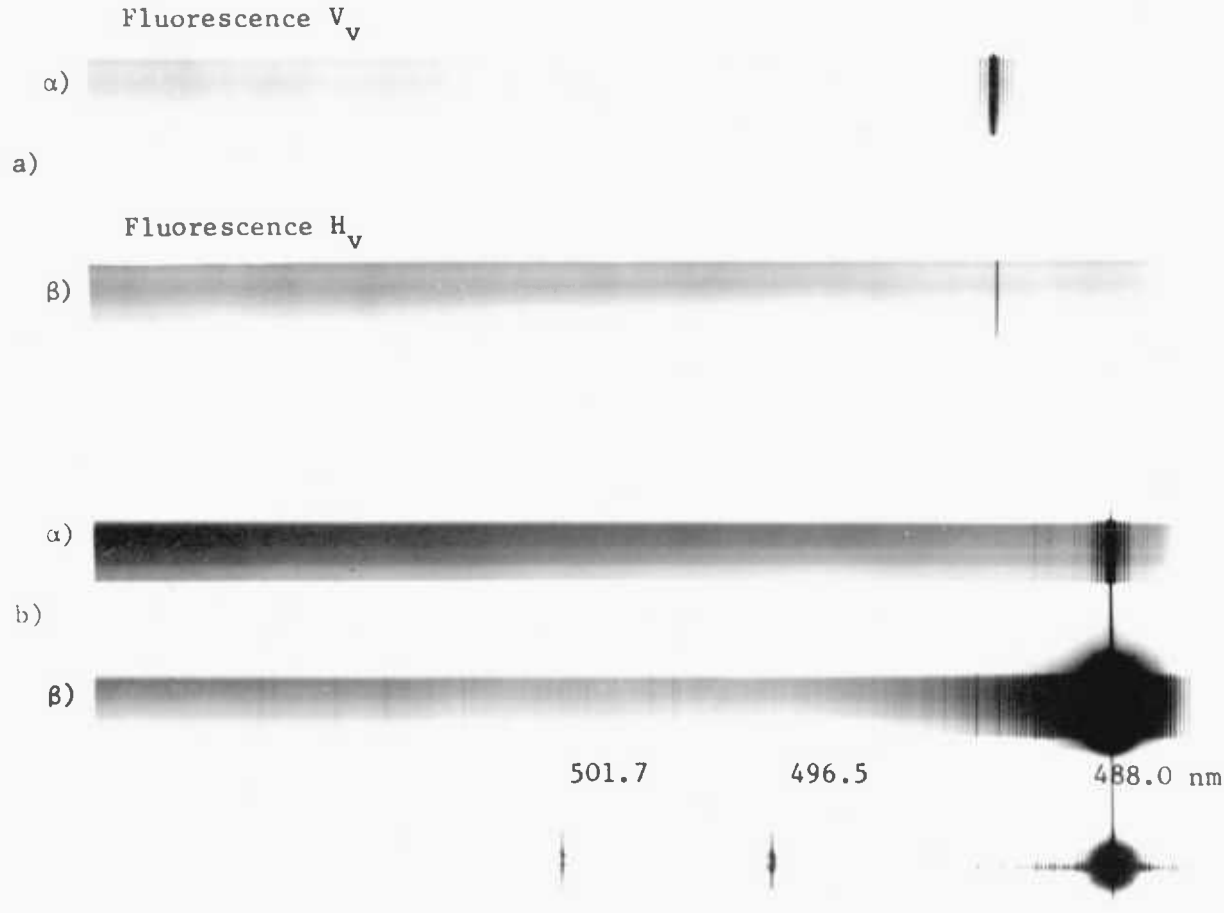

PLATE 2

which one can expect to absorb in the visible. The high fluorescence efficiencies are an indication that the fluorescence is caused by radicals, which usually have higher f-values than molecules and thus are likely to absorb more strongly than molecules. These are probably polycyclic aromatic radicals, though polyacetylenic radicals cannot be ruled out.

It is interesting to compare the continuous spectra observed in this work with the banded fluorescence spectra of the C_2 radical, measured by Hendra et al.[146] They used the argon ion laser lines at 501.7 and 514.5 nm to excite the C_2 radicals present in rich premixed flames. As C_2 does not absorb appreciably at 488 nm, this does not cause interference with the fluorescence described here.

It is a difficult question to decide whether or not the fluorescing species are actual precursors of soot particles or by-products[124,147]. However, one can argue that, under these very rich flame conditions, with CO and H_2 being the main combustion products and small reaction times, soot formation is effectively halted at an intermediate stage.

Therefore, in one experiment, the outer nitrogen shield surrounding the flame was switched off, allowing outer air to penetrate into the flame. This caused heavy soot formation in the test region and correspondingly a decrease in fluorescence. Plate 2(b) shows the resulting spectra, which were taken without a polariser (and again with 20 min. exposure time). In 2(b)(β) the fluorescence intensity is much less than in 2(b)(α), which was taken with the nitrogen shield on. It has to be noted here that the "line structure", especially in 2(b)(β) is caused by grating ghosts, due to the very high V_V scattering component at λ = 488 nm, from the soot particles formed.

With the high resolution spetroscopy apparatus it was possible to conduct some further experiments. As shown in plate 2(a)(β), the H_V depolarised Rayleigh component is clearly resolved from the fluorescent background. To measure the H_V in comparison with the V_V component, it was necessary to change over the photoelectric recording.

This was done in the following way. Again a hair was positioned into the laser beam and an adjustable slit was positioned in the focal plane of the spectrograph, so that the emerging cone of light from the image of the hair could be seen on a piece of transparent paper. The slit was then closed to 100 μm and a photomultiplier tube mounted behind it, which was connected to the Lock-in amplifier-chart recorder. After calibration of the photomultiplier against cathode voltage, the transmission through the spectrograph was measured for vertically and horizontally polarised light. For this measurement, a light bulb was positioned into the test volume with a chopper (and reference light source) in front of it. The transmission ratio of vertically/horizontally polarised light was measured as 3.0. As a check of proper alignment, the depolarisation ratios of nitrogen and oxygen were determined (see Table 6), giving excellent agreement with literature values and the theoretical prediction.

The V_V and H_V scattering components (relative to the V_V component of nitrogen) were measured for two flame positions as function of C/O ratio. Fig. 14 shows the results for h = 3.5 mm. Also included are the calculated flame temperatures T, the estimated residence times t and the gas phase V_V scattering components (see Appendix I). The latter were obtained from the calculated water gas equilibrium composition and the temperature, using formula VII-1. The H_V gas phase scattering components are completely negligible. One can see that the V_V scattering component is very small in this flame region and peaks around C/O = 0.9. Fig. 15 shows the V_V and H_V scattering components for h = 6.5 mm and 10 mm away from the centre axis of the burner. In this region, soot particles are present, causing much bigger scattering. The V_V scattering component peaks around C/O = 0.95 and is small for the highest C/O ratios.

More interesting are the depolarisation ratios, which are plotted in fig. 16. To obtain these from fig. 14, the gas phase scattering had to be subtracted from the measured V_V component. For the small residence times (corresponding to fig. 14), the depolarisation ratios are higher than for the conditions corresponding to fig. 15. For C/O = 1.43, 100 ρ_V reaches the very high values of 9.8 and 3.7 respectively.

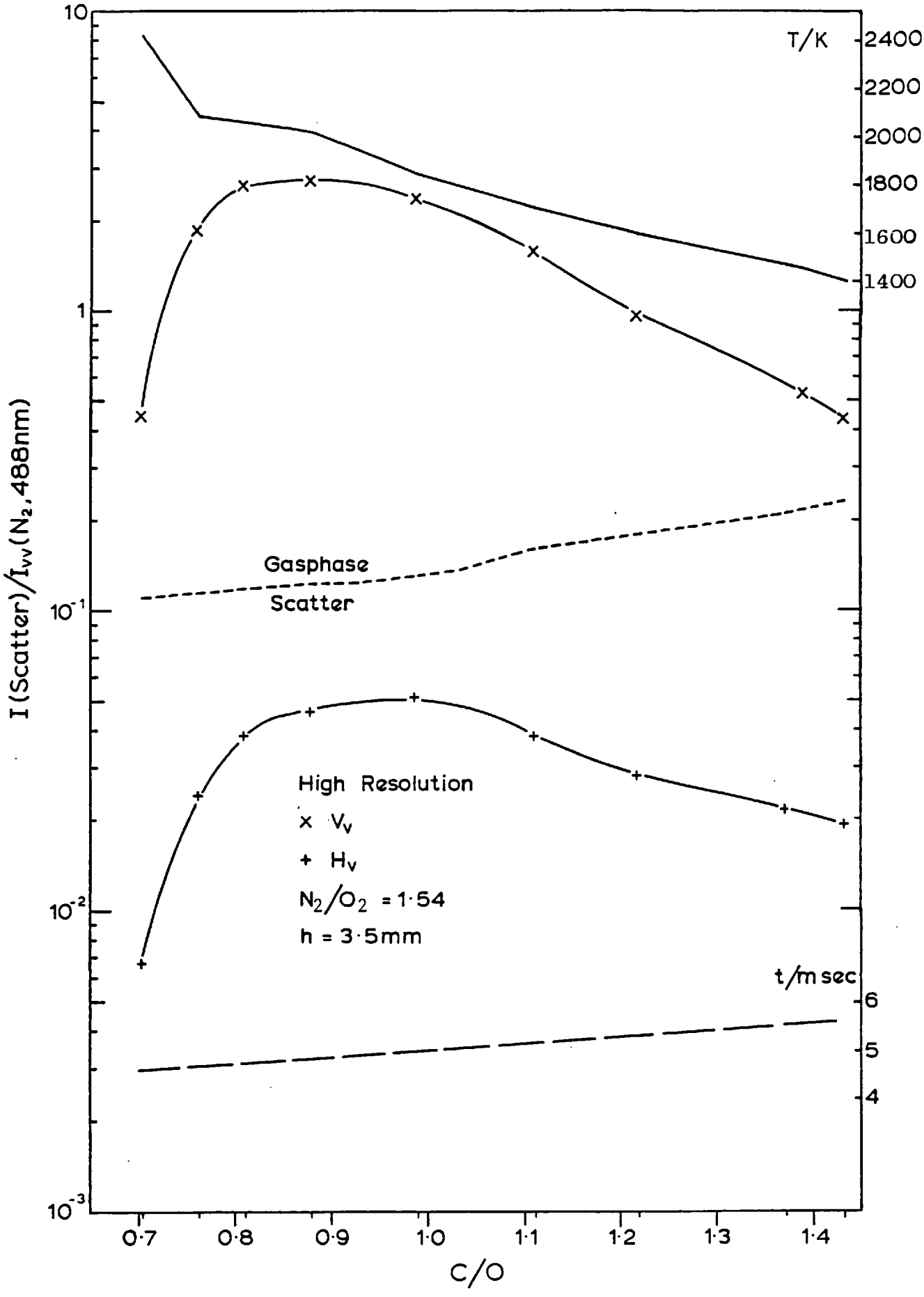

Fig. 14: Rayleigh components V_V and H_V as functions of C/O ratio measured in high resolution. Also calculated temperature T; residence times t and V_V gas phase scattering component.

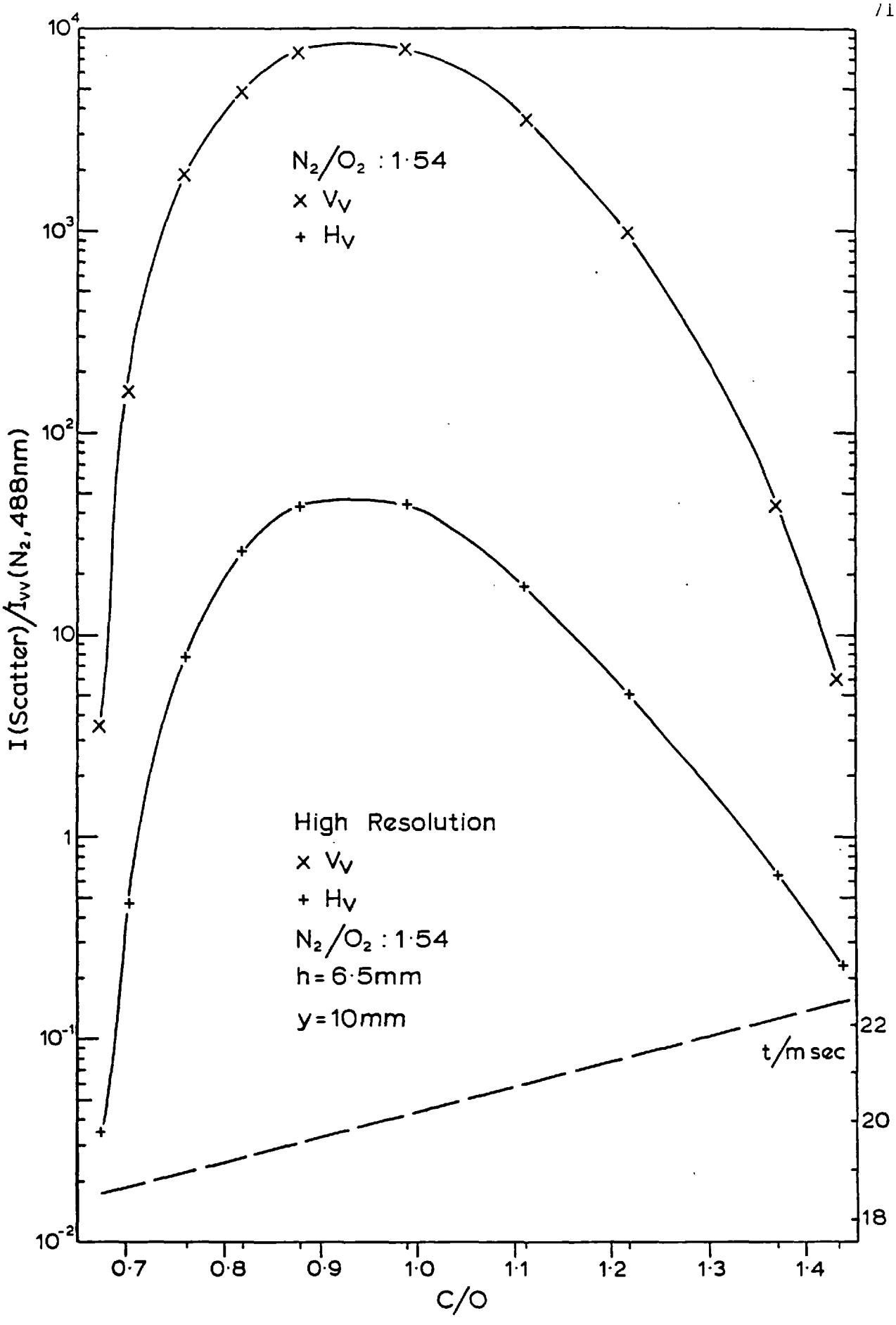

Fig. 15: As Fig. 14 but at height above burner h = 6.5 mm and y = 10 mm away from burner centre line.

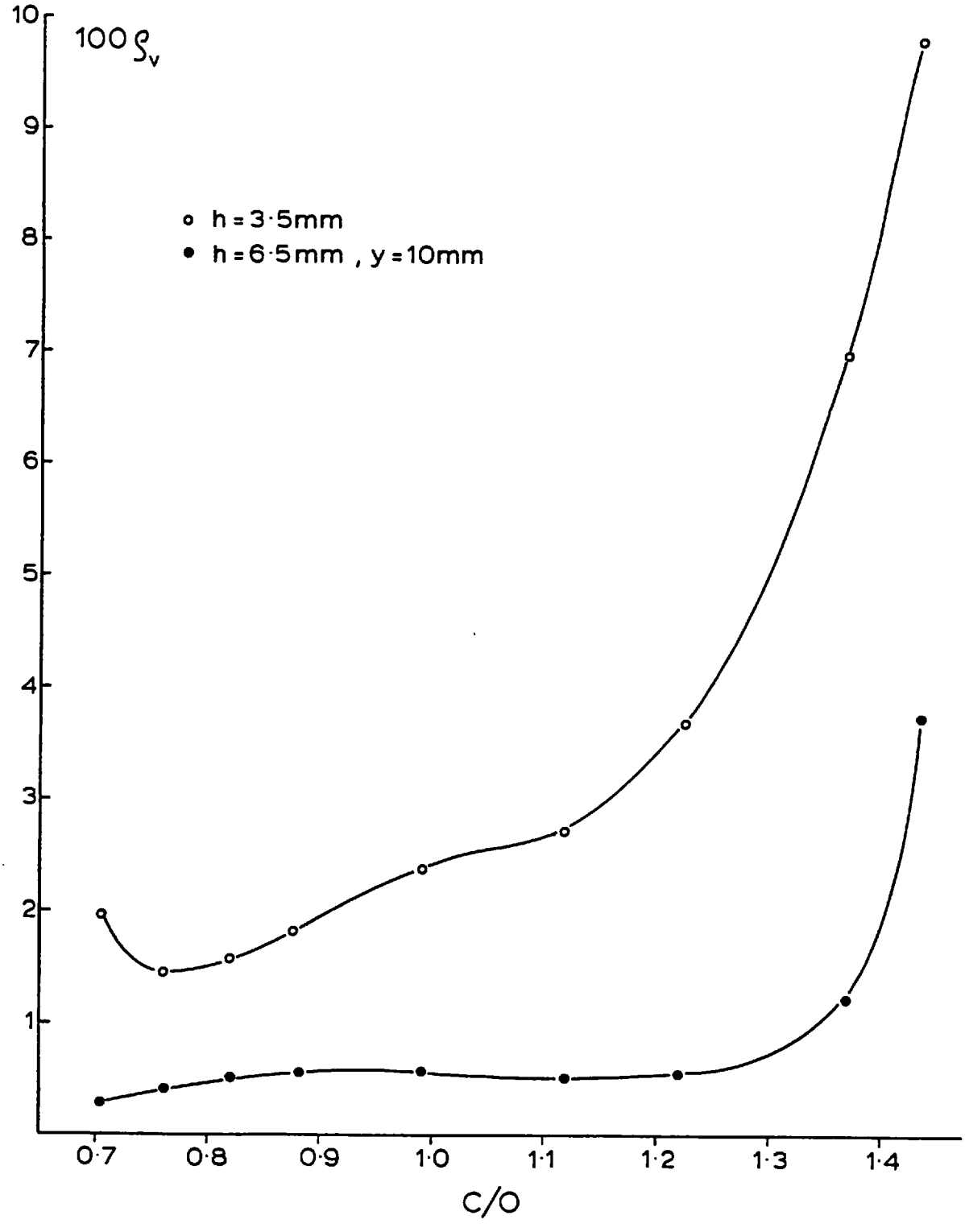

Fig. 16: Depolarisation ratios for both conditions of Figs. 14 and 15. The gas phase scattering contribution is subtracted.

The results can be explained in the following way. The H_V and the V_V scattering components at λ = 488 nm (with the gas phase contribution subtracted from the measured V_V) are composed of scattering contributions from the molecules (which cause the fluorescence) and from soot particles.

$$V_V = H_V\,(\text{soot}) + V_V\,(\text{molecules})$$
$$H_V = H_V\,(\text{soot}) + H_V\,(\text{molecules}) \qquad \text{V-1}$$

These contributions can be separated if three assumptions are made. First, we assume that at C/O = 1.43, and h = 3.5 mm (figs. 14, 16), no soot particles are present, so the depolarisation ratio of 0.1 is only caused by the anisotropy of the molecules. Secondly, we assume that for C/O around 1 and h = 6.5, y = 10 mm (figs. 15, 16), the soot particles dominate the scattering and thus the depolarisation ratio is 5×10^{-3} and is only caused by the anisotropy of the soot particles. Thirdly, we assume that the relative fluorescence intensity, H_V (550nm) at 550 nm, which was measured with the Hilger-Watts monochromator, is proportional to both the V_V and H_V scattering components (at λ = 488 nm) from the molecules. We then have:

$$V_V = V_V\,(\text{soot}) + a\,H_V\,(550\text{ nm}) \qquad \text{V-2}$$

$$H_V = \rho_V\,(\text{soot})\,V_V\,(\text{soot}) + a\,H_V\,(550\text{ nm})\cdot\rho_V\,(\text{molecules})$$
$$= 5 \times 10^{-3}\,V_V\,(\text{soot}) + a\,H_V\,(550\text{ nm}) \cdot 0.1$$

This yields for V_V (soot) and the proportionality constant a :

$$V_V\,(\text{soot}) = \frac{0.1\,V_V - H_V}{0.095}$$
$$a = \frac{V_V - V_V\,(\text{soot})}{H_V\,(550\text{ nm})} \qquad \text{V-3}$$

The validity of the above assumptions was judged by the constancy of a. The results of this calculation (corresponding to fig. 14) are shown in Table 7, together with the H_V (550 nm) data.

TABLE 7

C/O	H_V*	V_V*	H_V(550nm)†	V_V(soot)	a
1.43	1.95 E-2	0.19	0.70	0	0.28
1.37	2.18 E-2	0.32	0.77	0.1	0.28
1.22	2.80 E-2	0.77	0.95	0.52	0.27
1.12	3.80 E-2	1.40	1.25	1.07	0.26
0.990	5.20 E-2	2.22	1.60	1.29	0.27
0.879	4.60 E-2	2.58	1.30	2.23	0.27
0.821	3.80 E-2	2.50	1.10	2.23	0.24
0.764	2.40 E-2	1.75	0.65	1.59	0.25

All components relative to $I_{VV}(N_2)$.

* High resolution scattering measurements from fig. 14, gas phase contribution subtracted.

† Measured with the Hilger-Watts spectrometer, 200 μm slitwidth.

One can see that (a) is remarkably constant, which leads to the conclusion that the value of 0.1 for the depolarisation ratio of the (fluorescing) molecules present in the flame is correct.

However, it is not possible to determine unambiguously the shape of these molecules from the depolarisation ratio. This is caused by the lack of knowledge of their complex refractive index. Also, the concept of depolarised Rayleigh scattering is not strictly applicable in this case, as we are not dealing with an instantaneous light scattering process only. Instead, the molecules are excited into higher electronic states, which are de-excited by fluorescence and collisions. How these non-instantaneous processes alter the scattering on the Rayleigh

line cannot be predicted. Especially, it could well be possible, that some depolarised resonance fluorescence is present on the exciting wavelength, which would be indistinguishable from the Rayleigh scattering in these non-time-resolved measurements and thus result in a Rayleigh depolarisation ratio which is too high.*

Though these considerations have to be borne in mind, the major result of the high resolution Rayleigh scattering measurements - a depolarisation ratio of 0.1 for the macromolecules - is a good indication that these molecules are highly anisotropic. In order to obtain some quantitative information about the shape of the molecules, i.e., their axial ratio, let us now ignore the arguments about the validity of depolarised Rayleigh scattering.

Then we need information about their refractive index, as the depolarisation ratio is not only a function of axial ratio but also of refractive index (see, for example, Table 3(b)). However, if we make the assumption that the refractive index of the macromolecules is very large and also isotropic with respect to the molecular axes (i.e., we are only dealing with shape and not refractive index anisotropy), then the depolarisation ratio becomes a function of axial ratio only. This now allows for the comparison of the prolate or oblate spheroid approximation. Describing the macromolecule by a prolate spheroid (and using $\rho_V = 0.1$; $m = n - ik$; n, k large), we obtain an axial ratio of $\simeq 3$, whereas for an oblate spheroid we get $a/b \simeq 10$.

We can now draw some conclusions as to the nature of these macromolecules, which make sense together with the continuous structure of the fluorescence spectra. If the fluorescing species were polyacetylenes or polyacetylenic radicals, the Rayleigh depolarisation ratio of 0.1 suggests an axial ratio of $\simeq 3$. It is not very likely, that such a small polyacetylenic radical or molecule would absorb in the visible and cause fluorescence. Compared to that, if the fluorescing species were polycyclic aromatic radicals or molecules, the oblate spheroid model yields an axial ratio of $\simeq 10$, which is much nearer to what one would expect.

---

*It has to be noted here, that the species causing the fluorescence and the species responsible for the Rayleigh depolarisation might be different.

It is therefore most likely that the fluorescence originates from polycyclic aromatic radicals or molecules and that these, being highly anisotropic, also cause the observed Rayleigh depolarisation.

V-2 DETERMINATION OF THE SIZE AND NUMBER DENSITY OF SOOT PARTICLES FROM SCATTERING AND ABSORPTION MEASUREMENTS.

For the determination of the particle radius a and the number density N in the Rayleigh limit, it is required to measure the V_V particle scattering component and the particle absorption coefficient. To evaluate these measurements, it is also necessary to know the refractive index of the particles. The latter has not yet been measured for soot in situ in a flame; the theoretical work of Eiden[148] could well be useful for this purpose. Throughout this work, a value for the refractive index of m = 1.54 - 0.56i was chosen[76]. This value seems to be quite good for 'older' soot, whereas it could well be different for 'younger' soot because of its different composition (especially hydrogen content). However, as long as no in situ measurements of m are available, it is not possible to choose a better value. The value of m = 1.9 - 0.35i, recently reported by Chippet and Gray[149], will be discussed later on.

The determination of the V_V soot particle scattering component was found to be fairly straightforward and accurate, provided it was much stronger than the fluorescence and the gas phase contribution. For small heights above the burner this was not the case, as the fluorescence contribution near the exciting line was not negligible. To obtain the true particle V_V scattering component, the fluorescence contribution had to be subtracted from the measurements (see below).

More problematic is the determination of the particle absorption coefficient. Rayleigh theory predicts the particle absorption coefficient to be inversely proportional to the wavelength (see III-18). However, earlier extinction measurements of sooting flames were not in agreement with the $1/\lambda$ dependence. By introducing an experimental dispersion coefficient, $1<n<2$, the extinction coefficients were found to be proportional to $(1/\lambda)^n$. Similar experiments, measurements of the extinction coefficient versus wavelength were repeated recently[144,149] in an atmospheric pressure flame. These results from ref. 144 are shown in Fig. 17,

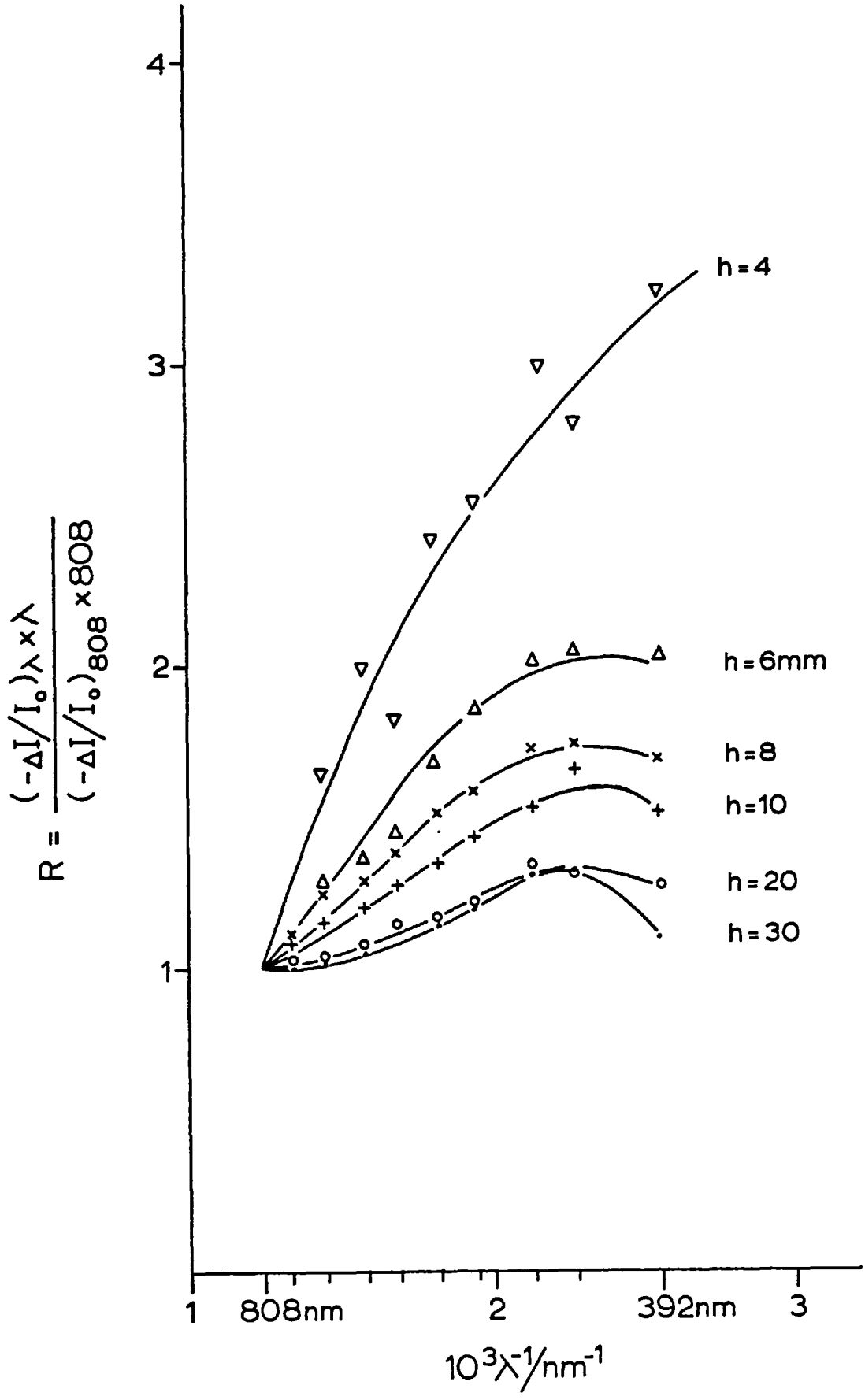

Fig. 17: Deviation of relative extinctions as function of $1/\lambda$ from R = 1, which is the result obtained by Rayleigh absorption theory. Ethylene-air flat flame; C/O = 0.760, v_o = 9.47 cm/sec, T = 1740 K. From ref. 144.

plotted as $R = (\lambda \cdot \Delta I/I_o)/(\lambda \cdot \Delta I/I_o)^*_{ref.}$ against $1/\lambda$, with the reference wavelength being 808 nm. If Rayleigh's law were valid, R would be equal to one for all wavelengths. One can see clearly from Fig. 17, that only for h > 20 mm, by extrapolation into the infrared, the curve can be anticipated to become parallel to the abscissa. This behaviour can be explained either by a significant dispersion of the refractive index with wavelength, causing Im $[(m^2 - 1)/(m^2 + 2)]$ to change, or by another light attenuation process with a completely different wavelength dependence.

The phenomenon of the fluorescence and of light absorption by molecular species, described in V-1, now allows for an explanation of the wavelength dependence of the total extinction coefficient. For the molecular absorption, involving non-instantaneous excitation with successive de-excitation by radiation and collisional quenching, one would obviously not expect a $1/\lambda$ dependence. The molecular transition would be strongly favoured by the right wavelength, at which absorption can occur. Also, one can expect that the absorption coefficient of the macromolecules in the flame is decreasing with increasing wavelength, as we are dealing with an electronic transition. This was already observed by Graham et al[93] who used the 3.39 μm He-Ne laser wavelength to distinguish between absorption by soot particles and absorption by molecular products.

In this work, a method was developed to determine the molecular absorption coefficient from the measurement of the fluorescence intensity at one wavelength far enough away from the exciting line. If we assume that the fluorescence process (i.e., the chemical nature of the fluorescing species) and the molecular absorption cross-section $C_{molecule}$ do not change very much with reaction time in the flame, then the fluorescence intensity is proportional to the number density N_{flu} of the fluorescing species. The molecular absorption coefficient $\varepsilon_{molecule}$ is also proportional to N_{flu}, therefore $I_{flu}(\lambda)$ is proportional to $\varepsilon_{molecule}$. Even if the molecular absorption cross-section would change with reaction time in the flame, the proportionality between $I_{flu}(\lambda)$ and $\varepsilon_{molecule}$ would still hold, provided the fluorescence quenching efficiency does not change. This was shown to be the case in V-1.

---

*The light attenuation was small in the experiments, so that $-\Delta I/I_o \simeq \varepsilon$.

The wavelength chosen for the fluorescence intensity measurements was λ = 550 nm. This was far enough away from the exciting laser line to make sure that no stray light from the optics of the Hilger-Watts spectrometer would perturb the measurement. In addition, all fluorescence measurements were made with horizontal polarisation axis of the analyser and vertical incidence polarisation. This ensured elimination of most of the light scattered from soot particles, except the weaker H_V depolarised (Rayleigh) component, before entering the spectrometer. Thus the fluorescence measurements were completely unperturbed from parasite stray light in the monochromator (grating ghosts), even with extremely high particle scattering. The fluorescence intensity was always measured relative to I_{VV} of nitrogen, but the spectrometer-photomultiplier correction according to Fig. 6 was <u>not</u> applied. The measurements were then multiplied by $\exp(\ell\varepsilon_{total})$, ℓ = 3 cm, ε_{total} at 488 nm, to take into account the attenuation of the laser power and fluorescence intensity through the flame.

To carry out the determination of the molecular absorption coefficients (for different wavelengths) from the fluorescence measurements, it was required to establish an empirical relation between them. The very rich flame conditions (C/O > 1.4), described already, were ideally suited for this as, except for a thin flame region, virtually no soot particles were present. By carefully selecting the flame regions, where the absorption and fluorescence measurements were taken, and monitoring the V_V scattering components at 488 nm, it was made sure that the measured absorption coefficients were equal to the molecular absorption coefficients and not perturbed by soot particle absorption. For the employed burner distance of d = 13 mm and C/O > 1.4 this was the case for h < 7 mm and h > 9.5 mm (see Figs. 20-21). Measurements in that region just $\approx$ 1 mm above the very faint flame luminosity, were specially useful. Strong fluorescence was present in that region, caused by diffusion of the molecular species into the counterflow of nitrogen from the top part of the burner. The diffusion flux of any soot particles was negligible.

The absorption coefficients were measured for eight wavelengths from 460.5 to 966 nm with the Cs hollow cathode lamp and the laser as light sources. Vertical spatial resolution for the lamp system was estimated to be about 1 mm; absorption measurements could be carried out for heights above the burner of $\gtrsim$ 2.5 mm. The lamp intensities I_o (without absorption) were measured for every wavelength, by letting the light pass through a lean flame. This allowed for the elimination of any Schlieren effects. The I_o, determined before and after each absorption experiment, was in good agreement.

In Fig. 18, the relative fluorescence intensities [as $H_V(550\ nm) = I_{HV}(550\ nm)/I_{VV}(N_2)$] are plotted against the molecular absorption coefficients, calculated from formula III-17. All measured points (not shown in the diagram) are very well positioned on the linear plot, corresponding to each wavelength.

On can see that even for very strong fluorescence ($H_V(550\ nm) > 10$), the molecular absorption coefficient is extremely small in the infrared, whereas ε strongly increases towards the shorter wavelengths. It is not surprising that there is some absorption by the molecular species in the infrared, as the fluorescence spectra were also found to extend into the near infrared. However, the very small absorption at 966 nm might also be caused by minute amounts of soot particles; this would not cause a considerable error.

We are interested in obtaining the soot particle absorption coefficient $\varepsilon_{abs.\ part.}$ under conditions where molecular, light absorbing species and soot particles are present simultaneously. $\varepsilon_{abs.\ part.}$ is given by

$$\varepsilon_{abs.\ part.}(\lambda) = \varepsilon_{total}(\lambda) - \varepsilon_{molecule}(\lambda) \qquad V\text{-}4$$

and $\varepsilon_{molecule}$ can be evaluated from the measured $H_V(550\ nm)$ and Fig. 18.

In order to simplify the numerical evaluation of $\varepsilon_{molecule}$ from $H_V(550\ nm)$ further, the logarithms of the reciprocal slopes of the straight lines in Fig. 18 were plotted against wavelength. This plot* gave a good straight line and therefore allowed for the expression of $\varepsilon_{molecule}$ as

*Fig. 19

$$\varepsilon_{molecule} = f(\lambda) \cdot H_V(550\ nm) \qquad V\text{-}5$$

with $\ell g\ f(\lambda) = -3.5 + 3.02 \times 10^{-3}\ (1000 - \lambda/nm)$

We now have

$$\varepsilon_{abs.\ part.} = \varepsilon_{total} - f(\lambda) \cdot H_V(550\ nm) \qquad V\text{-}6$$

Absorption measurements over the whole wavelength range were carried out for two flames. The flame conditions were C/O = 1.40, N_2/O_2 = 1.57 and C/O = 0.936, N_2/O_2 = 1.55.* The burner separation was set at 13 mm and the nitrogen flow velocity from the top was 3.5 cm/sec for both cases, achieving very good flame stability.

All the relevant light scattering measurements were carried out with the monochromator system at -90^0, the L.L.S. detector at -45^0 scattering angle and vertical laser polarisation. These angles were chosen for convenience. Some full angular measurements of V_V and H_H were carried out with the L.L.S. detector, to make sure that, under conditions of soot particle formation, these were still small enough to behave as Rayleigh scatterers.

The measured scattering components† were denoted in the following way:

V_V L.L.S. 45^0	Vertical setting of the polarisation axis of the analyser in the L.L.S. detector.

---

*The determination of the flame temperatures, mole numbers and flow velocities is outlined in Appendix I.

†The dimensionless scattering components must not be confused with the Rayleigh ratios, used only in Chapter III. The Rayleigh ratios (in cm^{-1}) are obtained by multiplying the scattering components with $N(N_2)\sigma_{VV}(N_2) = 2.2 \cdot 10^{-8}\ cm^{-1}$.

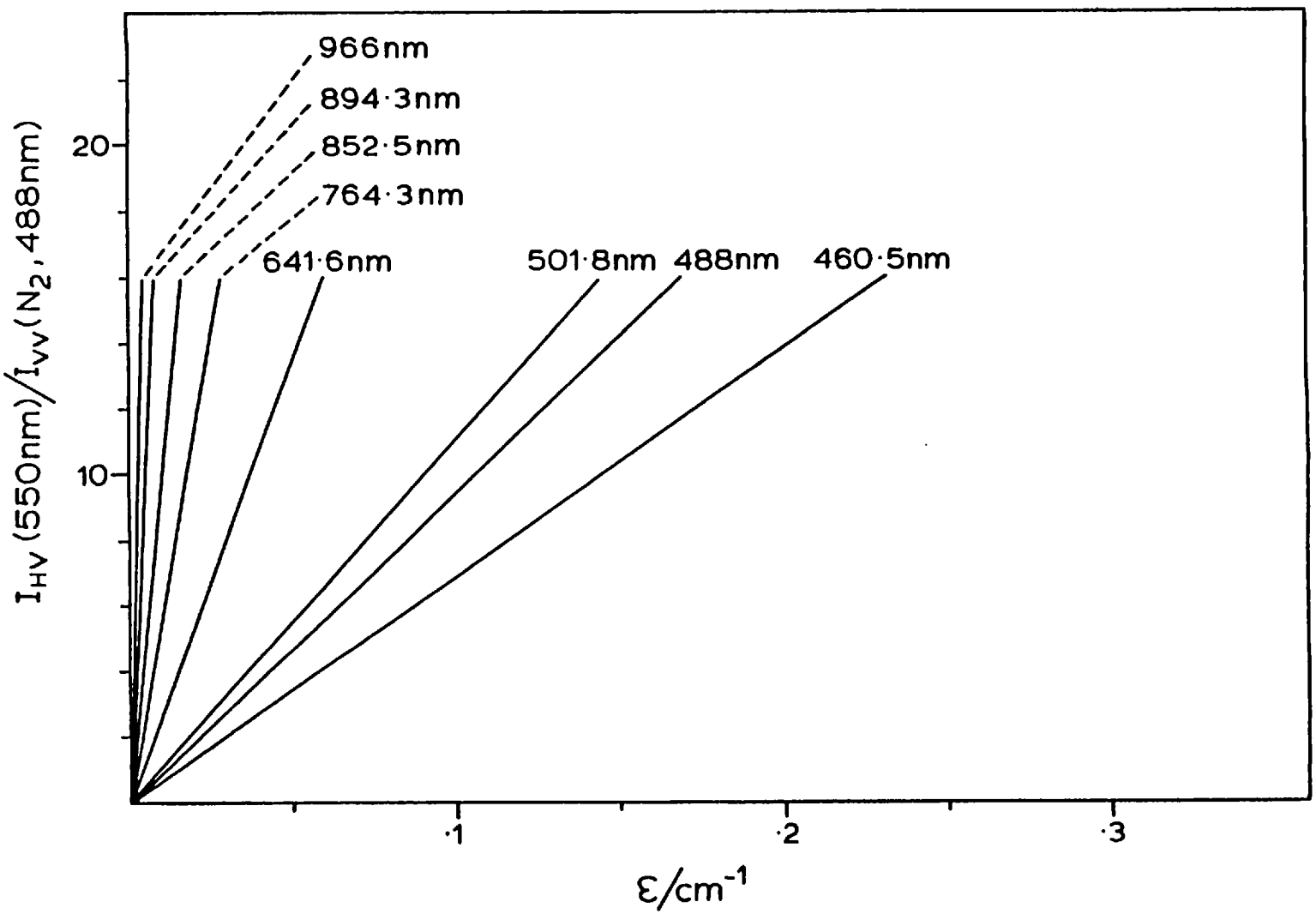

Fig. 18: Fluorescence intensity at 550 nm relative to $I_{VV}(N_2)$ (not corrected for spectrometer-photomultiplier transmission according to Fig. 6) versus extinction coefficients at different wavelengths.

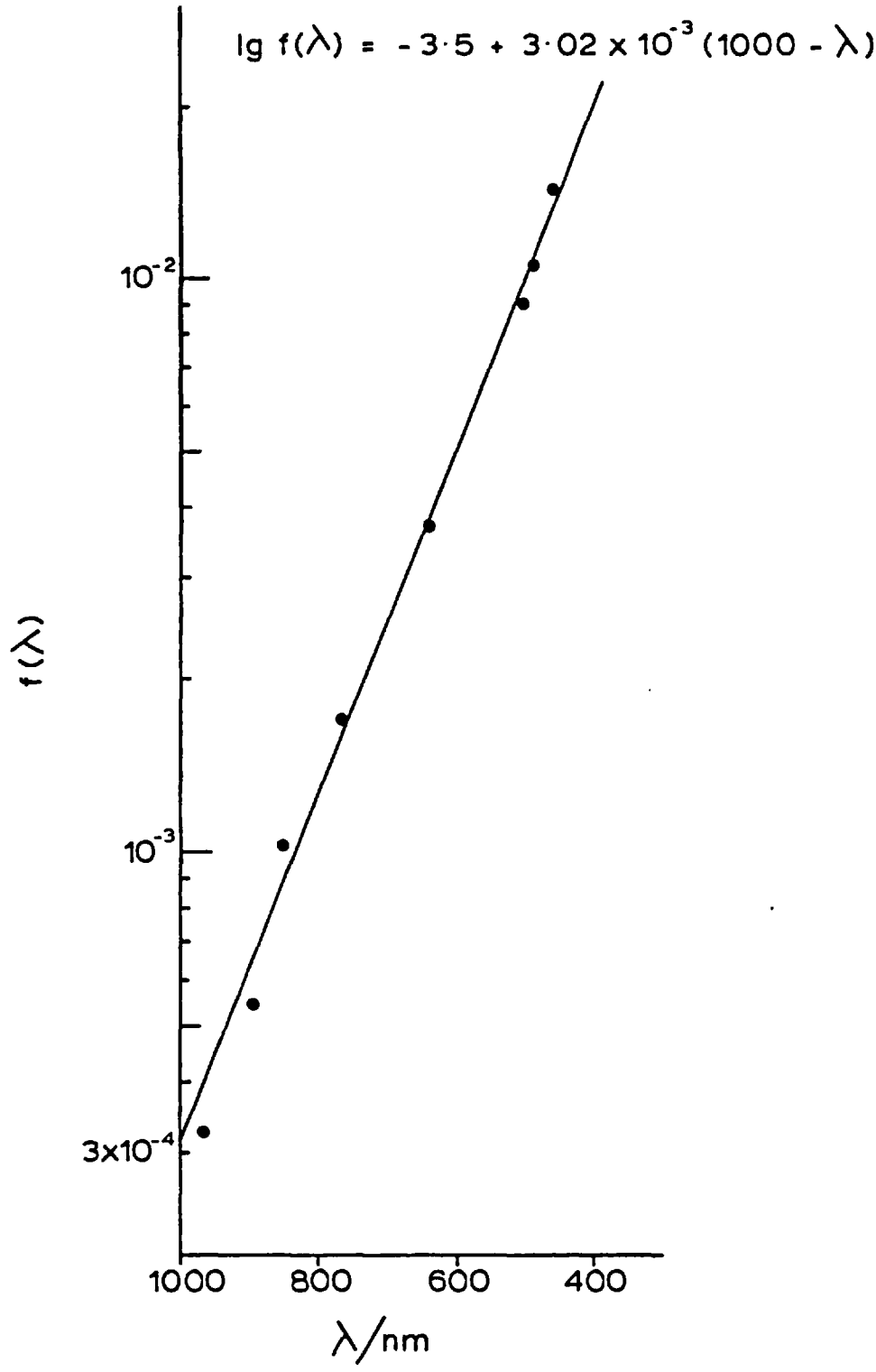

Fig. 19: Logarithmic plot of the inverse slopes of the straight lines in Fig. 18, versus wavelength.

H_V L.L.S. 45^0	Horizontal setting of the polarisation axis of the analyser in the L.L.S. detector.
V_V Monochromator 90^0	Vertical polarisation axis of the analyser; monochromator set at 488 nm.
H_V Monochromator 90^0	Horizontal polarisation axis of analyser; monochromator set at 488 nm.
H_V (550 nm)	Horizontal polarisation axis of analyser; monochromator set at 550 nm.

The extinction coefficients were measured as function of h - height above burner. Fig. 20 shows the results for ε_{total}, obtained from the flame of C/O = 1.40, plotted against h. The total extinction coefficients rise steadily with h, for all wavelengths and become nearly constant around h = 8 mm. This is caused by the flow structure of the flame, which is only unidimensional up to h = 7 mm. As under these specially chosen flame conditions (small burner distance) the reaction time is well below 20 msec (see as comparison Fig. 35), soot particle formation is effectively halted at an intermediate stage. This can clearly be seen from the dependence of ε_{total} at 966 and 894.3 nm. Only around h = 8 mm, the infrared absorption can no longer completely be attributed to the molecular species, but indicates the presence of a small volume fraction of soot particles. This interpretation is supported by the dependence of the scattering components, plotted against h in Fig. 22. Only between h = 7.5 and 9.5 mm is the presence of some soot particles indicated by the V_V scattering.

Fig. 21(a) shows the total extinction coefficients for different h, plotted against reciprocal wavelength. The dependence of ε_{total} on h is non linear, with ε_{total} increasing strongly with short wavelength. The measurements from ref. 144 suggest a decrease of ε_{total} in the ultraviolet; in this work, no absorption measurements in the UV could be carried out because standard glass optics were employed.

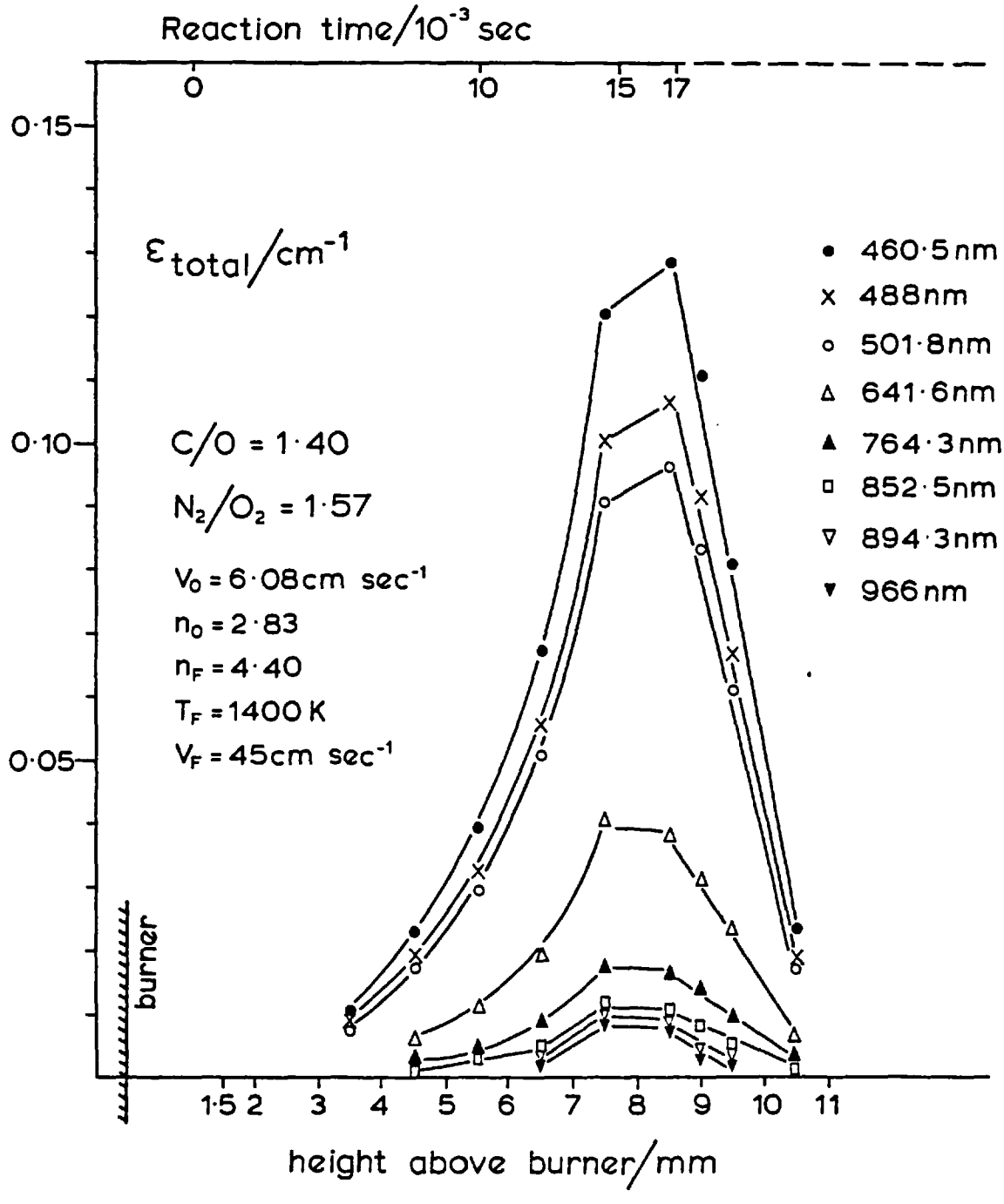

Fig. 20: Total extinction coefficients for different wavelengths as function of h.

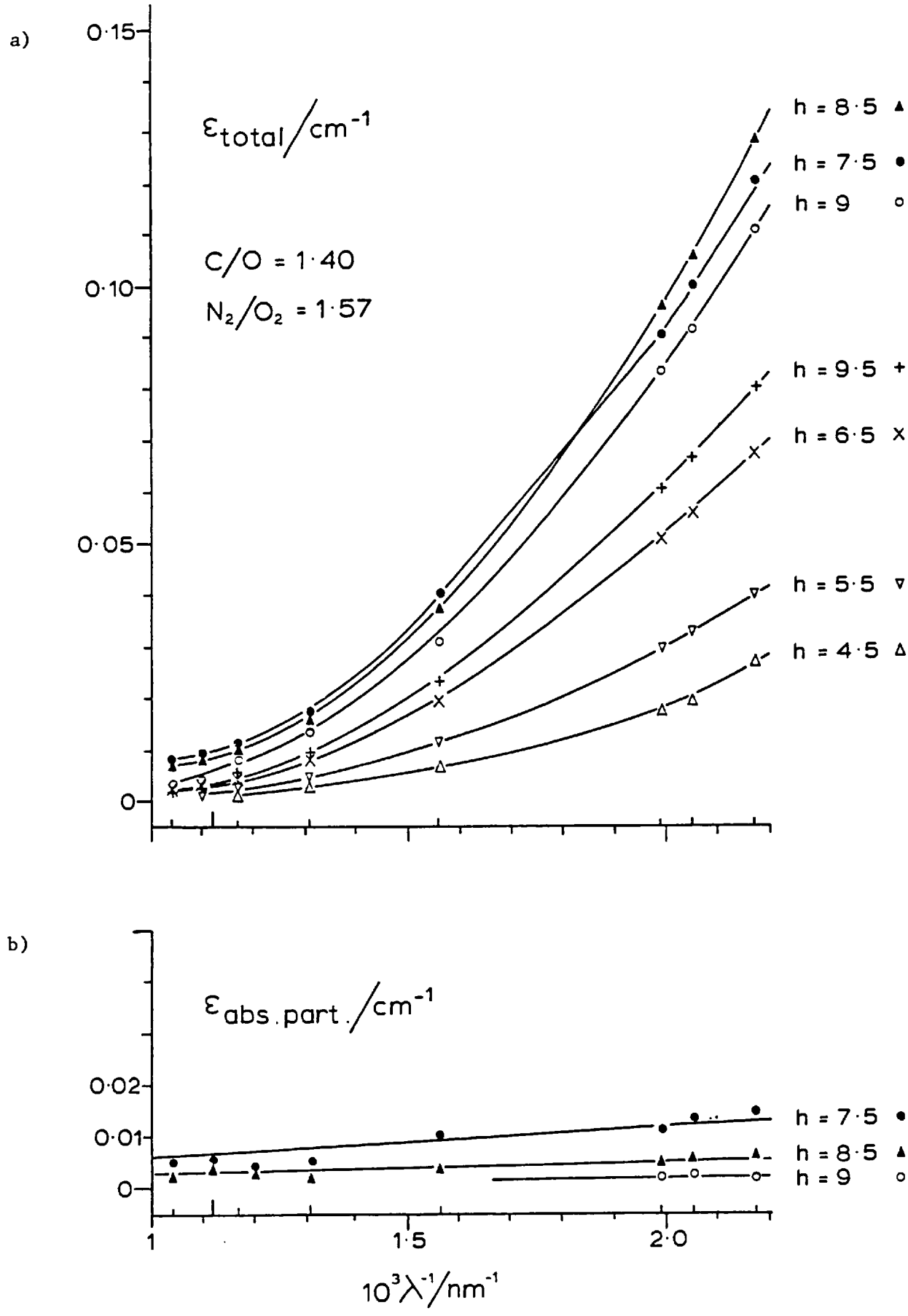

Fig. 21: a) Total extinction coefficients for different heights above burner in mm, as function of the inverse wavelength;

b) Particle absorption coefficients, obtained by subtracting the molecule absorption from the total extinction coefficients for some h/mm as function of the inverse wavelength.

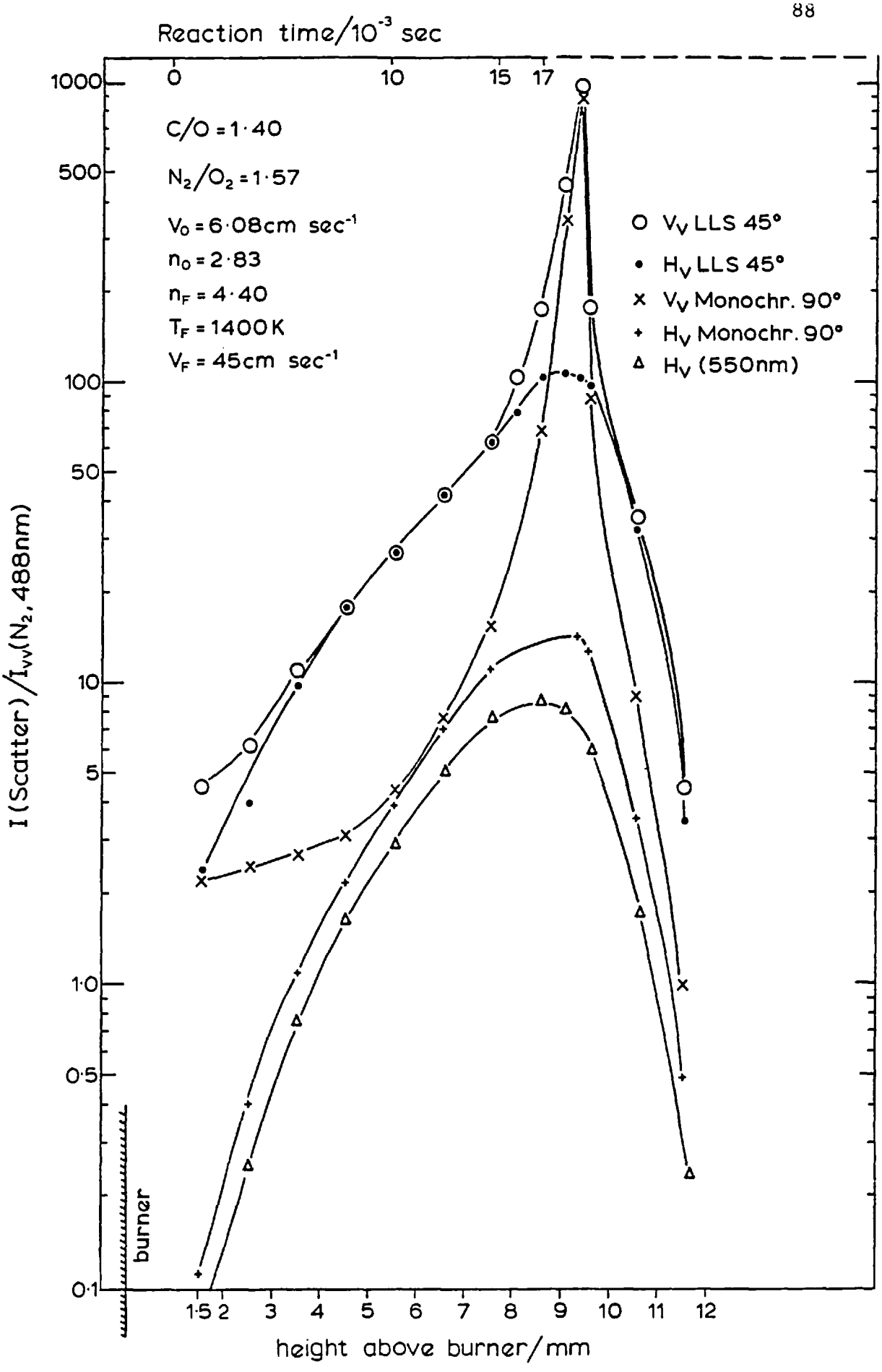

Fig. 22: Scattering data corresponding to Figs. 20 and 21.

Using formula V-6, the soot particle absorption coefficients were obtained for h = 7.5, 8.5 and 9 mm, using the H_V (550 nm) data from Fig. 22. These results are plotted against $1/\lambda$ in Fig. 21(b), showing a linear dependence on $1/\lambda$. However, because the soot volume feaction is so small and the fluorescence intensity and thus the molecular absorption coefficients is so high, the uncertainty of the data is considerable.

The scattering data (Fig. 22) exhibit some interesting features. Between h = 4.5 and 7.5 mm, the H_V (LLS) and V_V (LLS) are completely indistinguishable, as the amount of fluorescence passing through the interference filter is much bigger than the V_V Rayleigh component, which, therefore, is undetectable. Nearly the same applies for H_V (Monochr.) and V_V (Monochr.) which are also nearly equal in that region. Below h = 4.5 the V_V and H_V components can be distinguished as the fluorescence intensity is lower. There is some considerable V_V scattering present in this region, obtained as V_V (measured) - H_V (measured) (see Fig. 28*), which is bigger than the expected scattering contribution from water-gas combustion products only. However, in this very rich flame, the rate of combustion heat release cannot be treated as being instantaneous. Therefore the temperature increases gradually, causing the gas density and correspondingly the V_V scattering to decrease. The decrease of the corrected V_V scattering (with the fluorescence contribution subtracted) between h = 1.5 and h = 6 mm can be explained by the scattering from unburned fuel and this gradual temperature increase. In this flame region, it cannot be decided as to how far the reactions of the fuel towards higher molecular species are progressing. Towards the top of the flame, the V_V (Monochr.) becomes nearly the same as the V_V (LLS) as the particle scattering contribution in the collected light becomes more dominant

---

*This determination is much more erroneous than the results from the high resolution measurements, where the fluorescence contribution near the Rayleigh line was marginal (see Fig. 14).

compared to the fluorescence. Below h = 7.5, the V_V (LLS), H_V (LLS) and H_V (Monochr.) are dominated by the fluorescence and therefore directly proportional to the H_V (550 nm). Above h = 9.5, we see the effect of the counterflow of nitrogen from the top part of the burner, causing a rapid decrease of the particle scattering and a slower decrease of the fluorescence data.

All the data for the flame of C/O = 0.936, N_2/O_2 = 1.55 are displayed in Figs. 23 to 28. In Fig. 23, the total extinction coefficients are plotted against h for each wavelength. The ε_{total} rise linearly up to h = 4.5 and then again remain nearly constant (for the longer wavelengths) or rise more slowly (for the shorter wavelengths). As this flame is heavily sooting, there is strong absorption in the infrared. With the H_V (550 nm) data from Fig. 27, now the soot particle absorption coefficients can be obtained by the method outlined before (see formula V-6). The $\varepsilon_{abs.\ part.}$ data are shown in Fig. 24 as function of h. Again we see the nearly linear rise of $\varepsilon_{abs.\ part.}$ up to h = 4.5 mm, whereas the values are nearly constant between h = 4.5 and 6.5 mm. For this flame, the plots of ε_{total} and $\varepsilon_{abs.\ part.}$ against $1/\lambda$ (Figs. 25, 26) reveal a most interesting result. In Fig. 25, the total extinction coefficient is non linearly dependent on the reciprocal wavelength, though compared to Fig. 21(a) this non-linearity is somewhat less. However, the particle absorption coefficients against reciprocal wavelength show excellent linear behaviour for all values of h. Even more, extrapolating all the straight lines in Fig. 26 towards infinite wavelength ($1/\lambda \to 0$), they all cut the abscissa in the point $\varepsilon = 0$, $1/\lambda = 0$. This is exactly the prediction of Rayleigh absorption theory, that the particle absorption coefficient is proportional to $1/\lambda$. Of course, for a comparison with real absorption measurements in the further infrared, one would no longer expect the slope of $\varepsilon_{abs.\ part.}$ versus $1/\lambda$ to be linear. This, however, is caused by an increase of both parts of the complex refractive index[76] and not an invalidation of Rayleigh's law.

The main relevance of the results shown in Figs. 25 and 26 is that the wavelength dependence of the measured total extinction coefficients can be explained by the two processes of absorption from molecular species with non linear $1/\lambda$ dependence and from soot particles, behaving exactly like Rayleigh absorbers. Also, it is quite apparent, that the

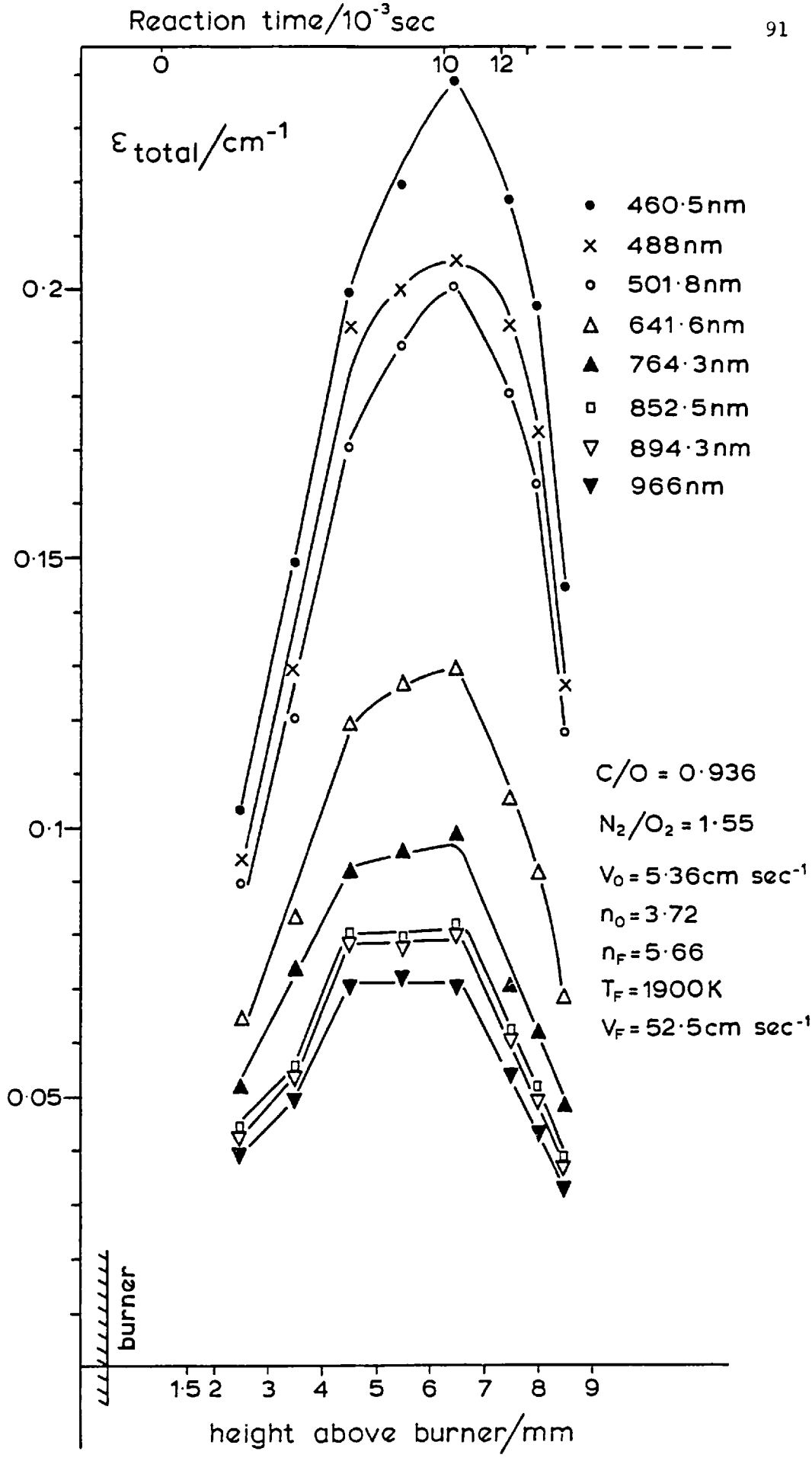

Fig. 23: Total extinction coefficients for different wavelengths as function of h.

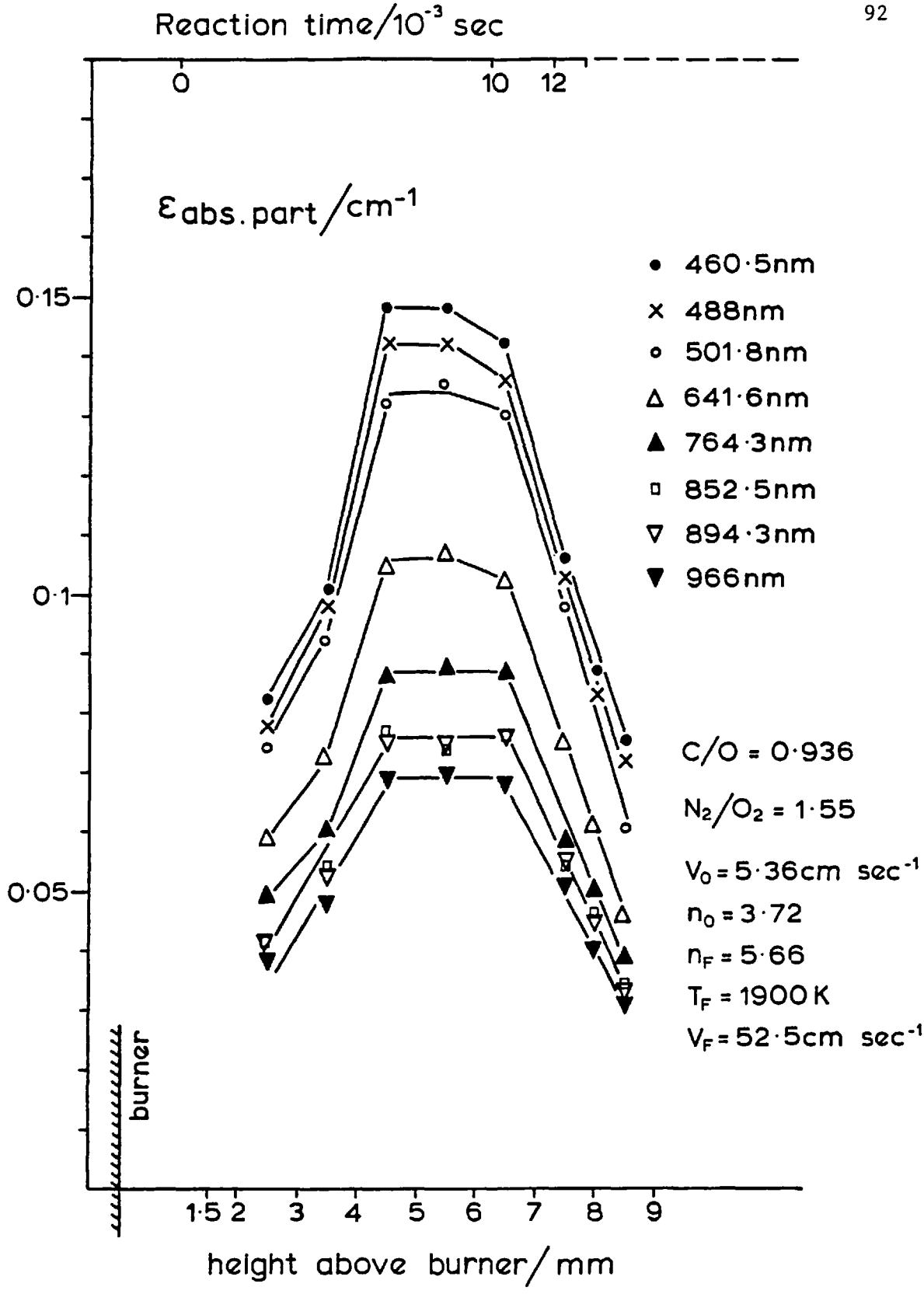

Fig. 24: Particle absorption coefficients, obtained by subtracting the molecule absorption from the total extinction coefficients for different wavelengths as function of h.

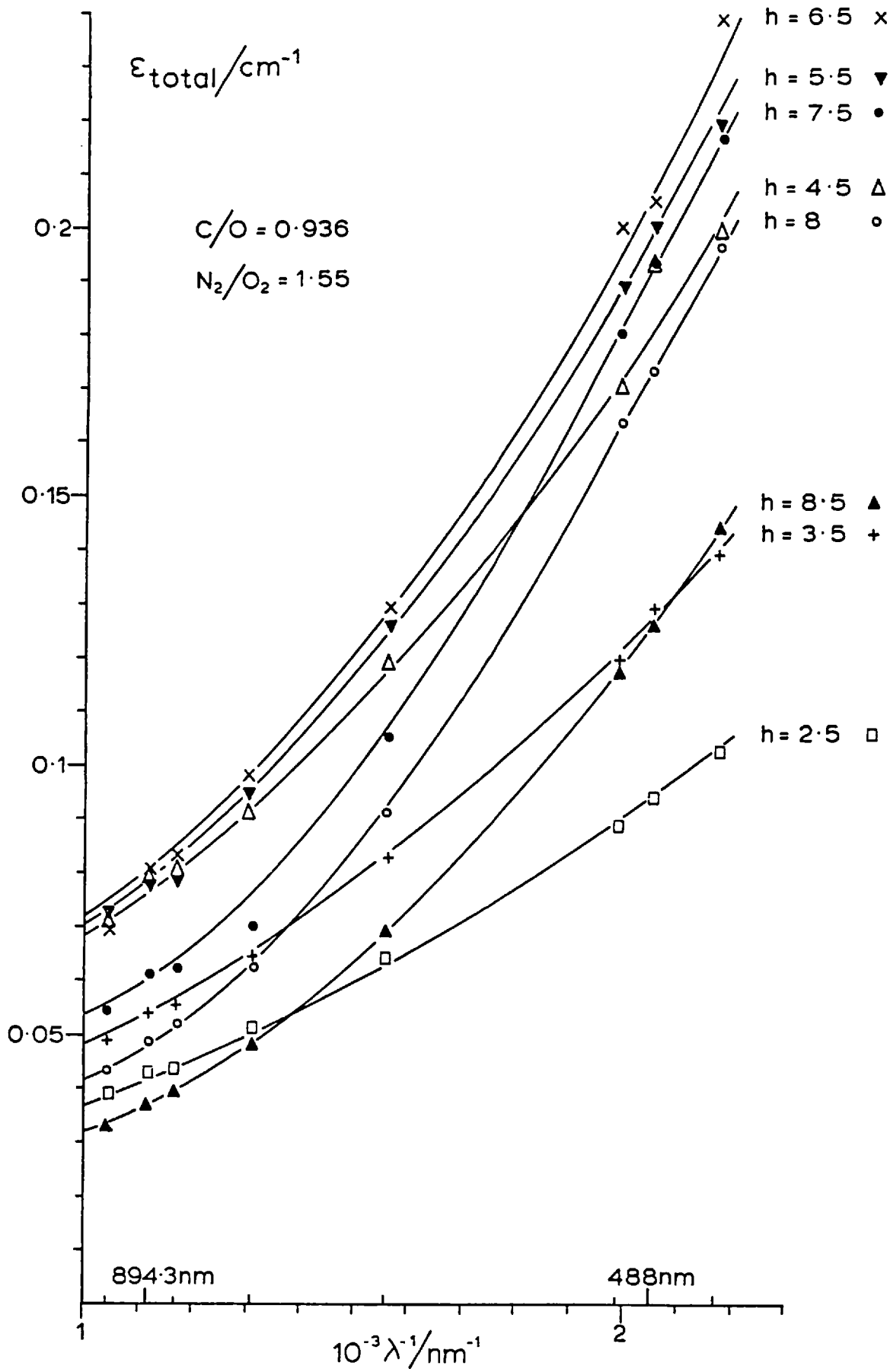

Fig. 25: Total extinction coefficients for different h/mm as function of inverse wavelength.

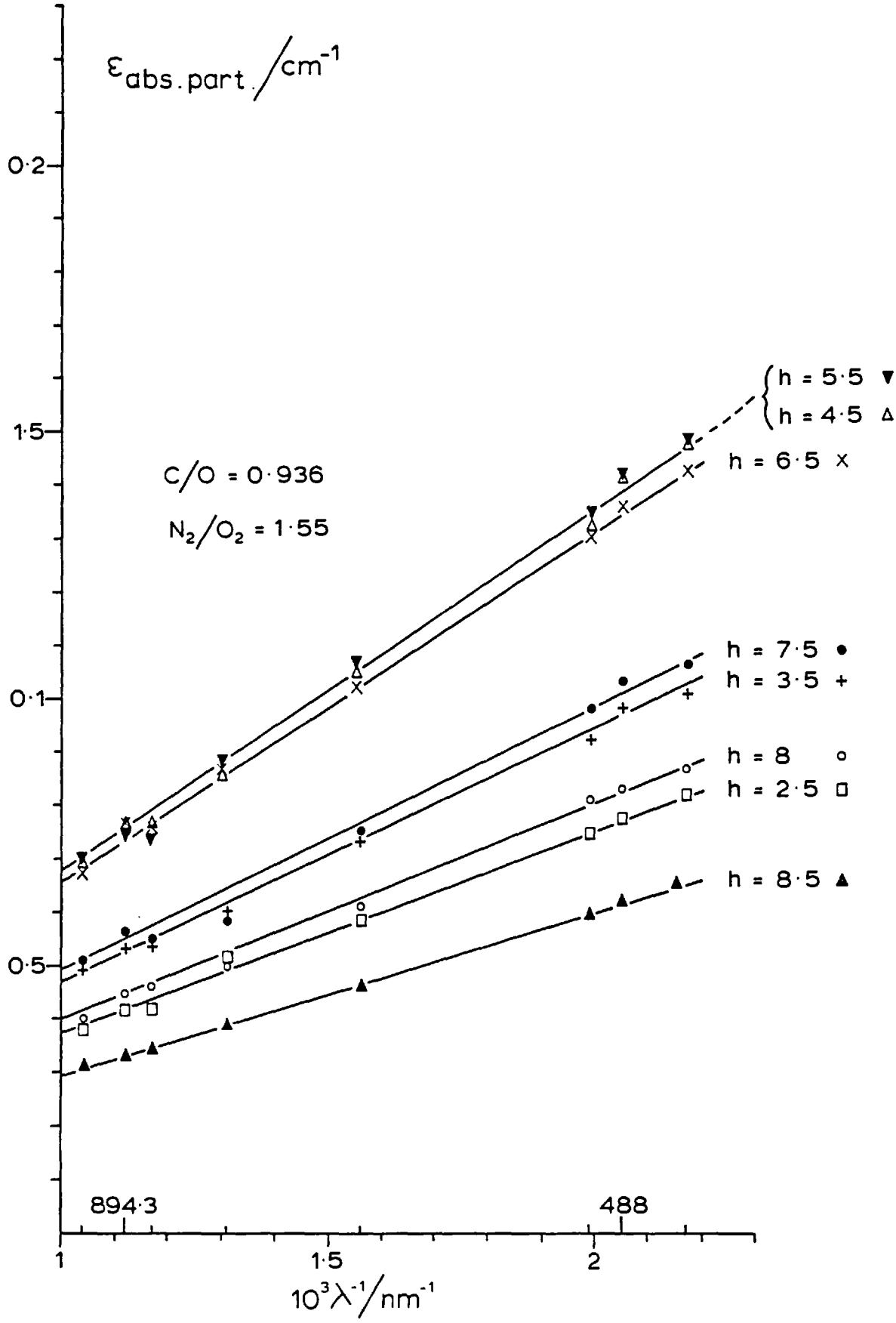

Fig. 26: Particle absorption coefficients for different h/mm as function of inverse wavelength.

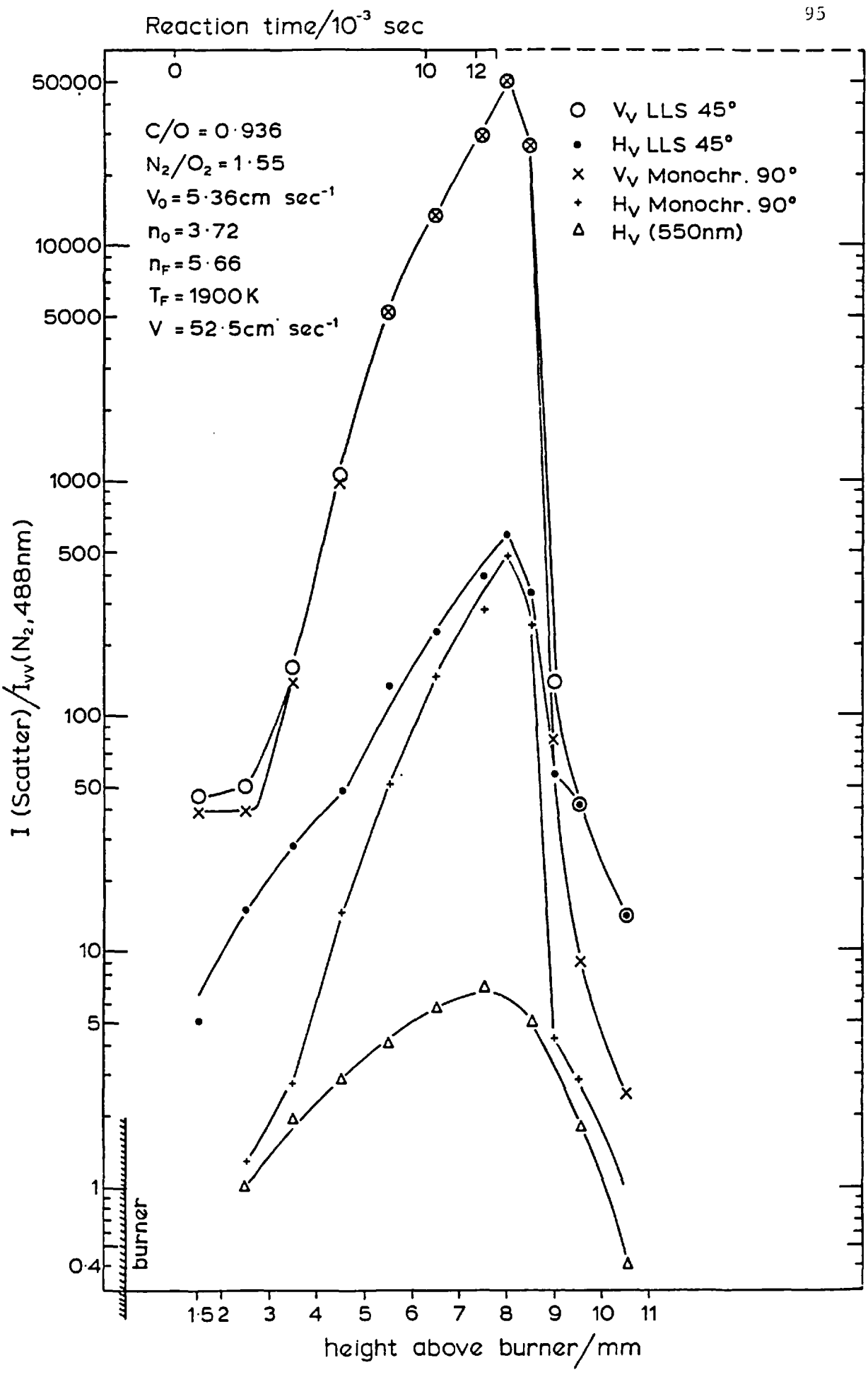

Fig. 27: Scattering data corresponding to Figs. 23-26.

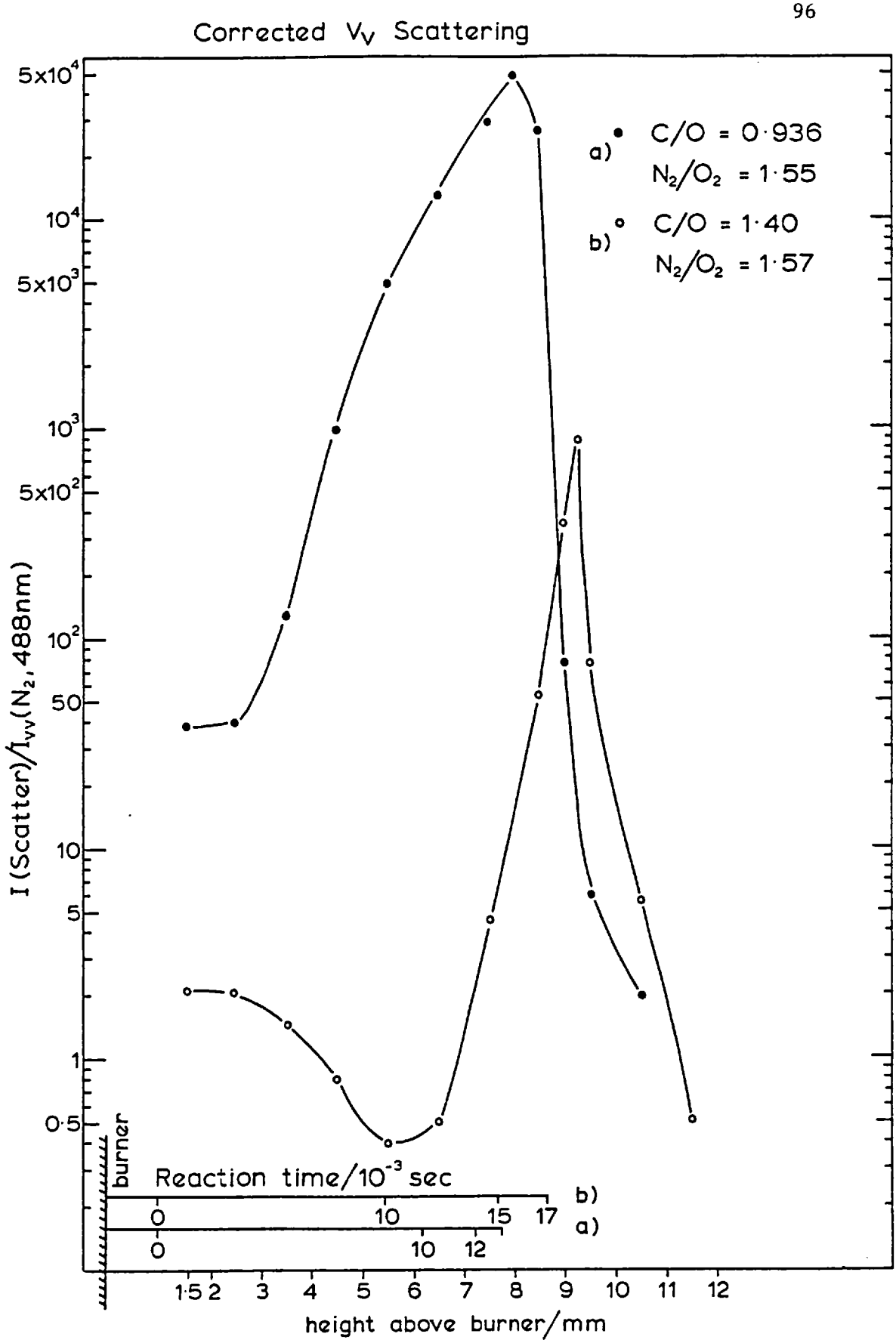

Fig. 28: V_V scattering components, corrected by subtracting the fluorescence contributions at λ = 488 nm. From Figs. 22 and 27.

refractive index, or more accurately, the imagin. part of $[(m^2-1)/(m^2+2)]$ is quite well constant over the whole wavelength range. Towards the infrared, a slight increase in $Im[(m^2-1)/(m^2+2)]$ might be the case, but this cannot be decided unambiguously. These results also give an explanation for the absorption measurements of Chippett and Gray[149] and their reported refractive index of 1.9 - 0.35i, which gives the value of 0.13 for $Im[(m^2-1)/(m^2+2)]$ compared to 0.27 obtained from m = 1.54 - 0.56i. As they determined the particle size by electronmicrography, they could only explain their ε_{total} measurements by deducing the above value for m. Also, the results reported here, prove that the $\varepsilon_{abs.\ part.}$ data can consistently be explained by the assumption of uniform size of the soot particles and it is not necessary to assume a size distribution for the soot particles[149].

The scattering data for this flame are quite different from Fig. 22. For C/O = 0.936, the H_V (550 nm) is stronger than for C/O = 1.40, up to h = 7 mm (at h = 2.5 mm, by a factor of four) and less above h = 7 mm. This can be explained by the more rapid reactions in the leaner flame. The H_V (LLS) is again directly proportional to H_V (550 nm) up to h = 4.5 mm, being dominated by the fluorescence, whereas the H_V (Monochr.) begins to rise consistently from h = 3.5 mm. If H_V (Monochr.) were dominated by the fluorescence, it would also be proportional to H_V (550 nm) as in Fig. 22. However, as we have seen from the high resolution experiments, the soot particles themselves cause some depolarisation on the Rayleigh line ($\rho_V = 5 \times 10^{-3}$). This depolarised Rayleigh component from the soot particles becomes more and more important with h increasing. The V_V (LLS) and V_V (Monochr.) converge to the same values for h = 4 mm onwards. Soot depolarisation ratios can be obtained in the following way from the H_V (Monochr.) and V_V (Monochr.) measurements. The fluorescence contribution is estimated by extrapolating the H_V (Monochr.) curve parallel to the H_V (550 nm) curve. These values then have to be subtracted from the measured H_V (Monochr.) and divided by V_V. The soot depolarisation ratios evaluated from Fig. 27 between h = 4 and 8 mm do not vary very much and are all around $\rho_V = 9 \times 10^{-3}$. Doing the same extrapolation for the H_V (LLS) curve beyond h = 4.5, and again calculating the depolarisation ratios, reasonable agreement with $\rho_V = 9 \times 10^{-3}$ is obtained. However, one has to bear in mind, that this determination of ρ_V involves three scattering measurements with their respective errors, the errors in burner position and the extrapolation of

the fluorescence contribution contained in H_V (Monochr.).

However, taking the calculated values from Table 3(a), and taking ρ_V to be between 5 x 10^{-3} and 10^{-2} we get an axial ratio between 1.6 and 2.0 for the prolate spheroid approximation. This seems to be an axial ratio large enough to be detected by electronmicrographic size analysis. However, primary soot particles have been found to be nearly spherical[65] and should therefore cause negligible Rayleigh depolarisation. This leaves the conclusion that the depolarisation of the light scattered from the soot particles is not caused by shape anisotropy but by anisotropy of refractive index. This is not unreasonable, as the 'building blocks' of soot are supposedly incorporated into some ordered structure, which can easily be different for the particle axes.

The V_V scattering components (with the fluorescence contribution subtracted - see Fig. 28) and the measured particle absorption coefficients can now be used to obtain the soot particle (volume) radius a and the number density N. As can be seen from Table 3, the Cabannes factor correction, giving the increase of the V_V scattering from an anisotropic particle compared to a spherical isotropic particle, is small for the refractive index used (m = 1.54 - 0.56i) and was therefore neglected. Combining formulae III 1, 2 and 18 we get

$$Na^3 = -\frac{\varepsilon_{abs.part.} \cdot \lambda_{abs.}}{8\pi^2 \, Im\{m^2-1)/(m^2+2)\}} \qquad V\text{-}7$$

and

$$Na^6 = \frac{I_{VV}(soot)}{I(N_2)} \; N_{room} \cdot \sigma_{VV}(N_2) \cdot \left|\frac{m^2-1}{m^2+2}\right|^{-2} \; \frac{\lambda^4}{16\pi^4}$$

and with $|m^2-1)/(m^2+2)|^2 = 0.21$, and $Im[(m^2-1)/(m^2+2)] = -0.27$, $N_{room} = 2.5 \cdot 10^{19}$ cm^{-3} and $\sigma_{VV}(N_2) = 8.78 \cdot 10^{-28}$ cm^2

$$Na^3 = 4.2 \cdot 10^{15} \, \varepsilon_{part.\ abs.} \text{ for } \lambda_{abs.} = 894.3 \text{ nm}$$

$$Na^3 = 2.29 \cdot 10^{15} \, \varepsilon_{part.\ abs.} \text{ for } \lambda_{abs.} = 488 \text{ nm} \qquad V\text{-}8$$

$$Na^6 = 3.8 \cdot 10^{14} \, [I_{VV}(soot)/I_{VV}(N_2)]$$

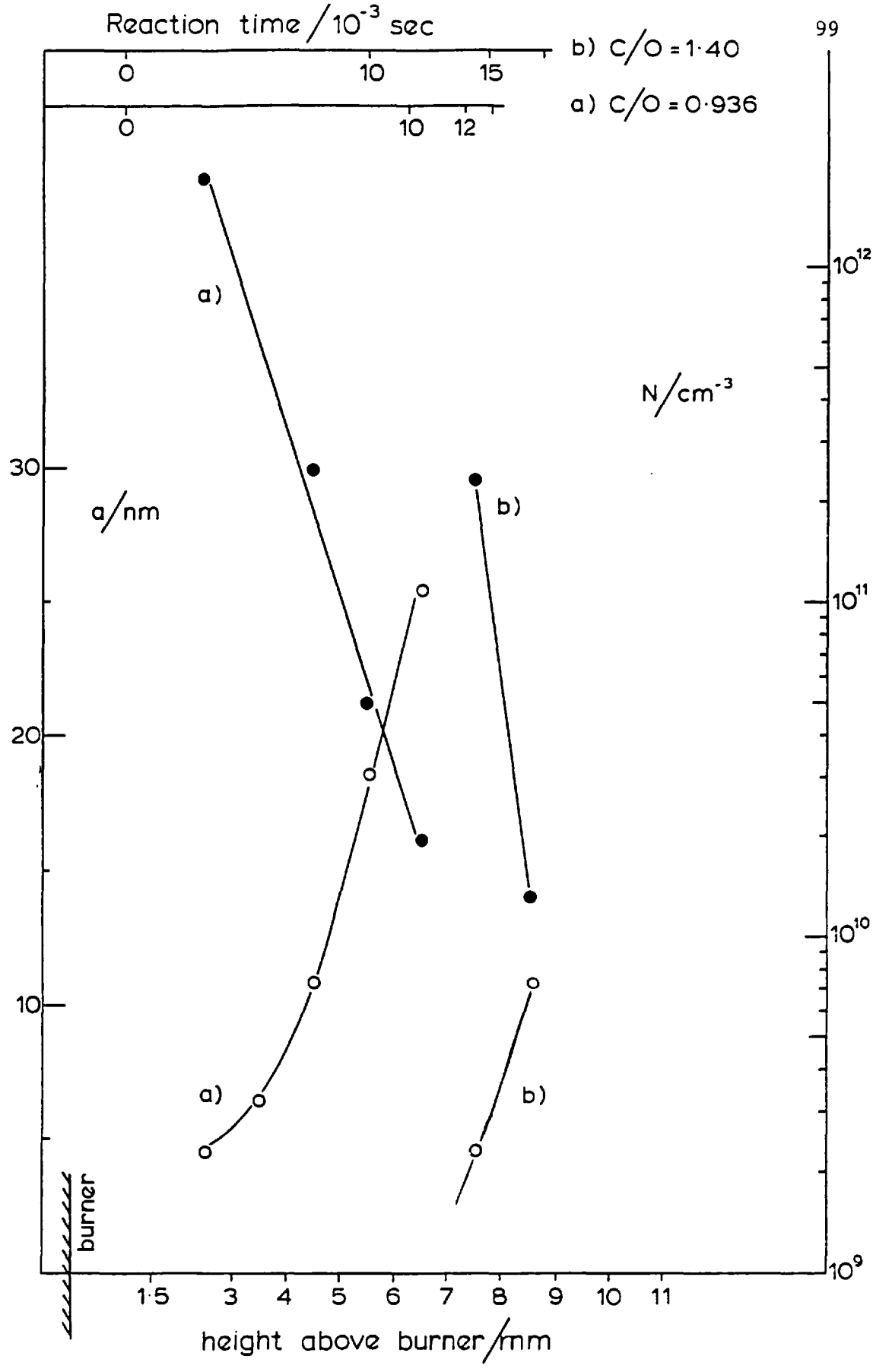

Fig. 29: Particle number density N● and particle radius a o as function of h. Corresponding to Figs. 20-28.

The dimensions of the above quantities are: N/cm^{-3}, a/nm and $\varepsilon_{abs.\ part.}/cm^{-1}$. Values for N and a can easily be calculated from the above formulae.

For both flames the results obtained for soot particle radius and number density are plotted aginst h in Fig. 29. For C/O = 1.40 only at h = 7.5 and 8.5 mm soot particles of a < 12 nm are present, with the number density falling from about $2 \cdot 10^{11}$ to 10^{10} cm^{-3}. For the flame at C/O = 0.936, soot particles are present much earlier, the particle radius rising from 4.5 nm at h = 2.5 mm to 26 nm at h = 6.5 mm. The number density correspondingly falls from $2 \cdot 10^{12}$ to $2 \cdot 10^{10}$ cm^{-3}. The rapid decrease in N and the associated rise in particle radius can be explained by coalescence of the soot particles. This will be discussed in Chapter VI, in the context of 'free molecule' coagulation theory for an aerosol of changing volume fraction $\phi = N \cdot V_{part.}$.

V-2-1 COMPARISON BETWEEN FLAMES CONTAINING PEROXIDES AND FLAMES WITHOUT PEROXIDES

In order to increase the length of the unidimensional region of the flame and to achieve longer reaction times, attempts were made to increase the separation between both parts of the burner, when burning rich premixed flames from the bottom. It was found that specially for the very rich flames, flame stability suffered severely, if the separation distance was considerably more than 20 mm. By setting the separation to 20 mm and optimising the nitrogen flow from the top, the flames still had good stability. The flow structure was unidimensional for reaction times of up to 20 - 25 msec.

From the extinction measurements already described, it was concluded that it would not be necessary to measure the extinction coefficients at all wavelengths and two wavelengths would be sufficient. The laser extinction at 488 nm had to be measured in any case, to normalise the scattering data. ε_{total} at 488 nm also offered the high spatial resolution of the focused laser beam. The Cs lamp was used to obtain the extinction coefficient at 894.3 nm. This line was much stronger and had better stability than the line at 966 nm and was far enough in the infrared, so that the total extinction coefficient would be dominated by soot particles, if these were present. The necessary subtraction of $\varepsilon_{molecule}$ from ε_{total}(894.3 nm)

to obtain $\varepsilon_{part.\ abs.}$(894.3 nm) therefore resulted in smaller errors for the particle absorption coefficient at 894.3 nm than at 488 nm. For the soot particle radius and number density determination the $\varepsilon_{part.abs.}$ values at 894.3 nm were taken and the measurements at 488 nm were used to check the results.

To study the effect of t-butyl-hydroperoxide (TBHP) and di-t-butylperoxide (DTBP) on soot particle size and number density, light scattering and absorption data were collected from ethylene flames containing either of the peroxides or none of them. In order to compare flames of the same C/O ratio, the 'fuel value' of the peroxides had to be taken into account. Therefore, with peroxide addition, the flow of ethylene had to be reduced correspondingly. The mass flow of peroxide*, contained in the nitrogen stream, was determined by the time it took to vaporise a small volume (typ. 2 ml) from the saturator. For a nitrogen flow of 20 mg/sec the vaporisation times were typically 12 min for 2 ml DTBP and 50 min for 2 ml TBHP. Two flames were investigated with and without TBHP present. These were burning with a C/O ratio of 1.00 (N_2/O_2 = 1.59), near the maximum C/O ratio for soot particle formation, and a C/O ratio of 1.51 (N_2/O_2 = 1.75) with far fewer soot particles being present.

The results for the flames of C/O = 1.00 are plotted in Figs. 30 - 33. The measured total extinction coefficients and the particle absorption coefficients obtained from formula V-6, using the corresponding H_V (550 nm) data are plotted against h in Figs. 30 and 32. Fig. 30 shows the values for ε_{total} and $\varepsilon_{part.\ abs.}$ at 894.3 and 488 nm for the flame containing only ethylene as fuel. The onset of the infrared absorption, indicating the presence of soot particles, is at h = 4.5 mm. There is already considerable extinction at 488 nm below h = 4.5 mm, which is caused by absorption from the molecular species and can fully be accounted for using formula V-5. All the ε values rise virtually linear with h and start to level off near $\simeq$ 20 msec reaction time†. Similar results were reported by Haynes et al[95] from their measurements of the total extinction coefficients in ethylene-oxygen-nitrogen flames, indicating that for t > 20 msec ε becomes constant.

---

*DTBP and TBHP were supplied by Interox Chemicals Ltd. The DTBP was of 95% purity and the TBHP contained 72% TBHP, the remainder being mainly DTBP.

†This is not caused by the flame flow structure, but a genuine effect, as the flames were unidimensional up to h = 15 mm.

One can clearly see from Fig. 30 that if one does not account for the contribution of the molecular absorption to the total extinction and would use ε_{total} in the visible for the size and number density determination of the soot particles (see formula V-7), a severe error arises. This error becomes less severe for longer reaction times, where $\varepsilon_{abs.\ part.}$ (488 nm) > $\varepsilon_{molecule}$ (488 nm), but still is far from negligible. At 894.3 nm, the molecular absorption accounts for only a fraction of the total extinction and therefore ε_{total} (894.3 nm) is only slightly bigger than $\varepsilon_{abs.\ part.}$ (894.3 nm). However, the particle absorption coefficients at 488 nm obtained from formula V-6 agree well with (894.3/488)·$\varepsilon_{part.\ abs.}$ (894.3 nm) showing the $1/\lambda$ dependence of $\varepsilon_{part.\ abs.}$.

It is interesting to compare Fig. 30 with Fig. 32. In Fig. 32, the total extinction and particle absorption at 894.3 and 488 nm are plotted against h for the flame containing TBHP (C/O = 1.00, N_2/O_2 = 1.59). The ε values in Fig. 32 are larger than in Fig. 30. Again, one observes a nearly linear rise of ε with h. The onset of particle absorption occurs earlier in the flame containing TBHP, but for reaction times near 20 msec, $\varepsilon_{part.\ abs.}$ (894.3) converges to the same value as for the flame containing no TBHP. This behaviour shows that in the flame containing TBHP, the soot particle volume fraction for t < 20 msec is bigger than in the flame containing no TBHP. The soot particle volume fraction then becomes equal for both flames near t = 20 msec.

The scattering data for the flame of C/O = 1.00 (N_2/O_2 = 1.59), with and without TBHP, are plotted in Figs. 31 and 33. The values for H_V (550 nm), measured from the flame with TBHP (see Fig. 33) are lower below and higher above h = 5.5 mm, than from the flame without TBHP (see Fig. 31). This accounts for the difference of the ε_{total} (488 nm) values of Figs. 32 and 30 around t = 20 msec, where the $\varepsilon_{part.\ abs.}$ (894.3 nm) values are equal. In Fig. 31, the H_V (LLS) is indistinguishable from the V_V (LLS) below h = 3.5 mm and is proportional to H_V (550 nm) up to h = 5.5 mm, as it is mainly dominated by the fluorescence. Above h = 5.5 mm, the H_V (LLS) starts to rise in a stronger fashion than could be attributed to the

fluorescence contribution - the depolarised Rayleigh scattering component from the soot particles becomes important. This, of course, shows up more clearly in the H_V (Monochr.) measurements, which are less influenced by the fluorescence than H_V (LLS). H_V (Monochr.) rises nearly proportional to H_V (550 nm) up to h = 5.5 mm and then increases rapidly as the soot particles begin to dominate the scattering. The V_V components, which we are most interested in, are rising continuously. The V_V (Monochr.) can always be distinguished from the H_V (Monochr.) in contrast to the V_V (LLS) and H_V (LLS). Between h = 6.5 and h = 9.5 mm, the V_V (LLS) and V_V (Monochr.) become equal, whereas above h = 10.5 mm, a slight difference occurs. This asymmetry in the scattering pattern shows that the soot particle size goes beyond the limit for which the Rayleigh scattering approximation holds (see below).

The depolarisation ratios for the soot particles between h = 6.5 and 11.5 mm are nearly constant, all values are between $\rho_V = 9 \cdot 10^{-3}$ and 10^{-2}. The constancy of ρ_V is a good indication that the depolarisation of the light scattered by the soot particles is caused by anisotropy of refractive index rather than shape; the former would presumably not change much with particle coalescence and surface growth, whereas an agglomeration process would lead to an increase in particle eccentricity and thus depolarisation ratio.

The scattering data from the flame containing TBHP (Fig. 33) look, on first sight, similar to the data in Fig. 31. However, there are some considerable differences. Between h = 2.5 and h = 4.5 mm, the V_V scattering component cannot be distinguished from the H_V component, even when the monochromator was used. This indicates, together with the non-vanishing particle absorption coefficient in the flame region (see Fig. 32), that the soot particles present there are extremely small (small scattering cross-section) and the number density correspondingly high (see below). Only from h = 6 mm onwards, does the V_V particle scattering become clearly defined. For all heights above the burner, the measured V_V values are below those in Fig. 31. Near the top of the flame, again a slight difference between V_V (LLS) and V_V (Monochr.) becomes apparent, indicating a small asymmetry in the angular scattering pattern. The depolarisation ratios from h = 7.5 to 11.5 mm are between $\rho_V = 9 \cdot 10^{-3}$ and 10^{-2} and are no different from the ρ_V obtained from the flame without TBHP.

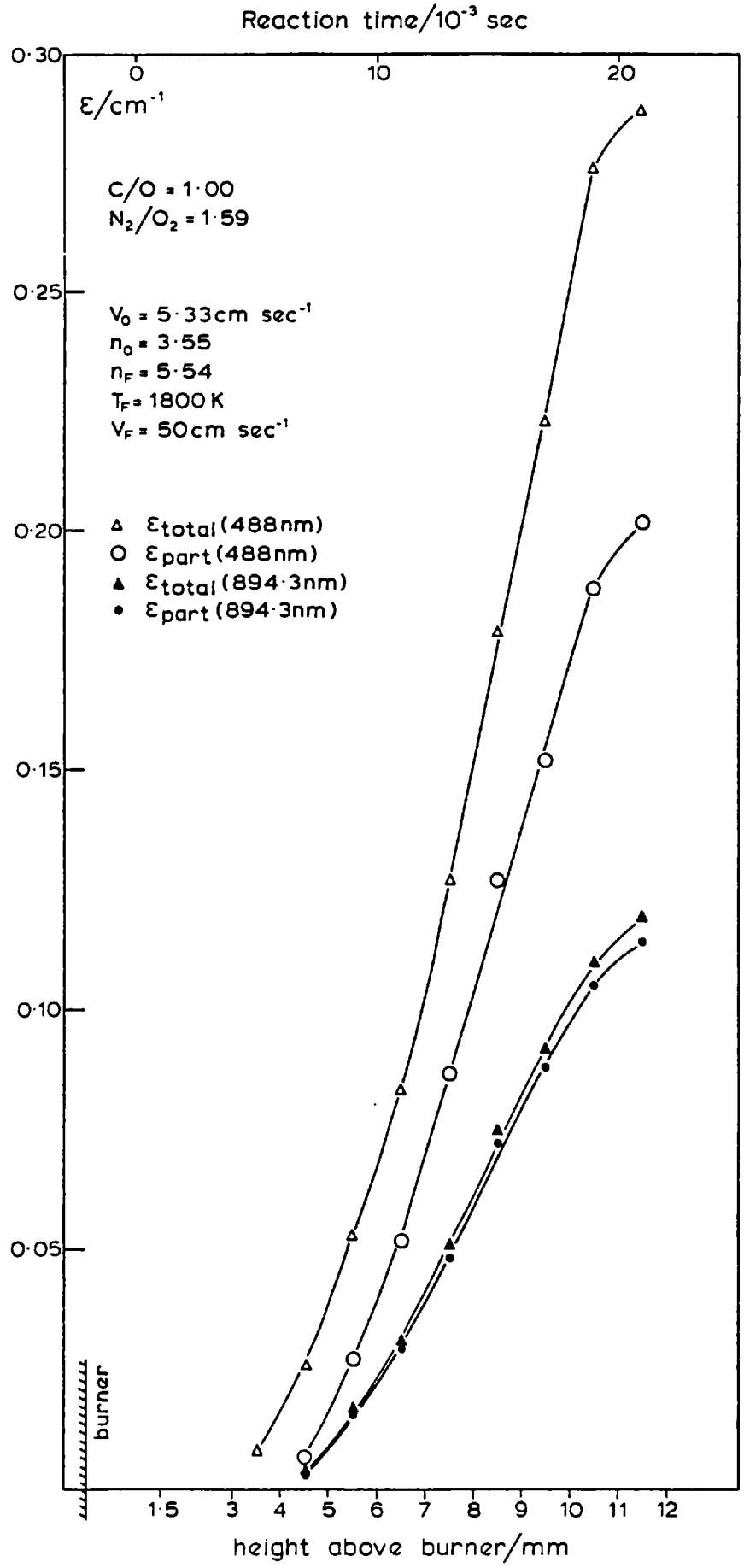

Fig. 30: Total extinction and particle absorption coefficients at 894.3 and 488 nm versus h.

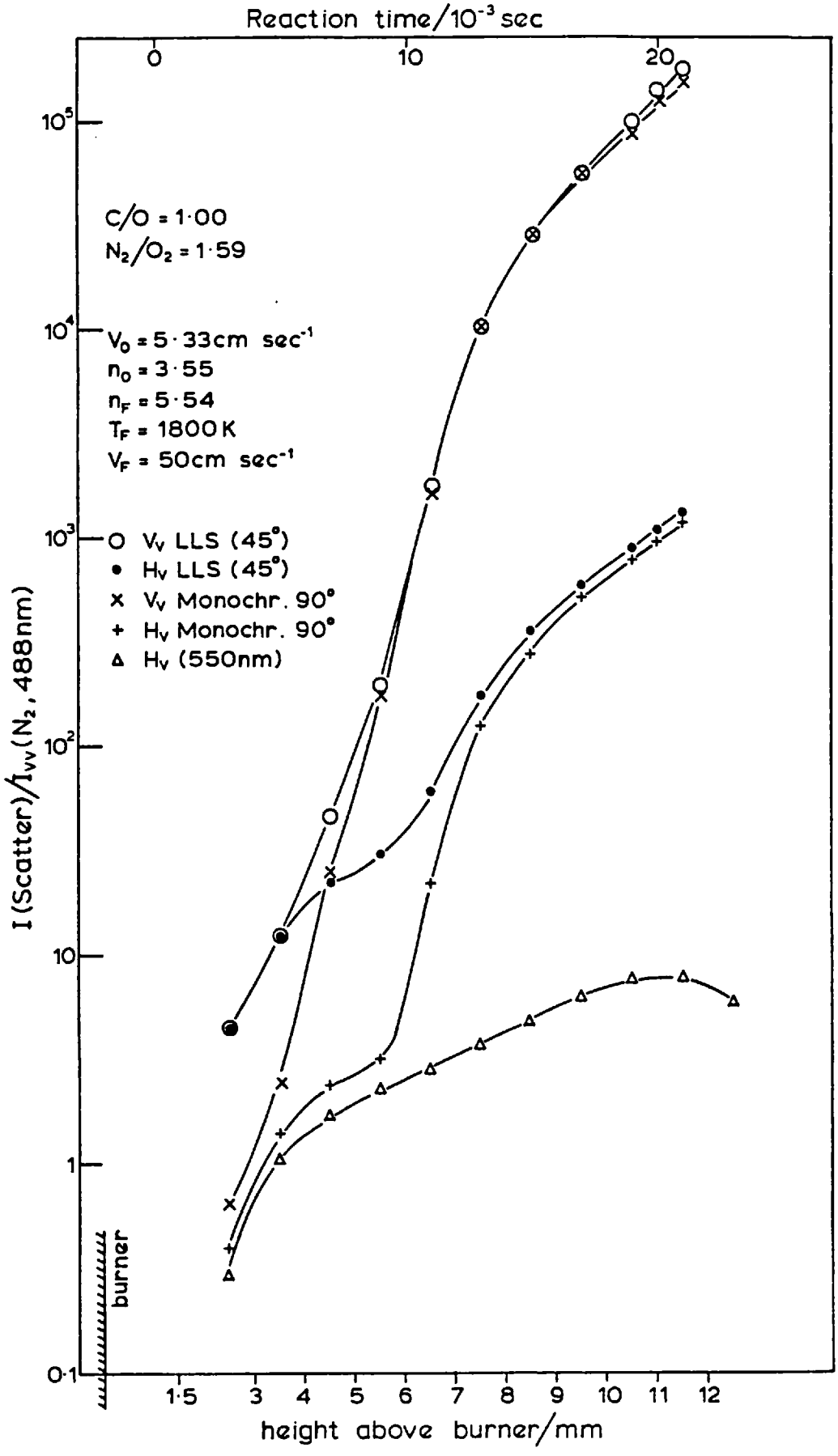

Fig. 31: Scattering data corresponding to Fig. 30.

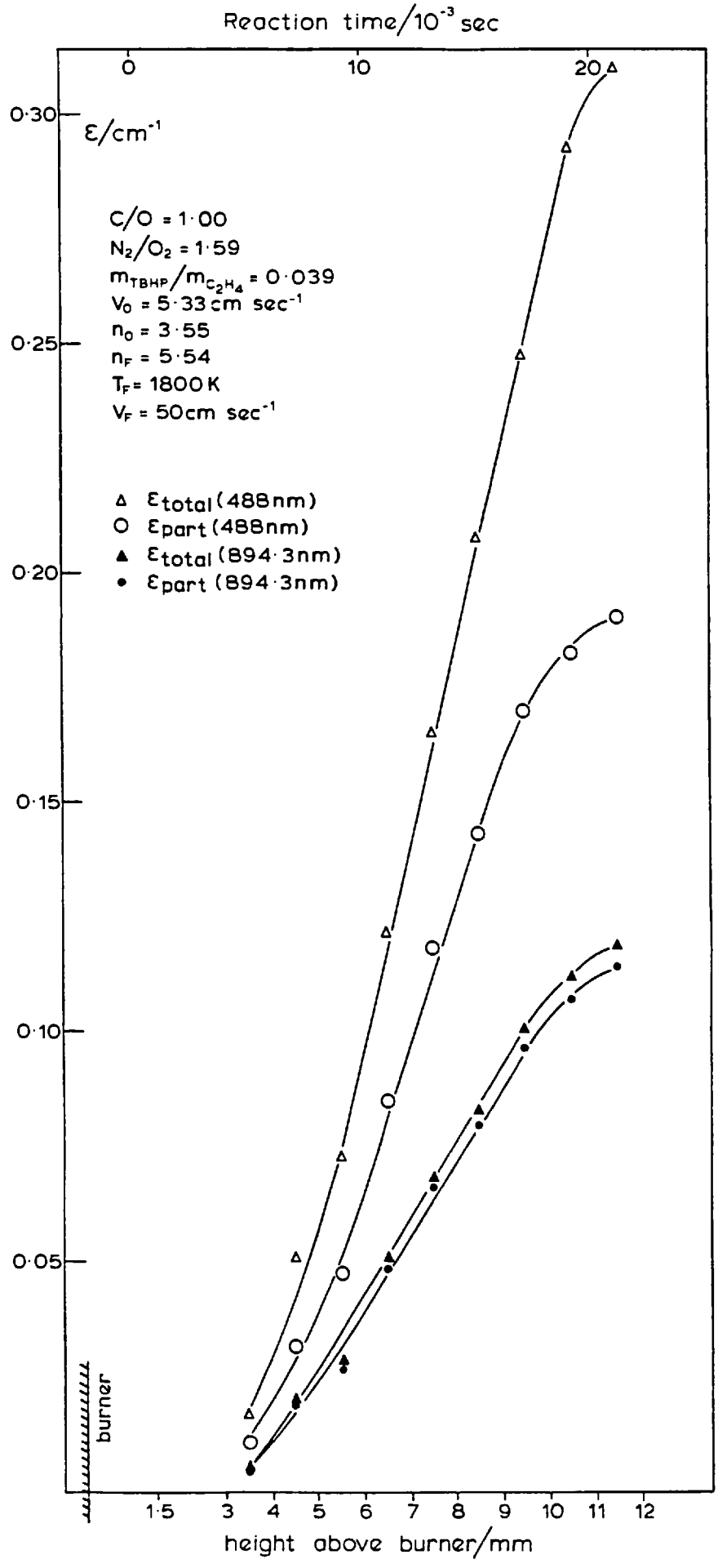

Fig. 32: Total extinction and particle absorption coefficients at 894.3 and 488 nm versus h. Same C/O and N_2/O_2 ratio as Fig. 30, but TBHP replacing some fuel.

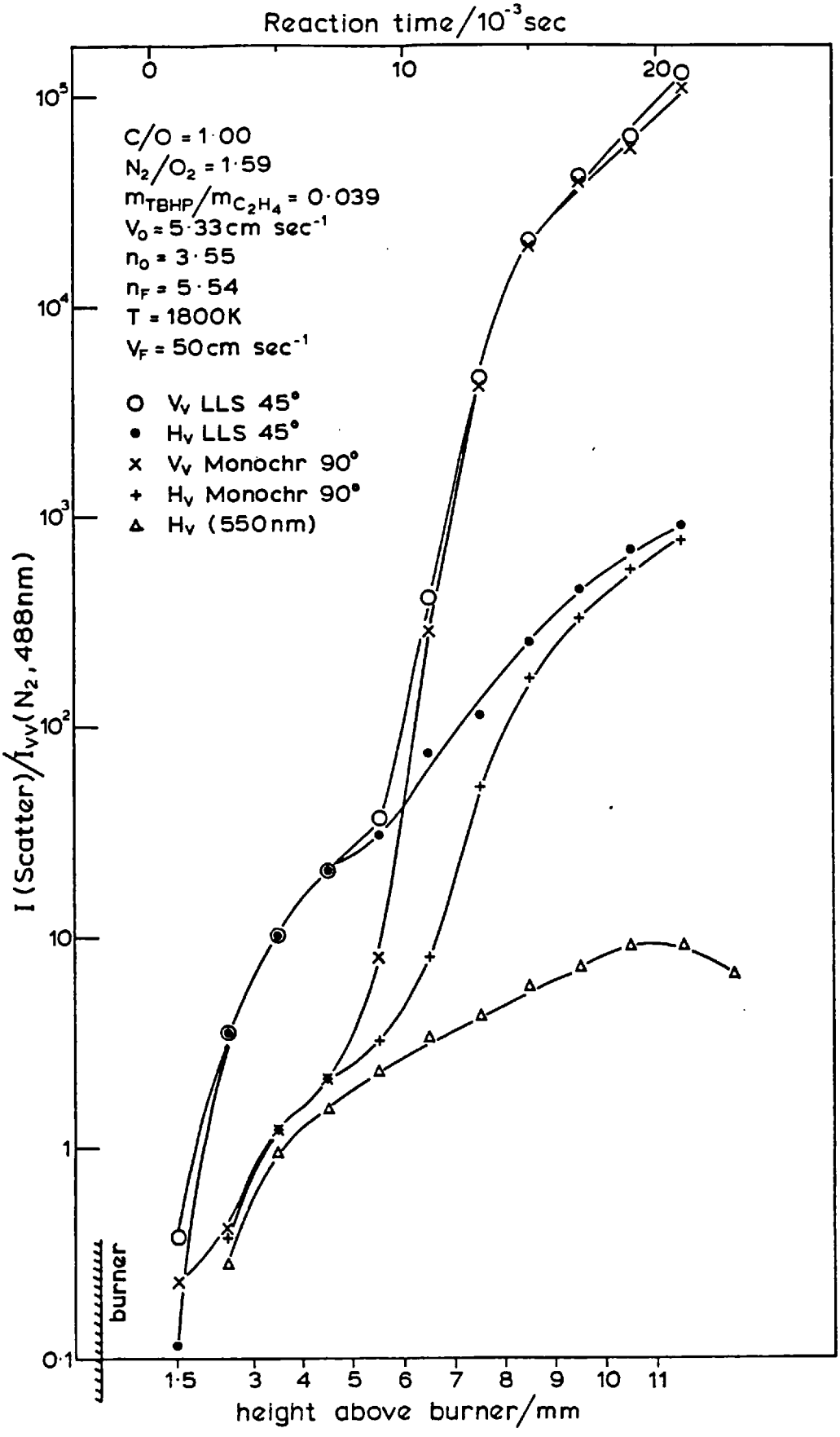

Fig. 33: Scattering data corresponding to Fig. 32.

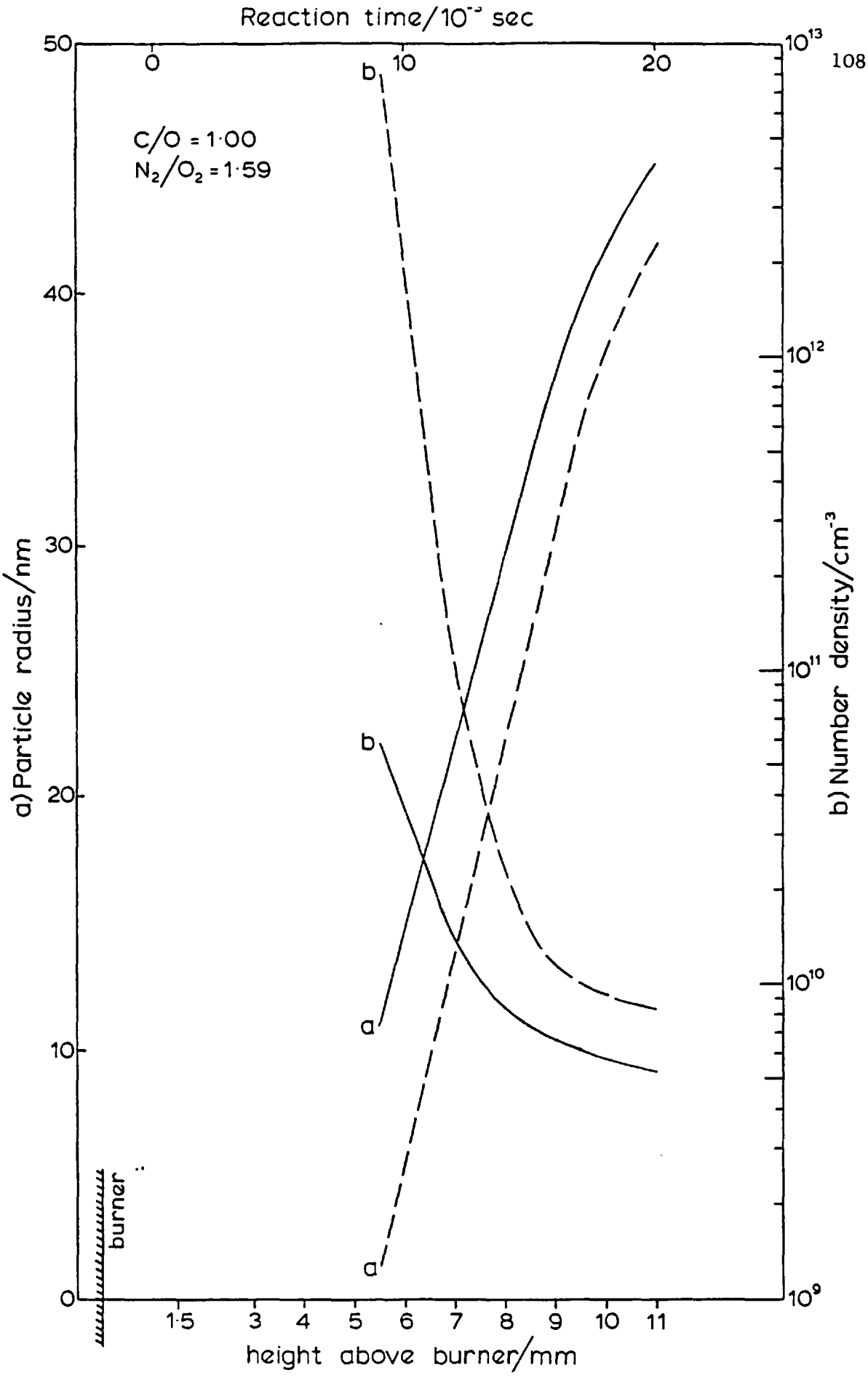

Fig. 34: Number density N (negative slopes) and particle radius a (positive slopes) versus h. Full lines: no TBHP added, corresponds to Figs. 30 and 31. Dashed lines: with TBHP, corresponds to Figs. 32 and 33.

From formula V-8, the soot particle radius a and the number density N were calculated. For the upper flame regions, the values for a obtained by Rayleigh theory were compared with the values of a obtained by fitting the disymmetry of the scattering pattern to the i_1 intensity function calculated from Mie theory. The agreement was good enough to justify the evaluation of the data by (simpler) Rayleigh theory only. Fig. 34 shows the results for both flames (C/O = 1.00, N_2/O_2 = 1.59) with or without TBHP. Below h = 5.5 mm no meaningful results are obtained, as the V_V scattering component of the soot particles itself cannot be determined with sufficient accuracy. The particle radius rises nearly linearly for both flames, with the difference in a becoming less distinct towards higher reaction times. At h = 5.5 mm, the radius of the soot particles in the flame containing TBHP is ten times smaller than in the flame without TBHP. Correspondingly, the particle number density at h = 5.5 mm differs by more than two orders of magnitude. The different gradients of the logarithmic plots of N versus h can be explained by the strong dependence of the particle coagulation rate on number density (approximately in the free molecule regime: $-dN/dt \sim N^2$, see Chapter VI).

The absorption and scattering data for the flames of C/O = 1.51, N_2/O_2 = 1.75 are displayed in Figs. 35 to 38. Fig. 35 shows the total extinction and particle absorption coefficients versus h for the flame without TBHP. The ε_{total} (488 nm) rises non linearly below h = 5.5 and decreases nearly linearly above. The onset of particle formation occurs around h = 6.5, where particle absorption becomes detectable. In comparison to the results in Fig. 20, one can see that, with the bigger burner separation soot particles are formed in this very rich flame, as the reaction times are long enough . However, compared to the results in Fig. 30, soot particle formation occurs later in the flame and the soot volume fraction is always much less than for C/O = 1.00. The $\varepsilon_{abs.\ part.}$ values rise virtually linearly between h = 6.5 and h = 11.5 mm. For the flame containing TBHP (Fig. 37), the $\varepsilon_{abs.\ part.}$ values are always higher than for the flame without TBHP, (indicating a larger soot volume fraction) and do not converge to the same value in the top flame region. Most remarkable in Figs. 35 and 37 are the great differences between the

ε_{total} and $\varepsilon_{abs.\ part.}$ values. At 488 nm, the total extinction coefficients are about five times larger than the particle absorption coefficients. Even at 894.3 nm, the molecular contribution to the total extinction coefficient is not negligible. However, even in these very rich flames, where the total extinction in the visible is dominated by the molecular absorption, the soot particle absorption coefficient can still be determined with sufficient accuracy using form. V-6. This is revealed by the comparison of $\varepsilon_{part.\ abs.}$ (488 nm) and $\varepsilon_{part.\ abs.}$ (894.3 nm), showing goood agreement with the $1/\lambda$ dependence of $\varepsilon_{part.\ abs.}$.

The scattering data for the flames of C/O = 1.51, N_2/O_2 = 1.75 are shown in Fig. 36 (flame without TBHP) and Fig. 38 (flame with TBHP). The fluorescence (H_V = 550 nm) from the TBHP containing flame is always stronger than from the flame without TBHP - three times at h = 3.5 mm. In the higher flame region the H_V (550 nm) becomes nearly equal for both flames. For the flame without TBHP (Fig. 36) the H_V (Monochr.) and H_V (LLS) are directly proportional to H_V (550 nm) - being dominated by the fluorescence - up to h = 8 mm. The V_V scattering components become clearly separable from the fluorescence contribution above h = 6.5 mm. Again, around h = 11 mm we can see a slight discrepancy between the V_V (Monochr.) and V_V (LLS), caused by the soot particle size going beyond the Rayleigh limit. As particle scattering starts later in this flame than for C/O = 1.00, the depolarised Rayleigh component also shows up later. The soot depolarisation ratios between h = 10.5 and 12.5 mm have values of $5 \cdot 10^{-3}$ to $6 \cdot 10^{-3}$. The scattering components from the flame containing TBHP show different behaviour. Caused by the strong fluorescence contribution, the H_V (Monochr.), V_V (Monochr.), H_V (LLS) and V_V (LLS) are all proportional to H_V (550 nm) up to h = 8.5 mm. Any V_V scattering from soot particles is completely undetectable in this region, even with the monochromator. Beyond h = 9 mm, soot particles show their presence by a rapid increase in the V_V scattering components. Similarly to the flame containing no TBHP, around h = 11 mm, a slight asymmetry in the V_V scattering pattern becomes detectable. The depolarised Rayleigh component from the soot particles becomes clearly distinguishable from the fluorescence contribution above h = 10.5 mm. The soot depolarisation ratios have values between $6 \cdot 10^{-3}$ and $8 \cdot 10^{-3}$ in that flame region.

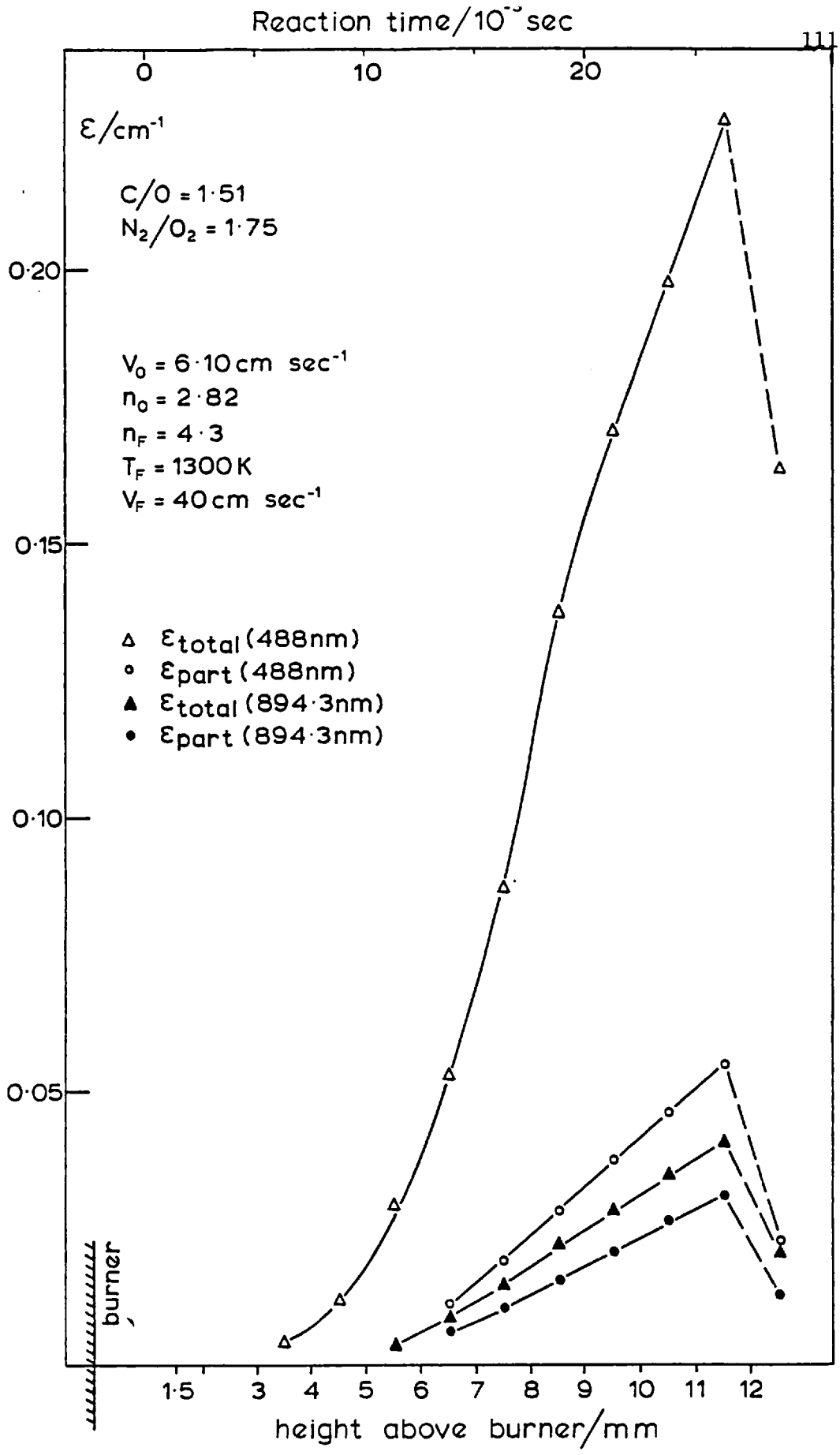

Fig. 35: Total extinction and particle absorption coefficients at 894.3 and 488 nm versus h.

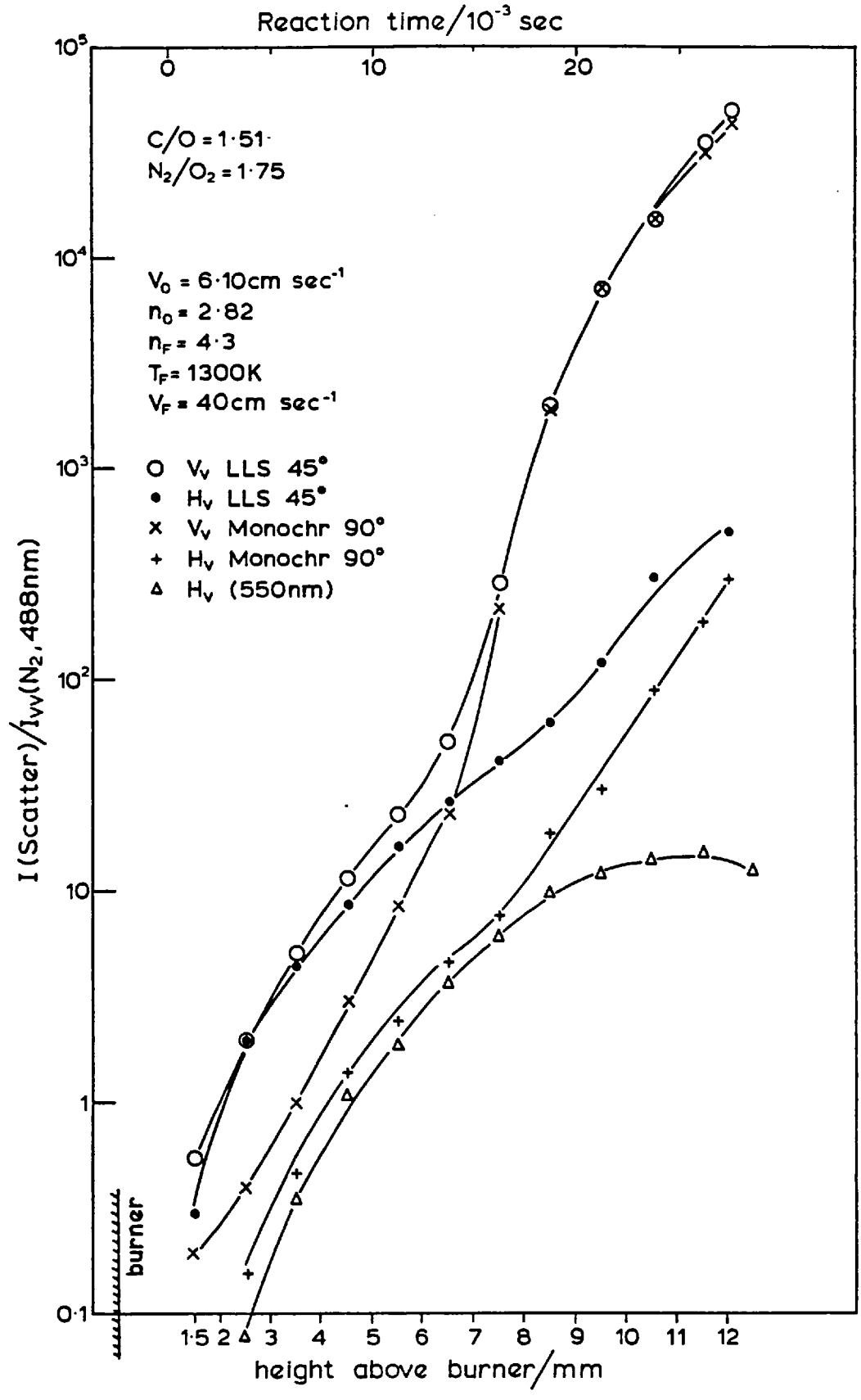

Fig. 36: Scattering data corresponding to Fig. 35.

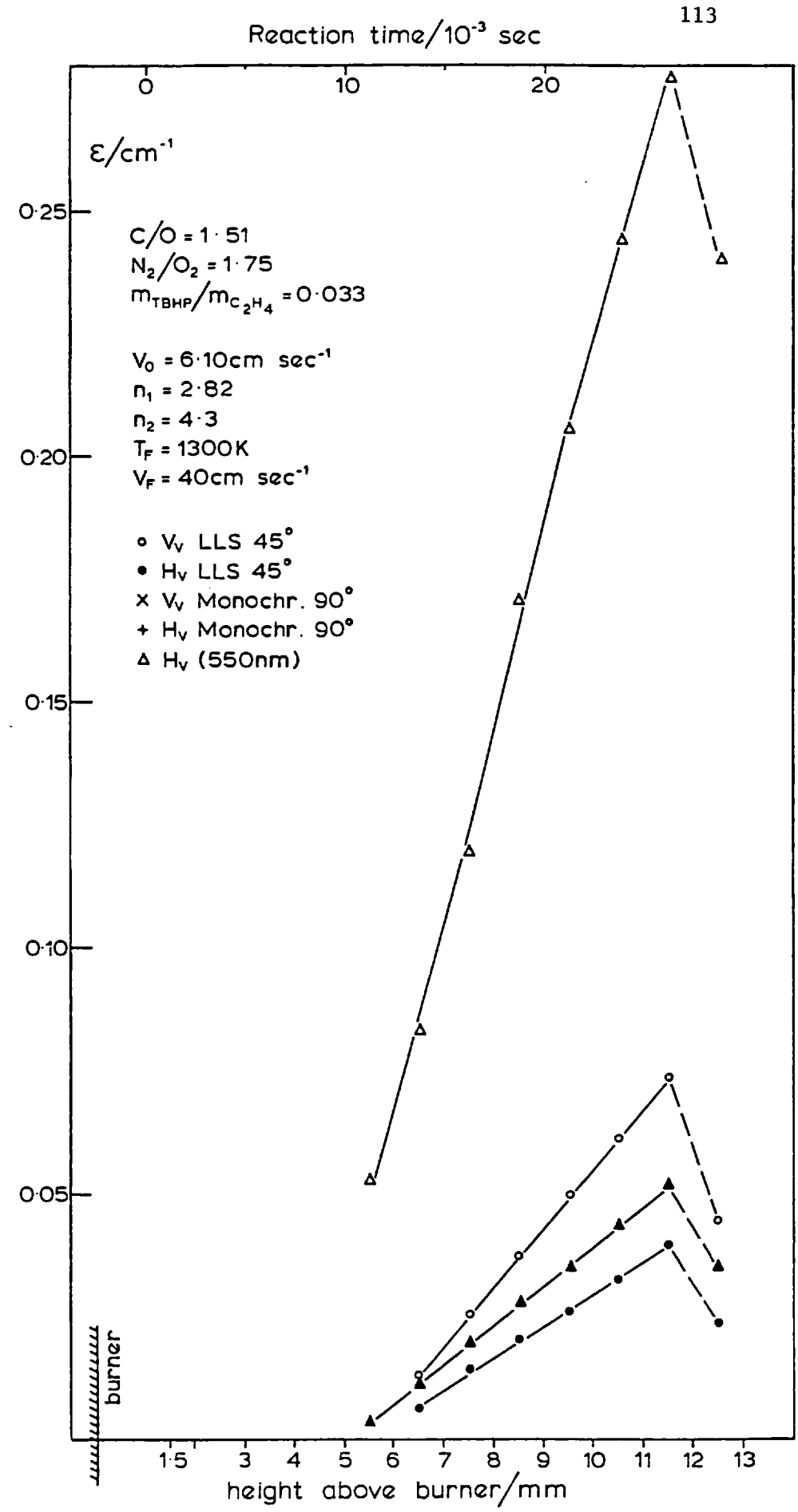

Fig. 37: Total extinction and particle absorption coefficients at 894.3 and 488 nm versus h. Same C/O and N_2/O_2 ratio as Fig. 36, but TBHP replacing some fuel.

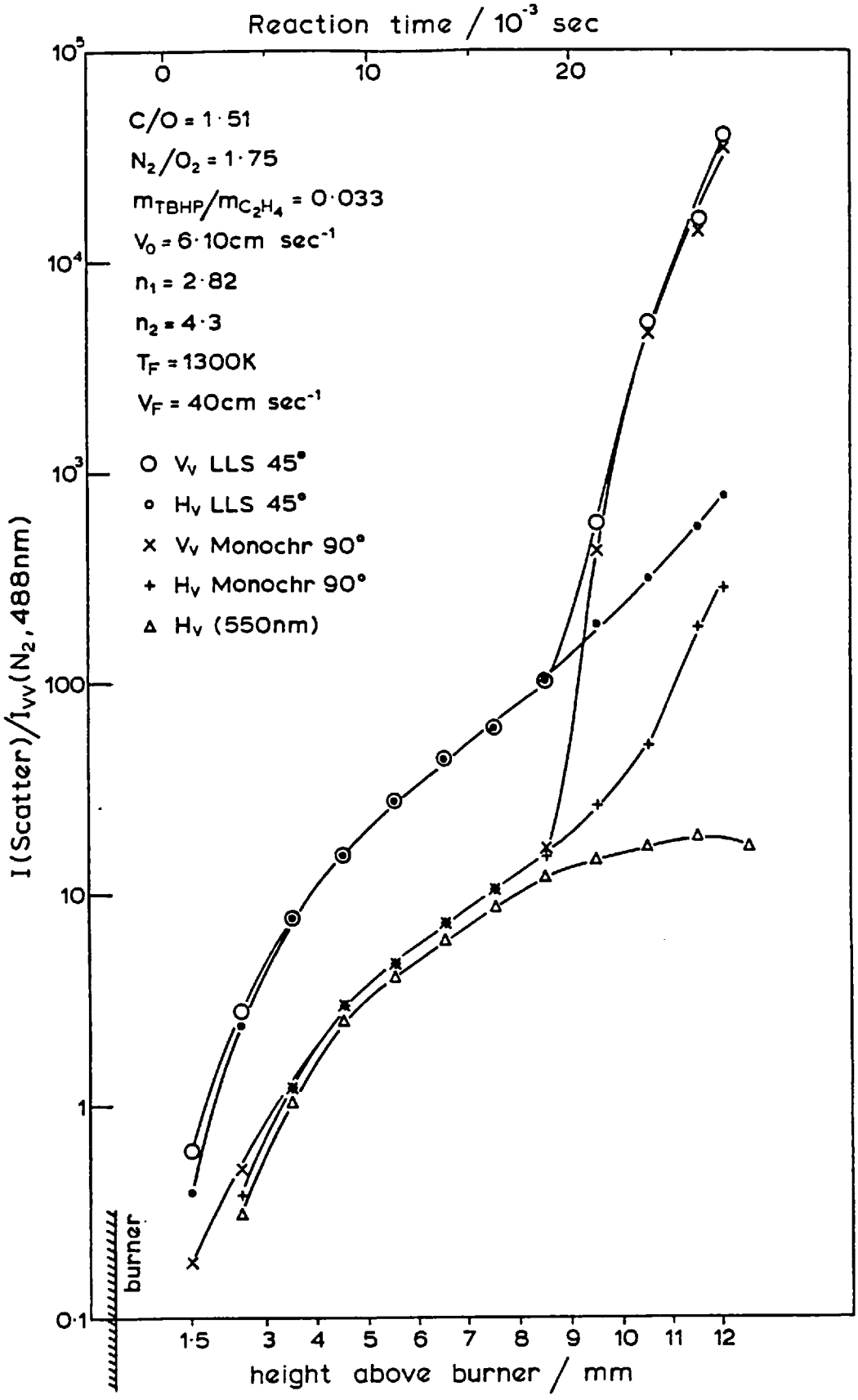

Fig. 38: Scattering data corresponding to Fig. 37.

Using form. V-8, the results from Figs. 35-38 allow for the determination of soot particle radius and number density. In Fig. 39, a and N are plotted for the flames of C/O = 1.51, N_2/O_2 = 1.75, with and without TBHP. For the flame containing no TBHP, only from h = 6.5 mm onwards can meaningful results be obtained, because the soot V_V scattering component and the particle absorption coefficient are undefined below h = 6.5 mm. The logarithm of the particle number density decreases nearly linearly with h between h = 6.5 mm ($N = 5 \cdot 10^{10}$ cm^{-3}) and h = 9.5 mm ($N = 2.5 \cdot 10^{9}$ cm^{-3}) and then starts to level off. Correspondingly, the particle radius rises from 9 nm at h = 6.5 mm to 48 nm at 11.5 mm with a virtually linear dependence on h. For the flame containing TBHP, the size and number density determination fails below h = 8.5 mm. This is caused by the undeterminability of the soot V_V scattering component, which is completely lost in the fluorescence. The onset of particle absorption (see Fig. 37) is already taking place at h = 6.5 mm, indicated by the non vanishing $\varepsilon_{\text{part. abs.}}$ at 894.3 nm. Therefore we have to draw the conclusion that in the flame containing TBHP, between h = 6.5 and 8.5 mm, soot particles are readily being formed. However, these particles must be so small (a < 0.5 nm) that their contribution to the V_V scattering is undetectable, in spite of the high number density ($N > 10^{14}$ cm^{-3}), which is indicated by the values for $\varepsilon_{\text{abs. part.}}$ at 894.3 nm. Even if the detection of the V_V scattering component was improved upon by employing a high resolution spectrometer (and thus eliminating most of the fluorescence background), the problem of determining V_V (soot) in this flame region could still not be solvable. This is caused by the gas phase V_V scattering component from water-gas combustion products and unburnt ethylene which is considerably stronger than the V_V scattering component of 0.01, calculated for soot particles of e.g. a = 0.5 nm and $N = 2 \cdot 10^{14}$ cm^{-3}. Above h = 8.5 mm, the particle radius rises linearly from 1.5 nm (at h = 8.5 mm) to 36 nm (at h = 11.5 mm). Correspondingly, the number density goes down from $2 \cdot 10^{13}$ to $3.5 \cdot 10^{9}$ cm^{-3}. In the flame containing TBHP, though the total soot volume fraction $\phi = N\,V$ is always higher, the individual soot particle radius is always much lower than in the flames without TBHP. The effect of TBHP is quite similar for both C/O ratios of 1.51 and 1.00, as a comparison of Fig. 39 and Fig. 34 shows.

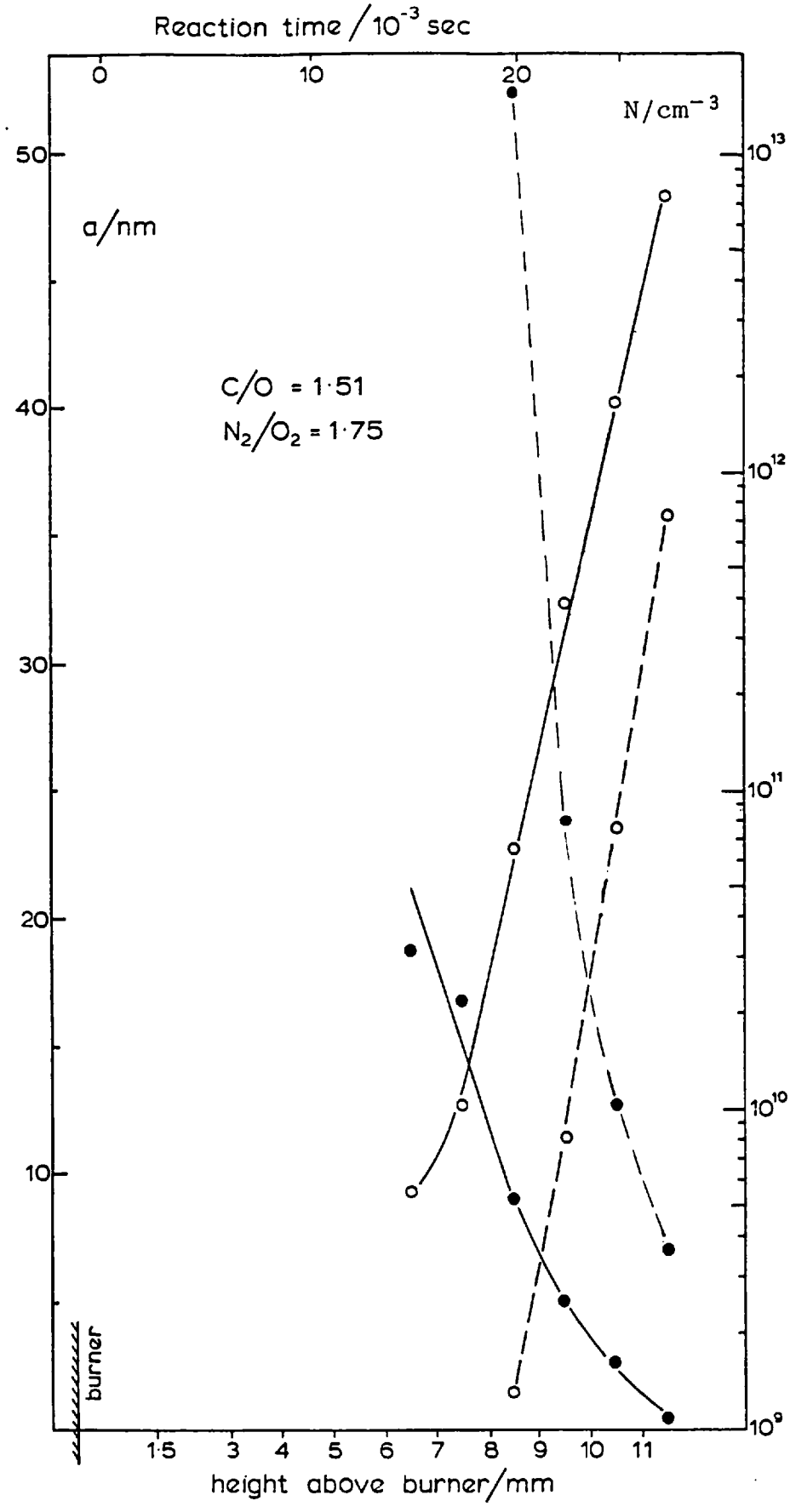

Fig. 39: Number density N (negative slopes) and particle radius a (positive slopes) versus h. Full lines: no TBHP added, corresponds to Figs. 35 and 36. Dashed lines: with TBHP, corresponds to Figs. 37 and 38.

The flames described so far, were very rich in fuel and therefore oxygen enriched air had to be used to maintain the flames. To extend the study to flames burning with air, an ethylene flame with a C/O ratio of 0.704 (not too far from the critical ratio for ethylene) and $N_2/O_2 = 3.76$ was investigated. The soot volume fraction in this flame was too small to measure the absorption on the laser wavelength reliably, as the employed laser power meter was not accurate enough. With the Cs lamp and the described detection apparatus, some difficulties were also encountered in detecting only about 1 - 2% of absorption. These were overcome by increasing the sensitivity of the Lock-in amplifier by a factor of ten and using the calibrated off-set to stay within the range of the chart recorder.

The results for $\varepsilon_{\text{part. abs.}}$ at 894.3 (again obtained by using form. V-6) and all the scattering data for the flame of C/O = 0.704, $N_2/O_2 = 3.76$ are plotted against h in Fig. 40a. Only above h = 11.5 mm is there enough absorption to be detected (lower right hand corner of Fig. 40a). The fluorescence from this flame is much lower than from the fuel richer flames described before. However, this must not lead to the conclusion that the molecular contribution to the total extinction would be negligible in this case, if one measures the absorption in the visible. At 488 nm and for h = 13 mm, about one third of the total extinction coefficient of $\simeq$ 0.018 would still be caused by absorption from molecules. Therefore, even for this not very rich ethylene-air flame, a severe error arises in the particle radius and number density determination, if one takes the total extinction coefficient in the visible for the particle absorption coefficient. The scattering data for the flame of C/O = 0.704, $N_2/O_2 = 3.76$ are also displayed in Fig. 40a. The H_V (LLS) and the H_V (Monochr.)* - up to h = 10 mm - are proportional to the H_V (550 nm). Above h = 10 mm the H_V (Monochr.) increases stronger than could be attributed to the fluorescence alone - the soot particles present show some (Rayleigh) depolarisation. As regards the V_V scattering components, in this flame, especially in the early

---

*The depolarised Rayleigh gas phase scattering component, which is not completely negligible in the earliest region of the flame, causes the apparent bending of the H_V (Monochr.) curve towards the H_V (550 nm) curve around h = 6.5 mm.

flame region, the gas phase scattering contribution has to be taken into account. The latter was estimated from the calculated water-gas composition and the corresponding temperature, which was taken to be constant above h = 2 mm. If the V_V gas phase scattering contribution is subtracted from the measured V_V, the resulting values are dominated by the fluorescence up to h = 9 mm and are therefore proportional to the H_V (550 nm). Above h = 9 mm the V_V starts to rise, because the scattering from soot particles becomes dominant compared to the fluorescence and the V_V gas phase contribution. The V_V (Monochr.) is always less than the V_V (LLS), as the monochromator system eliminates more of the fluorescence than the interference filter in the L.L.S. detector.

The measurements for the flame containing TBHP (C/O = 0.704, N_2/O_2 = 3.76) are shown in Fig. 41a. The particle absorption coefficient is marginally greater in this flame, compared to the flame without TBHP. Up to h = 6.5 mm, all the scattering data are virtually the same as for the flame containing no TBHP. Above h = 6.5 mm the H_V (550 nm) and, correspondingly, the H_V (Monochr.) and H_V (LLS) become greater, but the V_V (Monochr.) and V_V (LLS) become less than the values from the flame without TBHP. At h = 13.5 mm the V_V scattering components are the same for both flames. The soot depolarisation ratios between h = 11.5 and 13.5 mm, again obtained by subtracting the fluorescence contribution from the H_V (Monochr.), are for both flames estimated to be around 10^{-2}. This value should not be treated as being too accurate, as the errors in the determination of the true soot particle depolarised scattering component are quite high for the two flames. However, ρ_v(soot) is certainly not equal to zero and not higher than $1.5 \cdot 10^{-2}$.

From the data of Figs. 40a and 41a, the soot particle radius and number density were calculated between h = 11.5 and 13.5 mm, using form. V-8. The results, shown in Fig. 40b (41b), exhibit similar features as have been noted before in the richer flames. The particle size is much smaller than in the richer flames discussed before, whereas the number density and its time dependence is comparable to the richer flames. Again, we can see from Figs. 40b (41b), that, also for the flame of C/O = 0.704, the replacement of ethylene by TBHP results in a reduction in soot particle radius and an increase in number density; with increasing h these differences become less distinct.

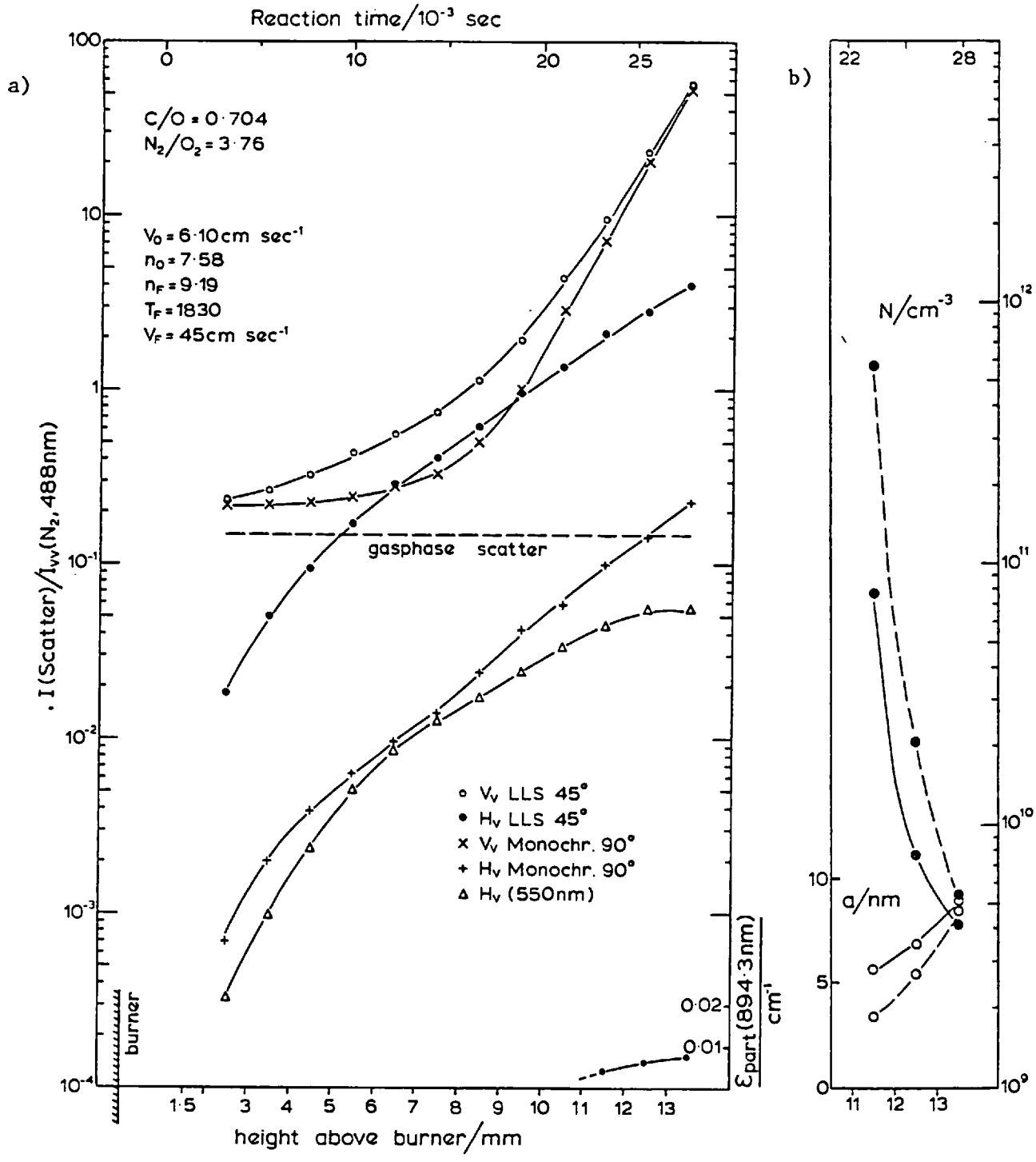

Fig. 40: a) Scattering data (with V_V gas phase scattering component) and particle absorption coefficient at 894.3 nm (lower right-hand side) versus h.

b) Number density N (negative slopes) and particle radius versus h. Full lines: no TBHP added; corresponds to Fig. 40a. Dashed lines:- with TBHP; corresponds to Fig. 41a.

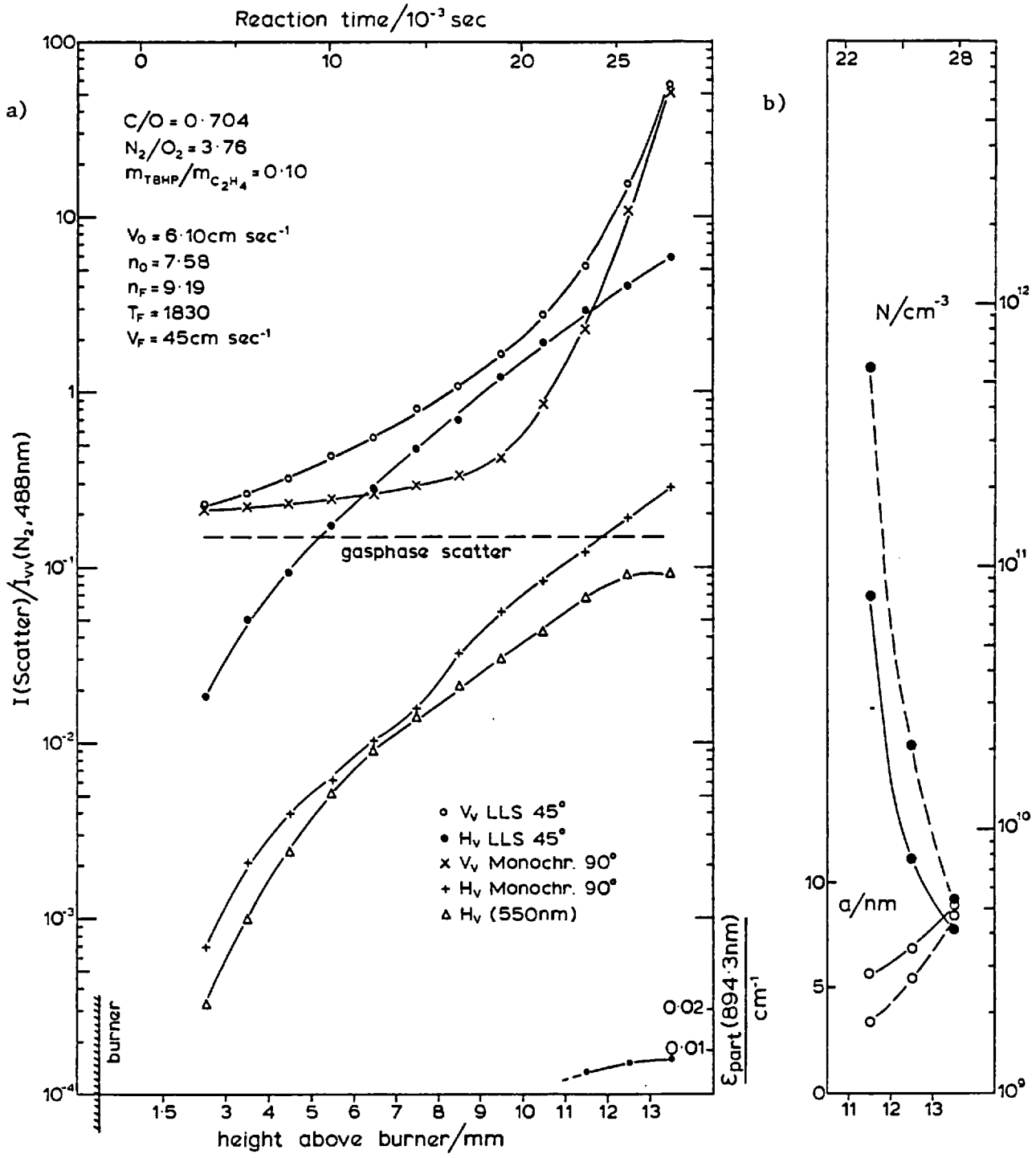

Fig. 41: a) Scattering data (with V_V gas phase scattering component) and particle absorption coefficient versus h.

b) As Fig. 40b.

The other organic peroxide to be studied in this work is di-tertiary-butyl-peroxide (DTBP), which, in its first step, decomposes into two tertiary-butoxy radicals (see Chapter II-1). Early experiments showed that this compound had to be added in larger quantities to the flames than TBHP, to detect effects on the soot formation process.

A flame of C/O = 0.963 and N_2/O_2 = 1.75, near the C/O ratio for maximum soot particle formation, was investigated. The total extinction and particle absorption coefficients at 894.3 and 488 nm measured in the flame without DTBP are plotted against h in Fig. 42. All the ε values rise virtually linearly beyond h = 5.5 mm; before soot particle absorption can be seen there is already some absorption from the molecular species. The onset of particle absorption occurs at h = 4.5 mm (as for the flame of C/O = 1.00 - see Fig. 30). For the DTBP containing flame of the same C/O ratio, we get a different dependence for the total extinction and particle absorption coefficients (see Fig. 44). Not only is the onset of detectable particle absorption later in the flame - at h = 6.5 mm - but also all the ε values are considerably smaller than in Fig. 42. This indicates a smaller soot particle volume fraction ϕ and also a lower concentration of the molecular, light absorbing species (compare also the lower H_V (550 nm) in Fig. 45 with those in Fig. 43). Fig. 44 shows that the particle absorption coefficient is linear between h = 6.5 mm and 8.5 mm and also linear, but with a higher slope, from h = 8.5 to 11 mm. With the high DTBP concentration in the fresh gas of the flame $(m_{DTBP})m_{ethylene}$ = 0.20), therefore an overall reduction in ϕ and the molecular species is obtained throughout the flame.

The scattering data for the flame of C/O = 0.963, N_2/O_2 = 1.75 are plotted against h in Fig. 43. The overall appearance of the measured values in Fig. 43 is similar to the results shown in Fig. 31 (flame of C/O = 1.00, N_2/O_2 = 1.59), not surprisingly, as the C/O ratios are not that different. The H_V (550 nm) values are virtually the same in Figs. 42 and 31, whereas the strong rise in the V_V scattering occurs somewhat later (at h = 5.5 mm) in the leaner flames of C/O = 0.963 than C/O = 1.00. The soot depolarisation ratios obtained from Fig. 43, between h = 7.5 and 11.5 mm, have values from $9 \cdot 10^{-3}$ to 10^{-2}. The scattering measurements for the DTBP containing flame (C/O = 0.963, N_2/O_2 = 1.75) are plotted in Fig. 45. The H_V (550 nm) values

are always about 20% lower than in the flames without DTBP; this was already indicated by the lower ε_{total} (488 nm) (see Figs. 44, 42). From h = 7 mm onwards, the V_V (soot) scattering components can be separated from the fluorescence. Below h = 6.5 mm, the H_V (Monochr.), V_V (Monochr.), H_V (LLS) and V_V (LLS) are dominated by the fluorescence and therefore proportional to H_V (550 nm). The V_V (Monochr.) and V_V (LLS) rise steadily from h = 7 to 11.5 mm, becoming equal above h = 9.5 mm, and remain well below the V_V components measured from the flame without DTBP. The soot depolarisation ratios - as obtained from Fig. 45 between h = 9.5 and 11.5 mm - have values around $\rho_v = 7 \cdot 10^{-3}$, somewhat lower than in the flame without DTBP.

The dependence of soot particle radius and number density on h, obtained from form. V-8, is shown in Fig. 46 for both flames, with and without DTBP (and C/O = 0.963, N_2/O_2 = 1.75). The particle radius rises linearly from 7 nm (at h = 6.5 mm) to 60 nm (at h = 11 mm) in the flame without DTBP and from 18 nm (at h = 8.5 mm) to 48 nm (at h = 11 mm) in the flame containing DTBP. Correspondingly, the number density decreases from $1.5 \cdot 10^{11}$ (at h = 6.5 mm) to $1.5 \cdot 10^{9}$ (at h = 11 mm) - without DTBP - and from $2 \cdot 10^{9}$ (h = 8.5 mm) to $9 \cdot 10^{8}$ (h = 11 mm) - with DTBP. With DTBP replacement of ethylene the particle radius is always smaller and the number density always higher than without DTBP. Below h = 8.5 mm, no meaningful results can be obtained for the DTBP containing flame, as the V_V (soot) scattering is not well resolvable and also the $\varepsilon_{abs.\ part.}$ values are quite low and therefore not too reliable.

Fig. 46 looks very similar to Fig. 34, although the quantitative differences are distinct, caused by the different C/O and N_2/O_2 ratios. However, TBHP seems to be at least five times more effective in particle size reduction in the flame than DTBP, though the soot volume fraction is not reduced with TBHP addition. DTBP has qualitatively the same effect on particle size (though only in higher concentrations than TBHP) but also, contrary to TBHP, reduces the total soot volume fraction. Another difference between the two peroxides is the increase in fluorescence with TBHP addition, whereas, with sufficient DTBP addition, the H_V (550 nm) is reduced.

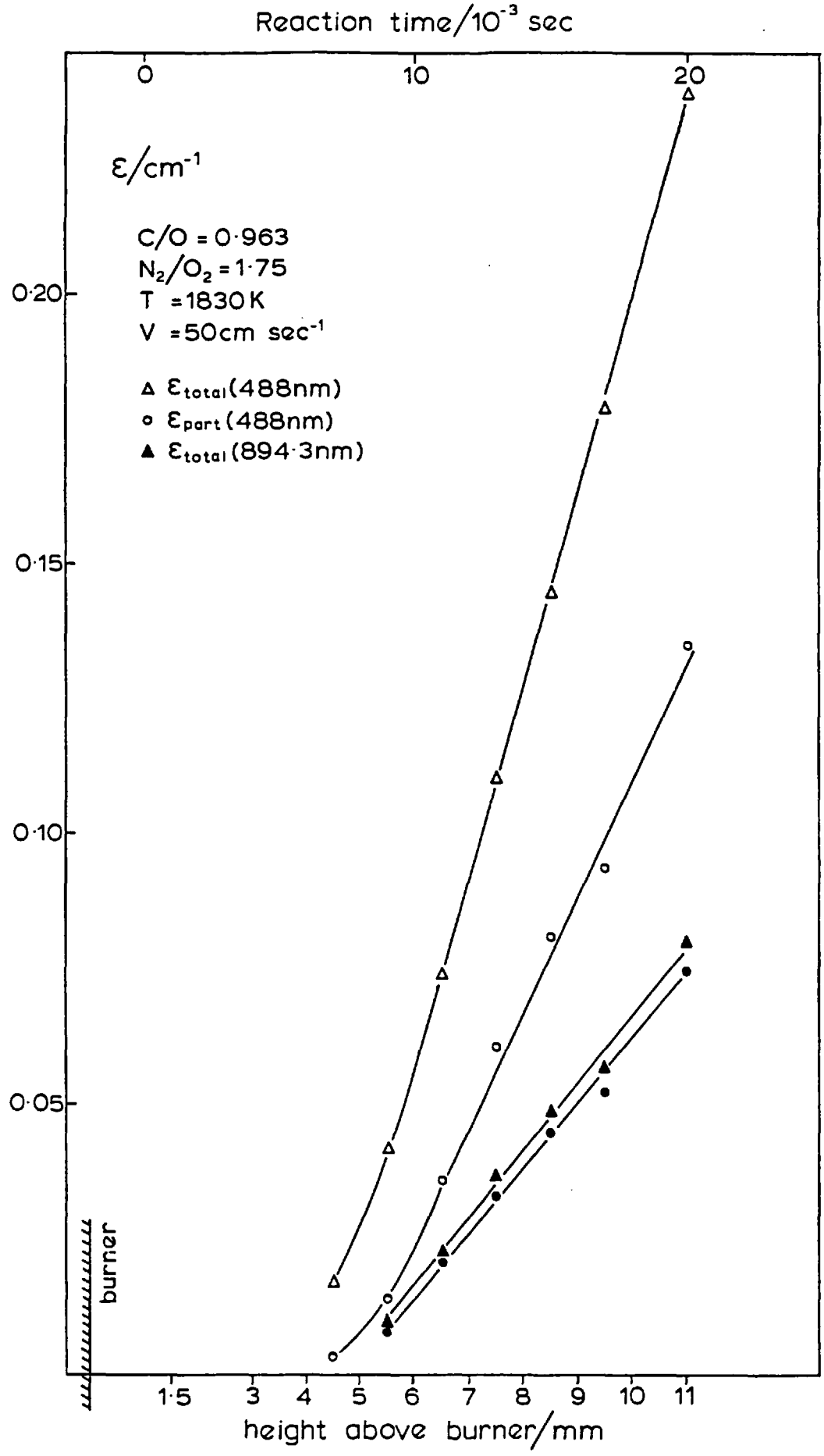

Fig. 42: Total extinction and particle absorption coefficients at 894.3 and 488 nm versus h.

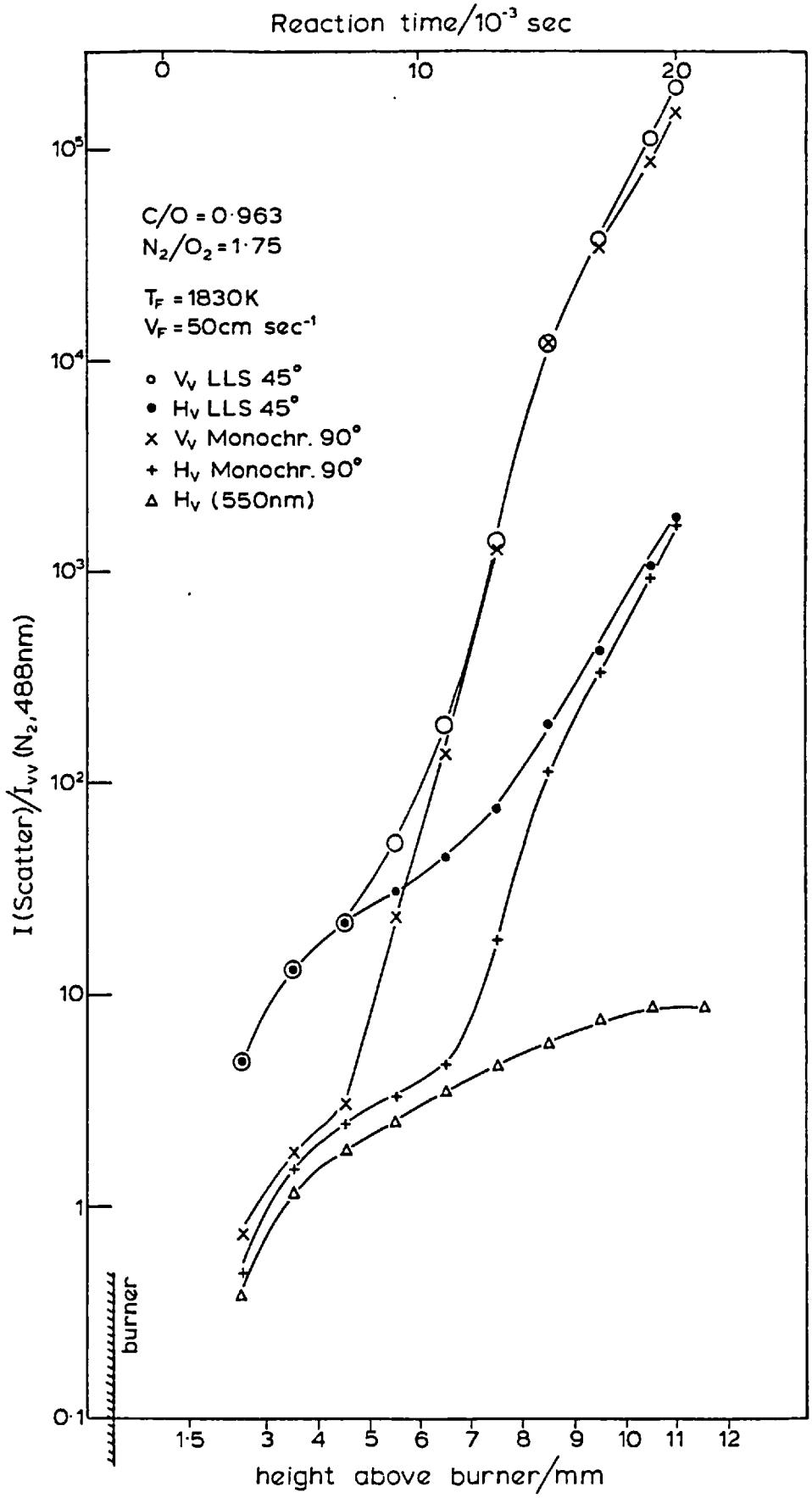

Fig. 43: Scattering data corresponding to Fig. 42.

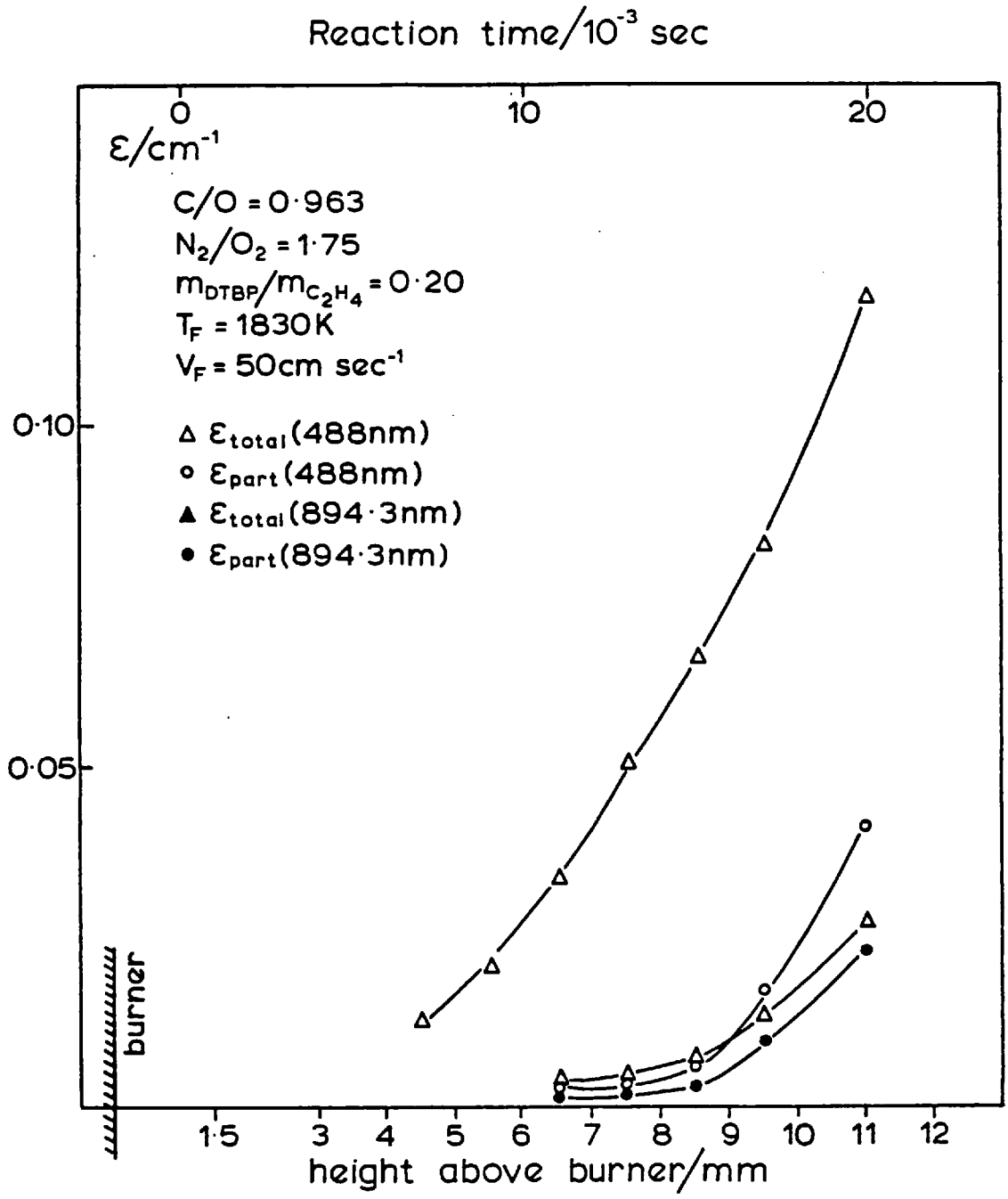

Fig. 44: Total extinction and particle absorption coefficients at 894.3 and 488 nm versus h. Same C/O and N_2/O_2 ratio as fig. 42, but some fuel replaced by DTBP.

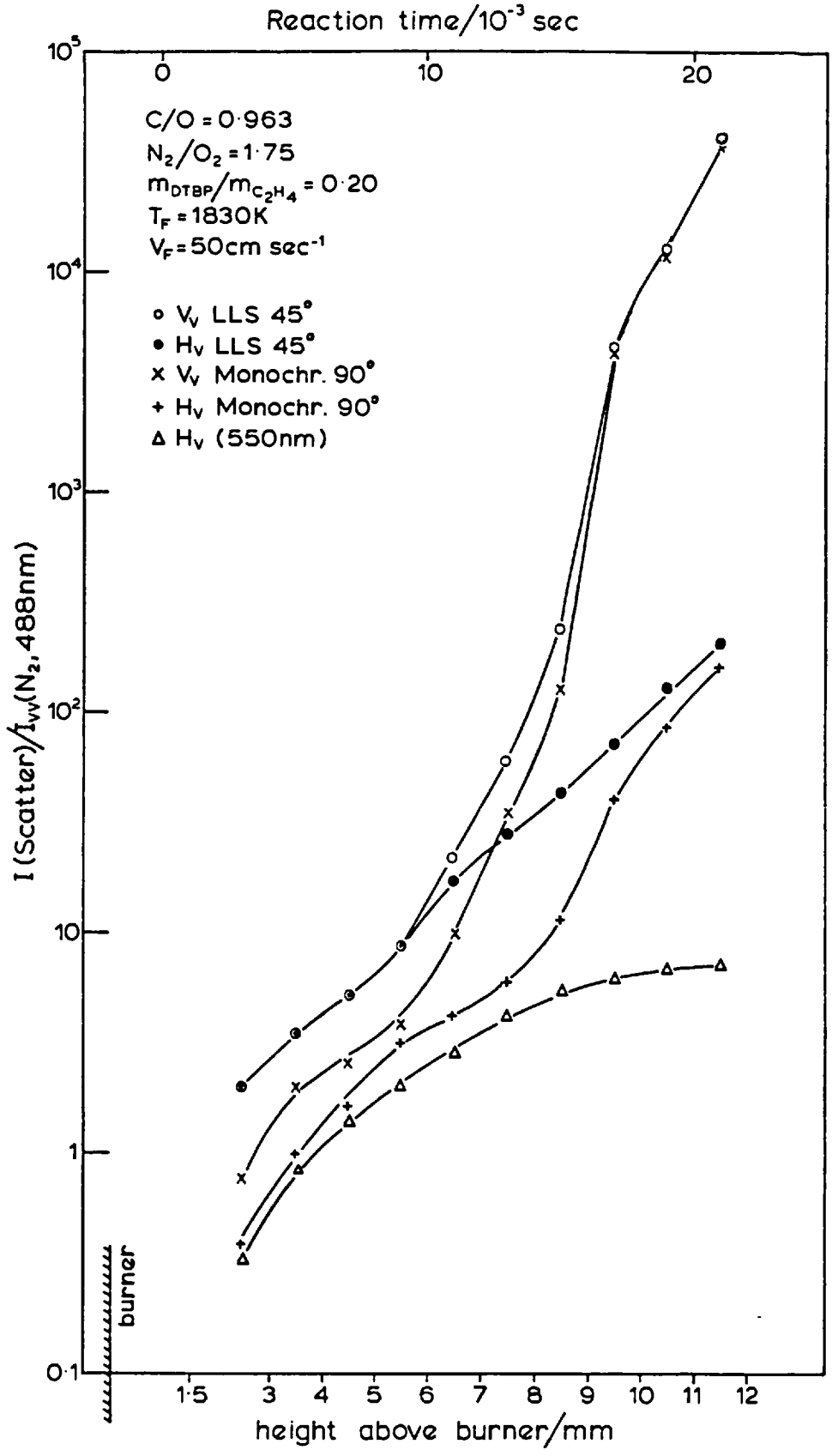

Fig. 45: Scattering data corresponding to fig. 44.

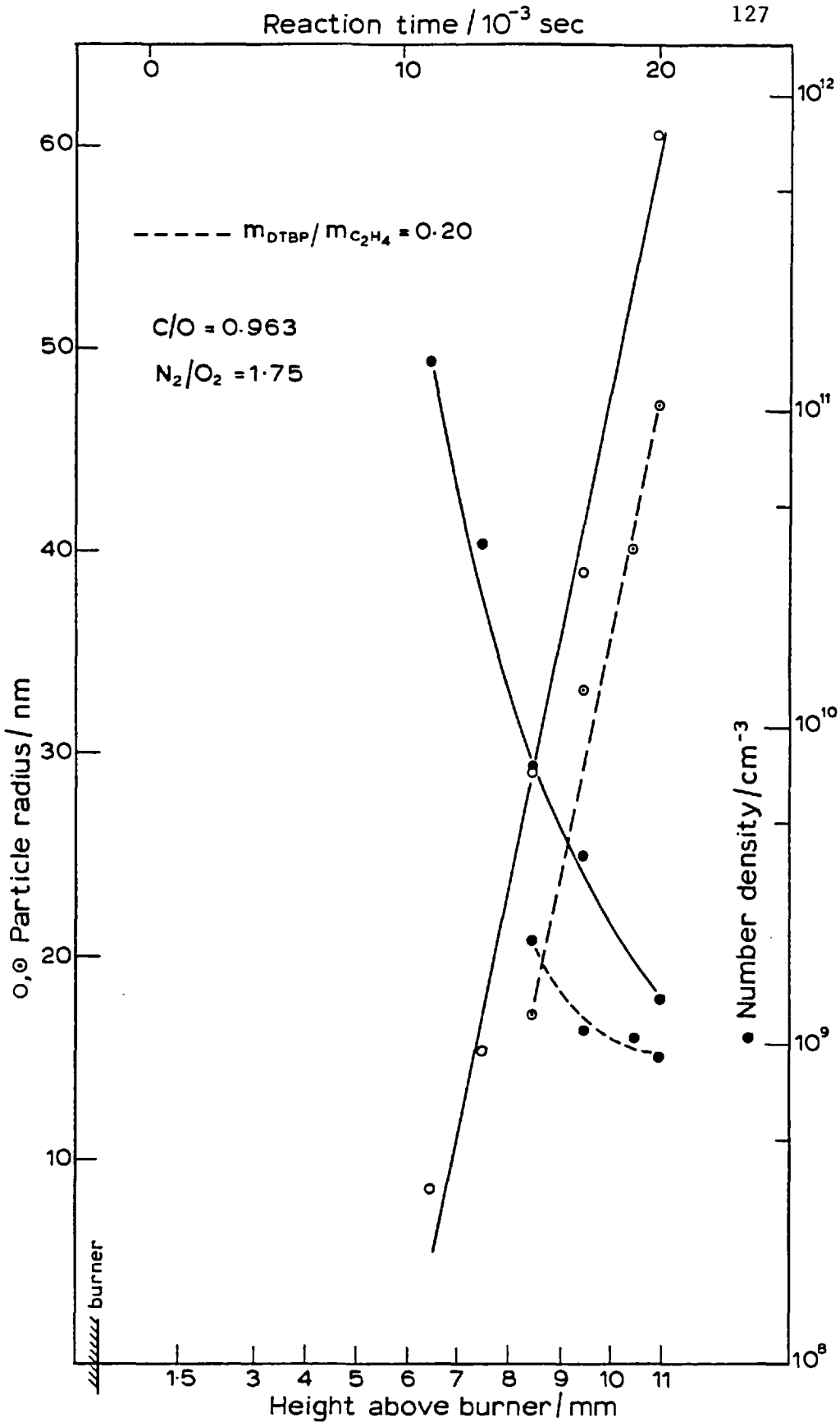

Fig. 46: Particle radius (positive slopes) and number density (negative slopes) as function of h. Full lines: no DTBP addition, corresponding to figs. 42 and 43. Dashed lines: 17 mass % DTBP in total fuel.

In order to obtain more experimental information from flames of different C/O ratios and DTBP/ethylene mass ratio, measurements were carried out for a constant N_2/O_2 ratio of 1.75 and a constant reaction time of 20 msec. The latter was estimated from the calculated flame temperatures T_F, the change in molenumbers during combustion and the inlet flow velocity v_o. For every condition (e.g. change of C/O ratio), the height above the burner, of the test space, was correspondingly adjusted to maintain t at 20 msec with reasonable reproducibility.

The effect of DTBP concentration was studied for flames of three C/O ratios: 1.00, 0.963 and 0.865. The particle absorption coefficients at 894.3 nm* are plotted againstDTBP/ethylene mass ratio in the bottom graph of Fig. 47. The $\epsilon_{\text{part. abs.}}$ and thus the soot volume fractions decrease linearly with DTBP/ethylene mass ratio for all three C/O ratios and become nearly equal for the highest DTBP concentrations. The logarithmic plot of the V_V scattering components (top graph of Fig. 47) shows their decrease with DTBP/ethylene mass ratio. The scattering from the leaner flame (C/O = 0.865) is higher than from the richer flame (C/O = 1.00), though the latter contains a higher soot volume fraction.

Fig. 48 shows the calculated soot particle radii and number densities evaluated from the corresponding results in Fig. 47. In the leaner flame the particle radius (and correspondingly the number density) is always higher (lower) than in the richer flames (see also Fig. 53). The particle radius decreases with increasing DTBP/ethylene mass ratio for all three C/O ratios. Most remarkable, however, is the finding that the number densities remain essentially constant (within a factor of two) for the three C/O ratios. The reduction in soot volume fraction by DTBP addition at t = 20 msec is therefore caused by a reduction in particle size. A higher DTBP/ethylene ratio than $\simeq$ 0.15 results only in a slighter decrease of particle radius compared to lower DTBP/ethylene ratios.

---

*The total extinction coefficients and the particle absorption coefficient at 488 nm are not reported here.

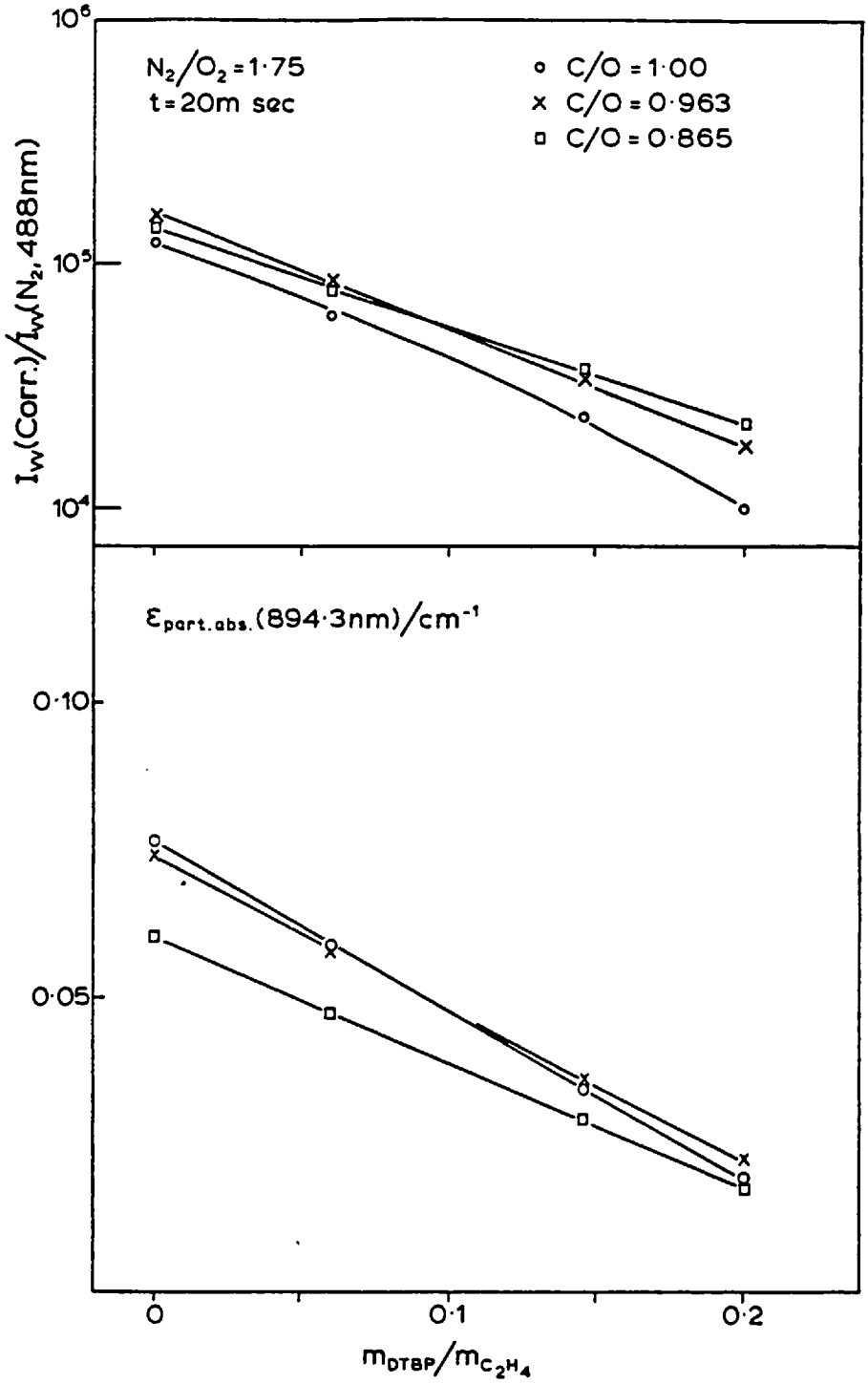

Fig. 47: Top part: V_V scattering component (with fluorescence contribution subtracted) and bottom part: particle absorption coefficient for three C/O ratios, N_2/O_2 = 1.75 and 20 msec reaction time as function of DTBP/ethylene mass ratio.

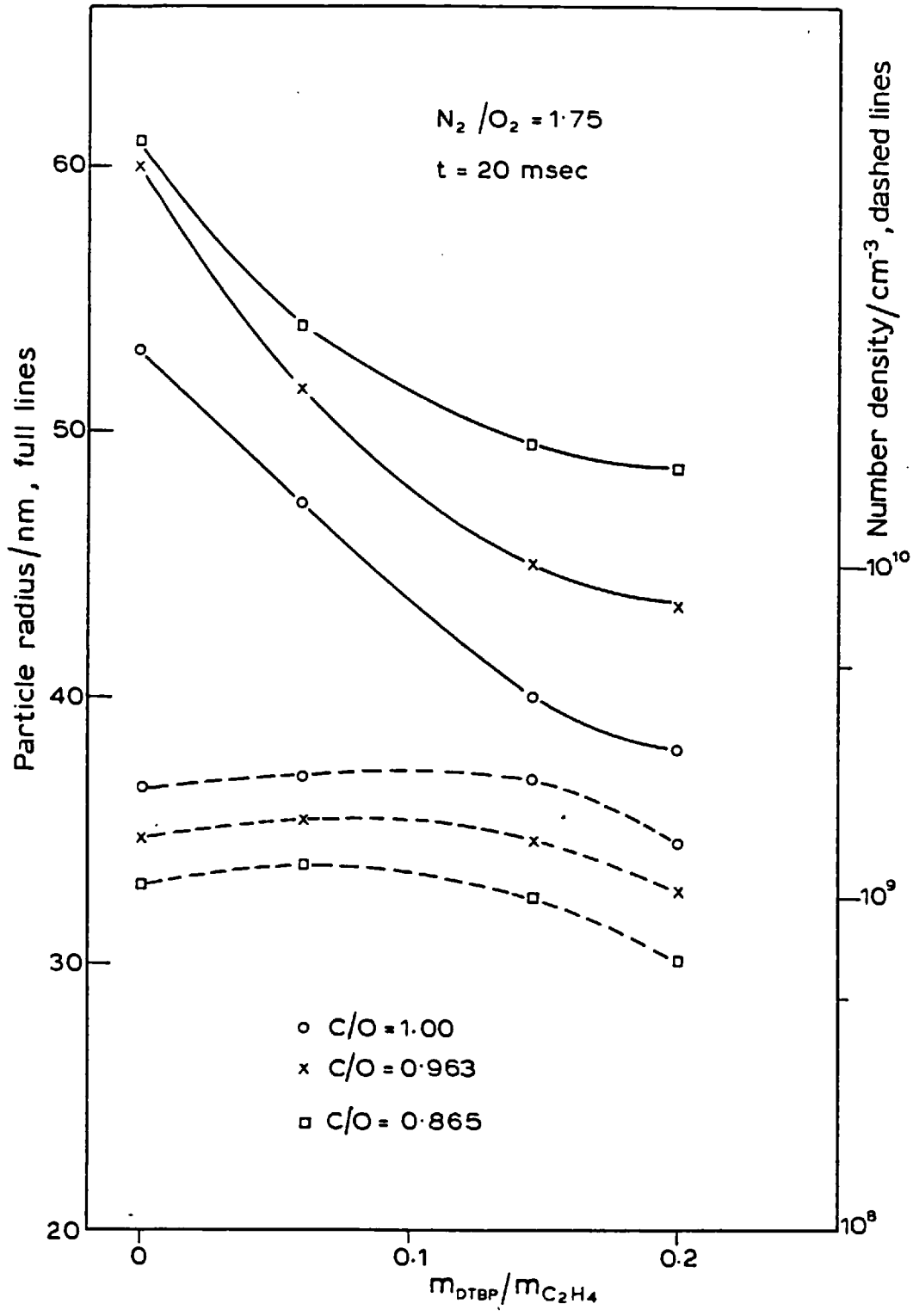

Fig. 48: Particle radius (full lines) and number density (dashed lines) for three C/O ratios, N_2/O_2 = 1.75 and 20 msec reaction time as function of DTBP/ethylene mass ratio. Corresponds to Fig. 47.

The same reaction time (20 msec) and N_2/O_2 ratio (1.75) was chosen for the experiments when varying the C/O ratio with and without DTBP addition. The results for the total extinction and particle absorption coefficients at 894.3 and 488 nm are plotted as function of C/O ratio in Fig. 49 for the flame without DTBP. All the ε values exhibit a clear maximum at C/O = 1, showing that the volume fraction ϕ reaches its maximum at C/O = 1. This C/O ratio is the critical ratio for solid carbon formation, calculated under the assumption of full thermodynamic equilibrium in the flame. This assumption is, of course, only justified for the stable water-gas flame compounds and not for the non-equilibrium soot formation process. However, it is quite interesting, that the maximum (particle) absorption and thus soot volume fraction occurs at this C/O ratio and in richer flames (C/O > 1) ε (and ϕ) go down. Also, Fig. 49 shows clearly the great discrepancy between the total extinction and particle absorption coefficient. This discrepancy is greatest for the high C/O ratios and becomes somewhat less for the leaner flames. The dependence of the scattering data (Fig. 50) on C/O ratio looks similar to the absorption data. There is also a distinct maximum in the V_V (Monochr.), V_V (LLS), H_V (Monochr.) and H_V (LLS), which occurs at C/O = 0.92. This shows that a maximum in ε (prop. to $N \cdot V$) does not imply a maximum in particle radius (V_V being prop. to $N \cdot V^2$). The peak in the V_V scattering at C/O = 0.92 and the lower particle absorption coefficient at C/O = 0.92 compared to C/O = 1.00 implies that the particle diameter does <u>not</u> reach a maximum at C/O = 1. The H_V (550 nm), representing the fluorescence, rises continually with C/O ratio from 3.8 at C/O = 0.8 to 9.5 at C/O = 1 and reaches a value of 11 at C/O = 1.5.

The measured data for the flames containing DTBP are shown in Figs. 51 and 52. In Fig. 51, the total extinction and particle absorption coefficients at 894.3 and 488 nm are plotted against C/O ratio for a DTBP/ethylene mass ratio of 0.146. Also shown is $\varepsilon_{\text{part. abs.}}$ (894.3 nm) versus C/O for a DTBP/ethylene mass ratio of 0.2. Again, there is a maximum in ε near C/O = 1, but this is shifted towards a somewhat lower value (C/O = 0.98) than for the case of no DTBP addition. The discrepancy between $\varepsilon_{\text{total}}$ and $\varepsilon_{\text{part. abs.}}$ is greater than for the flames without DTBP. This is caused by the fact, as already observed, that with DTBP addition, the particle absorption coefficient is lowered more strongly than the total extinction coefficient.

The scattering data for the flames containing DTBP are plotted versus C/O ratio in Fig. 52 for a DTBP/ethylene mass ratio of 0.146. The V_V scattering component from soot (with the fluorescence contribution subtracted) and the H_V (550 nm) values are also displayed for the DTBP/ethylene mass ratio of 0.2. Again, the V_V (Monochr.), V_V (LLS), H_V (Monochr.) and H_V (LLS) exhibit a peak near C/O = 0.92, on the leaner side of the maximum of ε in Fig. 51. The general dependence of the scattering data and ε on C/O ratio is thus similar to the flames without DTBP. The H_V (550 nm) (for DTBP/ethylene mass ratio 0.146) rises from 4.2 ar C/O = 0.85 to a maximum of 10.8 near C/O = 1.1 and then decreases again to a value of 3 for the highest C/O ratio of 1.59. This behaviour is different to the flames without DTBP, where the H_V (550 nm) was found to be independent of C/O ratio from C/O = 1.1 to 1.5. The reduction of the fluorescence by DTBP addition is stronger in the richer flames. The soot depolarisation ratios do vary somewhat with C/O ratio, especially for the DTBP containing flames. For the flames without DTBP ρ_v has values between $0.8 \cdot 10^{-3}$ and 10^{-2}. For the flames with DTBP, ρ_v varies from $5 \cdot 10^{-3}$ at C/O = 0.9 to $8 \cdot 10^{-3}$ at C/O = 1.1.

The determination of particle size and number density, using the results from Figs. 49-52, was carried out in the same way as already described (form. V-8). Fig. 53 shows the particle radius and number density versus C/O for the flames with and without DTBP. The number density N rises from 10^9 cm^{-3} at C/O = 0.8 to $6 \cdot 10^9$ cm^{-3} at C/O = 1.5. All the points obtained from the flames containing DTBP (DTBP/ethylene mass ratio = 0.146) are on the same curve as the points obtained from the flames without DTBP. For no peroxide addition, the particle radius exhibits a maximum at C/O = 0.95 and the particle radius decreases more rapidly for the richer than for the leaner flames. For addition of DTBP, the maximum in the particle radius a is shifted to a lower C/O ratio and a is always around 20% smaller than without DTBP.

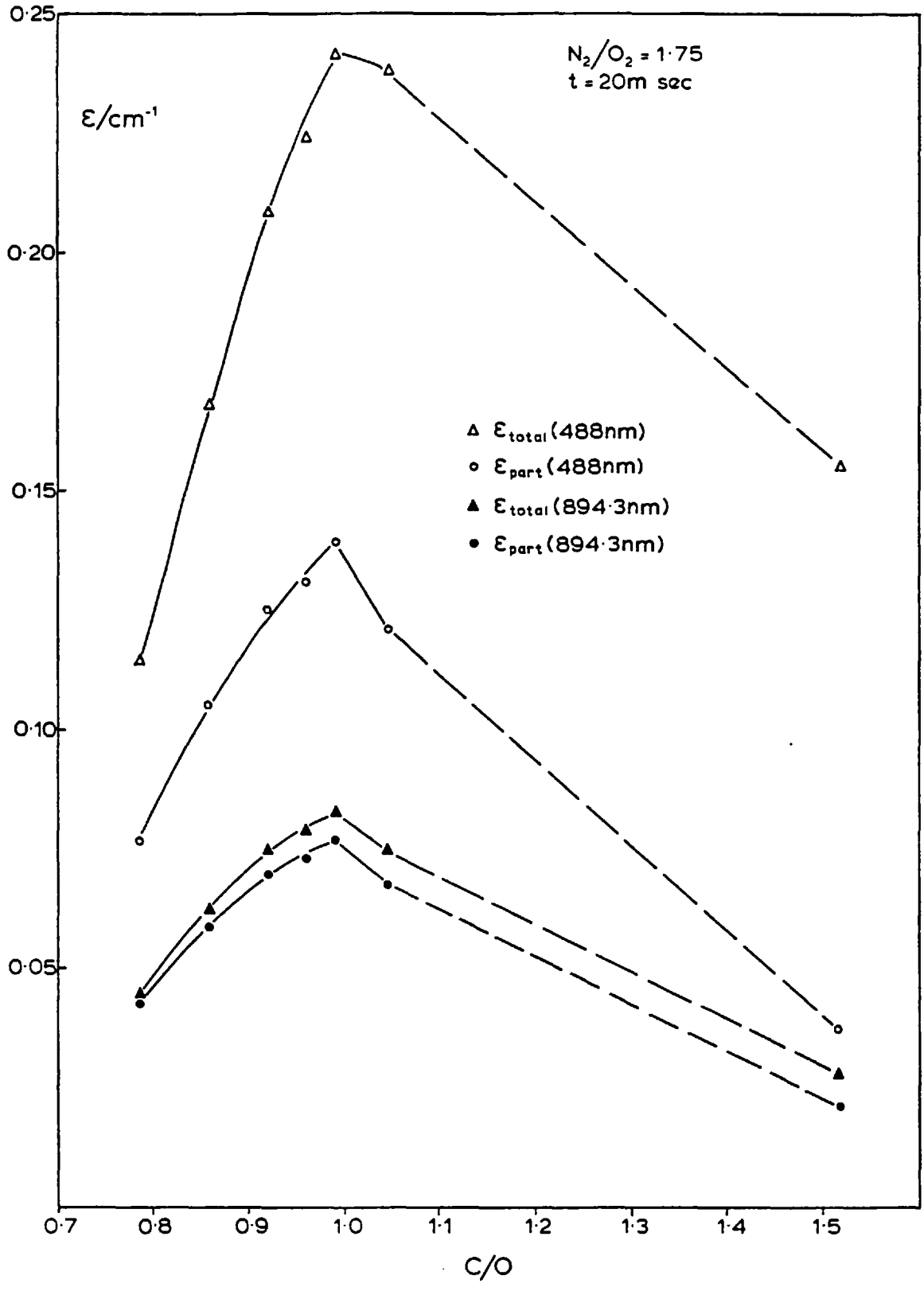

Fig. 49: Total extinction and particle absorption coefficients at 488 nm and 894.3 nm for N_2/O_2 = 1.75 and 20 msec reaction time as function of C/O ratio.

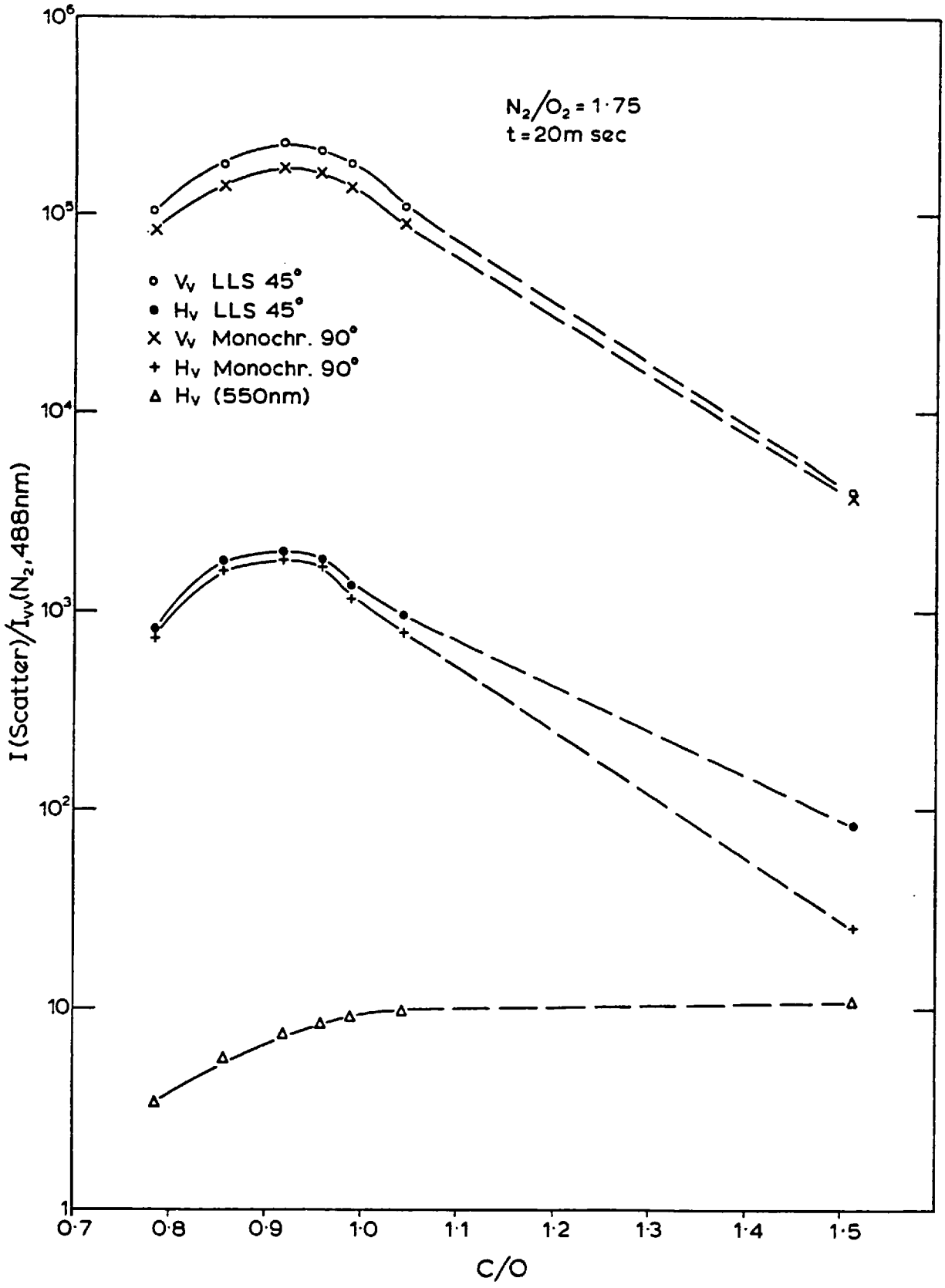

Fig. 50: Scattering data corresponding to fig. 49 as function of C/O ratio.

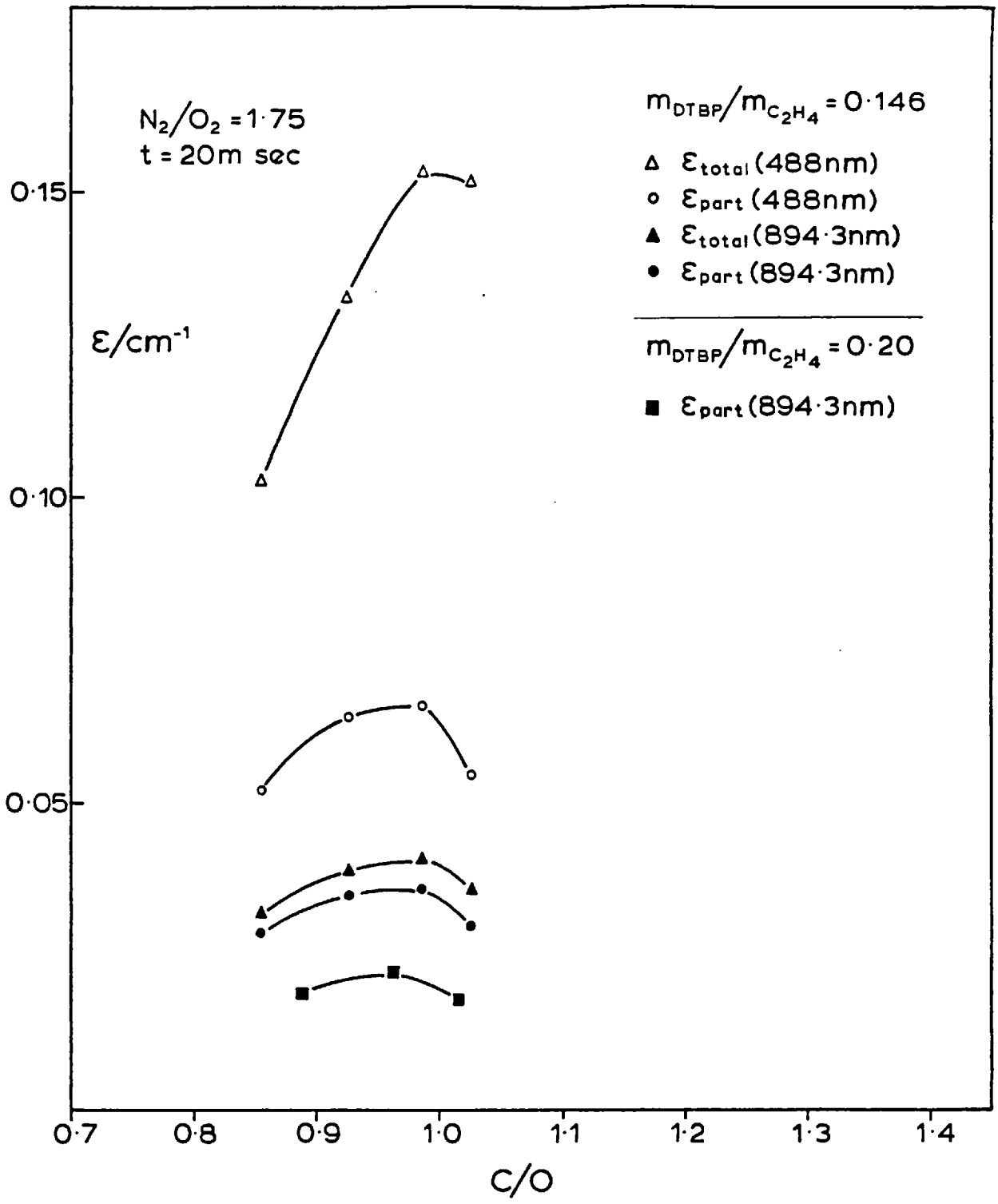

Fig. 51: Total extinction and particle absorption coefficients at 488 nm and 894.3 nm for N_2/O_2 = 1.75, 20 msec reaction time and DTBP /ethylene mass ratio of 0.146 (0.20) as function of C/O ratio.

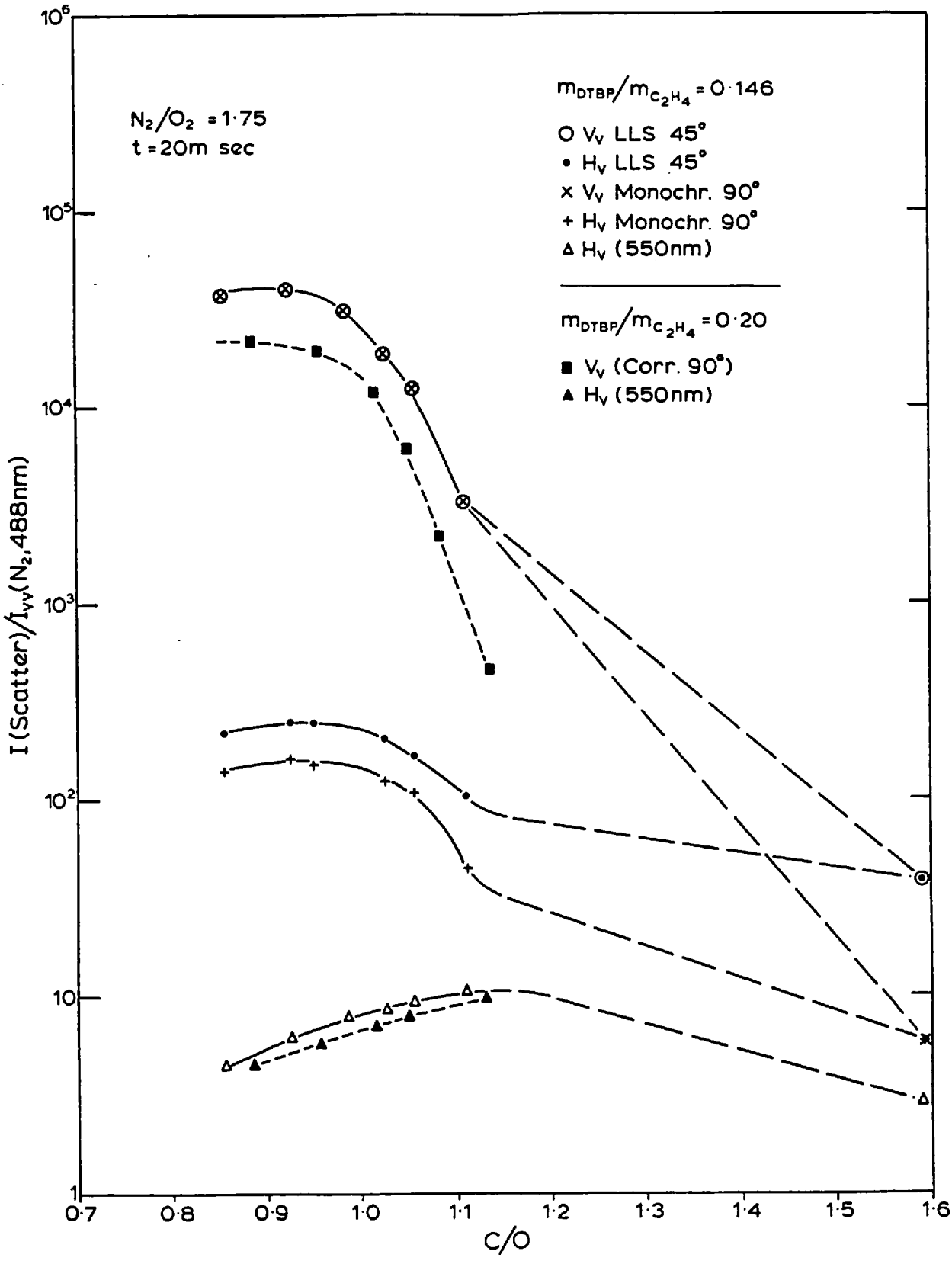

Fig. 52: Scattering data corresponding to fig. 51, as function of C/O ratio.

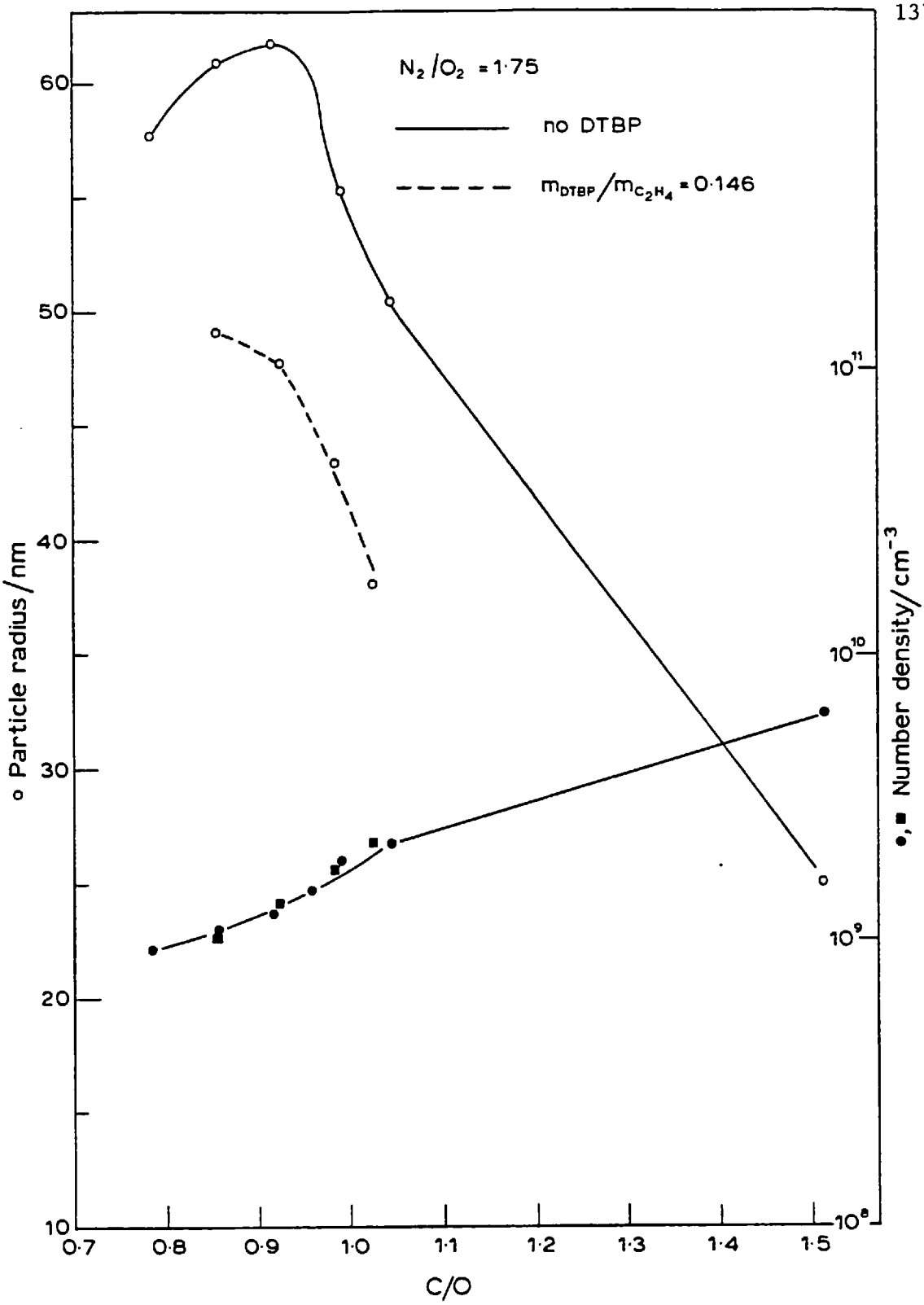

Fig. 53: Particle radius O and number density • for N_2/O_2 = 1.75 and 20 msec reaction time as function of C/O ratio. Full lines and • no DTBP present; dashed line and ■ DTBP/ethylene mass ratio 0.146.

V-3 'HOT PLATE' EXPERIMENT

To study the influence of small amounts of molecular and periodic oxygen on the pyrolysis of ethylene, the following experiment was designed. This is based on the counterflow of nitrogen diluted fuel against a flame. The previously described burner system (see Fig. 3) offered a very good opportunity to do this by using the top sinter tube to establish a flame upside down and the bottom sinter tube to let a gas (mixture) flow against this flame. In this system, the flow pattern is very similar to the pattern in a counterflow diffusion flame[141] and to the flow of a gas against a heated plate - hence the name 'Hot Plate' experiment. In addition, the established laser Rayleigh scattering technique allowed for the monitoring of the temperature in the gas counterflowing the flame (see also Chapter VII) - with certain constraints. The first problem that had to be resolved was to establish the best C/O ratio for the flame burning from the top part of the burner. The requirements for this flame were: its C/O ratio should be well below the critical C/O ratio for soot formation or production of fluorescing molecules and also it should not be lean enough for a second flame zone to be established. Also, in order to separate the top flame from the top sinter, it was diluted with nitrogen.

First experiments were carried out with a stoichiometric flame (products CO_2 and H_2O), with nitrogen-ethylene mixture in counterflow against it. For this case, a second flame zone with clearly visible blue emission was always established. This is presumably caused by still appreciable oxygen, HO, O and H radical concentrations in the 'burnt' gases. As this situation closely resembled a secondary counterflow diffusion flame, a change of C/O ratio in the top flame was required. It was found that, by increasing the C/O ratio in the top flame, the secondary flame zone became less and less distinct and vanished completely near C/O = 0.5. A flame of this C/O ratio can, by a first approximation, be assumed to yield mainly water and carbon monoxide as combustion products, as the rate of oxidation of CO to CO_2 by HO is well known to be slower than the rates of water production. Also, C/O = 0.5 is far enough away from the critical C/O ratio for soot formation (C/O = 0.6) for ethylene). All 'Hot Plate' experiments were carried out with a top flame of C/O = 0.5 and N_2/O_2 = 4.93, a burner separation of 16 mm and an outer nitrogen shield.

It was then possible to use laser Rayleigh scattering to determine the temperature profile in the gas counterflowing the flame. This was done by flowing pure nitrogen against the flame and measuring the Rayleigh V_V scattering intensity relative to nitrogen at room temperature (295 K). The results for two different nitrogen flow-rates are shown in Fig. 54α. The nitrogen flow-rates from the bottom burner were (at 295K, 1 bar) 20.4 cm^3/sec (23.6 mg/sec) for case a and 50.5 cm^3/sec (58.5 mg/sec) for case b. For the larger nitrogen flow-rate (b) the decrease in the relative Rayleigh scattering intensity is much less than for the lower flow-rate (a). Correspondingly, the temperatures are higher for case (a) than for (b).

When ethylene was added to the nitrogen flow from the bottom, similar measurements were carried out of the V_V scattering component. However, it was found that most of these measurements could not be employed for temperature determinations, using the relative differential scattering cross-section for the nitrogen-ethylene mixture (σ_r = 3.16). Above h = 3 mm, the values for the V_V scattering component became far too low, indicating a far too high temperature. This can be explained by the non-matched flow velocities from the bottom and top. The flame gases from the top flame emanate with a considerable momentum from the top flame, and hence the ethylene-nitrogen mixture becomes diluted with flame gas products of much lower scattering cross-section than ethylene. Hence we are not dealing with a pure ethylene-nitrogen mixture of known scattering cross-section and the temperature determination must fail. Also, it might be possible that some fragmentation of the ethylene occurs, leading to products of lower scattering cross-section than ethylene itself. Compared to that, for pure nitrogen from the bottom (when the flow velocities are also non-matched) the penetration of flame gases into the nitrogen is much less severe, as the scattering cross-section of the flame products has a value of σ_r = 1.08*, which is not much different from nitrogen (σ_r = 1). The final flame temperature for the top flame of T_F = 1860 K, using form. VII-2, indeed agrees with the calculated adiabatic flame temperature of 1880 K. As the transfer of flame gases into the counterflowing nitrogen stream could not be quantified, the

---

*obtained from detailed thermodynamic calculation of composition.

temperature profiles in Fig. 54α were calculated with assumption of pure nitrogen only being present. From h = 5 mm onwards, the temperatures are probably higher by a few percent.

Though the temperature profile in the ethylene-nitrogen mixture could not be measured directly from the V_V scattering component, it was possible to arrive at a good estimation. If one takes into account the different specific (molar) heat capacities of ethylene and nitrogen {$c_p(C_2H_4)/c_p(N_2) \simeq 2$ at 500 K and $\simeq$ 3 at 1000 K} and neglects the difference in the thermal conductivities, the temperature profile of the ethylene-nitrogen mixture comes out as very similar to case (b) in Fig. 54α.

The influence of combustion products from the top flame into the counterflowing mixture could have been minimised by strongly increasing the ethylene-nitrogen (or pure ethylene) flow-rate from the bottom. This was not done for two reasons. First, the large ethylene flows would have created a potential hazard - an explosive mixture in the laboratory or the extraction system. Secondly, the conditions could have been no longer comparable to the counterflow diffusion flame experiment (see section V-4).

In spite of the failure of directly obtaining the temperature in the ethylene-nitrogen (and additive) mixtures from the V_V scattering measurements, the latter could still be used to judge the presence of soot particles with a radius larger than 1 nm and a number density around 10^{13} - 10^{14} cm^{-3}. As we have seen before, a better criterion for the presence of a significant soot volume fraction is the (particle) absorption coefficient. Therefore the absorption was monitored.

In order to detect any reaction towards larger molecules in the ethylene-nitrogen (+ additive) mixtures, fluorescence measurements at 550 nm were carried out in the same way as already described, but with higher sensitivity. First, a mixture of ethylene (12.5 cm^3/sec , 14.7 mg/sec) and nitrogen (15.4 cm^3/sec, 17.8 mg/sec) was studied (295 K, 1 bar). Under these conditions, no fluorescence could be detected at all, even with the highest sensitivity of the detection apparatus, which was around $10^{-4}\sigma_{VV}(N_2)$ - see also the measurements of the nitrogen Raman vibrational cross-section (Table 6b). As much TBHP as possible was added to the same mixture, also

showing no detectable fluorescence*. When DTBP, which vapourises much faster than TBHP, was added to the mixture a very low level of fluorescence could be detected - (c) in Fig. 54β. Addition of small amounts of oxygen produced the same effect (d), (e) in Fig. 54β - the fluorescence intensity increasing with increasing oxygen concentration. Most interesting is the very similar shape of the H_V (550 nm) curves against h. All three curves exhibit a maximum. The decrease in H_V (550 nm) beyond the maximum can only partly be explained by the decreasing gas density with increasing h. If the temperature profile (b) in Fig. 54α were used to normalise the fluorescence intensity for the same gas density, the maxima in Fig. 54β are shifted by ≈ 1 mm to the right and the curves become nearly symmetrical. For the case of DTBP addition, the additional heat release is too small to cause a change in temperature in the ethylene-nitrogen mixture. The onset of fluorescence occurs in a temperature region of 600 - 800 K, where the half-life time of DTBP changes rapidly from a few milliseconds to below 10^{-5} sec. (see also Table 1). This explains why no fluorescence was detected below h = 4.5 mm, as the DTBP decomposition rates are not fast enough in that region.

For the case of oxygen addition, fluorescence is detected at h = 2.5 mm. Although the rise in H_V (550 nm) is presumably less than for DTBP addition, it is still quite rapid. If we again assume the temperature profile (b) in Fig. 54α, the highest rate of increase in H_V (550 nm) would correspond to a temperature of only ≈ 400 K, which is certainly too low. The reason for this is that, for both cases of oxygen addition the heat released by reactions of ethylene and oxygen can no longer be neglected in the region near to the bottom sinter and hence the temperature starts to rise earlier than in (b), Fig. 54α. Calculating the temperature under the assumption of all available oxygen being used up for the production of carbon monoxide and hydrogen, we get a temperature rise of 310 K for case (d) and 520 K for case (e). This temperature increase was also indicated by the stronger decrease in the observed V_V scattering component with oxygen addition compared to the pure ethylene-nitrogen mixture.

---

*This is caused by the too small amounts of available oxygen in the total mixture. With the existing system the TBHP concentration could only have been increased by heating the saturator, which was avoided for obvious safety reasons.

For all conditions, there was no indication at all of soot particle formation. Neither did the V_V scattering component increase, nor was absorption detectable at any stage.

The main result of the 'Hot Plate' experiment is that for a temperature regime below 1600 K the formation of fluorescing molecules (radicals) from ethylene is associated with the presence of oxygen (or oxygen containing radicals). The maxima in Fig. 54β are an indication that the reactions leading to the fluorescing molecules require radical initiation. If we assume that all oxygen is used up near the height above the bottom sinter, corresponding to the maximum in H_V (550 nm), the decline of H_V (550 nm) beyond the maximum can then be explained by the decomposition rate of the fluorescing molecules becoming faster (at the higher temperature nearer to the top flame) than their formation rates. This interpretation is also favoured by the results from the counterflow diffusion flame experiments (see Figs. 56, 59), where the H_V (550 nm) rises continuously in the fuel region. For that case the flame zone of the counterflow diffusion flame provides a steady flow of radicals into the fuel, the radical concentration being highest near the flame zone. The suggestion that oxygen and oxygen containing radicals initiate the radical reactions leading to large fluorescing molecules is also supported by the finding that in the pure ethylene-nitrogen mixture, counterflowing the top flame, no fluorescence was detected. In spite of the uncertainty of the temperature estimation, the temperature reached in the fuel should only be about 200 - 300 K, lower than in the fuel region of the counterflow diffusion flame. However, there is no indication of reaction towards larger molecules in the pure ethylene-nitrogen mixture. As the formation of the fluorescing molecules is always associated with soot formation (see section V-1,2) this implies that, below 1600 K soot formation requires the presence of oxygen. In comparison, it should be noted here that, at temperatures around 2000 K and higher, soot particles (and large absorbing molecules) are formed from aromatic fuels without oxygen being present[91].

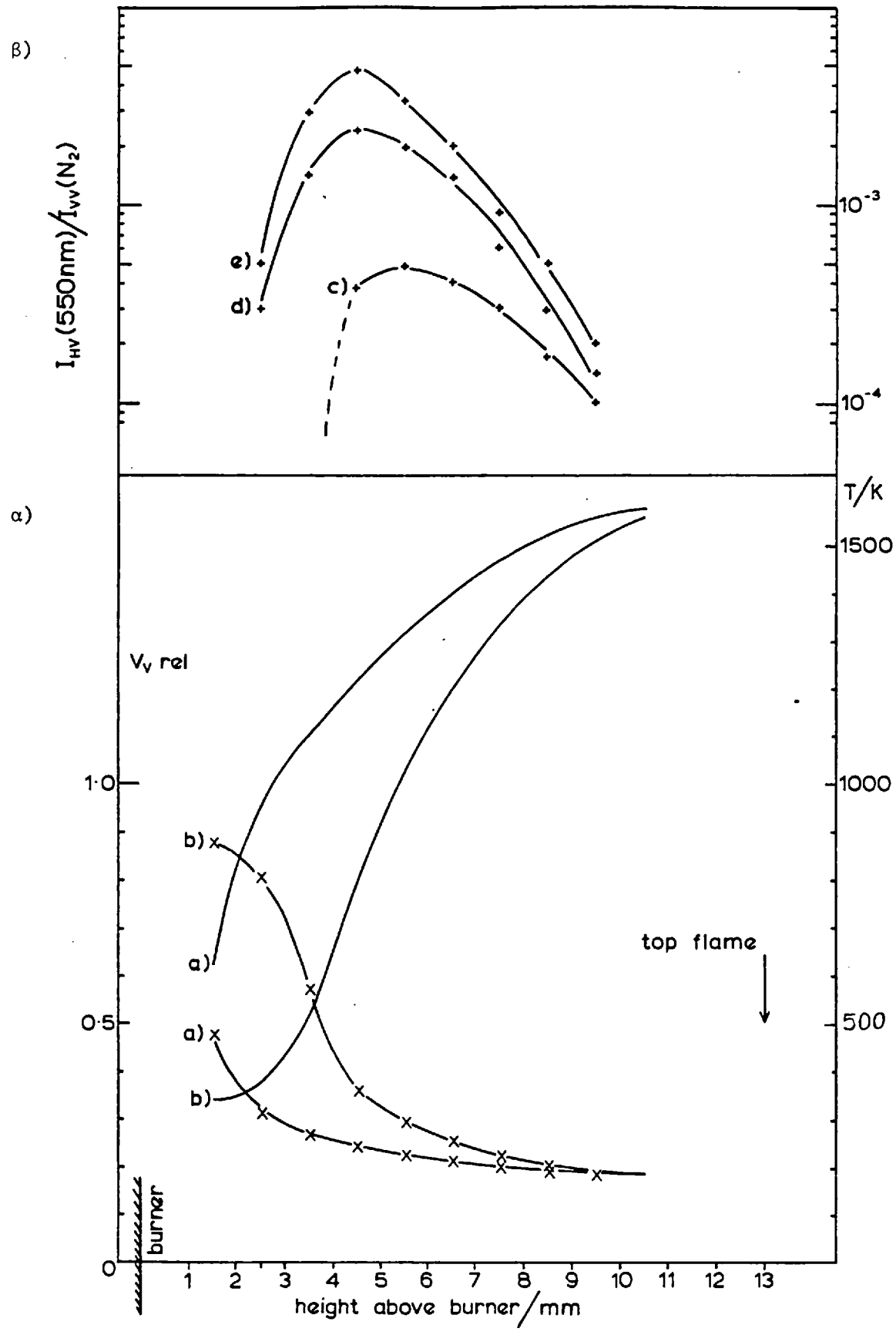

Fig. 54: 'Hot Plate' experiment (see over).

Fig. 54: (see previous page)

'Hot Plate' experiment. Nitrogen diluted flame with C/O = 0.5, N_2/O_2 = 4.93, v_o = 6.92 cm/sec, v_f = 47.5 cm/sec and T_f = 1880 K burning from the top of the burner shown in fig. 3.

α) V_V Rayleigh scattering x and temperature profile (full lines) as function of h. Nitrogen flow from bottom part of burner:-

a) $v_o(N_2)$ = 2.89 cm/sec,

b) $v_o(N_2)$ = 7.14 cm/sec.

β) Fluorescence intensity (relative to $I_{VV}(N_2)$) as function of h with DTBP or O_2 added to N_2-C_2H_4 mixture ($\dot{m}_{N_2}$ = 17.8, $\dot{m}_{C_2H_4}$ = 14.7 mg/sec).

c) $\dot{m}_{DTBP}$ = 0.205 mg/sec, C/O = 40.9,

d) $\dot{m}_{O_2}$ = 1.94 mg/sec, C/O = 8.62,

e) $\dot{m}_{O_2}$ = 3.66 mg/sec, C/O = 4.58.

V-4 SOOT MEASUREMENTS IN COUNTERFLOW DIFFUSION FLAMES

With the burner system employed very stable counterflow diffusion flames[141] could be produced. Ethylene is a specially suitable fuel for this type of flame, its density being virtually the same as nitrogen. In order to match the flow velocities from the top and bottom parts of the burner, the ethylene (introduced from the bottom) was always diluted with nitrogen and, correspondingly, the mixture from the top consisted of oxygen and nitrogen, usually richer in oxygen than air. The burner separation distance was set at the maximum, that was dictated by the essential requirement to obtain a stable flame. A burner separation of 11.5 mm was found to give stable flames. The bottom and top flow velocities were then always set in a way to maintain the flame half-way between the two burners.

The flame system was used to obtain information about the following parameters: i) size and number density of soot particles;

ii) anisotropy of soot particles;

iii) dependence of the fluorescence intensity;

iv) effect of TBHP and DTBP addition on (i) - (iii).

As regards (i) the main difference to the premixed flames described above is that in the very thin region of highest soot concentration in the counterflow diffusion flame, the simple approach of Rayleigh scattering and absorption theory can no longer be applied. The V_V scattering component from that flame region exhibits a strong influence on the scattering angle. This behaviour shows that particles of a size well beyond the Rayleigh limit are present. Other authors have reported a similar dependence of the V_V scattering pattern and have used Mie theory (see Chapter III) to evaluate the mean (spherical) soot particle size and, from an absolute intensity calibration, the particle number density[78-81]. However, Mie theory can only be applied for spherical particles (of arbitrary size). Electron-micrographic analysis has shown that soot particles older than 20 - 30 msec are irregular (anisotropic) aggregates[64,66]. As the aggregation could well be caused by the sampling process itself, it was regarded as desirable to monitor any agglomeration process of soot particles in situ. For this reason, light scattering measurements in this work were extended to obtain the depolarised components. Mie theory predicts the H_H (90^0) component

to be no longer zero, as it is in the Rayleigh approximation. However, if the particles were spherical, V_H and H_V should always be zero, even for a sphere larger than the Rayeigh limit. These two scattering components therefore provide a sensitive test, of whether particles are anisotropic. To be able to detect true particle depolarisation, possible interference by fluorescence had to be taken into account.

Jones[129] has predicted that, for chains of spherical Rayleigh particles of volume V, the i_1 and intensity function can always be matched by the i_1 Mie intensity function for an 'equivalent' sphere of volume V_s. However, the volume of the equivalent sphere is given by $V_s \approx n^6 V$ for a long chain of n particles and by $V_V \approx n^3 V$ for a cluster. The equivalent sphere size obtained from Mie theory would therefore be much larger than the volume of the aggregate. Also this theory predicts some dependence of V_H and H_V on scattering angle and an invalidation of the reciprocity theorem - V_H no longer equals H_V except at 0^0, 90^0 and 180^0 scattering angle. A solution to this question was attempted by measuring the full scattering pattern of the V_H and H_V components as accurately as possible.

Fig. 55 shows a typical polar diagram of all four scattering components from the region of maximum soot concentration in a counterflow diffusion flame. There seems to be a slight deviation of the H_V and V_H components with scattering angle. However, one has to bear in mind that, because the measurements at different scattering angles require time and the relevant flame region is so thin, even the smallest flame fluctuation can cause considerable error. Hence it is not possible at this stage to decide whether H_V and V_H change with scattering angle.

The V_V and H_H scattering components could well be matched with i_1 and i_2 Mie intensity functions; the best fit was obtained for a refractive index near m = 1.54 - 0.56i (see Appendix 2), leading to a ('equivalent sphere volume') particle radius of a = 78 nm and a particle number density of $N_{sca} = 3.4 \cdot 10^8$ cm^{-3}. The number density is calculated from (see also Table 4)

$$N_{sca,soot} = \frac{I_{VV}(soot)}{I_{VV}(N_2)} \cdot \frac{i_1(N_2) \cdot N_{N_2,room}}{i_1(soot)} \qquad V\text{-}9$$

for any scattering angle. This (Mie) particle radius corresponds to an extinction cross-section of $2.97 \cdot 10^{-10}$ cm^2, and, with the measured extinction coefficient of 0.110 cm^{-1}, we obtain $N_{ext} = 3.7 \cdot 10^8$ cm^{-3}

according to

$$N_{ext,soot} = \varepsilon_{ext}/C_{ext} \qquad V\text{-}10$$

It is quite surprising that there is such good agreement between the number density and size obtained from fitting the Mie intensity functions to the scattering pattern and the number density obtained from the measured extinction coefficient, using the Mie extinction coefficient for the particle size.

Before the problem of size and number density determination, using Mie theory, is discussed further, some other results are to be described. Fig. 56 shows the vertical dependence of V_V (LLS), H_V (LLS), V_V (Monochr.), H_V (Monochr.) and H_V (550 nm) in the centre line of a counterflow diffusion flame. Both V_V components rise very rapidly between h = 4.5 and h = 6.5 mm, accompanied by a similar rapid rise of the H_V components from h = 5.5 to h = 6.5 mm. On the oxidant side, there is a strong decrease in all scattering components. The fluorescence component H_V (550 nm) rises more gradually and reaches its maximum value near the region of maximum particle scattering. Most important is that the H_V (550 nm) is about 10 - 20 times less than in the rich premixed flames described in section V-1,2 and is comparable to the H_V (550 nm) from the leaner flame with C/O = 0.704 (see Fig. 40). In spite of this, the fluorescence could very well be seen by the naked eye in the fuel region of the counterflow diffusion flame, as no flame emission is present in that region. The consequence of the low fluorescence intensity is, that when measuring the extinction coefficient in the visible, the molecular contribution is only small, though not completely negligible.

In order to carry out extinction measurements in the counterflow diffusion flame, the Cs lamp system could not be used successfully, as its spatial resolution was not sufficient. The extinction was therefore measured on the laser wavelength , using the high spatial resolution of the focused beam to its full advantage. The results for the particle absorption coefficient (subtracting the small molecular contribution from the total extinction coefficient) are plotted in Fig. 57. ε shows a rapid increase on the fuel side and a more rapid increase on the oxidant side. One has to note here that, though the flame appears to be sooting much more heavily than a rich premixed flame, the soot volume fraction is actually higher in e.g., a premixed flame of C/O = 1, t = 20 msec than in the counterflow

diffusion flame. This effect is caused by the much larger particles emitted from the counterflow diffusion flame, compared to the premixed system.

The results reported in Figs. 56 and 57 were used to evaluate the soot particle size and number denstiy (see Fig. 58). In the early region, between h = 5 and 6 mm, Rayleigh theory could be applied, whereas around h = 6.5 mm, Mie theory was used. The number density decreases rapidly from $2 \cdot 10^{13}$ cm^{-3} at h = 5 mm to $4.5 \cdot 10^{8}$ cm^{-3} at h = 6.5 mm. Correspondingly, the particle radius rises from 1.5 nm, to 84 nm. On the oxidant side, we can observe a rapid decrease in particle size, whereas the number density remains essentially constant. The deviations in number density at h = 7 and 7.5 mm can be explained by errors in the absorption coefficient. For that flame region, the laser beam also passes twice through the outer layer of large soot particles. This contribution to the extinction was taken into account for the extinction coeff. at h = 7 and 7.5 mm, but the errors involved in the necessary subtration of the attenuation of the beam in the outer soot layer from the measured attenuation could be quite high. Hence the estimation of oxidation rates of soot particles from the decrease in particle radius in the oxidation region can only be assumed to be accurate to an order of magnitude.

The effect of addition of the two peroxides was assessed in the following way: the region of maximum soot concentration in the flame was selected for the measurements, which were taken for different distances y from the centre line of the burner. Scattering measurements at different scattering angles and extinction measurements were then carried out for DTBP or TBHP replacing fuel from the bottom or being added to the top, oxidant, side. To compare the latter measurements, it was also required to study a flame where an amount of ethylene, equivalent to the amount of peroxide, was added to the oxidant side. The scattering measurements at different angles were then used to obtain the (equivalent sphere volume) particle radius from Mie theory and the number density from the absolute intensity calibration. The extinction coefficients were used to check the results, which are given in Table 8. Generally, the soot volume fration ϕ decreases with distance from the centre line, e.g. from $1.2 \cdot 10^{-6}$ (y=0) to $5 \cdot 10^{-7}$ (y=2 cm) for case (a) in Table 8. This can easily be explained by the dilution of the soot particles caused by the radial flow structure in the flame. The dilution effect to some extent, is only counteracted by

additional soot formation along the horizontal y coordinate.

Both peroxides, if added to the fuel, cause an increase in soot particle volume and number density. This is the case for all three positions. The soot volume fraction ϕ is, compared to (a),increased by a factor of 1.7 (b) and of 1.25 (e). If the peroxides are added to the oxidant side, particle size and number density are reduced. This corresponds to a decrease in ϕ, compared to (a), by a factor of 0.45 (c) and of 0.75 (f). Taking the smaller concentration of TBHP compared to DTBP into account, it follows that TBHP, added to the fuel side, promotes soot formation more strongly than DTBP but, when added to the oxidant side, counteracts soot formation more strongly than DTBP. However, the observed effects are not very large for both peroxides.

As in the results obtained from Fig. 55, the use of the measured extinction coefficients for the number density (see form. V-10) always gives about 5-10% higher values for N, than those in Table 8. This can be interpreted by the extinction cross-section for a particle agglomerate (or more generally an anisotropic particle), being always larger than for a spherical particle of the same volume. The question as to whether the chain model, put forward by Jones[129], could explain this quantitatively, cannot be answered here.

Although the application of Mie theory seems to give a fairly consistent interpretation, especially when observing changes in a system, caused by an additive, there can be no doubt that a better theory is required to interpret in situ light scattering and absorption data from soot particles during their later stage of formation. This becomes quite apparent from the measurements of the soot particle polarisation ratios, again carried out in the region of highest soot concentration in the counterflow diffusion flame. The values for ρ_V(soot) as function of distance from the burner centre line are plotted in Fig. 59b with and without DTBP present in the fuel. The depolarisation ratios are higher than for the premixed flames and increase with increasing y. For the case of DTBP present in the fuel, ρ_V is always higher than without DTBP, although the (Mie) particle volume is only about 10% larger (see Table 8a,b). The steady increase in depolarisation ratio with distance from the centre line is a good indication that, in this case, we are dealing with shape anisotropy rather than with anisotropy of refractive index. Taking the depolarisation ratio and its increase as a measure of the extent of agglomeration of the soot particles, we can

now apply the Rayleigh scattering approximation for a spheroid, to obtain the axial ratio of the particle. This is, of course, only justifiable because of the lack of a more accurate theory for the scattering from a realistic soot agglomerate and the impracticability of the more rigorous scattering theory for a spheroid of arbitrary size[137]. The assumption of oblate spheroids for the soot agglomerate would lead to very high axial ratios (see Table 3b). The assumption of prolate spheroids, on the contrary, gives quite reasonable values for the axial particle ratio. The axial ratio rises from 2.4 (y=0) to 3.3 (y=2 cm) for the flame without DTBP and from 2.9 (y=0) to 3.9 (y=2 cm) for the flame containing DTBP. These axial ratios compare quite well with findings from electronmicrographic shape analyses[64, 66] and leave a very good indication that non-spherical soot agglomerates actually exist in the flame and are not necessarily an artifact of the sampling process.

To study the effect of DTBP on the fluorescence intensity, the vertical dependence of H_V (550 nm), when DTBP was present on the fuel side, was compared to the case of no DTBP being present in the flame. These results are shown in Fig. 59a. The H_V (550) is slightly higher on the fuel side for the case of DTBP presence than without DTBP. However, this is mainly caused by the slight shift downwards ($\simeq \frac{1}{2}$ mm) of the region of highest soot concentration for the DTBP containing flame. In comparison to the premixed flame (see Figs. 43, 45) DTBP causes no considerable effect on the fluorescence intensity.

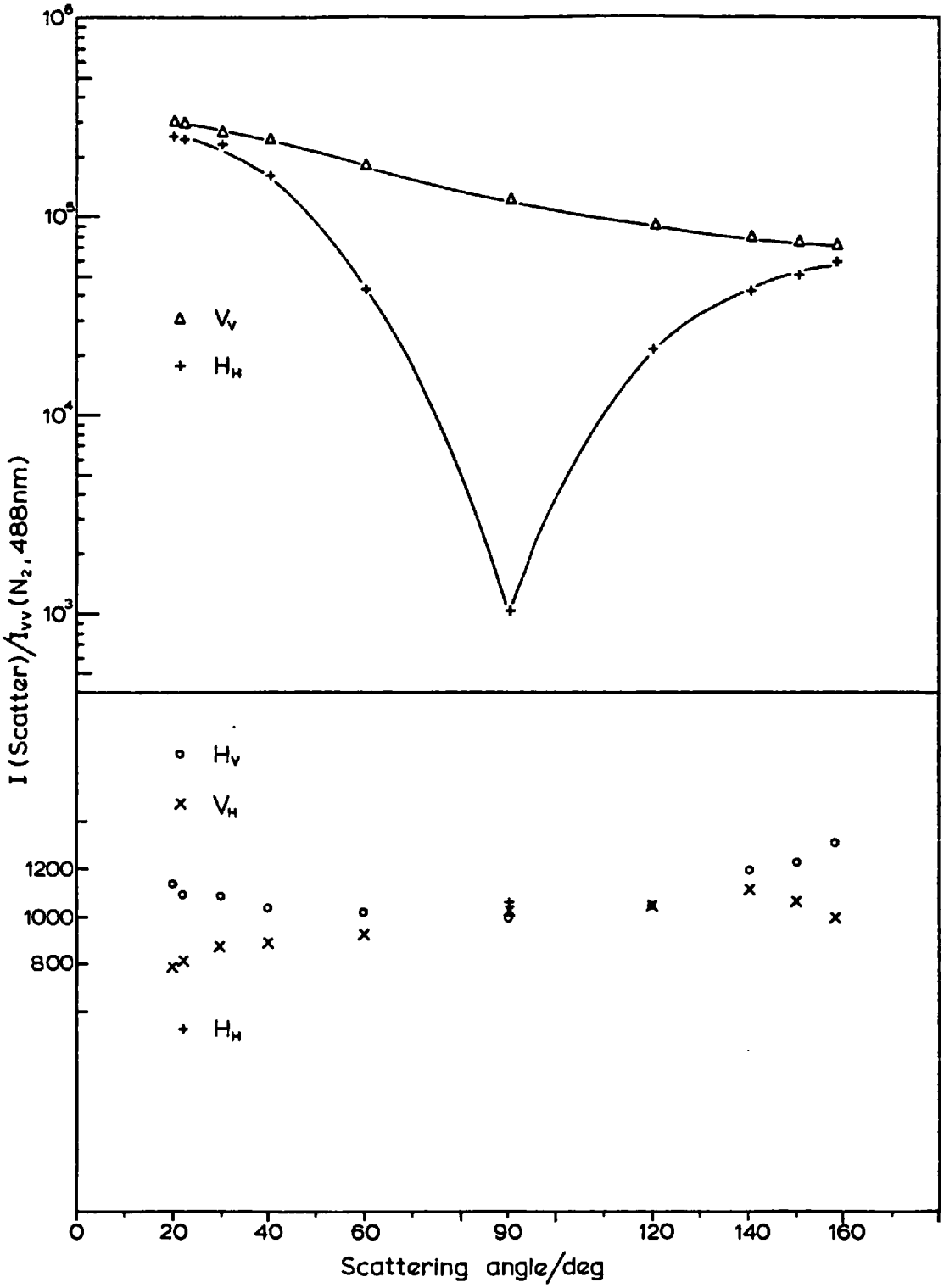

Fig. 55: Typical full polar diagram from region of maximum soot concentration in counterflow diffusion flame; $\dot{m}_{C_2H_4}$ = 11.2, $\dot{m}_{N_2}$ = 16.6; $\dot{m}_{O_2}$ = 9.64, $\dot{m}_{N_2}$ = 21.6 mg/sec.

Top graph: V_V and H_H scattering components.

Bottom graph: Depolarised scattering components H_V and V_H (and H_H (90^0). The fluorescence contribution is negligible.

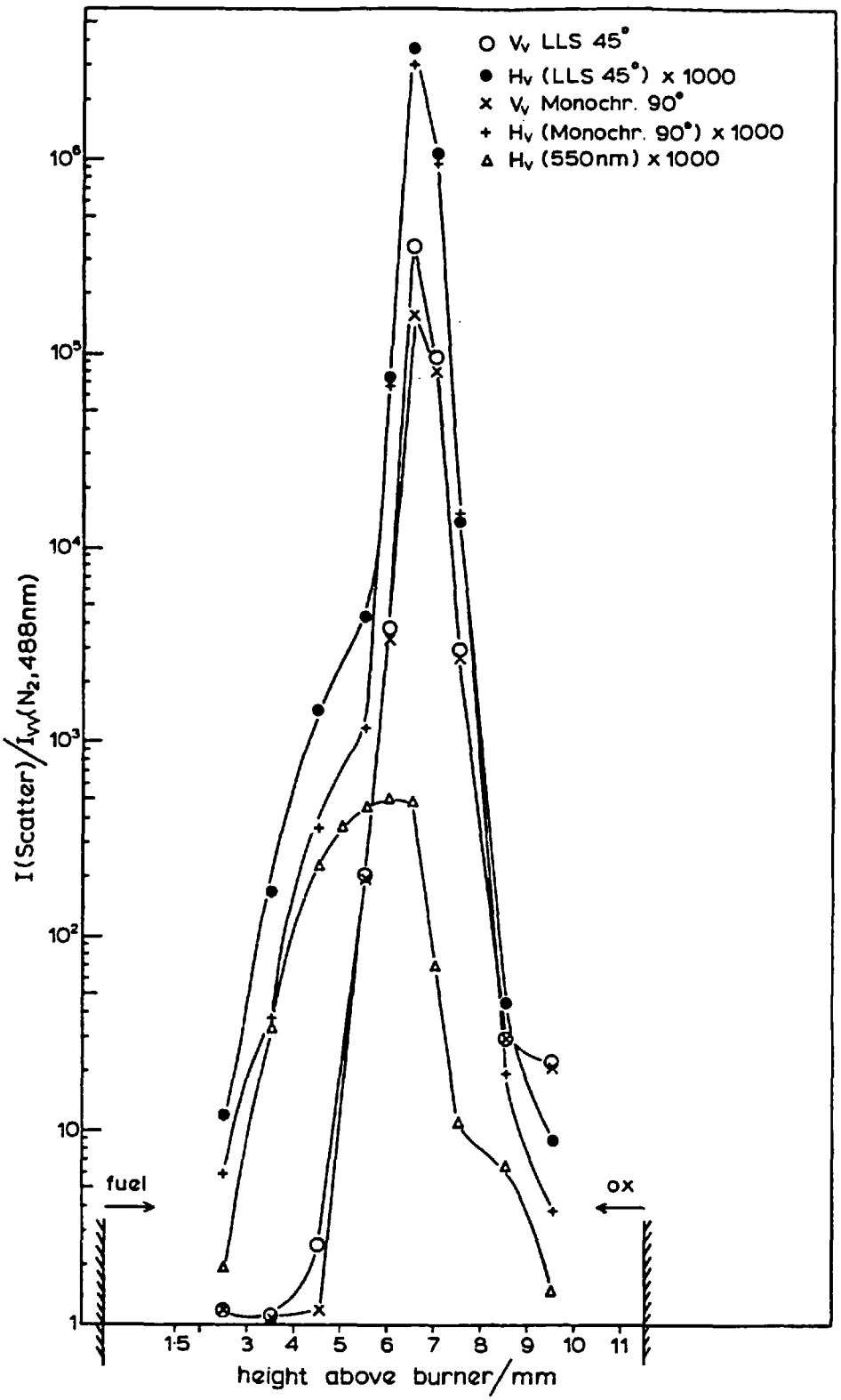

Fig. 56: Vertical dependence of scattering components from counterflow diffusion flame of $\dot{m}_{C_2H_4}$ = 11.5, $\dot{m}_{N_2}$ = 29.6 and $\dot{m}_{O_2}$ = 15.1, $\dot{m}_{N_2}$ = 16.5 mg/sec in the centre of the burner. Note that the values for H_V (LLS), H_V (monochromator) and H_V (550) are multiplied by 1000.

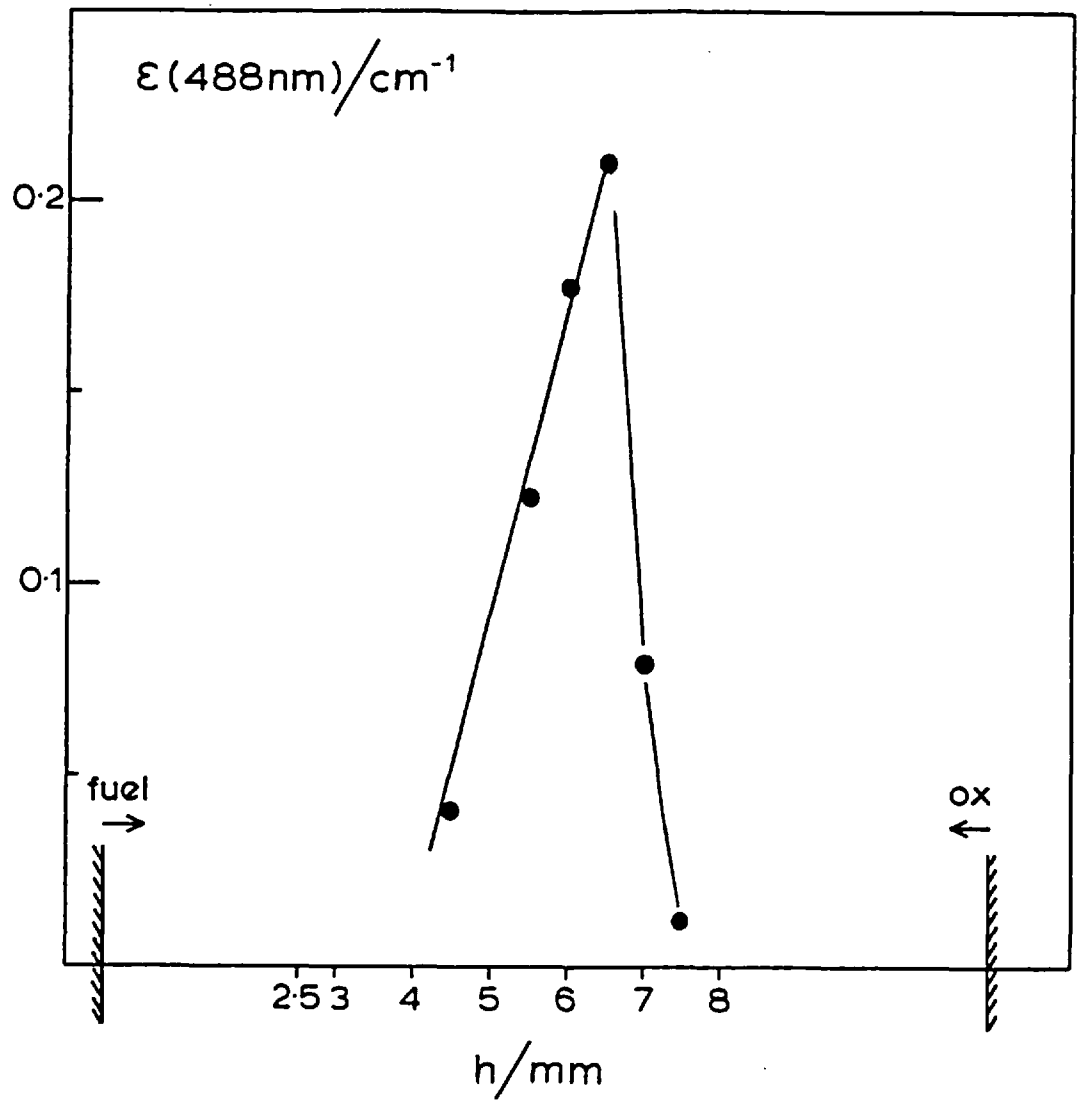

Fig. 57: Particle absorption coefficient at 488 nm as function of h, corresponding to fig. 56. Note that the total extinction coefficient is only slightly higher, as the fluorescence intensity and therefore absorption from molecules (radicals) is small.

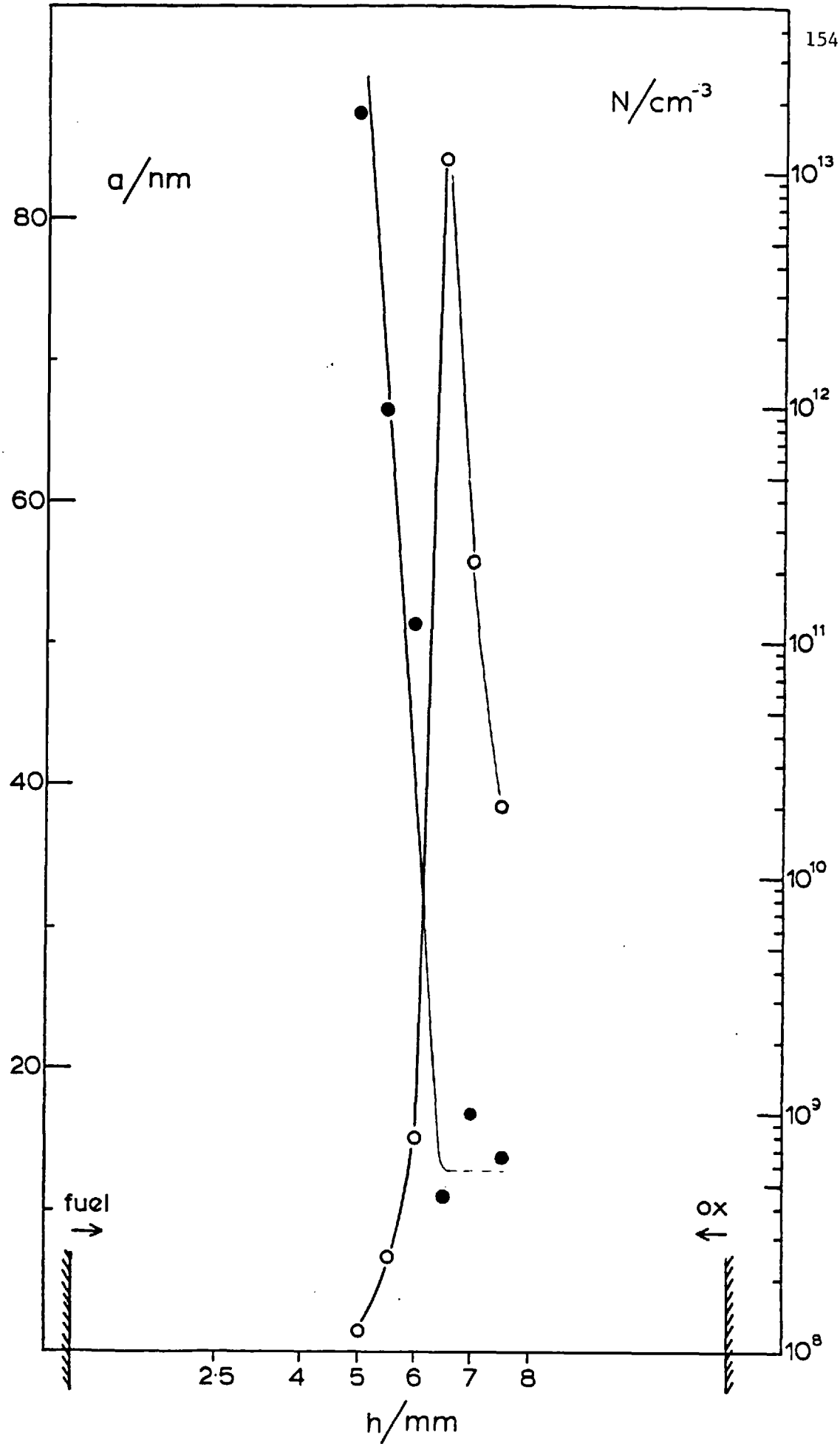

Fig. 58: Particle radius O and number density ● as function of h, Corresponding to figs. 56 and 57.

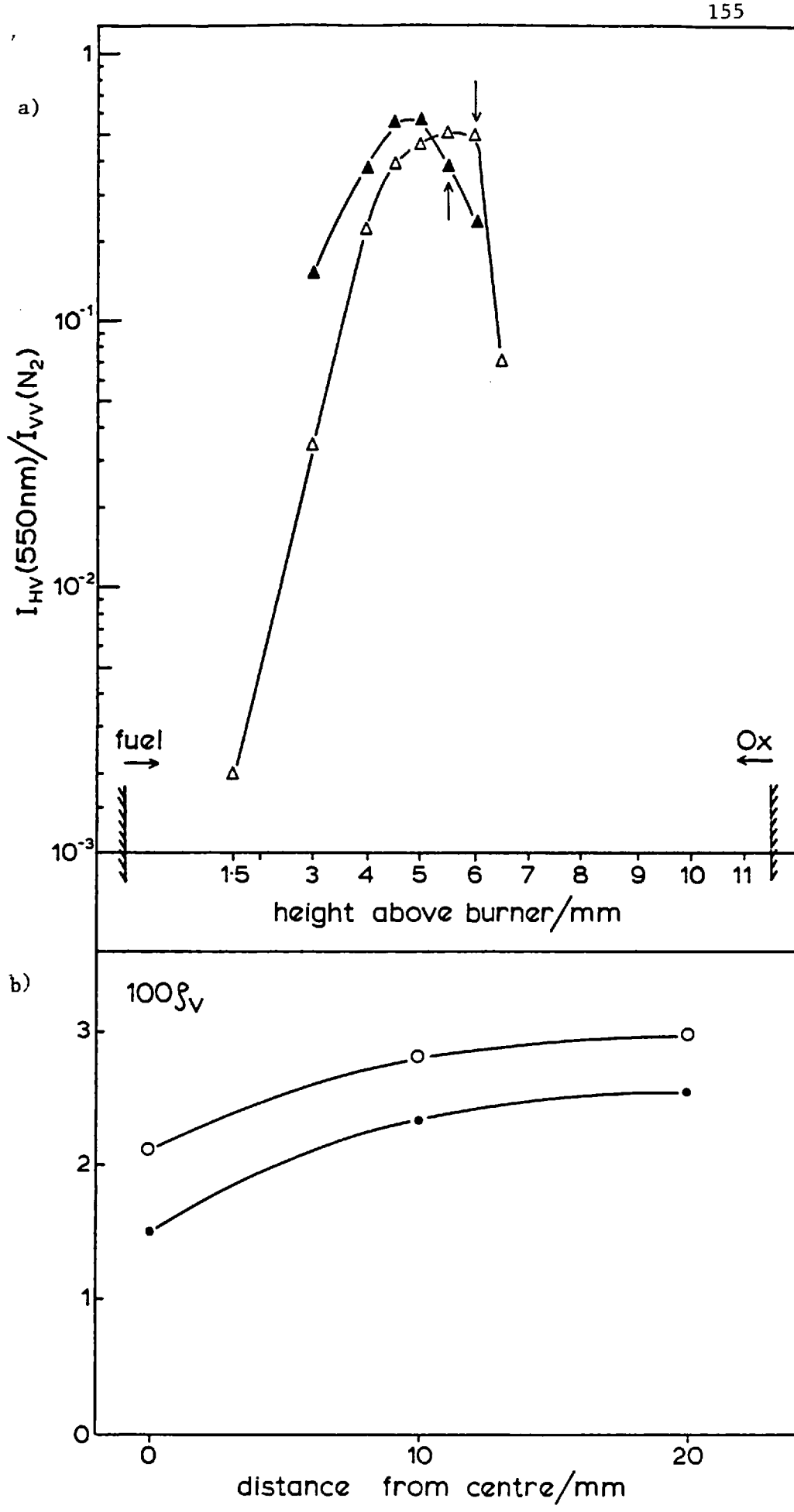

Fig. 59: see over

Fig. 59: Counterflow diffusion flame:

a) Fluorescence intensity as function of h and

b) particle depolarisation ratio ρ_V in the region of highest soot volume fraction as function of distance from the burner centre line.

Δ, ● without DTBP addition; Δ,O with DTBP/ethylene mass ratio 0.20.

Flame data $\dot{m}_{fuel}$ = 10.5 mg/sec

$\dot{m}_{N_2}$ = 27.8 mg/sec

$\dot{m}_{O_2}$ = 15.8 mg/sec

$\dot{m}_{N_2}$ = 16.2 mg/sec

The arrows in (a) denote maximum soot volume fraction.

TABLE 8: Soot particle radius and number density obtained from Mie theory (m = 1.54 - 0.56i) for different distances y from the burner centre line. The amount of peroxide contained in the system is always given as mass ratio of peroxide/ethylene, independent, whether the peroxide was added on the fuel or the oxidant side. For flame data see Fig. 59.

Experiment	Bottom	Top	$m_{per}/m_{C_2H_4}$	y = 0		y = 1 cm		y = 2 cm	
				a/nm	$N/10^{-8}$ cm^{-3}	a/nm	$N/10^{-8}$ cm^{-3}	a/nm	$N/10^{-8}$ cm^{-3}
(a)			-	84	4.8	86	3.3	90	1.6
(b)	DTBP		0.20	86	7.0	90	5.0	93	2.6
(c)		DTBP	0.15	78	3.3	77	2.0	78	1.0
(d)		C_2H_4		82	5.2	85	3.4	91	1.6
(e)	TBHP		0.043	84	6.4	87	4.1	90	2.0
(f)		TBHP	0.033	80	4.2	81	2.5	82	1.3

(d) contains an amount of ethylene from the top equivalent to the amount of DTBP in (c).

VI DISCUSSION AND INTERPRETATION OF RESULTS

Fluorescence spectra and molecular depolarisation ratios

The lack of band structure in the fluorescence spectra described in Section V-1 shows quite clearly that the molecules causing the fluorescence consist of a large number of atoms. Most probably, these molecules are polycyclic aromatic hydrocarbons (or radicals). A definite answer cannot be given here as to which PCAH's are present, but the dependence of $\varepsilon_{molecule}$ on wavelength (see Fig. 19), the fairly high fluorescence efficiency of 11% and the axial ratio of ≃ 10 derived from the Rayleigh depolarisation ratio, suggest that we are probably dealing with a mixture of PCAH's, each containing more than 10 benzene rings. Improvements in the assignment of the most likely PCAH's can probably be made by more detailed studies of the absorption spectra, also in the UV, and by exciting the fluorescence at different laser wavelengths, using a tunable laser.

Depolarisation ratios of soot particles

For the premixed flames studied the depolarisation ratio measurements always yield (in low resolution) values between $5 \cdot 10^{-3}$ and 10^{-2} for the soot particles, when these are still in the Rayleigh regime. The high resolution measurements of ρ_V, which gave a value of $\rho_V = 5 \cdot 10^{-3}$, are certainly much more reliable than the low resolution measurements. In any case, the associated axial ratio of $1.5 < a/b < 2$ (for the prolate spheroid assumption) associated with $5 \cdot 10^{-3} < \rho_V < 10^{-2}$ seems to be too high not to be detectable by electronmicrographic size analysis. Also, for each flame studied, ρ_V is apparently constant, considering all the errors, once it can be measured. Hence the depolarisation of the scattered light from the early soot particles is most likely to be caused by anisotropy of refractive index rather than shape, the particles being (nearly) spherical. The opposite is the case for the late soot particles as present in the counterflow diffusion flame. The significant growth of ρ_V with time and the larger values of ρ_V compared to the premixed flames strongly indicate an agglomeration process causing mainly anisotropy of shape. As the axial ratios obtained from Rayleigh theory agree quite well with mean axial ratios from electronmicrographic size analysis, the suggestion that the early (spherical) soot particles, given enough time, agglomerate in the flame, into non-spherical aggregates, is strongly supported.

Hot Plate pyrolysis

The experiments on ethylene pyrolysis in the presence of small quantities of DTBP or oxygen show that in the low temperature regime (around 600-800 K), reaction towards PCAH compounds proceeds only when oxygen or oxygen containing radicals are present. In these experiments, no soot particles could be detected. This does not necessarily mean that none are present, as the experimental set-up was only suitable to detect a light intensity loss of not much less than 1%. It would be very interesting to repeat these experiments using multipass absorption to increase sensitivity. This may then lead to the possibility of studying the formation of the earliest soot nuclei. However, this is probably quite a difficult experiment to carry out.

Also, it would be an improvement on the 'Hot Plate' system, if the mixing of the top flame gases with the counterflowing gas could be overcome, in order to use Rayleigh scattering temperature measurements to their full advantage.

Determination of soot particle size and number density

In this work, it has been demonstrated that by obtaining the absorption coefficient for the PCAH molecules, which are simultaneously present with soot particles, from a measurement of their fluorescence intensity, the correct absorption coefficient for the soot particles can be obtained. The latter is unambiguously proven by the wavelength dependence of $\varepsilon_{abs.\ part.}$ which strictly obeys Rayleigh's $1/\lambda$ law (see Fig. 26). The absorption from molecules also explains the $(1/\lambda)^n$, $n < 1 < 2$, dependence of the total extinction coefficient, using the experimental dispersion coefficient n. However, the use of n to obtain information about the size distribution of the soot particles[149], leads to severe errors - an overestimation of the number of soot particles outside the Rayleigh limit, as the molecular contribution to the extinction is not taken into account. If there exists a significant soot particle size distribution, containing enough particles outside the Rayleigh size limit*, this could be demonstrated by a deviation

*It has to be noted here, that if there exists a size distribution with all the particles being in the Rayleigh limit, the $1/\lambda$ law would still hold.

of the particle absorption coefficient from the $1/\lambda$ law. The result would be a $(1/\lambda)^{n'}$ dependence of $\varepsilon_{abs.\ part.}$, and the n' would indeed contain information about the particle size distribution. As a real n' has not been observed in this work, it is not required to go into the details of how to calculate the size distribution from n'.

It should be noted that the method of obtaining the molecular absorption coefficient from fluorescence measurements could further be improved upon by always measuring the fluorescence at several wavelengths instead of only one. This would also allow monitoring of possible small changes in the fluorescence efficiency and make the method of obtaining $\varepsilon_{abs.\ part.}$, whose principle has been demonstrated here, even more accurate.

If the total extinction coefficient at λ = 488 nm is used, instead of the particle absorption coefficient for the determination of particle size and number density, considerable errors are bound to occur. Typical errors for a premixed flame around C/O = 1 are

$$a\ (\text{using } \varepsilon_{total}) = 0.87\ a\ (\text{using } \varepsilon_{abs.\ part.})$$

$$N\ (\text{using } \varepsilon_{total}) = 2.2\ N\ (\text{using } \varepsilon_{abs.\ part.}).$$

Errors of this magnitude would occur in all flame regions.

If the total extinction coefficient in the infrared is used instead of the particle absorption coefficient, the errors incurred are much less - ≈ 2 - 3% for a, 20 - 40% for N. For some applications errors of this magnitude might be neglected.

Coagulation of soot particles

Several authors have treated the coagulation of soot particles in the collisional controlled limit as the 'free molecule' regime[67, 89, 95]. This should hold true if the particles were to stick together with every collision (no activation energy) and if there were no forces present, enhancing the collision rate, e.g., electrostatic or dispersion forces. More important is the requirement for the Knudsen number to be larger than 10, i.e. the

mean free path length of the gas surrounding the particle must be at least ten times the particle radius a. For nitrogen as the surrounding gas and a temperature of 1800 K, this leads to the requirement of $a < 50$ nm and, for 1300 K, to $a < 36$ nm. These requirements are certainly fulfilled in the early regions of the flames described here. The collision (and hence coagulation) rate is then given (for particle number density N) as

$$\frac{dN}{dt} = -Z\,N^2$$

where Z is the collision frequency multiplied by the unit volume. This leads to[89]

$$\frac{dN}{dt} = -\frac{1}{2}\left(\frac{3}{4\pi}\right)^{1/6}\left[\frac{6kT}{\rho}\right]^{\frac{1}{2}}(4\cdot 2^{\frac{1}{2}})\,\phi^{1/6}\,N^{11/6} = -k_1\,\phi^{1/6}\,N^{11/6} \qquad \text{VI-1}$$

Here, k is the Boltzmann constant, ρ is the density of the particle (1.8 g/cm for soot), $4\cdot 2^{\frac{1}{2}}$ is the collisional integral and instead of having the particle volume (mass) explicitly in eq. VI-1, it has been replaced by the more suitable volume fraction ϕ.

Values of k_1 are given below as function of temperature

T/K	1300	1400	1500	1600	1700	1800	1830
$10^9 \cdot k_1$	1.72	1.79	1.85	1.91	1.97	2.03	2.04 $cm^{5/2}\,msec^{-1}$

To account for collision enhancement forces or a possible activation energy barrier, decreasing the coagulation rate, a factor G is introduced into eq. VI-1.

$$\frac{dN}{dt} = -k_1\,G\,\phi^{1/6}\,N^{11/6} \qquad \text{VI-2}$$

Similarly, for the rate of volume increase for an individual particle we obtain

$$\frac{dV}{dt} = k_1\,G\,\phi\,V^{1/6} + \frac{V}{\phi}\,\frac{d\phi}{dt} \qquad \text{VI-3}$$

If ϕ is constant, the second term in eq. VI-3 is zero, and both equations can easily be integrated[89]. However, the experimental results described in Chapter V show an increase (in $\varepsilon_{abs.\ part.}$ and hence) in ϕ for reaction times below 20 msec. If, in good approximation, we take the rise in ϕ to be linear, we can describe ϕ as $\phi = A \cdot t + \phi_o$. Equations VI-2 and VI-3 can then be solved with the boundary conditions $\phi = \phi_o$, $V = V_o$ and $N = N_o$ for $t = 0$.

The solutions are:

$$N(t) = \{N_o^{-5/6} + \frac{5}{7}\frac{k_1}{A} G[(At + \phi_o)^{7/6} - \phi_o^{7/6}]\}^{-6/5} \qquad \text{VI-4}$$

$$V(t) = (At + \phi_o)\{\left(\frac{V_o}{\phi_o}\right)^{5/6} + \frac{5}{7}\frac{k_1}{A}[(At + \phi_o)^{7/6} - \phi_o^{7/6}]\}^{6/5} \qquad \text{VI-5}$$

The values for A and ϕ_o for the different experiments are summarised in Table 9.

When either eqs. VI-2, 3 or VI-4, 5 are used for the interpretation of the results for the particle size and number density, it is easily established, that the factor G is usually not equal to one, a finding which has been reported by other authors[67,91,95]. However, although the factor G is always larger than 1 for the flames without TBHP or DTBP, it is found that G has values below 1 in the region of flames containing peroxide (N around 10^{13}) of very high particle number density.

To obtain G, the integrated equation VI-3 could be used, but it was found to be more convenient to use the differential equation VI-2 itself, avoiding the approximation $\phi = At + \phi_o$.

G is then given by (using form. III-21, $\phi = f\varepsilon$)

$$G = -\frac{d(\ln N)}{dt} \cdot \frac{1}{k_1 f^{1/6} \varepsilon^{1/6} N^{5/6}} \qquad \text{VI-6}$$

The values obtained for G are given in Table 10.

TABLE 9

Values for A and ϕ_o, taking the dependence of the total soot particle volume fraction ϕ as $\phi = At + \phi_o$. Where appropriate, ranges for the linear approximation of ϕ are given in terms of h - height above burner and t - reaction time. For flame conditions, see the respective figures.

Figure	$10^8\phi_o$	10^7A/msec	h/mm	t/msec
30	6.16	1.12	4.5 - 6.5	7.0 - 11.0
30	51.0	1.68	6.5 -10.5	11.0 - 19.0
30	6.16	1.48	4.5 -10.5	7.0 - 19.0
32	7.04	1.33	3.5 - 9.5	5.0 - 17.0
35	10.6	0.359	6.6 -11.4	14.0 - 26.0
37	11.4	0.484	6.6 -11.4	14.0 - 26.0
40	6.16	0.16	11.5 -13.5	23.3 - 27.8
41	8.8	0.16	11.5 -13.5	23.3 - 27.8
42	14.1	1.04	5.5 -11.0	9.0 - 20.0
44	2.64	3.3E-3	6.5 - 8.5	11.0 - 15.0
44	4.4	0.70	8.5 -11.0	15.0 - 20.0
57*	38.4	2.5	4.5 - 6.5	0.0 - 6.6

*The temperature assumed just below the flame zone was 1800 K.

TABLE 10

Values for G as function of h - height above burner, t - total reaction time and Δt - residence time difference from the point in the flame where particles could first be detected. Also given are the total number densities and the ratio N_o/N.

a) no additive - Fig. 34

h/mm	t/msec	Δt/msec	N/cm^{-3}	N_o/N	G
5.5	9	0	5.8E10	1	3.3
6.5	11	2	2.2	2.6	5.4
7.5	13	4	1.0	5.8	5.7
8.5	15	6	7.1E9	8.2	3.4
9.5	17	8	6.1	9.5	1.9
10.5	19	10	5.7	10.0	1.2
11.5	21	12	5.4E9	10.7	≈1

b) TBHP addition - Fig. 34

5.5	9	0	8 E12	1	0.16
6.0	10	1	1.9E12	4.2	0.45
6.5	11	2	3.6E11	22	1.7
7.5	13	4	4.1E10	195	5.5
8.5	15	6	1.5	550	5.0
9.5	17	8	9.7E9	825	2.4
10.5	19	10	9.0E9	890	0.64

c) no additive - Fig. 39

h/mm	t/msec	Δt/msec	N/cm^{-3}	N_o/N	G
6.6	14	0	4.6E10	1	6.2
7.4	16	2	1.8	2.6	12
8.2	18	4	7.2E9	6.4	25
9.0	20	6	3.4	13.5	31
9.2	22	8	2.1	22.4	27
10.6	24	10	1.5	31.7	26
11.4	26	12	1.1E9	40.7	21

d) TBHP addition - Fig. 39

8.5	18.8	0	1.6E13	1	0.15
8.9	19.8	1	1.7E12	9.4	0.98
9.3	20.8	2	2.2E11	7.3E1	5.3
9.7	21.8	3	5.0E10	3.2E2	7.9
10.1	22.8	4	2.0E10	8.0E2	12.6
10.9	24.8	6	5.9E9	2.7E3	20
11.3	25.8	7	4.1E9	3.9E3	19

e) no additive - Fig. 40b

11.5	23.3	0	2.8E10	1	11
12.5	25.5	2.2	7.8E9	10	18
13.5	27.7	4.4	4.2E9	18.5	13

f) TBHP addition - Fig. 41b

11.5	23.3	0	5.8E11	1	2.7
12.5	25.5	2.2	2.1E10	27.6	15.4
13.5	27.7	4.4	5.5E9	106	24

g) no additive - Fig. 46

h/mm	t/msec	Δt/msec	N/cm^{-3}	N_o/N	G
6.5	11	0	1.45E11	1	2.9
7.0	12	1	5.8E10	2.5	5
7.5	13	2	2.8	5.2	7
8.5	15	4	7.7E9	18.8	16
9.5	17	6	3.4	42.6	19
10.5	19	8	1.85	78.4	25
11.0	20	9	1.4E9	104	28

h) DTBP addition - Fig. 46

8.5	15	0	2.1E9	1	49
9.0	16	1	1.5E9	1.36	43
9.5	17	2	1.2E9	1.75	36
10.5	19	4	9.8E8	2.14	14
11.0	20	5	9.2E8	2.28	9

i) counterflow diffusion flame*, no additive - Fig. 58

5	0	2E13	1	0.14
5.5	1.7	1E12	20	0.8
6	3.4	4E10	5E2	11
6.5	5.0	4.5E8	4.4E4	-

*assumed temperature - 1800 K

The significance of these results is that, in the flame region, where the particle radius is small and correspondingly the number density is very high (see (b) in Table 10) not every collision results in particle coalescence. This implies that these very small particles still behave like reacting molecules - with a certain activation energy required for coalescence. It would be too speculative here to estimate the activation energy as this could only be done successfully when studying flames of the same composition but different flame temperatures - a task which would have gone well beyond the scope of this work.

Conversely, when the particle becomes larger, and thus number density becomes smaller, their coagulation rate becomes larger than the non-enhanced collision rate (G=1) for the free molecule regime. This can be explained by electrostatic forces[66], caused by charging of the particles[113-114] and by dispersion forces[66,89]. When the particles are small (N high), electrostatic and dispersion forces seem to be insignificant and one could draw the conclusion that soot particle charging does not occur in the earliest stage of their formation.

Most interesting are the results for G in (h) - Table 10 - which show a very large value for G, decreasing from 49 to 9 for Δt = 5 msec. Although a fully consistent explanation cannot be presented here, one can assume, that in this flame, below h = 7-8.5 mm, the high DTBP concentration presumably causes oxidation of intermediates leading to particle nuclei and of the nuclei themselves. Hence nucleation and successive coagulation and surface growth can only occur at a later stage, when the oxidation processes caused by the peroxide are no longer important. If the 'delayed' nucleation would still be important in the region, where particles in this flame are first detectable (at h = 8.5 - see Fig. 46), the resulting dispersion forces can be expected to be very large, resulting in a large G value. Below h = 8.5 mm it was not possible, as already discussed, to monitor particle size and number density in this flame, because of the undefined V_V scattering component. However, the equivalent surface growth rates in the DTBP containing flame (see next section) are an indication that simultaneous nucleation, together with coagulation and surface growth, is important around h = 8.5 mm in this flame.

It shall at least be mentioned here, that without great theoretical justification, the apparent correlation between G and N_o/N (as long as G is rising) was used to establish a very approximate relation between them. This relation was found to be

$$G \approx (N_\infty/N)^n \cdot G_o \qquad (N_\infty > N_o) \qquad \text{VI-7}$$

and with $n \simeq 0.77$, $G_o \simeq 0.14$, $N_\infty \simeq 10^{13}$ reasonable agreement was reached for the N(t) and V(t) dependence, when integrating VI-2 with the help of VI-7.

To summarise the coagulation behaviour of soot particles in flames, it is fair to say that free molecule coagulation theory is suitable to describe the results (dependence of N, a on reaction time) at least qualitatively. If better theoretical evaluations for the G factor were possible, the theory would probably be improved to be valid generally for very different flames. However, the very important question of the mechanism of soot nucleation is far from solution. This might explain why, although qualitative results from flames of different C/O and N_2/O_2 ratio are quite comparable, the detailed analysis shows, that considerable changes occur (e.g., in G or in the surface growth rates) with not very large changes in C/O or N_2/O_2 ratio e.g., compare (a) and (g) in Table 10).

Surface growth of soot particles

The (equivalent) surface growth rate $\dot{S}$[67] is obtained from each point in the flame from the rate of change in the soot volume fraction ϕ, $d\phi/dt$, or the rate of change in the particle absorption coefficient ε, $d\varepsilon/dt$, and the particle radius a at that point

$$\dot{S} = d\phi/4\pi a^2 N\, dt = a\, d\phi/3\phi dt \qquad \text{VI-8}$$
$$\dot{S} = a\, d\varepsilon/3\varepsilon dt$$

This neglects a possible increase in ϕ by simultaneous nucleation and assumes that the nucleation rate is negligible compared to the particle surface growth rate. This seems to be justified (except for the DTBP containing flame), as there are distinct maxima in $\dot{S}$ (see Fig. 67), showing that it is highest in a flame region where the particle radius

is already much bigger than the radius of a soot nucleus and the total increase in particle radius, da/dt, is always much larger than $\dot{S}$. However, nucleation might not always be negligible[67], hence form. VI-8, more correctly gives the equivalent surface growth rate, including simultaneous nucleation.

The highest surface growth rates (see Fig. 67) occur in the flame of C/O = 1.00. For smaller or bigger C/O ratios the maximum in the $\dot{S}$ curve versus h is shifted to higher values of $\dot{S}$. For the case of the flames containing TBHP, the maxima in $\dot{S}$ are shifted to higher values of h and also $\dot{S}$ is always much smaller than in the flames containing no TBHP.

A completely different situation arises for the flame containing DTBP (see also Table 10h and Fig. 46). For this case, the equivalent surface growth rate $\dot{S}_a$ at h = 8.5 mm, obtained from eq. VI-8, is much bigger than the rate of increase of particle radius da/dt = 5.8 nm/msec, as found from Fig. 46. This shows that the DTBP causes a 'delayed' nucleation process, resulting in a very high increase in ϕ in a flame region, where presumably no DTBP is present any more. The high values for $\dot{S}_a$, which are mainly to be attributed to the high nucleation rate around h = 8.5 mm, can be explained by the DTBP causing oxidation in the earlier flame regions. These oxidation processes would result in the accumulation of species capable of forming nuclei, after oxidation has become unimportant. Another consequence of the high $\dot{S}_a$ values for the DTBP containing flame is that the values for the mean particle radius a, shown in Fig. 46, are somewhat small and correspondingly, the values for the number density N are too high. The reason for this is that a significant part of the particle absorption can be attributed to nucleation, whereas the V_V scattering component is mainly dominated by the larger particles. Beyond h = 8.5 mm, $\dot{S}_a$ becomes smaller, indicating that nucleation becomes less important compared to true particle surface growth.

It now becomes possible to try to find an answer to the question as the whether the species causing the surface growth of soot particles are identical to those causing the fluorescence. This is done in the following way, again using collision theory. If we take a single particle of volume V and radius a, surrounded by species B of volume $V_B << V$, density ρ_B, and concentration c_B, the rate of volume increase of the particle, if every collision results in surface reaction, is given by

$$\frac{dV}{dt} = \left(\frac{8\pi kT}{\rho_B}\right)^{\frac{1}{2}} a^2 \, V_B^{\frac{1}{2}} \, c_B \qquad \text{VI-9}$$

VI-9, representing surface growth in terms of particle volume increase, must be equal to the second term in the differential equation VI-3, $Vd\phi/\phi dt$, which also represents the surface growth rate in terms of particle volume change. If we now take the approximation for ϕ, $\phi = At+\phi_o$, $d\phi/dt = A$ and, assuming that the fluorescing species cause the surface growth, take $c_B = c \cdot H_V$ (550 nm), we get

$$c \cdot V_B^{\frac{1}{2}} = \frac{1}{3}\left(\frac{2\pi\rho_B}{kT}\right)^{\frac{1}{2}} \cdot \frac{a}{H_V \text{ (550 nm)}} \cdot \frac{A}{At + \phi_o} \qquad \text{VI-10}$$

If we now take species B as a PCAH molecule of 10 benzene rings, V_B is approximately 10^{-21} cm^3. Using the data for a, H_V (550 nm), A and ϕ_o for the different flames, values for c of around 10^{12}- 10^{13} cm^{-3} are calculated, resulting in concentrations of B of the order of 10^{13}-10^{14} cm^{-3}. These values do not seem to be unreasonable for the concentration of a surface growth species. However, one has to bear in mind that the H_V (550 nm) curves do not show the typical behaviour, which one would expect from a species being depleted by surface growth. As long as no information is available about the formation rates of the fluorescing species and about the detailed mechanism of the dependence of the surface growth on e.g. soot particle size and reactivity of the surface, the question stated above, as to whether the fluorescing species are the surface growth species, cannot be answered.

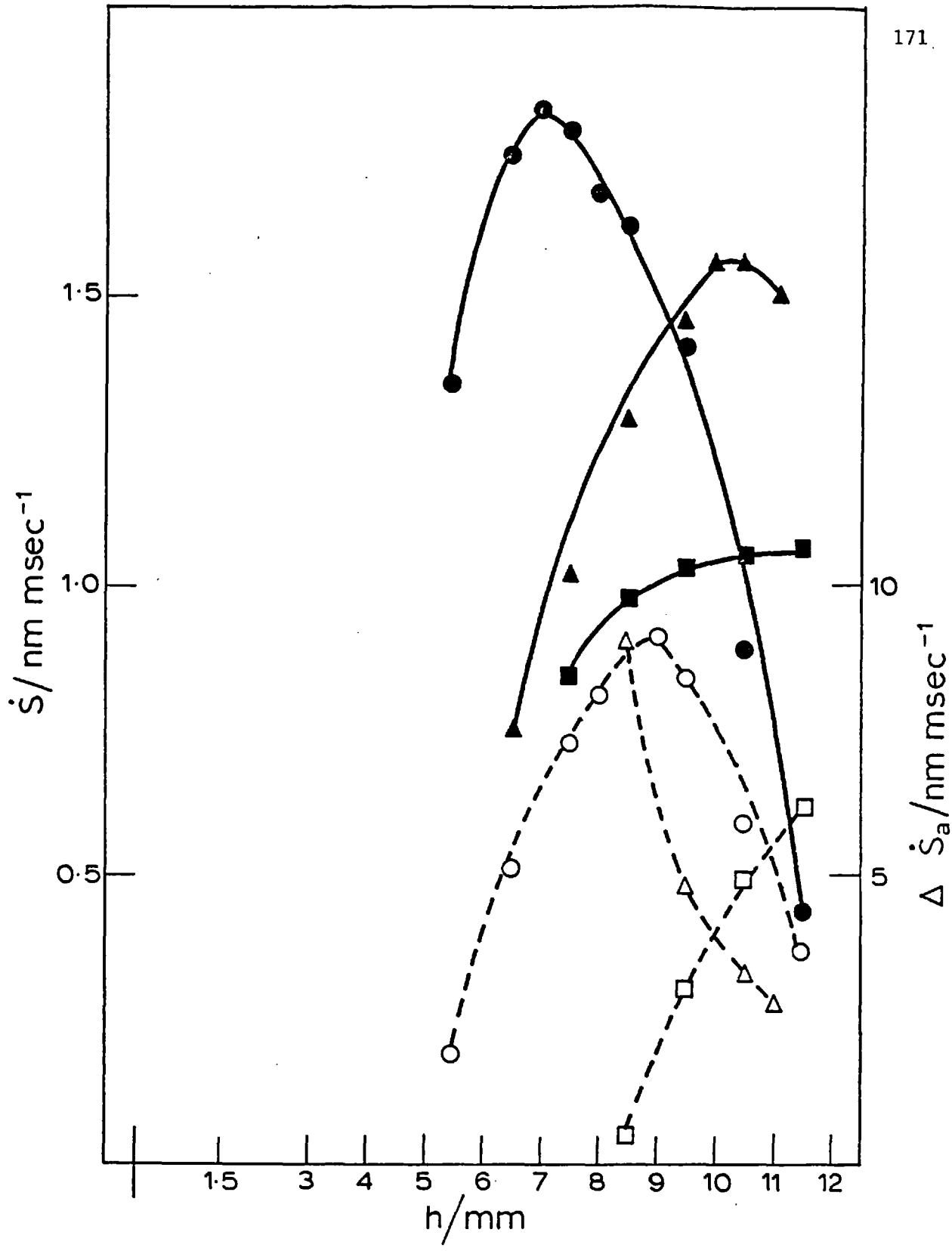

Fig. 67: Surface growth rates $\dot{S}$ of soot particles for different flames, left hand side ordinate versus height above burner:
C/O = 1.00, N_2/O_2 = 1.59 (Fig. 34): ● no TBHP, ○ plus TBHP;
C/O = 1.51, N_2/O_2 = 1.75 (Fig 39): ■ no TBHP, □ plus TBHP;
C/O = 0.963, N_2/O_2 = 1.75 (Fig. 46): ▲ no DTBP.
right hand side ordinate: equivalent surface growth rate for flame of C/O = 0.963, N_2/O_2 = 1.75, plus DTBP Δ .

CONCLUSIONS

1) Size and number density of soot particles can be obtained from light scattering and absorption measurements, provided a correction for the absorption from molecules is made.

2) Soot formation is always accompanied by the formation of large molecules or radicals, probably polycyclic aromatics containing more than 10 benzene rings. These species might be involved in the surface growth of soot particles, but it is also possible that they are mainly by-products.

3) Even the smallest primary soot particles depolarise the (Rayleigh) scattered light - probably by anisotropy of refractive index.

4) The depolarisation of the scattered light from soot particles at long residence times (diffusion flame) can be explained by shape anisotropy, caused by an agglomeration process in the flame.

5) TBHP in small concentrations, present in a premixed flame, reduces the size, but increases the number density of the soot particle.

6) DTBP in higher concentrations, present in a premixed flame, reduces particle size, number density and the measured fluorescence intensity.

7) In the region of highest soot concentration in diffusion flames, the angular dependence of the scattered light can always be fitted to the Mie intensity functions, thus obtaining a mean equivalent sphere size.

8) Both TBHP and DTBP increase soot particle size and number density when added to the fuel side of a diffusion flame. When added to the oxidant side, particle size and number density are reduced.

VII) BURNING VELOCITIES AND THE ADDITION OF ORGANIC PEROXIDES

Though there exists a variety of chemical compounds (e.g. halogenated hydrocarbons) which effectively inhibit combustion processes, the search for strong combustion promoters has encountered many difficulties. The enhancement of combustion intensities and burning velocities has proved to be particularly appropriate to burning lean mixtures. Stabilising lean flames is of obvious interest for two reasons; first, there is a large potential amount of energy buried in low grade (e.g. air diluted) fuels, which cannot be released by conventional means, and secondly, high temperature pollutants could, in principle, be reduced to their thermodynamic equilibrium level.[150]

Burning leaner mixtures, e.g. in an internal combustion engine like the Otto motor can only be achieved up to certain limits because otherwise the mixture would not ignite and burn rapidly enough to expand the gas sufficiently 'instantaneously'. Thus, although it is desirable to burn fuel-air mixtures very lean to make combustion and energy release go to completion and decrease NO_x production significantly because of the lower flame temperatures, this is normally impossible because burning rates decrease rapidly as the mixture is made leaner. Eventually, with too much excess air, combustion becomes incomplete until the flame is extinguished at the lean flammability limit.

An easy way to overcome this limitation is to preheat the reactants thereby enhancing chemical reaction rates. This is, of course, only sensible in a kinetically controlled flame and not in a diffusion-controlled one, because the effect of temperature on diffusion is marginal compared to that on chemical reaction. Supplying this heat from another combustion source would only transfer the problem, whilst other sources (e.g. electrical preheating) are likely to be uneconomical. An elegant solution is the use of 'borrowed heat' from the flame itself by allowing the hot burnt gases to heat up the fresh gas with minimum losses, e.g. in the Swiss roll burner[151 - 154] or in combination with fluidised beds.[155, 156]

These devices have made the term lean 'flammability limit' virtually meaningless, and because there is such an excess of air combustion is complete, whereas NO_x production

is strongly decreased because of the much lower temperatures. From those experiments it follows that the question, 'What is a fuel?' has to be re-examined. Other experiments using plasma jets as sources of radicals and excited molecules and atoms have shown that lean fuel air mixtures can be burnt at much faster rates, when active species are added.[157]

Also there has been some recent progress in improving the ignition of lean methane-air mixtures under engine conditions. This was done by injection of hydrogen atoms from a pulsed plasma source.[158]

Instead of breaking up stable molecules (such as N_2, H_2, H_2O) in plasma jets at high temperatures and adding the generated radicals to combustible mixtures, radicals can also be produced by decomposition of organic peroxides (see table 1).

To assess whether organic peroxides as additives can promote combustion, the burning velocity was chosen as the experimental parameter. In order to distinguish between small effects of additives a highly accurate method of burning velocity measurement was required. This requirement has been met by developing a new technique based on the porous plug method with optical temperature measurement above the reaction zone using laser Rayleigh scattering. The opportunities afforded by the method have also been exploited to investigate the effects on burning velocity of traces of inhibitor and to decide if it is influenced by electric fields in normal and inhibited flames.

Although burning velocity is perhaps the most important empirically determined parameter in combustion, the experimental methods available lead to appreciable discrepancies in results - for example see review by Andrews and Bradley.[159]

A method capable of potentially a very high accuracy is based on determining the velocity at lift-off of flames stabilized by heat losses to a porous disc burner.[160] So long as the flow velocity is less than the normal burning velocity of the unperturbed flame in that mixture, the flame front burns close to the porous disc and is modified (non-adiabatic) by heat loss to it. As the flow velocity is increased to approach the unperturbed burning velocity, the normal flame structure re-establishes itself downstream of the porous disc, the gradients in temperature and in all the other flame

variables falling to zero above it. The disc temperature then reverts to that of the incoming reactants, even in the absence of cooling, and the final flame temperature to its adiabatic value. The accuracy of the method depends on the precision with which this "end-point" can be determined.

In the original work[160], the water cooling system was used as a flow calorimeter and the adiabatic condition was inferred by extrapolating the heat loss from the flame to zero. In subsequent work, the final flame temperature was measured by thermocouples[161, 162]. Alternatively the saturation current from the flame under the application of electric fields was measured[162, 163]. The saturation current is drawn at potentials above those for which the flame ion current varies with applied voltage and is constant, independent of electrode configuration[164]. It is highly temperature-dependent, a doubling in saturation current being often produced by a 60K rise in the final flame temperature[165]. Since absolute measurement of flame temperature is not required here, this becomes one of the most accurate measurements[111] of any kind available in combustion.

However, as regards determining the end-point with accuracy, a variety of problems are associated with calorimetry and thermometry. Coolant pipes are not easily associated with sinters and it is very difficult to combine uniform cooling of the disc with a uniform velocity distribution across it. Thermometry should be independent of flow velocity and preferably confined to a small region at the centre of the flame. Although the flame temperature reaches its adiabatic value at the end-point, and thereafter stays constant with increasing flow rate, practical thermometers tend to be sensitive to changes in flow pattern, velocity or flame shape. Thus, the reading of thermocouples depends on the heat transfer coefficient which increases with flow velocity and this leads to imprecision in the end-point, even with a theoretical extrapolation - see bB, Fig. 60. Line reversal requires seeding, which may perturb the flame, and is difficult to introduce either below or above a sintered disc. Integration along its path length is another difficulty and this also affects interferometry, particularly because of the strong influence of boundary effects, which change with the flow pattern. It is, of course, not necessary to measure absolute temperatures : any temperature-dependent variable will do. As mentioned above, the measurement of saturation current combines the advantages of simplicity and very

high sensitivity. However, even if we discount the possibility that burning velocities are affected by the presence of a field, saturation current does not become a constant at the end-point either. Although the saturation current density attains its constant maximum value there, the flame area and hence the total current becomes proportional to the volumetric flow rate of the reactants [164], once adiabatic flame stabilisation is attained. Although the relationship between saturation current and flow velocity becomes linear beyond this point, the slope is far from zero - see aA Fig. 60 - which again detracts from the accuracy of determining the end-point.

The optimum choice appeared to be a laser-based method giving temperature, independent of flow velocity, over a small region defined by the focal volume of the focused beam. Selection of the small volume at any height allows for flame movement (indeed for mixtures of large quenching distances, the initial temperature immediately above the burner disc could be measured, allowing the end-point to be determined by its reversion to room temperature). Rayleigh scattering [125, 126] was chosen in preference to Raman [145] chiefly because the scattered intensities are some three orders of magnitude higher.

VII-1 Experimental

The optical set up (fig. 1) and the burner-flow system have already been described. For the experiments on peroxide addition, the top part of the burner in fig. 3 was removed. Whenever electrical fields were applied a burner incorporating a 25 mm diam. brass sinter was used.

VII-2 Rayleigh Scattering for a Mixture of Gases

In order to determine the absolute temperature of a gas from Rayleigh scattering, the composition of the mixture and the differential cross section of each component must be known. This information is not essential for burning velocity measurements since, for a constant composition, the scattered intensity from the products is a unique function of temperature, being essentially proportional to density. Indeed, for burning velocity measurement it is only necessary to record the change in scattered intensity - see Fig. 61 . However, most of the burning velocity determinations reported here were carried out for very lean flames, for reasons discussed in the next section, and, under these conditions, a simple measurement of the absolute scattering

intensity also provides a good approximation to the final flame temperature. It will be apparent from Fig. 61, 62 and 63 that the use of either differential or absolute intensity allows burning velocity to be determined with great precision as the intersection between a horizontal straight line and one of appreciable slope on the graph against velocity (in contrast to the methods illustrated in Fig. 60).

For a mixture of gases with components of number density N_i, assuming ideal gas behaviour, the scattered intensity I_{vv} per unit volume is given by

$$I_{vv} = \frac{1}{r^2} \sum_{i=1}^{n} N_i \, \sigma_{oi}^{c} \qquad \text{VII-1}$$

For lean flames containing a large excess of nitrogen, where combustion is complete because the temperatures are high enough whilst not giving rise to dissociation, the final mixture is essentially composed of N_2, O_2, CO_2 and H_2O only. The scattered intensity (relative to nitrogen) from the flame is then given by (using the cross sections relative to nitrogen)

$$\frac{I_{\text{flame}, T_f}}{I_{N_2, T_o}} = \frac{T_o}{T_f} \left(c_{N_2} + \sum_{i=1}^{n} c_i \, \sigma_{ri} \right) \qquad \text{VII-2}$$

and taking the overall reaction as

$$C_2H_4 + (3+\Delta)O_2 + d\,N_2 \rightarrow 2\,CO_2 + 2\,H_2O + d\,N_2 + \Delta O_2$$

with $n = 4 + d + \Delta$.

The flame temperature can be obtained as

$$T_f = \frac{T_o \, I_{N_2, T_o}}{n \, I_{\text{flame}, T_f}} \left(d + \Delta \sigma_r(O_2) + 2\sigma_r(H_2O) + 2\sigma_r(CO_2) \right)$$

$$T_f = \frac{T_o \cdot I_{N_2, T_o}}{n \, I_{\text{flame}, T_f}} \left(d + 0.833\Delta + 6.06 \right) \qquad \text{VII-3}$$

using the relative cross-sections of Table 2.

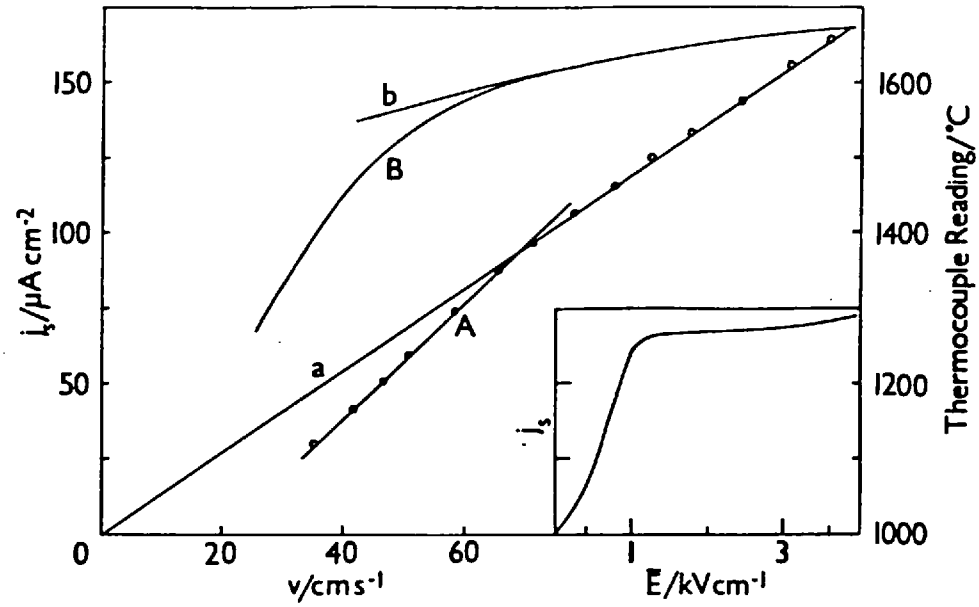

Fig. 60: Burning velocity end-point determination by thermocouple (b, B) and by saturation current, j_S, measurement (a, A)[162]

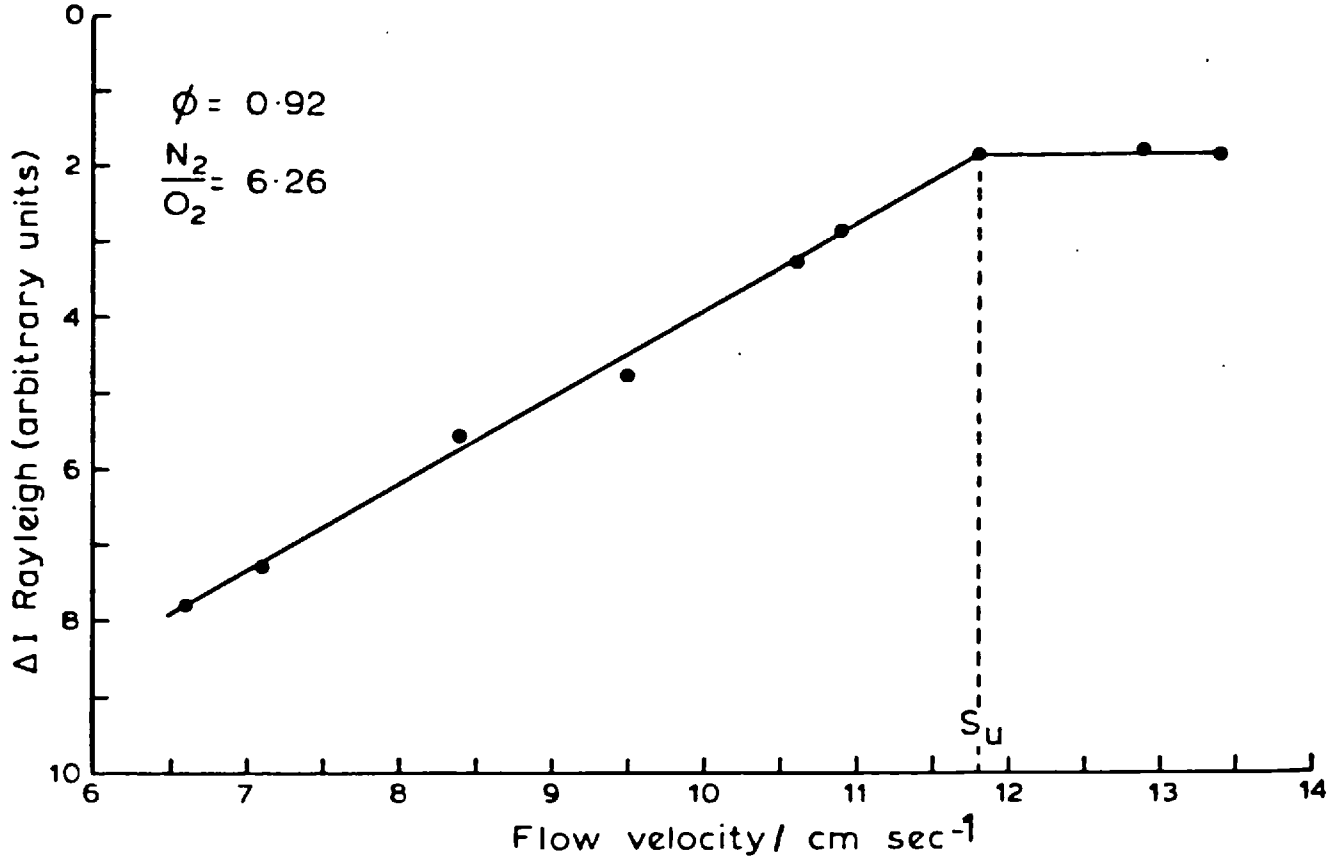

Fig. 61: Burning velocity end-point determination by differential Rayleigh scattering. C_2H_4-N_2-O_2 mixture.

Fig. 62: Determination of burning velocity by absolute scattered intensity (approx. temperature) measurement plotted against flow velocity. Full lines: C_2H_4 only; • C/O = 0.291, + C/O = 0.306. Dashed lines: tertiary butyl hydroperoxide (TBHP) added. o C/O = 0.294, $m_{TBHP}/m_{C_2H_4}$ = 1.1%, x C/O = 0.298, $m_{TBHP}/m_{C_2H_4}$ = 2.5%. All for N_2/O_2 = 6.77.

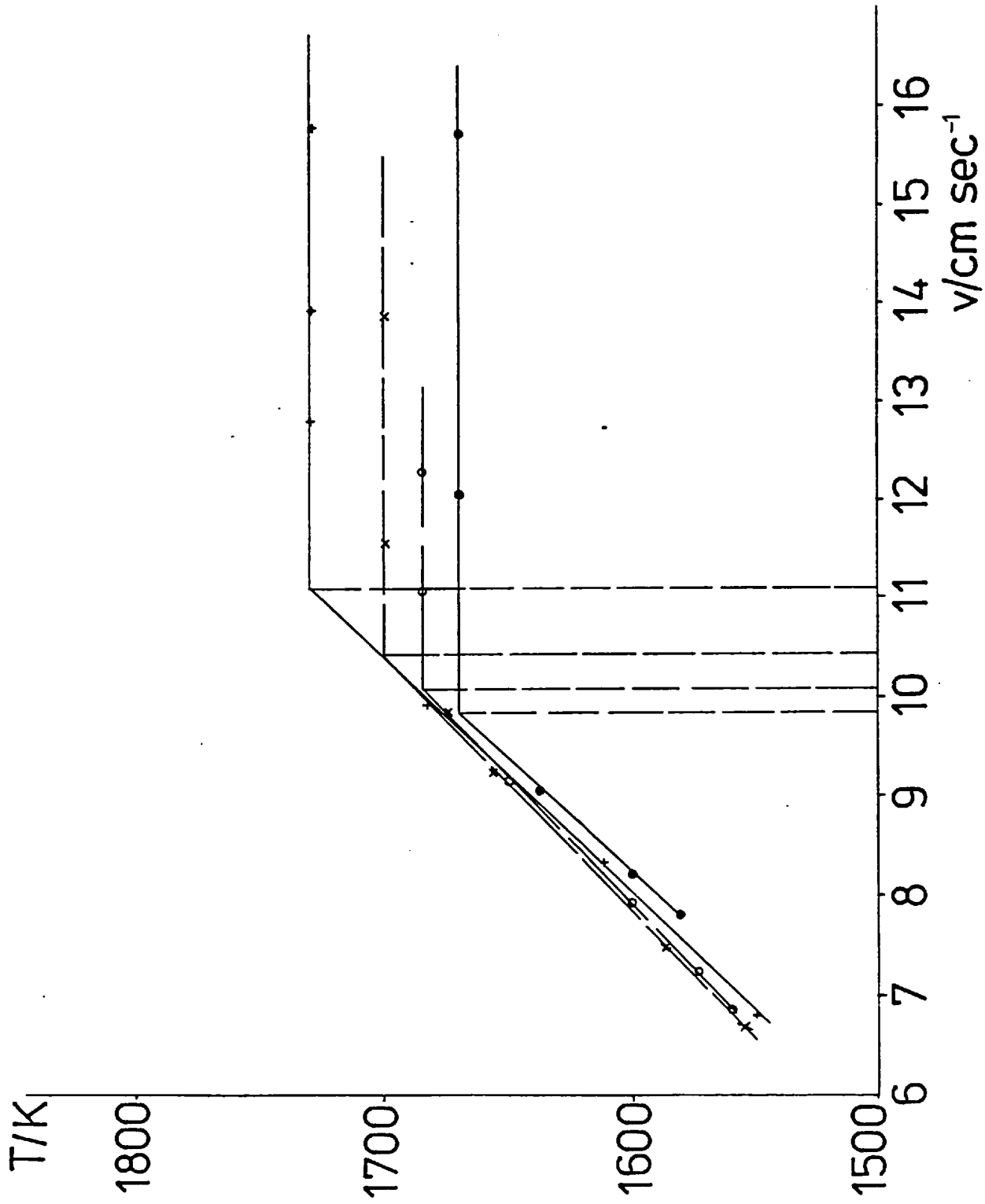

Fig. 63: As Fig. 62. Full lines C_2H_4 only; o C/O = 0.291, + C/O = 0.350. Dashed lines di-tertiary butyl peroxide (DTBP) added; o C/O = 0.314, $m_{DTBP}/m_{C_2H_4}$ = 7.9%; x C/O = 0.319, $m_{DTBP}/m_{C_2H_4}$ = 9.8%. All for N_2/O_2 = 6.77.

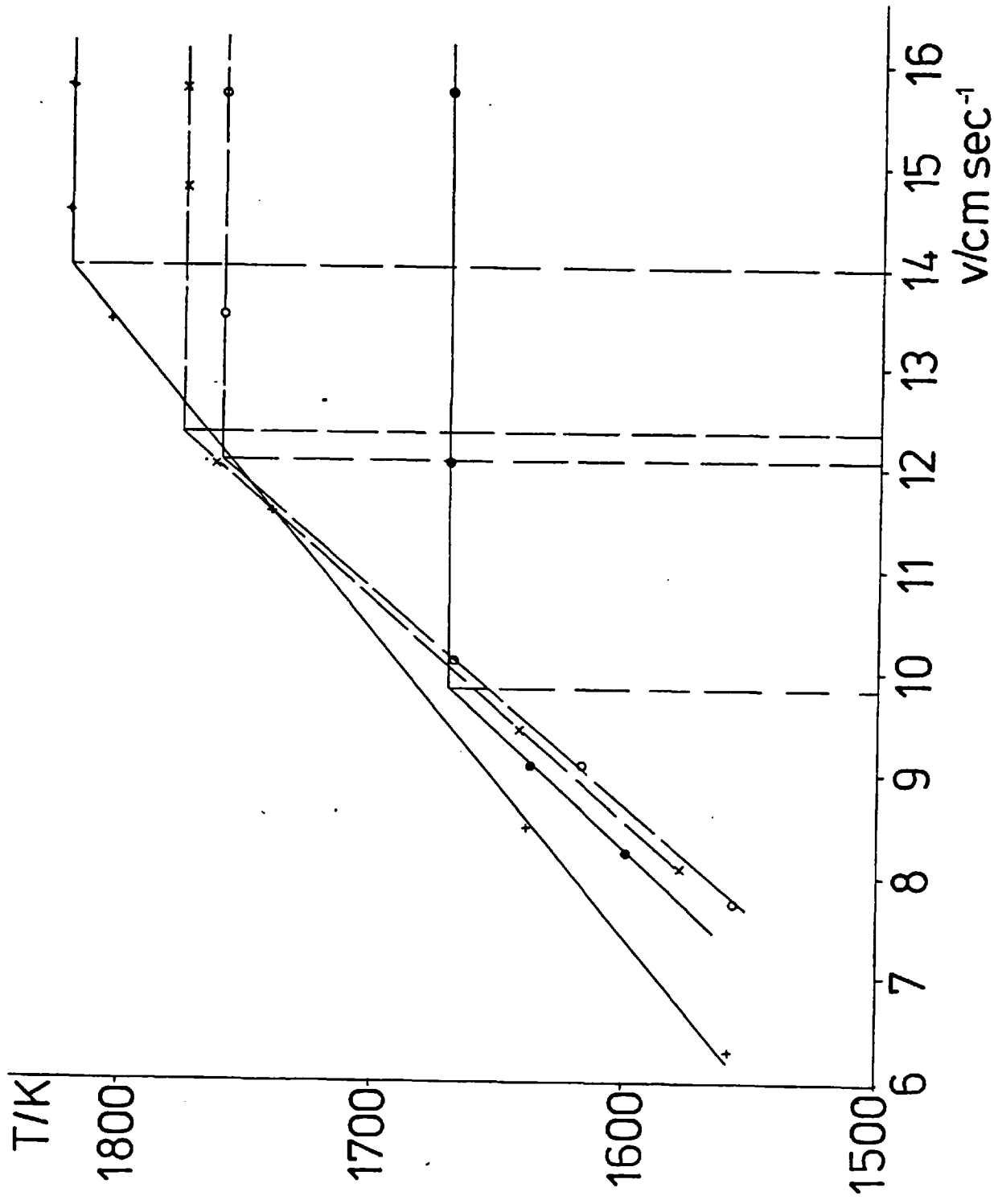

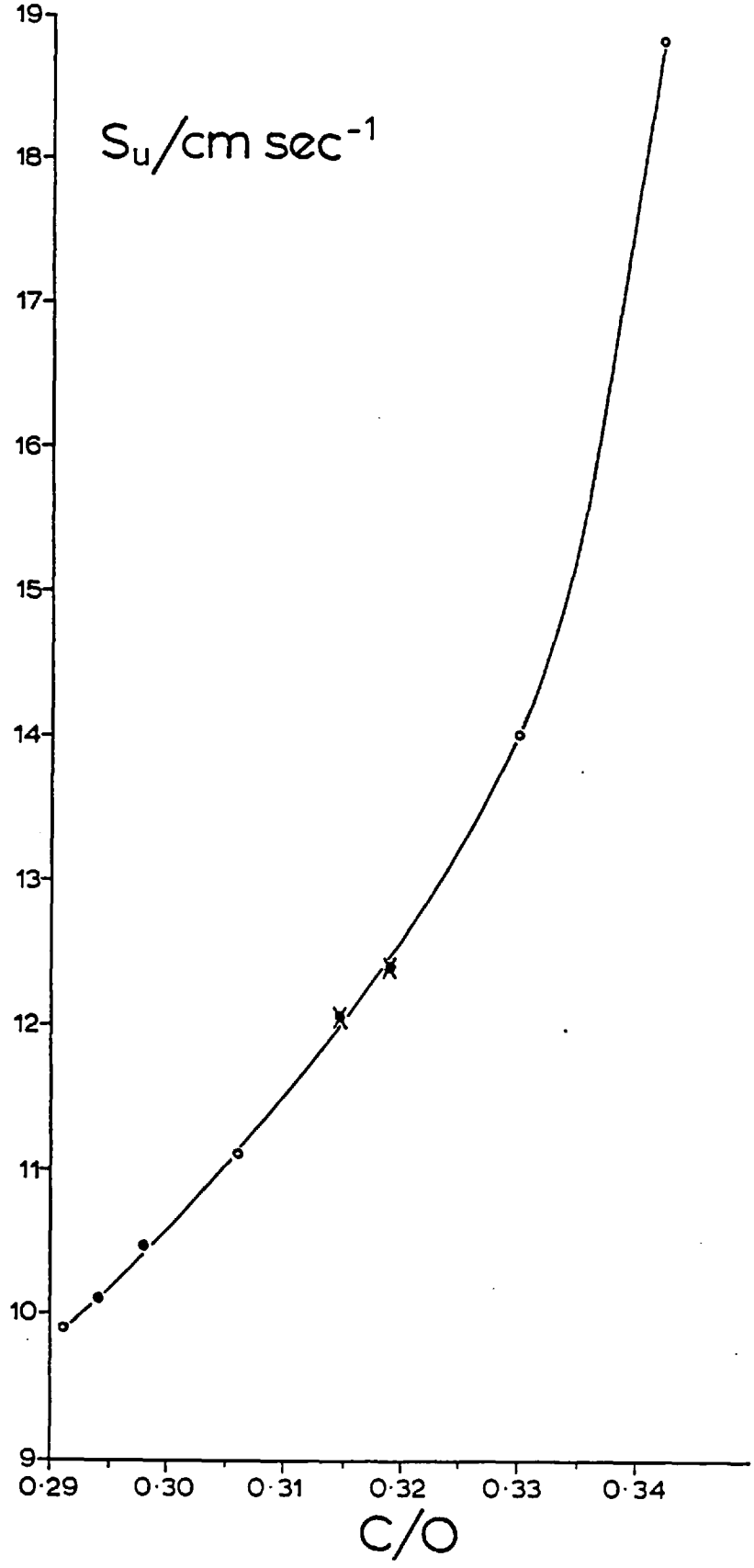

Fig. 64: Burning velocity against total C/O ratio for N_2/O_2 = 6.77.
o : C_2H_4 only, ● : with TBHP, ✖ : with DTBP.

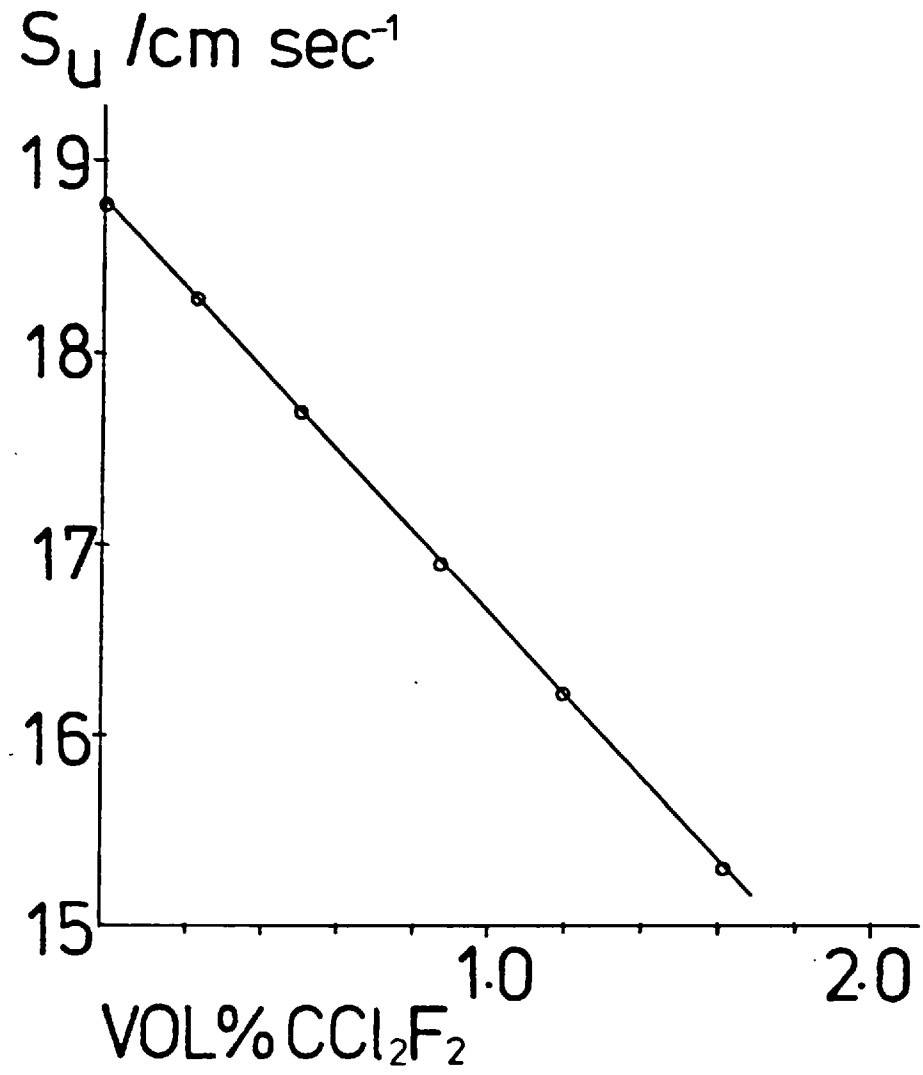

Fig. 65: Variation of burning velocity with Freon 12 traces. C_2H_4 flame with C/O = 0.341 and N_2/O_2 = 6.77.

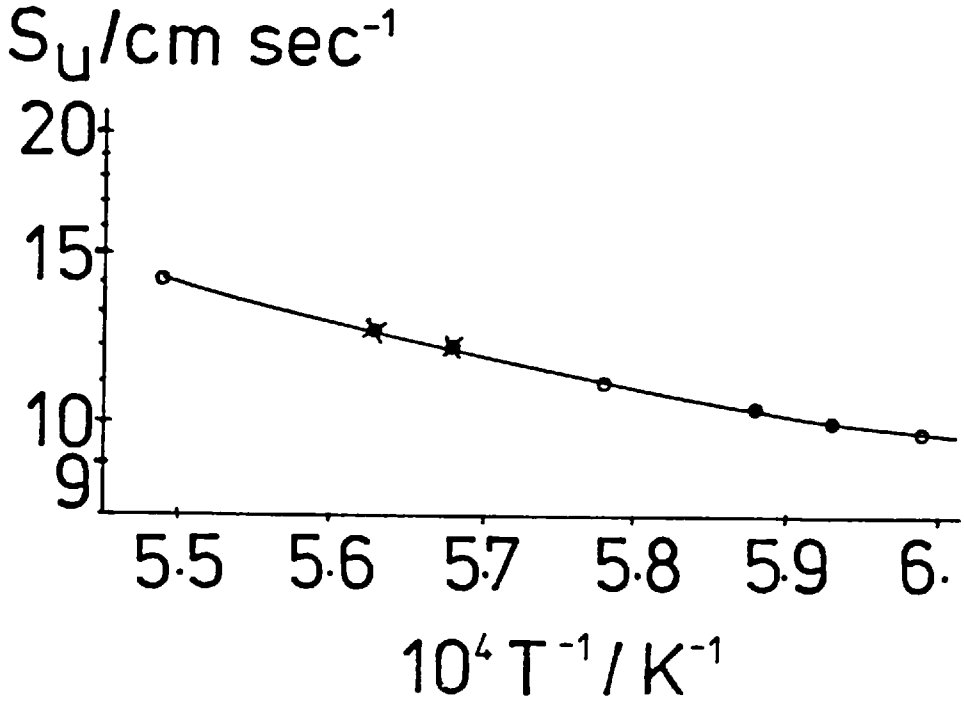

Fig. 66: Log plot of burning velocity against reciprocal temperature. N_2/O_2 = 6.77; o C_2H_4 only; • with TBHP; ✖ with DTBP.

VII - 3 Results

Lean flames in highly dilute mixtures were used in the work reported here in order to obtain maximum sensitivity to the effect of additives and other perturbations. This is particularly applicable to the addition of (hydro) peroxides which, in addition to any effect of the alkoxy (HO) radicals, also act as fuels. The mixtures chosen were close to where the rate of change of burning velocity with mixture strength is a maximum. Under these conditions, the temperatures obtained from Rayleigh scattering by the calculation outlined above, agree quite closely with the calculated adiabatic flame temperatures - for the reasons discussed in the theoretical section. The measured values are in fact all about 20 to 30 K below the calculated adiabatic temperatures. It would therefore be possible to monitor both the fuel content and burning velocity from Rayleigh scattering measurements for such mixtures.

The availability of a very precise method of burning velocity measurement offered the opportunity to resolve a variety of other issues.

The question of whether electric fields affect burning velocity has been the subject of much discussion.

The effect of inhibitors on burning velocity is of interest in its own right : its associatian with an electric field arose from the suggestion[166] that the inhibition itself involves electrical effects, entailing the attachment of an electron as a first step. It is trivially easy to prevent any electrons from reaching the pre-flame zone by applying an appropriate electric field. This question should therefore be resolvable, on the basis of having previously explored whether there is any effect of electric fields on their own.

The effects of added ditertiary butyl peroxide and tertiary butyl hydroperoxide are shown in Figs. 62 and 63. Since both act partly as fuel, Fig. 64 shows the dependence of burning velocity on carbon to oxygen ratio, incorporating results of varying fuel concentration alone as well as additions of each of the two peroxides. Figure 65 illustrates the effect on burning velocity of a particular inhibitor - freon 12 (CCL_2F_2). The effect of fuel concentration is shown in Fig. 66 as the logarithm of burning velocity plotted against the reciprocal of absolute temperature. The latter was obtained both by Rayleigh scattering measurement and by detailed calculation, allowing for dissociation

where appropriate, but on this scale any differences are indistinguishable. No measurable effect was observed for electric fields of either polarity and magnitudes up to 400 V/cm (mean). This applied equally for uninhibited and inhibited flames.

VII-4 Conclusions

The primary conclusion of this work lies in the establishment of a very precise method of measuring burning velocity. Since the stability of the laser and associated electronics is better than 0.5%, the accuracy of the method is limited only by that of the flow meters and of any non-uniformity of the sinters. However the results of the various illustrative experiments carried out are interesting in their own right and lead to the following conclusions.

Variation with fuel concentration The dependence of burning velocity on the fuel content was investigated first. It is not only the most obvious and usual measurement but was required, in this instance, to assess the effect of the fuel value of the peroxide. The appropriate points are marked in Figs. 62 - 64 but in some ways the most interesting is Fig.66 . Several workers have used the dependence of burning velocity on temperature to obtain overall activation energies for the flame reaction. With the accuracy of the present method it is seen that the gradient of a logarithmic burning velocity plotted against the reciprocal of absolute temperature is not constant, showing that the global kinetics concept may not be applied even over quite small ranges of burning velocity.

Additives Peroxide groups appear to exercise no measurable effect on burning velocities (though they do affect some other flame parameters). The organic peroxides show an effect which can be represented entirely by their fuel values (see Figs. 62,63 and 64).

To be of practical value, appreciable effects would be required from small quantities of additives.

It is appropriate to compare this with the effect of freon 12 which has a pronounced inhibiting effect in precisely these quantities. Figure 65 is a good illustration of this and of the sensitivity of the method of measurement.

Electric fields Once again we were unable to detect any effect of electric fields on burning velocity[162] - and this time by measurements that do not involve the use of electric field in their method and would have easily shown up a change of .5 cm/s. The observation that rapid removal of electrons from the reaction zone has not the slightest effect on the burning velocity of strongly inhibited flames presumably also disposes of the suggestion[166] that electron attachment is an important first step in flame inhibition.

REFERENCES

1) Weinberg, F.J.
Fifteenth Symp. (Int.) on Combust.
The Combust.Inst. 1975, pp. 1 - 17

2) Jones, B.A., Weil, B.H. and Graham, M.H.
Literature of the Combustion of Petroleum.
ACS Advances in Chemistry No. 20 (publ. 1958)

3) Padovani, C., Paleari, C. and Renzanigo, F.
Rivista dei Combustibili 14 (3), 193 - 204 (1960)

4) Salooja, K.C.
J. Inst. Petr. 48, 119 - 129 (1962)

5) Flagan, R.C., Galant, S. and Appleton, J.P.
Combust. Flame 22, 299 (1974)

6) Mardanov, M.A.
Azerb. Khim. Zh. 1, 3 (1965)

7) Puchin, V.A. et al.
Russ. Pat. 236897 (1967)

8) Puchin, V.A. et al.
Russ. Pat. 214710 (1967)

9) Vaughan, W.E. and Rust, F.F.
U.S. Pat. 2378341 (1945)

10) Barusch, M.R. and Mixer, R.Y.
US Pat. 2655440 (1953)

11) Interox Chemicals Ltd., unpublished results (1976)

12) Kaptein, Robert
Thermal and Photochemical decomposition of aliphatic acylperoxides and related compounds; from Chemical Induced Magnetic Polarizability, pp. 137 - 96 (1973) ed. Lepley, A.R., Wiley : New York

13) Fischer, Hans
Aroyl peroxide decomposition, ebda., pp. 197 - 222

14) Koenig, Th.
Decomposition of peroxides, from: Free Radicals, 1, 113 - 55 (1973) ed. Kochi, J.K. Interscience New York

15) Hawkins, E.G.E.
Reactions of peroxides, from : MTP Int. Rev. Sci. : Org. Chem. Ser. one (1973), 10, pp.95 - 138 ed. Waters, W.A. Butterworths : London.

16) Molnar, S.
Period. Polytechn., Chem. Eng., 17 (3), 257 (1973)

17) Frost, A.A. and Pearson, R.G.
Kinetics and Mechanism
Wiley, N.Y., Chapman & Hall, London, 1953

18) Batt, L. and Benson, S.W.
J. Chem. Phys. 36, 895 (1962)

19) Gray, P., Shaw, R. and Thynne, J.C.J.
Progr. React. Kinetics, 4, 63 (1967)

20) Benson, S.W.
Thermochemical Kinetics
Second ed., Wiley, N.Y. and London, 1976

21) Batt, L.
The Fifth Int. Symp. on Gas Kinetics, UMIST, July 1977, p.3

22) Selby, K. and Waddington, D.J.
The Fifth Int. Symp. on Gas Kinetics, UMIST, July 1977, p.61

23) Street, J.C. and Thomas, A.
Fuel 34, 4 (1955)

24) Müller-Dethlefs, K. and Schlader, A.
Combust. Flame, 27, 205-215 (1976)

25) Smithells, A. and Ingle, H.
J. Chem. Soc. 61, 204 (1892)

26) Behrens, H.
a) Naturwissenschaften 32, 297, 299 (1944)
b) Z. Phys. Chem. A 196, 78 (1950)
c) Fourth Symp. (Int.) on Combust.
Williams & Wilkins, Baltimore 1953, p.538

27) Jost, W., Krug, J. and Sieg, L.
Fourth Symp. (Int.) on Combust. 1953, p.535

28) Jost, W. and Krischer, B.
Z. Phys. Chem. N.F.5, 398 (1955)

29) Krischer, B.
Z. Elekrochemie 60, 1017 (1956)

30) Wright, F.J.
12th (Int.) Symp. on Combust.
The Combustion Institute 1969, p. 867

31) Millikan, R.C.
J. Phys. Chem. 66, 794 (1962)

32) Homann, K.H., Mochizuki, M. and Wagner, H. Gg.
Z. Phys. Chem. NF 37, 299 (1963)

33) Homann, K.H. and Wagner, H. Gg.
Ber. Bunsenges. Phys. Chem. 69, 20 (1965)

34) Bonne, U. and Wagner, H. Gg.
Ber. Bunsenges. Phys. Chem., 69, 35 (1965)

35) Flossdorf, J. and Wagner, H. Gg.
Z. Phys. Chem. NF 54, 8 (1967)

36) Bonne, U., Homann, K.H. and Wagner, H. Gg.
Tenth Symp. (Int.) on Combust.
The Combust. Inst. 1965, p. 503

37) Homann, K.H. and Wagner, H. Gg.
Eleventh Symp. (Int.) on Combust.
The Combust. Inst. 1967, p. 371

38) Homann, K.H.
Combust. Flame 11, 265 (1967)

39) Homann, K.H.
Angew. Chemie, 80, 425 (1968)

40) Cullis, C.F. and Franklin, N.H.
Proc. Roy. Soc. A280, 139 (1964)

41) Cullis, C.F., Read, I.A. and Trimm, D.L.
Eleventh Symp. (Int.) on Combust.
The Combust. Inst. 1967, p.391

42) Zaghini, N., Mangolini, S., Cornetti, G., Salvatori, T. and Rizzi, G.
Combust. Sci. Techn. 5, 225 (1972)

43) Franceschi, A., Gerbaz, G.P. and Mangolini, S.
Combust. Sci. Techn. 14, 33 (1976)

44) Franceschi, A., Zanelli, S. and Cornetti, G.M.
Combust. Sci. Techn. 14, 57 (1976)

45) Lee, M.L., Prado, G.P., Howard, J.B. and Hites, R.A.
Biomed. Mass Spectrometry 4, 182 (1977)

46) Chakraborty, B.B. and Long, R.
Combust. Flame 12 (1968)
p. 168, p.226, p.237, p. 469

47) Fenimore, C.P., Jones, G.W. and Moore, G.E.
Sixth Symp. (Int.) on Combust.
The Combust. Inst. 1956, p.242

48) Fenimore, C.P. and Jones, G.W.
J. Phys. Chem. 71, 593 (1967)

49) Fenimore, C.P. and Jones, G.W.
Combust. Flame 12, 196 (1968)

50) Fenimore, C.P. and Jones, G.W.
Combust. Flame 13, 303 (1969)

51) Ates, H.F. and Page, F.M.
Second Symp. (Eur.) on Combust. 1975, p.380

52) Miller, Newman and Page
unpublished results

53) Park, C. and Appleton, J.P.
Proc. Ninth Int. Shock Tube Symp.
ed. by D. Bershader and W. Griffith, Stanford Univ. Press 1973, p.793

54) Park, C. and Appleton, J.P.
Combust. Flame 20, 369 (1973)

55) Gosling, A.J., Lampard, D. and Fussey, D.E.
First Symp. (Eur.) on Combust.
Academic Press 1973, p.388

56) Fussey, D.E., Gosling, A.J. and Lampard, D.
Combust. Flame 32, 181 (1978)

57) Wagner, H. Gg., priv. comm. from ref. 56

58) Lowes, T.M. and Newall, A.J.
Combust. Flame 16, 191 (1971)

59) Thring, M.W. and Lowes, T.M.
Combust. Sci. Techn. 5, 251 (1972)

60) Serag-El-Din, M.A.H.
Ph.D. Thesis, Univ. of London, Aug. 1976

61) Greenberg, J.M.
J. Colloid Int. Sci. 39, 513 (1972)

62) Jones, A.R.
J. Phys. D : Appl. Phys. 5, L1 (1972)

63) Jones, A.R.
First Symp. (Eur.) on Combust.
Academic Press 1973, p.376

64) Medalia, A.I. and Heckman, F.A.
Carbon 7, 567 (1969)

65) Howard, J.B.
Twelfth Symp. (Int.) on Combust.
The Combust. Inst. 1969, p. 877

66) Ball, R.T. and Howard, J.B.
Thirteenth Symp. (Int.) on Combust.
The Combust. Inst. 1971, p.353

67) Wersborg, B.L., Howard, J.B. and Williams, G.C.
Fourteenth Symp. (Int.) on Combust.
The Combust. Inst. 1973, p.929

68) Wersborg, B.L., Yeung, A.C. and Howard, J.B.
Fifteenth Symp. (Int.) on Combust.
The Combust. Inst. 1975, p.1439

69) Howard, J.B., Wersborg, B.L. and Williams, G.C.
Faraday Symp. Chem. Soc. 7, 109 (1973)

70) Bittner, J.D., in press

71) Lahaye, J., Prado, G. and Donnet, J.B.
Carbon 12, 27 (1974)

72) Lahaye, J. and Prado, G.
ACS Symp. Series 21, Petroleum Derived Carbons,
ed. by Deviney, M.L. and O'Grady, T.M., 1975, p.335

73) Millikan, R.C.
J. Opt. Soc. Am. 51, 698 (1961)

74) Bonne, U., Dissertation (Dr. rer. nat.)
Univ. Gottingen, 1964

75) Homann, K.H., Morgeneyer, W. and Wagner, H.Gg.
First Symp. (Eur.) on Combust.
Academic Press 1973, p.394

76) Dalzell, W.H. and Sarofim, A.F.
ASME Trans. C : J. Heat Transfer, 91, 100 (1969)

77) Erickson, W.D., Williams, G.C. and Hottel, H.C.
Combust. Flame 8, 127 (1964)

78) Dalzell, W.H., Williams, G.C. and Hottel, H.C.
Combust. Flame 14, 161 (1970)

79) Kunugi, M. and Jinno, H.
Eleventh Symp. (Int.) on Combust.
The Combust. Inst. 1967, p.257

80) D'Alessio, A., Beretta, F. and Venitozzi, C.
Combust. Sci. Techn. 5, 263 (1972)

81) D'Alessio, A., Di Lorenzo, A., Beretta, F. and Ventozzi, C.
Fourteenth Symp. (Int.) on Combust.
The Combust. Inst. 1973, p.923

82) D'Alessio, A., Di Lorenzo, A., Beretta, F., Sarofim, A.F., Masi, S.
and Ventiozzi, C.
Fifteenth Symp. (Int.) on Combust.
The Combust. Inst. 1975, p.1427

83) D'Alessio, A., Di Lorenzo, A., Borghese, A., Beretta, F. and Masi, S.
Sixteenth Symp. (Int.) on Combust.
The Combust. Inst. 1977, p.695

84) D'Alessio, A., Di Lorenzo, A., Micera, G. and Beretta, F.
Sec. Simp. Dinamica Reazione Chim.
Padova 1975, p. 147

85) Stephenson, A.F.
J. Appl. Phys. 24, 1134 (1953)

86) D'Alessio, A., Ferrara, P., Sarofim, A.F. and Venitozzi, C., in press

87) Ferrara, P.
Tesi di Laurea in Ingegneria Chimica
Universita di Napoli, 1977

88) D'Alessio, A., priv. comm.

89) Graham, S.C. and Homer, J.B.
Faraday Symp., Chem. Soc. 7, 86 (1973)

90) Graham, S.C. and Homer, J.B.
Proc. Ninth Int. Shock Tube Symp.
Stanford Univ. Press 1973, p.712

91) Graham, S.C., Homer, J.B. and Rosenfeld, J.L.J.
Proc. Roy. Soc. A 344, 259 (1975)

92) Graham, S.C., Homer, J.B. and Rosenfeld, J.L.J.
Second Symp. (Eur.) on Combust. 1975, p. 374

93) Graham, S.C. and Homer, J.B.
Proc. Tenth Int. Shock Tube Symp.
Kyoto (Jap.) 1975, p. 621

94) Graham, S.C.
Sixteenth Symp. (Int.) on Combust.
The Combust. Inst. 1977, p. 663

95) Haynes, B.R., Jander, H. and Wagner, H. Gg.
Seventeenth Symp. (Int.) on Combust.
Leeds, Aug. 1978, in press

96) Chippett, S. and Gray, W.A.
Combust. Flame 31, 149 (1978)

97) Tesner, P.A.
Seventh Symp. (Int.) on Combust.
The Combust. Inst. 1959, p.546

98) Tesner, P.A., Snegirova, T.D. and Knorre, V.G.
Combust. Flame 17, 253 (1971)

99) Tesner, P.A., Tsygankova, Guilazetdinov, L.P., Zuyev, U.P. and Loshakova, G.V.
Combust. Flame 17, 279 (1971)

100) Tesner, P.A.
Faraday Symp. Chem. Soc. 7, p.104 (1973)

101) Hidy, G.M.
J. Colloid Sci. 20, 123 (1965)

102) Hidy, G.M. and Brock, J.R.
J. Colloid Sci. 20, 477 (1965)

103) Pich, J., Friedlander, S.K. and Lai, F.S.
Aerosol Sci. 1, 115 (1970)

104) Hidy, G.M. and Brock, J.R.
The Dynamics of Aerocolloidal Systems
Pergamon, Elmsford, N.Y., 1970

105) Lai, F.S., Friedlander, S.K., Pich, J. and Hidy, G.M.
J. Colloid Int. Sci. 39, 395 (1972)

106) Carabine, M.D.
Chem. Soc. Rev., Vol. 1, No.3, London 1972, p.411

107) Ulrich, G.D.
Combust. Sci. Techn. 4, 47 (1971)

108) Ulrich, G.D., Milnes, B.A. and Subramanian, N.S.
Combust. Sci. Techn. 14, 243 (1976)

109) Ulrich, G.D. and Subramanian, N.S.
Combust. Sci. Techn. 17, 119 (1977)

110) Place, E.R. and Weinberg, F.J.
Proc. Roy. Soc. A 289, 192 (1965)

111) Lawton, J. and Weinberg, F.J.
Electrical Aspects of Combustion
Clarendon Press, 1969

112) Mayo, P.J. and Weinberg, F.J.
Proc. Roy. Soc. A 319, 351 (1970)

113) Weinberg, F.J.
Faraday Symp., Chem. Soc., 7, 120 (1973)

114) Hardesty, D.R. and Weinberg, F.J.
Fourteenth Symp. (Int.) on Combust.
The Combust. Inst. 1973, p.907

115) Bowser, R.J. and Weinberg, F.J.
Combust. Flame 27, 21 (1976)

116) Bowser, R.J. and Weinberg, F.J.
Nature, 249, 339 (1974)

117) Prado, G.P. and Howard, J.B.
Advances Chem. Ser., ACS, ed. by Zung, J.T.
Washington D.C., in press

118) Cotton, D.H., Friswell, N.J. and Jenkins, D.R.
Combust. Flame, 17, 87 (1971)

119) Jenkins, D.R.
Combust. Sci. Techn. 5, 245 (1972)

120) Feugier, A.
First Symp. (Eur.) on Combust., p.406
Second Symp. (Eur.) on Combust., p.362

121) Palmer, H.B. and Cullis, C.F.
The Chemistry and Physics of Carbon, Vol. 1
ed. by Walker, P.L., Marcel Dekker, N.Y. 1965, p.265

122) Lahaye, J. and Prado, G.
The Chemistry and Physics of Carbon, Vol. 13
ed. by Walker, P.L., Marcel Dekker, N.Y.

123) Bittner, J.D. and Howard, J.B.
from : Alternative Hydrocarbon Fuels,
Progr. in Aeronautics and Astronautics, Vol. 62
ed. C.T. Bowman and J. Birkland, Am. Inst. Aeron. Astron., 1978

124) Wagner, H. Gg.
Plenary Lecture, Seventeenth Symp. (Int.) on Combust.,
Leeds, Aug. 1978

125) Van de Hulst, H.C.
Light scattering by small Particles,
Wiley, 1957

126) Kerker, M.
The Scattering of Light, Acad. Press, London, 1969

127) Jones, A.R. and Schwar, M.J.R.
High Temperatures - High Pressures, 1, 369 (1969)

128) Jones, A.R.
Prog. Energy Combust. Sci., in press

129) Jones, A.R.
Proc. Roy. Soc., in press

130) Rudder, R.R. and Bach, D.R.
J. Opt. Soc. Am. 58, 1260 (1968)

131) Penney, C.
J. Opt. Soc. Am. 59, 34 (1969)

132) Rowell, R.L., Aval, G.M. and Barrett, J.J.
J. Chem. Phys. 54, 1960 (1970)

J. Colloid. Int. Sci., 39, 472 (1972)

133) Stein, R.S.
J. Chem. Phys. 21, 1193 (1953)

134) Landolt-Bornstein, Ed.
Zahlenwerte und Funktionen aus Physik, Chemie, Astronomie und Technik, Band II, 8. Teil, Optische Konstanten, Springer, Berlin, 1962

135) Atlas, D., Kerker, M. and Hitschfeld, W.
J. Atm. Terr. Phys. 3, 108 (1953)

136) Gans, R.
Ann. Phys. 37, 881 (1912)

137) Asano, S. and Yamamoto, G.
Appl. Optics 14, 29 (1975)

138) Ravey, J.C.
J. Colloid Int. Sci. 46, 139 (1974)

139) Mie, G.
Ann. Phys. 25, 377 (1908)

140) Yariv, A.
Quantum Electronics, Wiley, N.Y., 1975

141) Pandya, T.P. and Weinberg, F.J.
Proc. Roy. Soc. A279, 544 (1964)

142) Thorne, A.P.
Spectrophysics, Chapman & Hall, London 1974

143) Gaydon, A.G.
The Spectroscopy of Flames, second ed.
Chapman & Hall, London, 1974

144) Haynes, B.R. and Müller-Dethlefs, K.,
unpublished results

145) Lapp, M.
in : Laser Raman Gas Diagnostics, p. 107
ed. by Lapp, M. and Penney, C.M.
Plenum Press, N.Y. and London 1974

146) Hendra, P.J., Vear, C.J., Moss, R. and Macfarlane, J.J.
in : Laser Raman Gas Diagnostics, p. 153
ed. by Lapp, M. and Penney, C.M.
Plenum Press, N.Y. and London 1974

147) Gaydon, A.G. and Wolfhardt, H.G.
Flames - Their Structure, Radiation and Temperature,
Fourth Ed., Chapman & Hall, London 1979

148) Eiden, R.
Applied Optics 10, 749 (1971)

Applied Optics 14, 2486 (1975)

149) Chippet, S. and Gray, W.A.
Combust. Flame 31, 149 (1978)

150) Weinberg, F.J.
15th Int. Symp. Comb. pp.1- 17 (1975)

151) Lloyd, S.A. and Weinberg, F.J.
Nature 251, 47 (1974)

152) Lloyd, S.A. and Weinberg, F.J.
Nature 257, 367 (1975)

153) Hardesty, D.R. and Weinberg, F.J.
Comb. Sci. Tech. 8, 201 (1974)

154) Jones, A.R., Lloyd, S.A. and Weinberg, F.J.
Proc. Roy. Soc. Lond. A 360, 97 (1978)

155) Lloyd, S.A. and Weinberg, F.J.
Comb. Flame 27, 391 (1976)

156) Khoshnoodi, M. and Weinberg, F.J.
Combust. Flame 33, 11 (1978)

157) Hilliard, J.C. and Weinberg, F.J.,
Nature 259, 556 (1976)

158) Weinberg, F.J., Hom, K.,Oppenheim, A.K. and Teichman, K.
Nature 272, 341 (1978)

159) Andrews, G.E. and Bradley, D.
Combustion and Flame, 18, 133 (1972)

160) Botha, J.P. and Spalding, D.B.
Proc. Roy. Soc. (London) A 225, 70 (1954)

161) Kaskan, W.E.
Sixth Symposium (International) on Combustion, p. 134, Reinhold, 1957

162) Bowser, R.J. and Weinberg, F.J.
Combustion and Flame, 18, 296 (1972)

163) Van Tiggelen, P.J.
private communication

164) Fox, M.D. and Weinberg, F.J.
Thirteenth Symposium (International) on Combustion, p. 641, The Combustion Institute, 1971

165) Lawton, J. and Weinberg, F.J.
Proc. Roy. Soc. (London) A 277, 468 (1964)

166) Mills, R.M.
Combustion and Flame, 12, 513 (1968).

167) Jones, G.W., Lewis, B., Friauf, J.B. and Perrott, G. St. J.
J. Am. Chem. Soc. 53, 869 (1931)

168) Müller-Dethlefs, K.
Diplomarbeit, Univ. Gottingen, 1975

169) JANAF Thermochemical Tables

APPENDIX

A1 CALCULATION OF FLAME TEMPERATURES

The determination of the (adiabatic) flame temperatures described here follows closely from an algorithm presented by Lewis et al[167]. At temperatures below 2000 K dissociation into atoms and radicals can be neglected without substantial error. For the few temperatures above 2000 K which occurred during this work (see high resolution spectroscopy) a computer program including dissociation was used. This has been employed in earlier work by the author[168]. Following the overall reaction (for 1 mole of fuel)

$$C_a H_{2b} + c O_2 + d N_2$$

$$a x CO_2 + a(1-x)CO + b y H_2O + b(1-y) H_2 + d N_2$$

and assuming water gas equilibrium, the fractions x and y were then calculated. This was done by guessing a reasonable value for the water gas equilibrium constant, at constant pressure, $K_{P\,w\,g}$, and mass balancing.

The sum of the heats of formation at 295 K of the products and the fuel was then compared with the sum of the enthalpis of the burned gases for the temperature associated with K_{Pwg}. The assumed temperature is correct if both sums are (nearly) equal. With better temperature and K_{Pwg} values the calculation is repeated until the desired agreement is reached.

The equilibrium constants and the enthalpis were taken from the JANAF tables[169]. For the flames of $C/O > 1$ only CO and H_2 were taken as combustion products, as the amounts of CO_2 and H_2O are too small to contribute significantly to the sum of the heats of formation. An upper value for the temperature was then calculated with the assumption that the unburnt fuel remained as ethylene. A lower value of the temperature was obtained by assuming that all ethylene would react to acetylene, to take into account the formation of endothermic products. The temperature for these flames was then taken to be the arithmetic means of the upper and lower limit.

The flow velocity in the burned gas of the investigated flames was correspondingly calculated from the change in mole numbers of the unburnt gas n_o to the burnt gas n_F, the inlet flow velocity v_o and the ratio of the temperatures T_F/T_{room}.

APPENDIX

A2 INFLUENCE OF REFRACTIVE INDEX ON MIE-INTENSITY FUNCTIONS AND COMPARISON WITH EXPERIMENTAL INTENSITY DISTRIBUTION AS FUNCTION OF SCATTERING ANGLE

The experimental results for the V_v and H_H scattering from fig. 55 were fitted with Mie intensity functions, by varying α and m. An existing computer program* was changed to allow for graphical output and interactive data handling on a Tektronix terminal. A refractive index near 1.5 - 0.5 i gave a very good fit to the scattering pattern, both for the i_1 and i_2, as can be seen from the following graphs. The soot particle numbers were obtained for the best α from the absolute intensity calibration, as the scattering intensity at any angle is proportional to the number density. For this, i_1 and i_2 were used, both at 45°.

$$\text{PARTN 1} = \left\{I_{VV}(\text{soot})/I_{VV}(N_2)\right\} \quad N_{N2}\, i_1(N_2)/i_1(\text{soot},\alpha)$$

$$\text{PARTN 2} = \left\{I_{HH}(\text{soot})/I_{VV}(N_2)\right\} \quad N_{N2}\, i_1(N_2)/i_2(\text{soot},\alpha)$$

These values agree quite well with the number densities obtained (for the α from Mie - theory) from the measured extinction coefficients according to

$$N_{ext} = \varepsilon_{ext}/C_{ext}(\alpha)$$

though N_{ext} was always found to be somewhat bigger than the particle numbers obtained from the scattering measurements.

---

* The supply of a computer program for the calculation of the i_1 and i_2 by Dr. A.R. Jones is gratefully acknowledged.

SELECT CONTPOL OPTION NDELTA,NX,HARD,END &HARD&
PAGE 1 OF HARDCPY COMPLETE - TYPE GO TO CONTINUE *

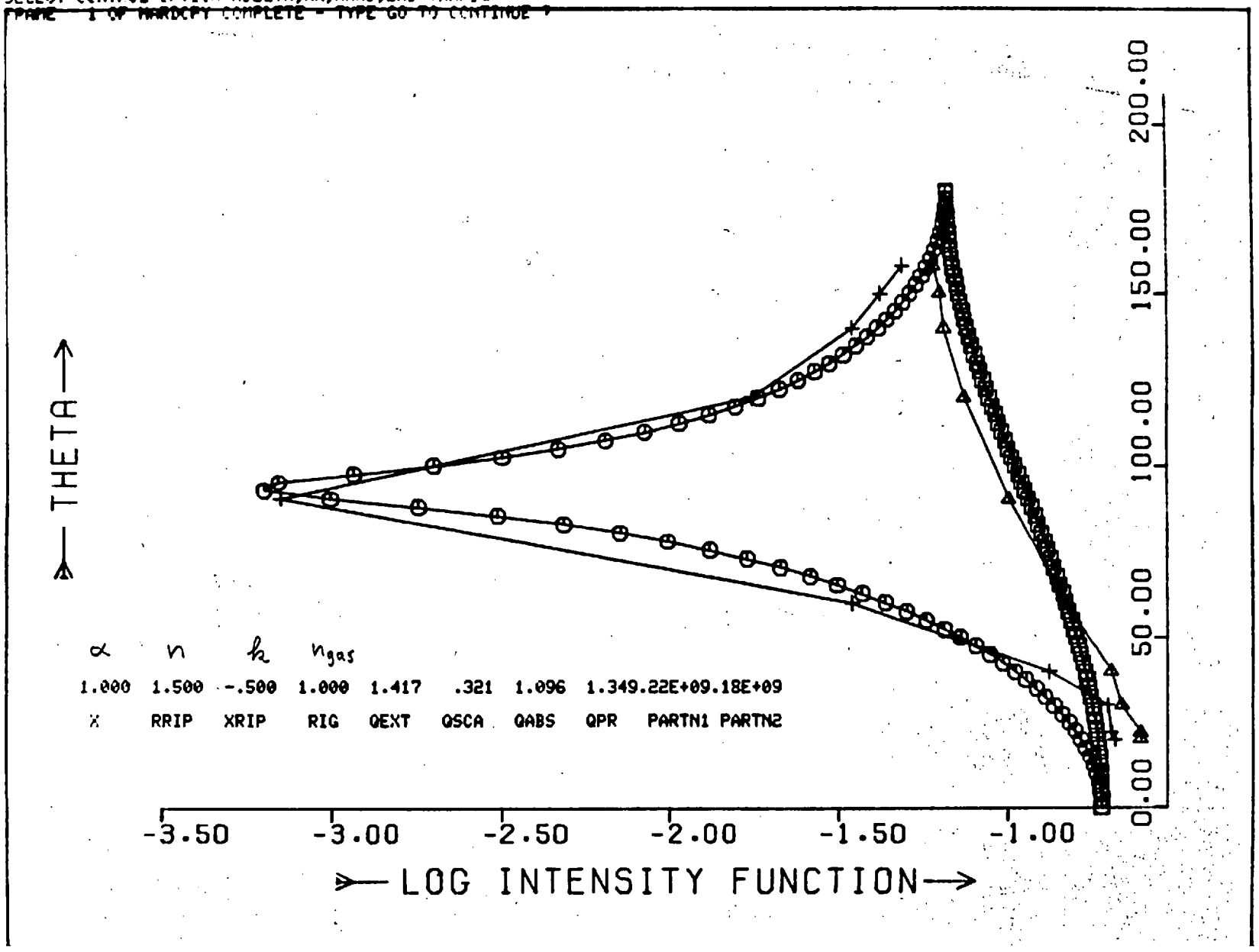

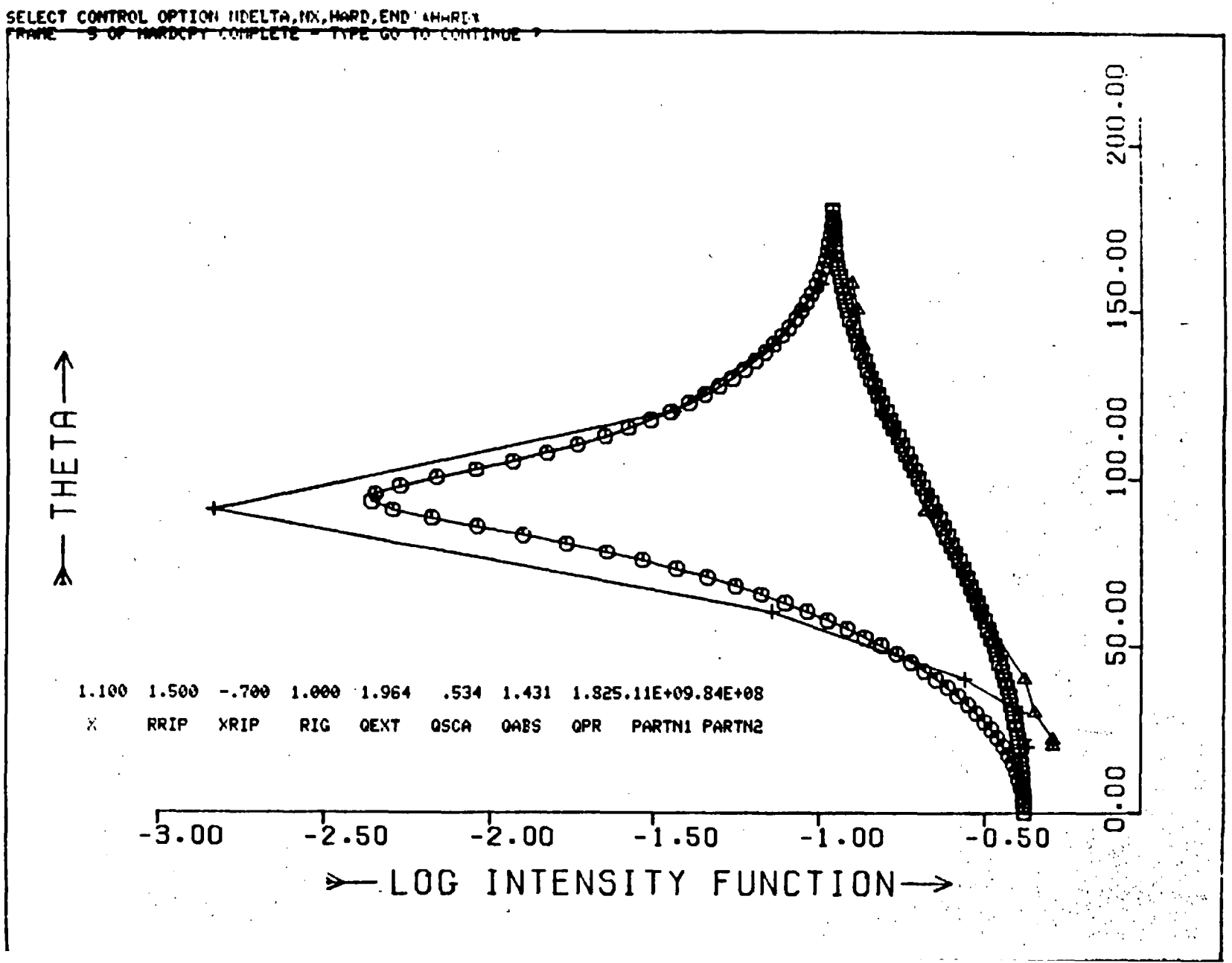
SELECT CONTROL OPTION (DELTA,MX,HARD,END
FRAME 5 OF HARDCPY COMPLETE - TYPE GO TO CONTINUE
THETA
200.00
150.00
100.00
50.00
0.00
1.100 1.500 -.700 1.000 1.964 .534 1.431 1.825.11E+09.84E+08
X RRIP XRIP RIG QEXT QSCA QABS QPR PARTN1 PARTN2
-3.00
-2.50
-2.00
-1.50
-1.00
-0.50
LOG INTENSITY FUNCTION

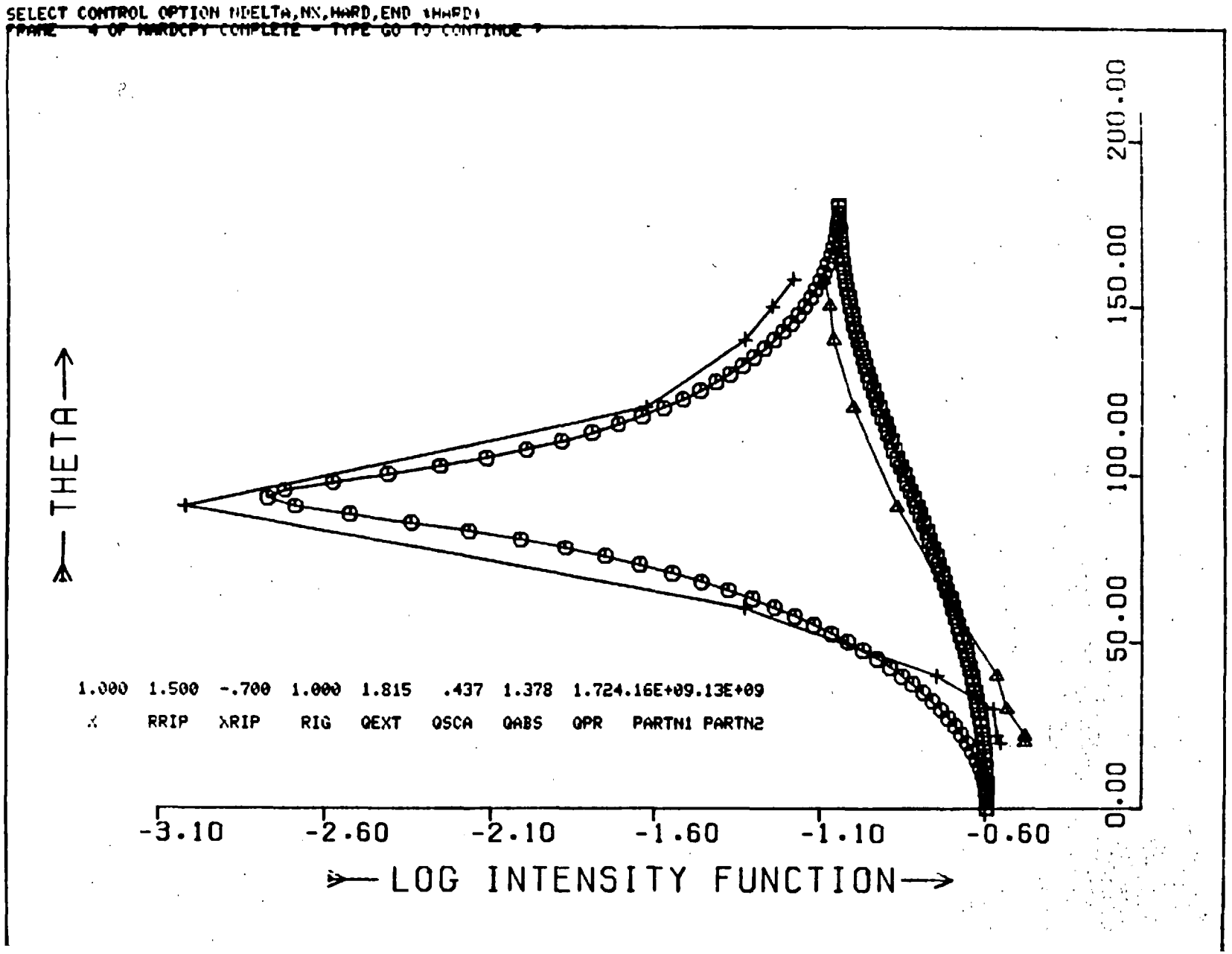
SELECT CONTROL OPTION NDELTA,NX,HARD,END (HARD)
PAGE 4 OF HARDCPY COMPLETE - TYPE GO TO CONTINUE
THETA
200.00
150.00
100.00
50.00
0.00
1.000 1.500 -.700 1.000 1.815 .437 1.378 1.724.16E+09.13E+09
X RRIP XRIP RIG QEXT QSCA QABS QPR PARTN1 PARTN2
-3.10
-2.60
-2.10
-1.60
-1.10
-0.60
LOG INTENSITY FUNCTION

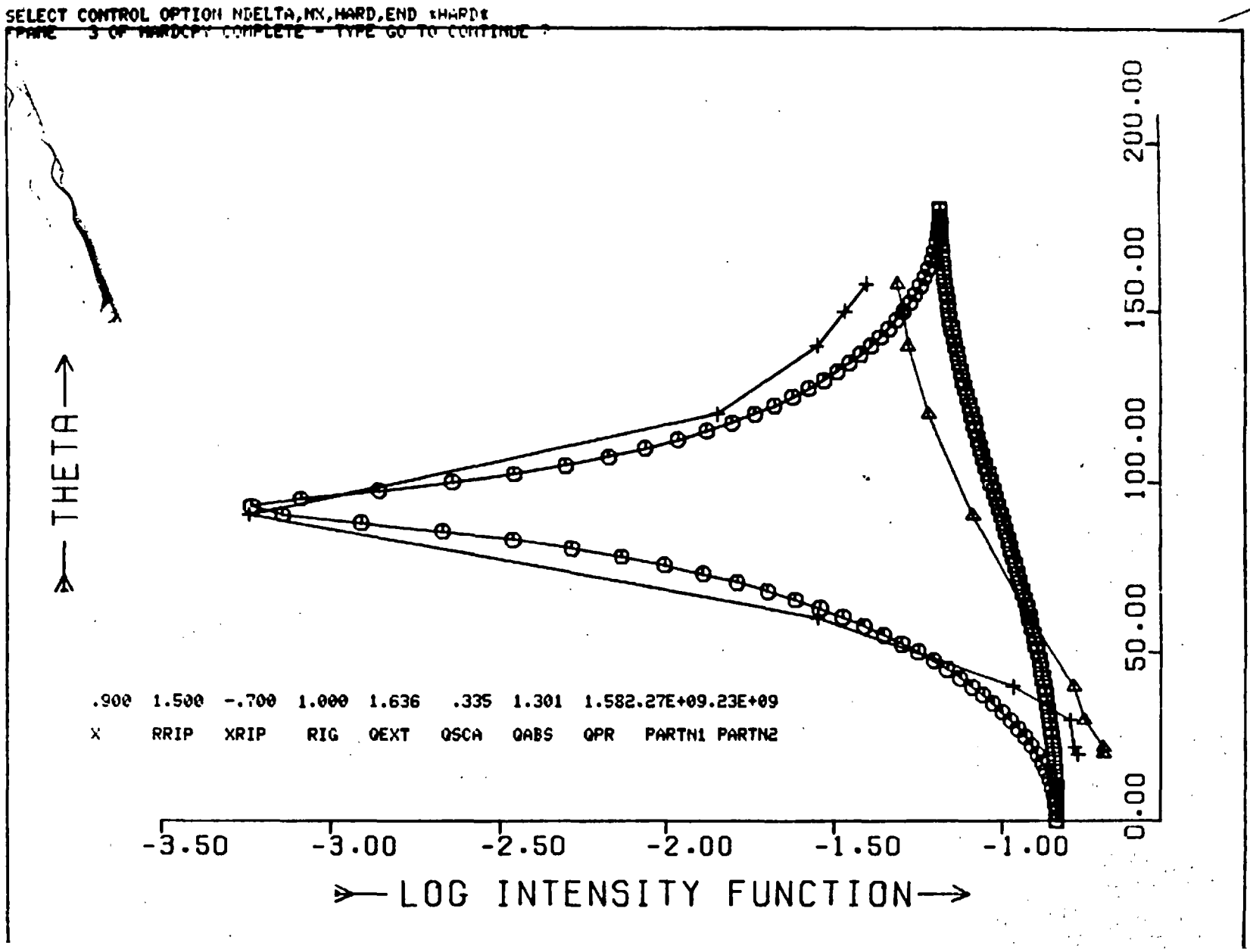
SELECT CONTROL OPTION NDELTA,MX,HARD,END *HARD*
FRAME 3 OF HARDCPY COMPLETE - TYPE GO TO CONTINUE ?
THETA
200.00
150.00
100.00
50.00
0.00
.900 1.500 -.700 1.000 1.636 .335 1.301 1.582.27E+09.23E+09
X RRIP XRIP RIG QEXT QSCA QABS QPR PARTN1 PARTN2
-3.50
-3.00
-2.50
-2.00
-1.50
-1.00
LOG INTENSITY FUNCTION

SELECT CONTROL OPTION (DELTA,NX,HARD,END (HARD)

FRAME 2 OF HARDCPY COMPLETE - TYPE GO TO CONTINUE →

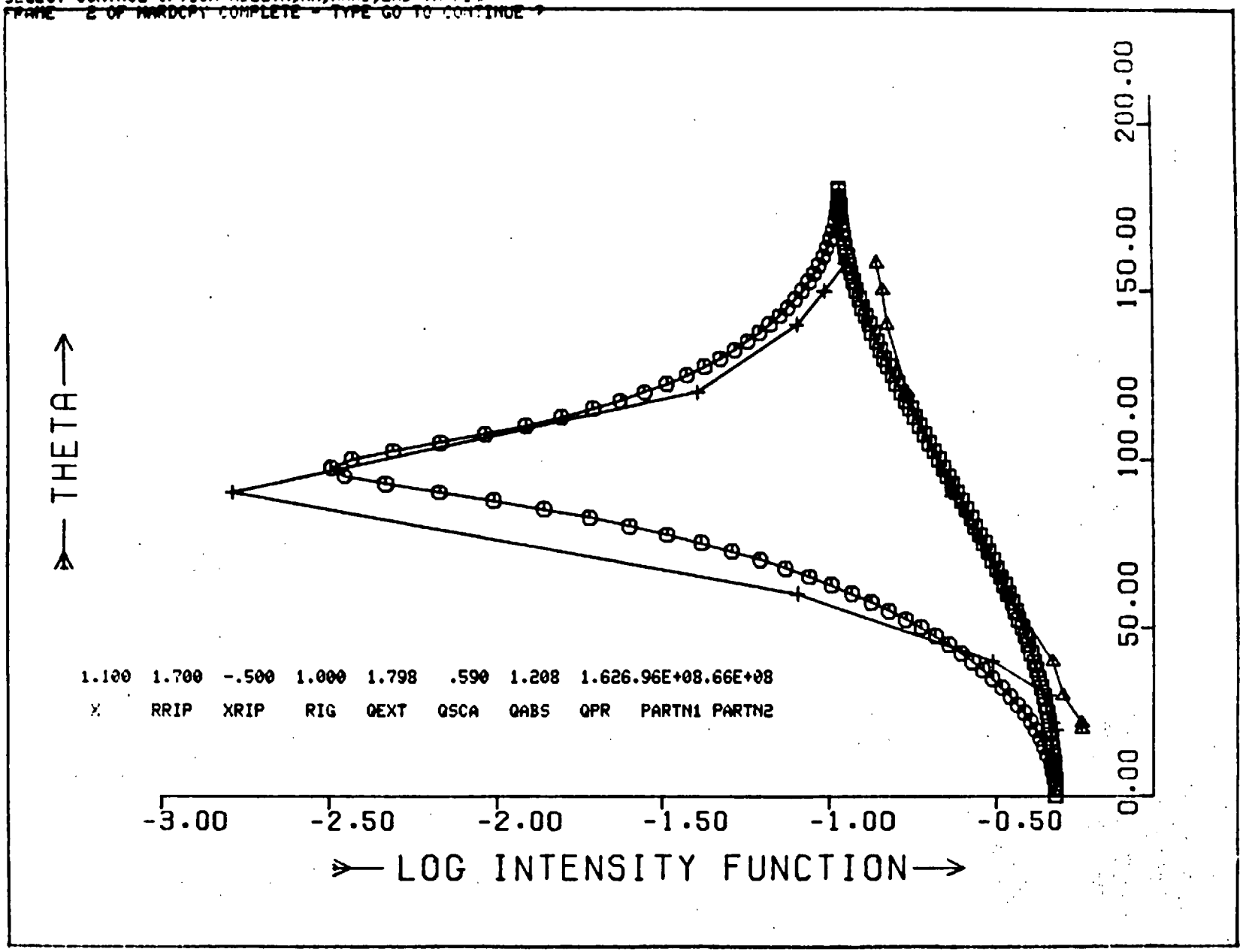

SELECT CONTROL OPTION NDELTA,NX,HARD,END $HARD1
FRAME 1 OF HARDCPY COMPLETE - TYPE GO TO CONTINUE ?

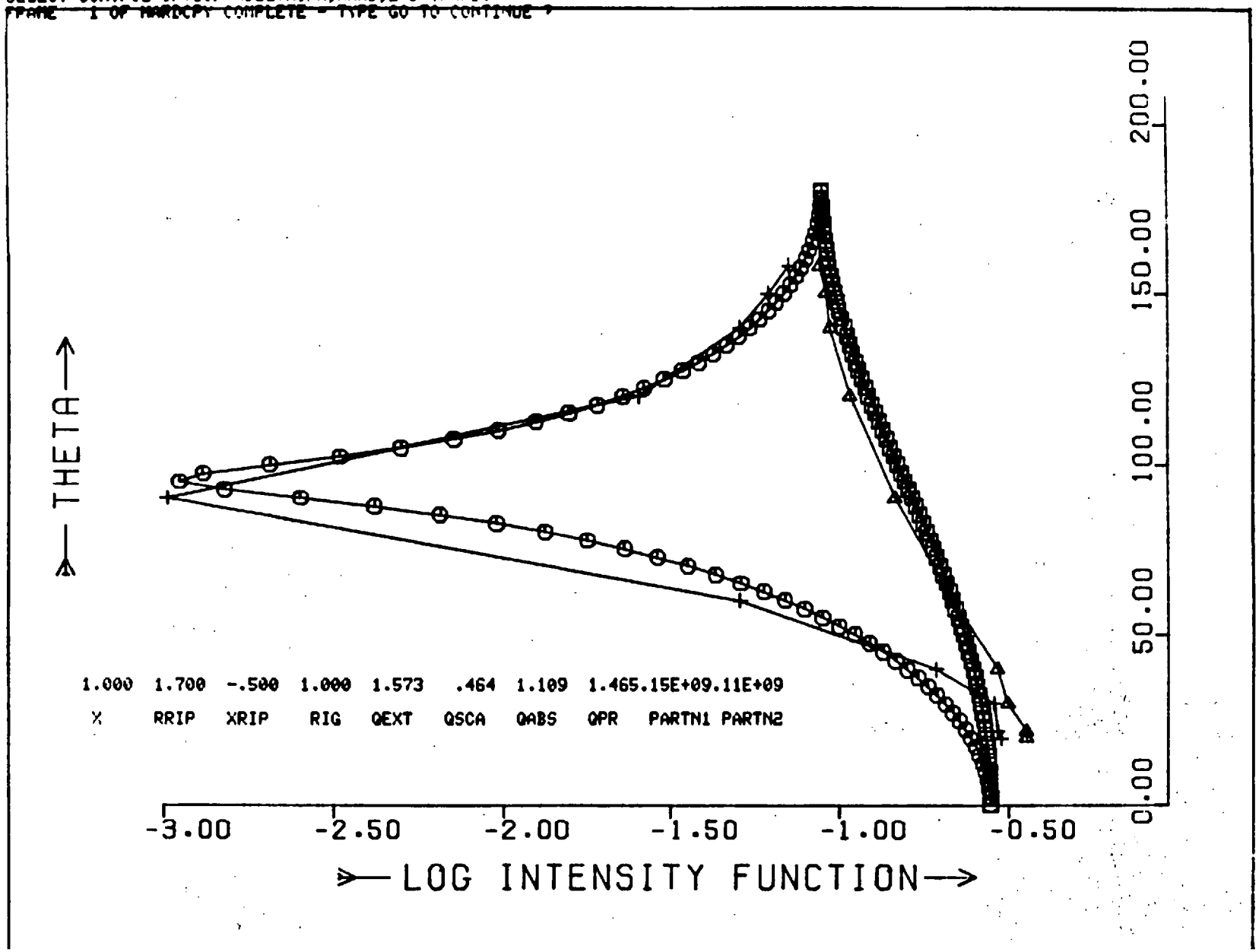

SELECT CONTROL OPTION NDELTA,NX,HARD,END $HARDx

FRAME 3 OF HARDCPY COMPLETE - TYPE GO TO CONTINUE *

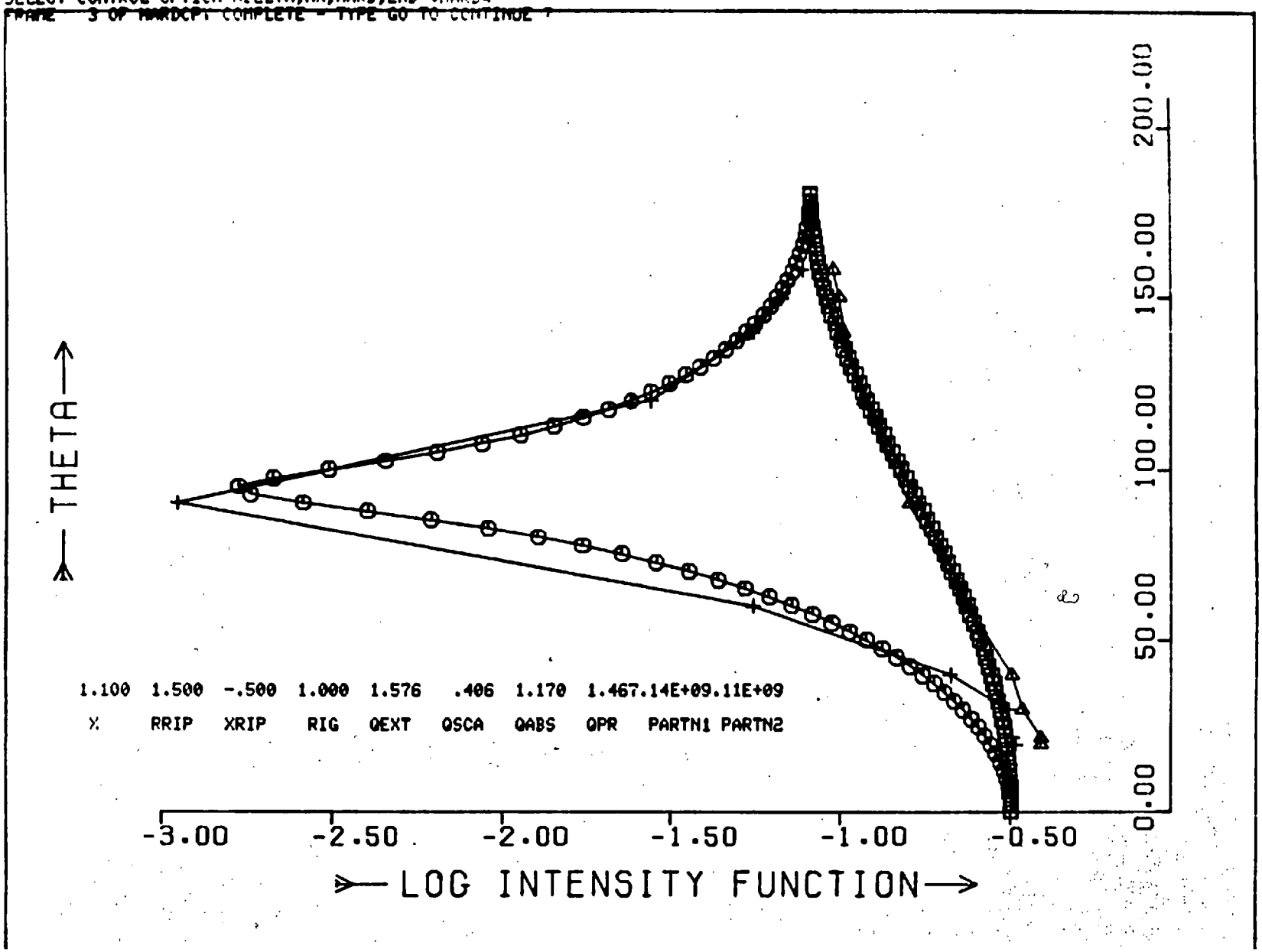

SELECT CONTROL OPTION NDELTA,NX,HARD,END $HARD$

FRAME 3 OF HARDCPY COMPLETE - TYPE GO TO CONTINUE *

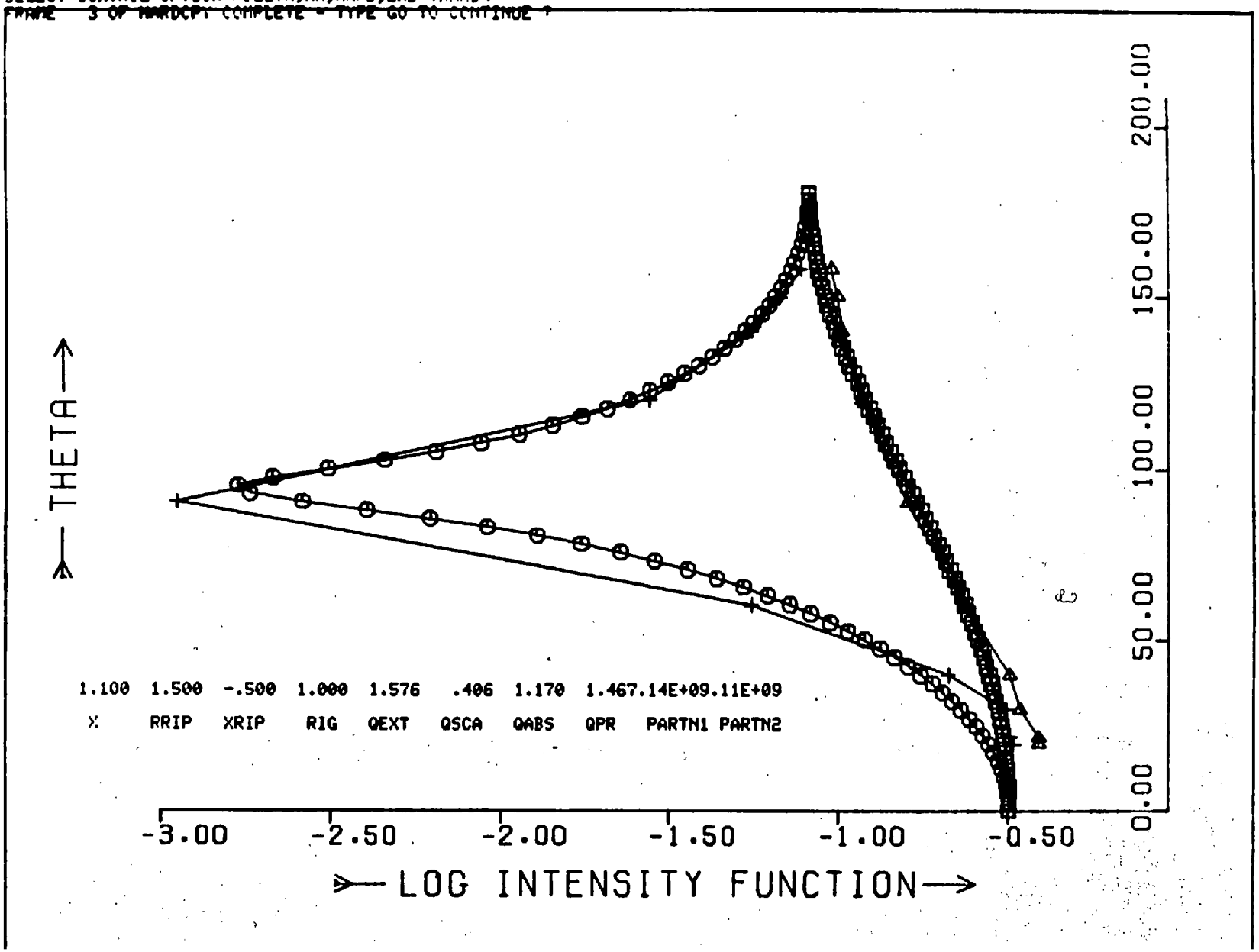

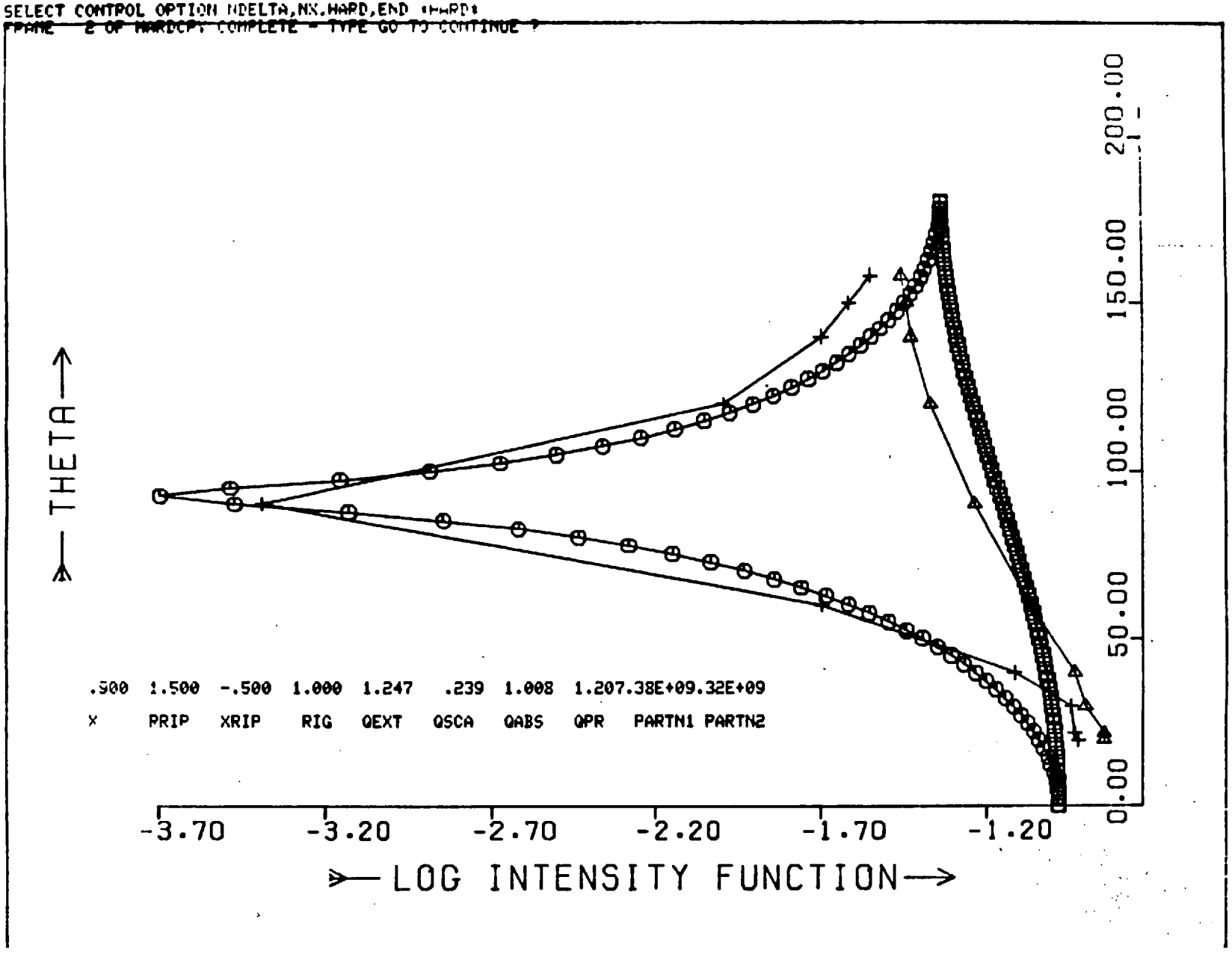
SELECT CONTROL OPTION NDELTA,NX,HARD,END (HARD)
FRAME 2 OF HARDCPY COMPLETE - TYPE GO TO CONTINUE ?
THETA
200.00
150.00
100.00
50.00
0.00
.900 1.500 -.500 1.000 1.247 .239 1.008 1.207.38E+09.32E+09
X PRIP XRIP RIG QEXT QSCA QABS QPR PARTN1 PARTN2
-3.70
-3.20
-2.70
-2.20
-1.70
-1.20
LOG INTENSITY FUNCTION